SPECTROSCOPIC AND MOLECULAR MODELING STUDIES ON THE INTERACTION OF TYROSINE KINASE INHIBITORS WITH HUMAN SERUM ALBUMIN

MD. ZAHIRUL KABIR

FACULTY OF SCIENCE
UNIVERSITY OF MALAYA
KUALA LUMPUR

2018

SPECTROSCOPIC AND MOLECULAR MODELING STUDIES ON THE INTERACTION OF TYROSINE KINASE INHIBITORS WITH HUMAN SERUM ALBUMIN

MD. ZAHIRUL KABIR

THESIS SUBMITTED IN FULFILMENT OF THE REQUIREMENTS FOR THE DEGREE OF DOCTOR OF PHILOSOPHY

INSTITUTE OF BIOLOGICAL SCIENCES
FACULTY OF SCIENCE
UNIVERSITY OF MALAYA
KUALA LUMPUR

2018

UNIVERSITY OF MALAYA
ORIGINAL LITERARY WORK DECLARATION

Name of Candidate: Md. Zahirul Kabir
Matric No: SHC 140015
Name of Degree: Doctor of Philosophy (Ph.D.)
Title of Dissertation: "Spectroscopic and molecular modeling studies on the interaction of tyrosine kinase inhibitors with human serum albumin"

Field of Study: Biochemistry

I do solemnly and sincerely declare that:

(1) I am the sole author/writer of this work;
(2) This Work is original;
(3) Any use of any work in which copyright exists was done by way of fair dealing and for permitted purposes and any excerpt or extract from, or reference to or reproduction of any copyright work has been disclosed expressly and sufficiently and the title of the Work and its authorship have been acknowledged in this Work;
(4) I do not have any actual knowledge nor do I ought reasonably to know that the making of this work constitutes an infringement of any copyright work;
(5) I hereby assign all and every rights in the copyright to this Work to the University of Malaya ("UM"), who henceforth shall be owner of the copyright in this Work and that any reproduction or use in any form or by any means whatsoever is prohibited without the written consent of UM having been first had and obtained;
(6) I am fully aware that if in the course of making this Work I have infringed any copyright whether intentionally or otherwise, I may be subject to legal action or any other action as may be determined by UM.

Candidate's Signature Date:
Subscribed and solemnly declared before,

Witness's Signature Date:
Name: Professor Dr. Saad Tayyab
Designation: Supervisor

Witness's Signature Date:
Name: Dr. Saharuddin Bin Mohamad
Designation: Supervisor

Witness's Signature Date:
Name: Associate Professor Dr. Zazali Bin Alias
Designation: Supervisor

SPECTROSCOPIC AND MOLECULAR MODELING STUDIES ON THE INTERACTION OF TYROSINE KINASE INHIBITORS WITH HUMAN SERUM ALBUMIN

ABSTRACT

Targeted therapies, involving new class drug molecules have shown inhibitory activities against signaling pathways that are responsible for triggering various carcinomas. Tyrosine kinases form an important class of enzymes of these signaling pathways and can be a useful target to develop effective therapeutic agents as tyrosine kinase inhibitors to treat various cancers. Some of the FDA-approved drug molecules, known as tyrosine kinase inhibitors are vandetanib (VDB), lapatinib (LAP), gefitinib (GEF) and sunitinib (SU), which are currently being used for the treatment of medullary thyroid, breast, lung and renal cancers, respectively. Interaction mechanisms of VDB, LAP, GEF and SU binding to human serum albumin (HSA), the major transport protein in the human blood circulation were explored using various spectroscopic techniques such as fluorescence, absorption and circular dichroism (CD) along with *in silico* studies. Quenching of the protein fluorescence upon addition of these ligands was characterized as the static quenching, which confirmed the complex formation between the ligand and the protein. Such complex formation was also affirmed by absorption spectral results. Moderate binding affinity for these interactions was evident from the binding constant (K_a) values, obtained at 298 K, which had fallen in the range of 10^4–10^5 M^{-1} except VDB–HSA interaction, which showed relatively weaker binding affinity. Thermodynamic data for the binding equilibria predicted involvement of hydrophobic and van der Waals interactions along with hydrogen bonds in stabilizing drug–HSA complexes, which was also supported by molecular docking results. The far-UV and the near-UV CD spectra showed changes in the secondary and the tertiary structures, respectively, of HSA upon ligand binding. Three-dimensional fluorescence

spectral results also indicated ligand-induced microenvironmental perturbations around protein fluorophores. Binding of these ligands to HSA offered significant protection to the protein against thermal denaturation. Competitive site-marker displacement results as well as molecular docking analyses revealed preferred binding location of these drug molecules primarily at site I for VDB and SU while at site III for LAP and GEF, located in subdomains IIA and IB, respectively, of HSA. The influence of a few common ions on the binding reaction between the ligand and HSA was also noticed.

Keywords: tyrosine kinase inhibitors, human serum albumin, ligand–protein interaction, fluorescence quenching, molecular docking

KAJIAN SPEKTROSKOPI DAN PERMODELAN MOLEKUL MENGENAI INTERAKSI PERENCAT TIROSIN KINASE DENGAN ALBUMIN SERUM MANUSIA

ABSTRAK

Terapi sasaran melibatkan kelas dadah baru telah menunjukkan aktiviti perencatan terhadap laluan isyarat yang bertanggungjawab mencetus pelbagai jenis karsinoma. Tirosina kinase membentuk suatu kelas enzim yang penting dalam laluan isyarat tersebut, serta merupakan sasaran berguna untuk membangunkan agen terapeutik berkesan seperti perencat tirosina kinase bagi mengubati pelbagai jenis kanser. Antara contoh dadah jenis perencat tirosina kinase yang diluluskan Pentadbiran Makanan dan Dadah (FDA) adalah vandetanib (VDB), lapatinib (LAP), gefitinib (GEF) dan sunitinib (SU), yang kini digunakan untuk rawatan kanser tiroid medula, kanser payudara, kanser paru-paru dan kanser ginjal. Mekanisme interaksi VDB, LAP, GEF dan SU dengan albumin serum manusia (HSA), iaitu protein pengangkut utama dalam sistem peredaran darah manusia, telah diselidik menggunakan pelbagai kaedah spektroskopik seperti kependarfluoran, penyerapan dan dikroisme bulatan (CD) serta kajian *in silico*. Pelindapkejutan kependarfluoran protein dengan penambahan ligan-ligan tersebut telah dicirikan sebagai pelindapkejutan statik, sekaligus mengesahkan pembentukan kompleks antara ligan dan protein. Pembentukan kompleks tersebut juga disokong oleh hasil kajian spektra penyerapan. Afiniti pengikatan bagi interaksi-interaksi tersebut didapati sederhana daripada nilai konstan kesatuan (K_a) pada suhu 298 K yang ditemui dalam julat 10^4–10^5 M^{-1}, kecuali bagi interaksi VDB-HSA yang menunjukkan afiniti pengikatan yang lebih lemah secara relatif. Data termodinamik bagi keseimbangan pengikatan meramalkan penglibatan daya hidrofobik dan van der Waals serta ikatan hidrogen dalam penstabilan kompleks dadah−HSA, yang juga disokong hasil eksperimen dok molekular. Spektra CD ultralembayung jauh dan dekat menggambarkan

perubahan terhadap struktur sekunder dan tertier HSA apabila diikat dengan ligan. Hasil eksperimen spektra pendarfluor tiga dimensi juga menunjukkan gangguan dalam persekitaran mikro fluorofore protein oleh ligan. Pengikatan ligan-ligan tersebut dengan HSA memberi perlindungan ketara kepada protein tersebut daripada penyahaslian terma. Hasil eksperimen anjakan dadah kompetitif serta analisis dok molekular mendedahkan keutamaan tapak pengikatan molekul-molekul dadah tersebut di tapak I bagi VDB dan SU dan tapak III bagi LAP dan GEF, masing-masing terletak dalam subdomain IIA dan IIB HSA. Beberapa ion lazim juga didapati mempengaruhi tindak balas pengikatan antara ligan dengan HSA.

Kata kunci: perencat tirosina kinase, albumin serum manusia, interaksi ligan–protein, pelindapkejutan kependarfluoran, dok molekular

ACKNOWLEDGEMENTS

With deep regards and profound respect, I am exceedingly grateful for the leadership and direction of my supervisors Professor Saad Tayyab, Dr. Saharuddin Bin Mohamad and Associate Professor Dr. Zazali Bin Alias throughout my doctoral program. Their wisdom, vision, and experience have greatly benefitted me in my study. I highly appreciate their never-ending kindness and encouragement and consider myself very fortunate to have worked under their tutelage.

I heartily owe my sincere gratitude and thankfulness to Professor Dr. Zanariah Abdullah**,** Dean, Faculty of Science and Associate Professor Dr. Nurhayati Zainal Abidin, Head, Institute of Biological Sciences, University of Malaya for providing necessary facilities to complete the research work.

Drs. Shevin Rizal Bin Feroz and Wong Yin How are sincerely acknowledged and appreciated for providing valuable and constructive suggestions and being supportive during the experimental work. I would like to give hearty thanks to Nurul Iman Ahamed Kameel for her inspirative support throughout the research work.

The financial assistance from the University of Malaya in the form of Doctoral Fellowship under the Bright Sparks Program (BSP/APP/1892/2013) is gratefully acknowledged. This PhD study would not have been possible without the financial support, I received under this program. I also acknowledge the financial support, received from the University of Malaya in the form of Postgraduate Research Fund (PPP) (Project Number: PG236-2015A).

I express my small adoration and heartfelt devotion to my beloved parents for their countless blessings, affection and incessant inspiration that has given me the strength during my study.

Md. Zahirul Kabir
April, 2018

TABLE OF CONTENTS

LIST OF FIGURES

LIST OF TABLES

LIST OF SYMBOLS AND ABBREVIATIONS

ABL	:	Abelson tyrosine kinase
Ack	:	Activated CDC42 kinase
Ala	:	Alanine
ALK	:	Anaplastic lymphoma kinase
Arg	:	Arginine
Asn	:	Asparagine
ATP	:	Adenosine triphosphate
Asp	:	Aspartic acid
a.u.	:	Arbitrary unit
Å	:	Angstrom
$BaCl_2$	:	Barium chloride
BSA	:	Bovine serum albumin
BTK	:	Bruton's tyrosine kinase
$CaCl_2$	:	Calcium chloride
CD	:	Circular dichroism
CDK4/6	:	Cyclin-dependent kinase 4/6
cm	:	Centimeter
Csk	:	C-terminal Src kinase
$CuCl_2$	:	Copper (II) chloride
Cys	:	Cysteine
Da	:	Dalton
DGT	:	Digitoxin
DMSO	:	Dimethyl sulphoxide
DZM	:	Diazepam

3-D	:	Three-dimensional
e.g.	:	Latin phrase *exempli gratia* (for example)
EGFR	:	Epidermal growth factor receptor
Eq.	:	Equation
ERK	:	Extracellular signal-regulated kinase
ESA	:	Equine serum albumin
FAK	:	Focal adhesion kinase
FDA	:	Food and Drug Administration
Fes	:	Feline sarcoma
FGFR	:	Fibroblast growth factor receptor
FI	:	Fluorescence intensity
GEF	:	Gefitinib
Gln	:	Glutamine
Glu	:	Glutamic acid
Gly	:	Glycine
ΔG	:	Gibbs free energy change
h	:	Hour
HER2	:	Human epidermal growth factor receptor 2
HGFR/MET	:	Hepatocyte growth factor receptor
HMN	:	Hemin
His	:	Histidine
HSA	:	Human serum albumin
ΔH	:	Enthalpy change
i.e.	:	Latin phase *id est* (that is)
Ig	:	Immunoglobulin
Ile	:	Isoleucine

IDM : Indomethacin

J : Joules

Jak : Janus kinase

K : Kelvin

K_a : Association / binding constant

KCl : Potassium chloride

KTN : Ketoprofen

K_{SV} : Stern-Volmer constant

k_q : Bimolecular quenching rate constant

kJ : Kilojoules

LAP : Lapatinib

Leu : Leucine

Lys : Lysine

M : Molar

mABs : Monoclonal antibodies

MAPK : Mitogen-activated protein kinase

Met : Methionine

MEK : Tyrosine/serine/threonine protein kinase

mdeg : Millidegree

mg : Milligram

$MgCl_2$: Magnesium chloride

min : Minute

ml : Milliliter

mM : Millimolar

$MnCl_2$: Manganese (II) chloride

MW : Molecular weight

nm : Nanometer

nRTK : Non-receptor tyrosine kinase

μM : Micromolar

μm : Micrometer

PBZ : Phenylbutazone

PDB : Protein Data Bank

PDGFR : Platelet-derived growth factor receptor

PDK1 : 3-Phosphoinositide-dependent protein kinase 1

pH : Potential of hydrogen

PI3K : Phosphoinositide 3-kinase

Phe : Phenylalanine

PTEN : Phosphatase and tensin homolog

PTK : Protein tyrosine kinase

Pro : Proline

PVDF : Polyvinylidene fluoride

R : Gas constant

r : Correlation coefficient

RETR : Rearranged during transcription receptor

RSA : Rabbit serum albumin

RTK : Receptor tyrosine kinase

s : Second

Ser : Serine

SH1 : Src homology 1

SH2 : Src homology 2

SH3 : Src homology 3

Src : Sarcoma

SU : Sunitinib

Syk : Spleen tyrosine kinase

ΔS : Entropy change

T : Temperature

Tec : Tyrosine kinase expressed in hepatocellular carcinoma

TKI : Tyrosine kinase inhibitor

Thr : Threonine

TOR : Target of rapamycin

Trp : Tryptophan

Tyr : Tyrosine

UV : Ultraviolet

UV-Vis : Ultraviolet-visible

V : Voltage

Val : Valine

VDB : Vandetanib

VEGFR : Vascular endothelial growth factor receptor

viz. : Latin phrase *videlicet* (that is to say)

v/v : Volume / volume

WHO : World Health Organization

$ZnCl_2$: Zinc chloride

λ_{em} : Emission wavelength

λ_{ex} : Excitation wavelength

~ : Approximate

% : Percentage

> : Greater than

CHAPTER 1: INTRODUCTION

Cancer is one of the major leading causes of deaths globally. According to the World Health Organization (WHO) report, the most common cancer incidences, estimated worldwide are those of the lung, breast and large bowel cancers (Stewart & Wild, 2014). Due to undesirable side effects of traditional cancer therapies (Shih & Wang, 2007), newer approaches for cancer treatments are in great demand. Targeted therapies are being developed, which use new class drug molecules to inhibit signaling pathways that are responsible for triggering various carcinomas, *viz.*, breast, lung, thyroid and kidney cancers (Vanneman & Dranoff, 2012). Since tyrosine kinases play an important role in signaling pathways, various key promising drug molecules, known as tyrosine kinase inhibitors are being synthesized and tested as therapeutic agents to treat various cancers (Gross-Goupil et al., 2013). Four tyrosine kinase inhibitors, namely, vandetanib (VDB), lapatinib (LAP), gefitinib (GEF) and sunitinib (SU) are Food and Drug Administration (FDA)-approved drug molecules, which are currently being used in the treatment of different carcinomas. Whereas, VDB is used for treating medullary thyroid cancer, LAP, GEF and SU are employed in the treatment of breast, lung and renal cancers, respectively (Brassard & Rondeau, 2012; Higa & Abraham, 2007; Tourneau et al., 2007; Yanase et al., 2004). These drug molecules compete with ATP for the ATP-binding site of the 'epidermal growth factor receptor' (EGFR) and the 'vascular endothelial growth factor receptor 2 (VEGFR2)' tyrosine kinases and subsequently freeze the functions of certain signal transduction pathways, essential for tumour cell growth, thus control cancer development (Raymond et al., 2000). Therefore, these drugs are being used as a supplementary therapy along with chemotherapy and radiation therapy (Vanneman & Dranoff, 2012).

The study of drug–protein interaction is of fundamental importance in understanding its action in the body. Transport, disposition and pharmacokinetics of a drug can be

influenced by its reversible binding to the transport proteins (Kragh-Hansen, 2013). Such interactions are important as low binding affinity of a drug to the protein may result in its poor distribution and short half-life in the blood, whereas high binding affinity interferes with the desired drug efficacy (Hall et al., 2013; Kragh-Hansen et al., 2002). Binding of a drug to the protein may also affect protein's conformation as well as its physiological action (Kragh-Hansen et al., 2013). Therefore, insights into the specificity of the drug's binding to the transport protein might be vital for therapeutic agent's development (Kragh-Hansen et al., 2002).

Serum proteins, *i.e.*, serum albumin and α-1-acid glycoprotein as well as lysozyme are generally used as the model carrier proteins in ligand-protein interaction studies (Ajmal et al., 2016; Barreca et al., 2013; Feroz et al., 2015; Shen et al., 2015). Among serum proteins, human serum albumin (HSA) is the main transporter of many drugs to their target sites through the bloodstream (Peters, 1996) due to its ability to bind reversibly a wide variety of drugs with higher affinity (Kragh-Hansen, 1990). It is a single polypeptide chain of 585 amino acid residues, distributed in three domains I, II and III, which are further compartmentalized into subdomains A and B. Three well-characterized ligand binding sites, *viz.*, I, II and III, located in the hydrophobic cavities of subdomains IIA, IIIA and IB, respectively, of HSA are primarily responsible for the effective transport of various drugs in the blood circulation (Kragh-Hansen et al., 2002; Sudlow et al., 1975). Therefore, it is important to understand the characteristics of a drug–HSA interaction.

1.1 Problem statement

Despite several reports, highlighting the pharmacological significance of VDB, LAP, GEF and SU, various questions remain to be answered.

1. Are these drugs, *viz.*, VDB, LAP, GEF and SU transported through binding to HSA in blood circulation?
2. Do the above drugs form stable drug–HSA complex?
3. Is there any affect of the drug binding on HSA conformation and stability?

1.2 Aim and objectives of the study

Therefore, the aim of the present research was to explore the binding characteristics of ligand (VDB, LAP, GEF and SU)–HSA interaction.

In order to answer the above questions and to achieve the research goal, following objectives were set.

1. To study the characteristics of the interaction of four ligands, *i.e.*, VDB, LAP, GEF and SU with HSA in terms of binding affinity and forces involved in the ligand–protein complex formation.
2. To investigate ligand-induced alterations in the secondary and tertiary structures of HSA upon ligand–protein complexation.
3. To probe the changes in the microenvironment around protein fluorophores upon ligand binding.
4. To evaluate the effect of ligand binding on the thermal stability of HSA.
5. To investigate the influence of metal ions on the ligand–HSA interaction.
6. To identify location of the ligand (VDB, LAP, GEF and SU) binding site on HSA and corroborate the binding sites of these ligands with molecular docking.

CHAPTER 2: LITERATURE REVIEW

2.1 Background

Knowledge about the incidence and mortality statistics of cancer is vital to prevent and manage the disease. In 2012, World Health Organization (WHO) estimated 14.1 million new incidences along with 8.2 million deaths caused by various cancers worldwide (Stewart & Wild, 2014). Among the large number of cancers diagnosed each year, lung, breast, kidney and thyroid cancers remain the most common causes of death. Significant cancer deaths were estimated in 2012 from these cancers, *viz.*, 1.69 million from lung cancer, 0.57 million due to breast cancer, 0.32 million due to kidney cancer and 0.23 million from thyroid cancer globally (Stewart & Wild, 2014). Several external factors, *e.g.*, tobacco, unhealthy diet and physical inactivity and internal factors such as mutations are primarily responsible for increasing the incidences of cancer (Torre et al., 2016). These factors mainly influence regular functions of the cellular signaling pathways that control cell growth, division and differentiation. Such influences may lead to overexpression, mutation and dysregulation of protein tyrosine kinases that are key regulatory elements of certain signaling pathways (Raval et al., 2016). Therefore, various cancers can be induced as a result of the uncontrolled activities in the cellular signaling pathways. In order to control and prevent the cancer mortality, it is crucial to identify molecular as well as cellular targets that are responsible for different cancers. In view of it, protein tyrosine kinases can be the ideal targets for the therapeutic developments in cancer management (Raval et al., 2016).

2.2 Signal transduction pathways and protein tyrosine kinases

Signal transduction is the cellular process by which outside signals are transmitted into the cell through its membrane receptors. Binding of various ligands such as growth factors and hormones to their receptors at the cell surface activates the signal transduction pathways, which may trigger protein kinase cascades and subsequently

stimulate the intracellular chain of signaling molecules (Bode & Dong, 2005, Rowinsky, 2003). Protein tyrosine kinases (PTKs), which play vital roles in such type of signal transduction pathways (Mano, 1999) are enzymes, primarily responsible for regulation of various cellular functions such as cell signaling, growth, migration, differentiation and survival. PTKs catalyze the transfer of the phosphate group of ATP to tyrosine residues of protein substrates. However, the functions of PTKs are strictly regulated in normal cells (Hubbard & Till, 2000). Autophosphorylation is the key regulatory mechanism to control the normal cellular activities of PTKs (Hubbard & Till, 2000). Protein phosphorylation through addition of a phosphate group to protein's tyrosine residues induces conformational change in the protein, which regulate the activation or deactivation of PTKs (Summers et al., 2011). Abnormal activation of PTKs may result in the uncontrolled cell proliferation, progression and migration, which are considered to be vital in the process of cancer development (Rowinsky, 2003).

PTKs are divided into two classes, namely, receptor tyrosine kinases (RTKs) and non-receptor tyrosine kinases (nRTKs). RTKs are transmembrane proteins, which are subdivided into several families, *viz.*, 'epidermal growth factor receptor' (EGFR), 'vascular endothelial growth factor receptor' (VEGFR), 'platelet-derived growth factor receptor' (PDGFR), 'fibroblast growth factor receptor' (FGFR) and 'hepatocyte growth factor receptor' (HGFR/MET) (Hubbard & Till, 2000). On the other hand, nRTKs are present in the nucleus, the cytosol and the inner surface of the plasma membrane. The Src, 'abelson tyrosine kinase' (ABL), 'focal adhesion kinase' (FAK) and Janus kinase are well known members of nRTKs subfamilies (Hubbard & Till, 2000). RTKs are activated upon ligand binding and trigger the activation of subsequent downstream signaling pathways in cells, which induce cell proliferation, differentiation and migration (Hubbard & Till, 2000). Due to the presence of the ligand binding sites as

well as transmembrane domains in RTKs, they are extensively studied as the molecular targets for anti-cancer drug delivery (Hubbard & Till, 2000; Raval et al., 2016).

2.3 Receptor tyrosine kinases

Receptor tyrosine kinases (RTKs) are transmembrane proteins, which are composed of an extracellular part, a transmembrane α−helix and an intracellular portion. The extracellular part of RTKs includes a cluster of various globular domains such as immunoglobulin (Ig)-like, EGF-like, fibronectin type III-like and cysteine-rich domains (Hubbard & Till, 2000). On the other hand, organization of the intracellular portion of RTKs involves juxtamembrane region, tyrosine kinase catalytic domain and a carboxy-terminal region (Figure 2.1) (Hubbard & Till, 2000). The tyrosine kinase domain is divided into two parts, which are joined by a flexible polypeptide linker, the kinase insert. Intracellular juxtamembrane region, activation loop of the kinase domain and the C-terminal tail check the activity of kinase domain in the absence of ligand. Regions along with the kinase insert are populated with Tyr residues, which undergo autophosphorylation upon ligand binding (Hubbard & Till, 2000; Toffalini & Demoulin, 2010). The activation of RTKs results in dimerization and autophosphorylation of intracellular tyrosine residues within the receptor protein, which leads to the activation of downstream signaling pathways (Segaliny et al., 2015). As shown in Figure 2.2, two principal intracellular signaling pathways, *viz.*, mitogen-activated protein kinase (MAPK) / RAS and phosphoinositide 3-kinase (PI3K) / AKT play key role in the RTK-mediated signal transduction processes (Wicki et al., 2016). Binding of a ligand, such as growth factor to the extracellular domain initiates the physiological activation of RTKs, which triggers RTK dimerization and Tyr autophosphorylation. This allows opening of the essential docking sites for other regulatory proteins to bind (Segaliny et al., 2015; Wicki et al., 2016). Thus, MAPK and

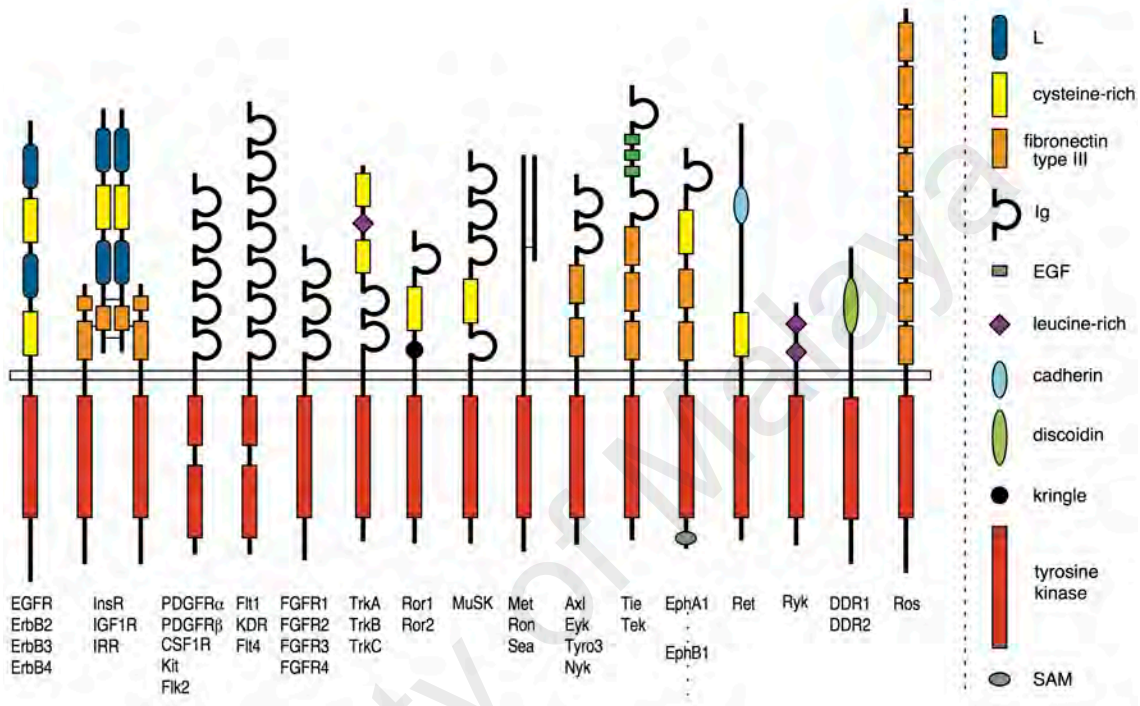

Figure 2.1: Diagram showing domain organization for receptor tyrosine kinase (RTKs) families. The extracellular part (top), the cytoplasmic portions (bottom), involving the tyrosine kinase domain of some RTKs are marked.
(Taken from Hubbard & Till, 2000).

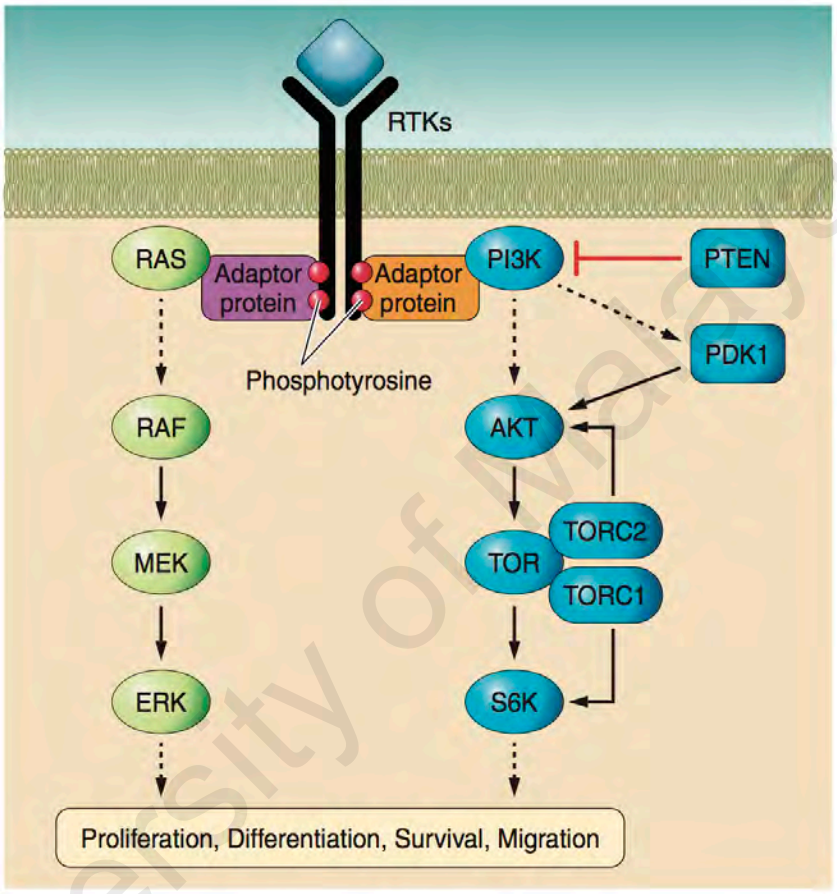

Figure 2.2: Diagram showing signaling pathways of receptor tyrosine kinases. (Taken from Wicki et al., 2016).

PI3K/AKT signaling pathways are activated, which can initiate subsequent cellular responses at transcriptional and translational levels (Wicki et al., 2016). In MAPK / RAS signaling cascade, activated RAS triggers protein kinase activity of RAF kinase, which phosphorylates and subsequently activates 'tyrosine/serine/threonine protein kinase' (MEK) and 'extracellular signal-regulated kinase' (ERK) (Figure 2.2) (Wicki et al., 2016). On the other hand, MAPK / RAS pathway can also activate the PI3K signaling pathway while the 'phosphatase and tensin homolog' (PTEN) is responsible for the regulation of PI3K signaling (Milella et al., 2010). By receiving regulatory signals from RAS pathway, the PI3K activates AKT or '3-phosphoinositide-dependent protein kinase 1' (PDK1). Activated AKT transduces signals towards the 'target of rapamycin' (TOR) complexes, including TORC1 and TORC2. The TORC1 pathway subsequently stimulates the ribosomal S6 kinases (S6K) (Figure 2.2). These downstream signaling pathways of RTKs can induce cell proliferation, differentiation, survival and migration (Milella et al., 2010; Wicki et al., 2016).

Since overexpression, dysregulation and mutation of RTKs trigger various cancers (Raval et al., 2016), these have attracted the attention of researchers to search inhibitor molecules for RTK family members to be used as therapeutic agents for the treatment of RTK-dependent cancers (Boettner & Aelst, 2002; Evelyn et al., 2007).

2.4 Non-receptor tyrosine kinases

Non-receptor tyrosine kinases (nRTKs) contain neither extracellular ligand-binding domain nor transmembrane region. Therefore, most nRTKs are mostly resided in the cytoplasm. However, some nRTKs are connected to the cell membrane through amino-terminal modification (Hubbard & Till, 2010). The nRTKs possess important tyrosine kinase catalytic domain, comprising of 275 amino acid residues (Figure 2.3). Additional domains that facilitate protein-protein, protein-lipid and protein-DNA interactions are also present in nRTKs. The Src homology 2 (SH2) and 3 (SH3) domains are the most

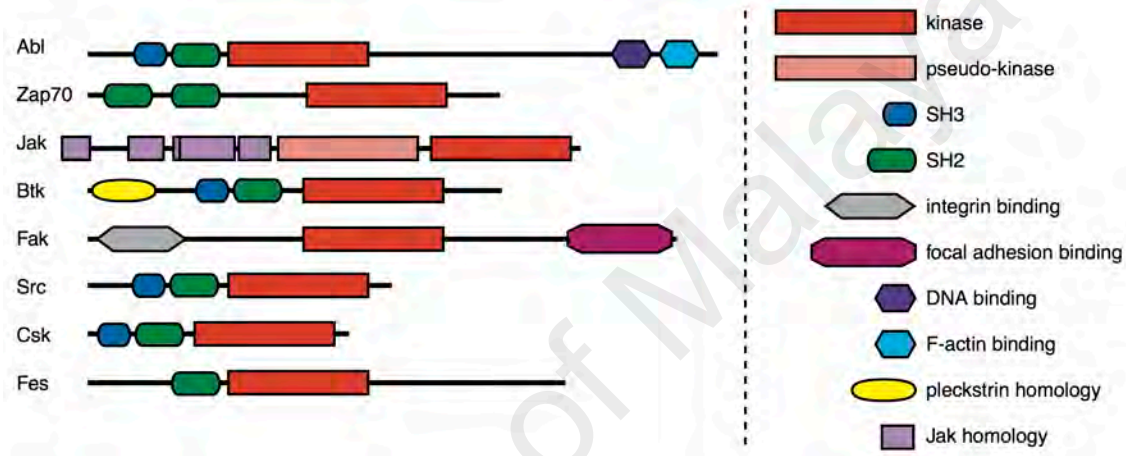

Figure 2.3: Diagram showing domain organization of the major subfamilies of non-receptor tyrosine kinase (nRTKs). The amino terminus (left) and the carboxy terminus (right) are also displayed.
(Taken from Hubbard & Till, 2000).

common protein-protein interaction domains in nRTKs (Figure 2.3) (Hubbard & Till, 2000). The catalytic Src Homology 1 (SH1), p-Tyr binding Src Homology 2 (SH2) and protein–protein interaction Src Homology 3 (SH3) domains share a high degree of homology (Gocek et al., 2014). Although some nRTKs lack SH2 and SH3 domains (e.g., Jak and Fak families) but contain subfamily-specific domains used for protein-protein interactions (Hubbard & Till, 2000). Based on similarities in kinase domain structures, nRTKs are further subdivided into nine (*viz.*, Abl, Ack, Csk, Fak, Fes, Jak, Src, Tec and Syk) subfamilies. Among nRTKs, Src forms the largest family and regulation of Src catalytic activity has been extensively studied (Hubbard & Till, 2000; Gocek et al., 2014).

Activation of nRTKs are initiated by RTKs as well as other cell surface receptors such as G protein-coupled receptors and receptors of the immune system (Hubbard & Till, 2000). Similar to RTKs, activity of nRTKs is strictly controlled in normal cells. Dysregulation, overexpression and mutation of nRTKs are associated in malignant transformation as well as carcinogenesis (Gocek et al., 2014). These nRTKs are also considered as the molecular targets for anticancer drug development. Several potent nRTKs inhibitors are currently being used in the treatment of various cancers and many are under investigation (Gocek et al., 2014).

2.5 Cancer control and management

Traditionally, cancers are being treated with conventional therapies such as chemotherapy, radiation therapy, surgery and hormonal supplements. These treatments often cause a variety of side effects including damaging normal cells, pain, vomiting, excessive hair loss and depression (Shih & Wang, 2007). Due to these undesirable side effects, a new line of targeted therapeutic agents, *i.e.*, promising anticancer drug molecules is being developed for the treatment of various carcinomas (Shih & Wang, 2007). Targeted therapies involving new class drug molecules have shown less harmful

effects on normal tissues and their functions, act on cancer-associated specific molecular targets, less toxic and provide better quality of life for the patients (Arteaga, 2001; Saini et al., 2012; Salomon et al., 1995). These promising drug molecules increase the therapeutic effect by blocking / inhibiting the targets of RTKs signaling pathways. The drug molecules, extracted from natural sources and / or synthetic compounds are being used for cancer treatment in combination with chemotherapy, radiation therapy and surgery (Neidle & Thurston, 2005; Nobili et al., 2009). Natural products obtained from the plants, microorganisms and animals have significantly contributed to the development of promising drug molecules with therapeutic potential for various cancers (Demain & Vaishnav, 2011; Nobili et al., 2009). On the other hand, chemically synthesized small-molecule compounds, based on various molecular targets of cancers have shown encouraging results (Neidle & Thurston, 2005). These products have exhibited potential anti-cancer activities by interfering with certain signaling pathways and blocking the development and progression of tumor cells (Nobili et al., 2009). Various chemically synthesized molecules have been found to be novel inhibitors of RTKs and nRTKs signaling pathways (Table 2.1) and have shown promising therapeutic potential in the treatment of numerous human carcinomas (Evelyn et al., 2007; Sahai & Marshall, 2002).

2.6 Tyrosine kinase inhibitors

A family of small molecules, known as tyrosine kinase inhibitors (TKIs) has shown substantial inhibitory activities against different signaling pathways (Vanneman & Dranoff, 2012). However, monoclonal antibodies (mABs) have also been developed as promising agents for various cancer treatments that target RTKs of cell membrane (Raval et al., 2016). These inhibitor molecules can quickly reach their specific target sites in signaling pathways and reduce or block the abnormal proliferation of various carcinomas (Brassard & Rondeau, 2012). TKI molecules have drawn attention

of scientists due to their multi-targeted functions by offering a wide range of anticancer activities along with reduced toxic effects (Arteaga, 2001). These molecules compete with ATP for the ATP binding site and subsequently fit themselves inside the tunnel of the catalytic domain of RTKs, thus inhibit their activation. On the other hand, mABs are able to block the binding of ligand to the extracellular part of RTKs and induce deactivation of RTKs by avoiding their essential conformational rearrangement, and thus halt the activation of downstream signaling pathways (Fauvel & Yasri, 2014). Various antibody drugs (*viz.*, panitumumab, pertuzumab and trastuzumab) and their molecular targets of RTKs along with therapeutic interest are well studied (Table 2.1). In the absence of active RTKs, signaling cascade of the kinases is blocked, which is responsible for the growth and migration of cancers (Fabbro et al., 2002). Figure 2.4 shows the overview of the mechanism(s) of action of some TKIs (e.g., imatinib, gefitinib, erlotinib, nilotinib, dasatinib, sorafenib and sunitinib), which can interfere with the MAPK / RAS and PI3K / AKT signaling pathways (Eckstein et al., 2014). Owing to the anticancer properties of TKIs, several such inhibitor molecules have been developed as promising anticancer drugs and got the approval of Food and Drug Administration, USA, (FDA) for the treatment of various cancers (Table 2.1). In this study, four FDA-approved potential TKIs, *i.e.*, vandetanib (VDB), lapatinib (LAP), gefitinib (GEF) and sunitinib (SU), which are currently being used in anticancer therapy were selected to investigate their interaction with human serum albumin (HSA).

2.6.1 Vandetanib

Vandetanib (N-(4-bromo-2-fluorophenyl)-6-methoxy-7-[(1-methyl-4-piperidinyl)methoxy]-4-quinazolinamine), whose chemical structure is shown in Figure 2.5, is a chemically synthesized potential and selective tyrosine kinase inhibitor of the VEGFR2, EGFR and RETR (‘rearranged during transcription receptor’) (Brassard & Rondeau, 2012; Sano et al., 2011). VDB was approved by FDA in 2011 for clinical applications

Table 2.1: Different tyrosine kinase inhibitors, their molecular targets and therapeutic interests for cancers.

Tyrosine Kinase Inhibitor	Molecular Target	Therapeutic Interest	Reference
Afatinib	EGFR	Non-small-cell lung cancer	Minkovsky & Berezov (2008)
Alectinib	ALK	Non-small-cell lung cancer	McKeage (2015)
Axitinib	VEGFR	Renal cell carcinoma	Gross-Goupil et al. (2013)
Bosutinib	BCR-ABL, SRC	Chronic myelogenous leukemia	Cortes et al. (2011)
Brigatinib	ALK, EGFR	Non-small-cell lung cancer	Huang et al. (2016)
Brivanib	VEDFR2	Hepatocellular carcinoma	Huynh et al. (2008)
Cabozantinib	c-MET, VEGFR2	Medullary thyroid cancer Renal cell carcinoma	Lee & Smith (2014) Smith et al. (2014)
Canertinib	EGFR	Breast cancer	Allen et al. (2002)
Cediranib	VEGFR	Lung, Kidney and Colorectal cancers	Goss et al. (2009)
Ceritinib	ALK	Non-small-cell lung cancer	Shaw et al. (2014)
Cetuximab	EGFR	Lung, Colorectal, Head and Neck cancers	Messersmith & Ahnen (2008)
Cobimetinib	MEK	Advanced melanoma	Larkin et al. (2014)
Crizotinib	ALK	Non-small-cell lung cancer	Sahu et al. (2013)
Dabrafenib	MEK	Advanced melanoma	Gibney & Zager (2013)
Dasatinib	Src	Chronic myelogenous leukemia	Keskin et al. (2016)

Table 2.1: continued.

Tyrosine Kinase Inhibitor	Molecular Target	Therapeutic Interest	Reference
Dovitinib	VEGFR	Breast cancer	Musolino et al. (2017)
Emtansine	ERBB2	Breast cancer and Gastric cancer	Barok et al. (2014)
Erlotinib	EGFR	Lung cancer Pancreatic cancer	Furugaki et al. (2011) Nabhan et al. (2009)
Gefitinib	EGFR	Non-small-cell lung cancer	Yanase et al. (2004)
Ibrutinib	BTK	Chronic lymphocytic leukemia	Kaur & Swami (2017)
Imatinib	PDFGR BCR-ABL	Chronic myelogenous leukemia Acute lymphocytic leukemia	Tiffany et al. (2004) Mathew et al. (2004)
Lapatinib	EGFR, HER-2	Breast cancer	Tevaarwerk & Kolesar (2009)
Leflunomide	PDGFR	Prostate cancer	Ko et al. (2001)
Lenvatinib	VEGFR	Thyroid cancer	Matsui et al. (2008)
Neratinib	VEGFR	Breast cancer	Echavarria et al. (2017)
Nilotinib	PDGFR BCR-ABL	Chronic myelogenous leukemia	Laurie & Goss (2013)
Onantinib	VEGFR, PDGFR, EGFR	Lung, Breast, Kidney, Gastric and Prostate cancers	Trzcinska-Daneluti et al. (2012)
Osimertinib	EGFR	Non-small-cell lung cancer	Tan et al. (2015)

Table 2.1: continued.

Tyrosine Kinase Inhibitor	Molecular Target	Therapeutic Interest	Reference
Palbociclib	CDK4, CDK6	Breast cancer	Finn et al. (2009)
Panitumumab	ErbB1, EGFR	Colorectal cancer	Gibson et al. (2006)
Pazopanib	VEGFR, PDGFR	Renal cell carcinoma	Laurie & Goss (2013)
Pertuzumab	ERBB2	Breast cancer and Gastric cancer	Barok et al. (2014)
Ponatinib	BCR-ABL	Acute lymphocytic leukemia and Chronic myeloid leukemia	Cortes et al. (2011)
Semaxinib	VEGFR	Acute myeloid leukemia	Fiedler et al. (2003)
Sorafenib	VEGFR2, VEGFR-3	Renal and Hepatocellular carcinomas	Eckstein et al. (2014)
Sutent	VEGFR, PDGFR	Kidney cancer	Mendel et al. (2002) Eskens (2004)
Sunitinib	PDGFR, VEGFR	Renal cancer and Gastrointestinal stromal tumors	Tourneau et al. (2007)
Trastuzumab	ERBB2	Breast cancer and Gastric cancer	Barok et al. (2014)
Vatalanib	VEGFR	Colorectal, Liver, Prostate and Renal cell cancers	Steward et al. (2003); Bergsland (2004)
Vandetanib	EGFR, VEGFR, RET	Medullary thyroid cancer	Wedge et al. (2002)

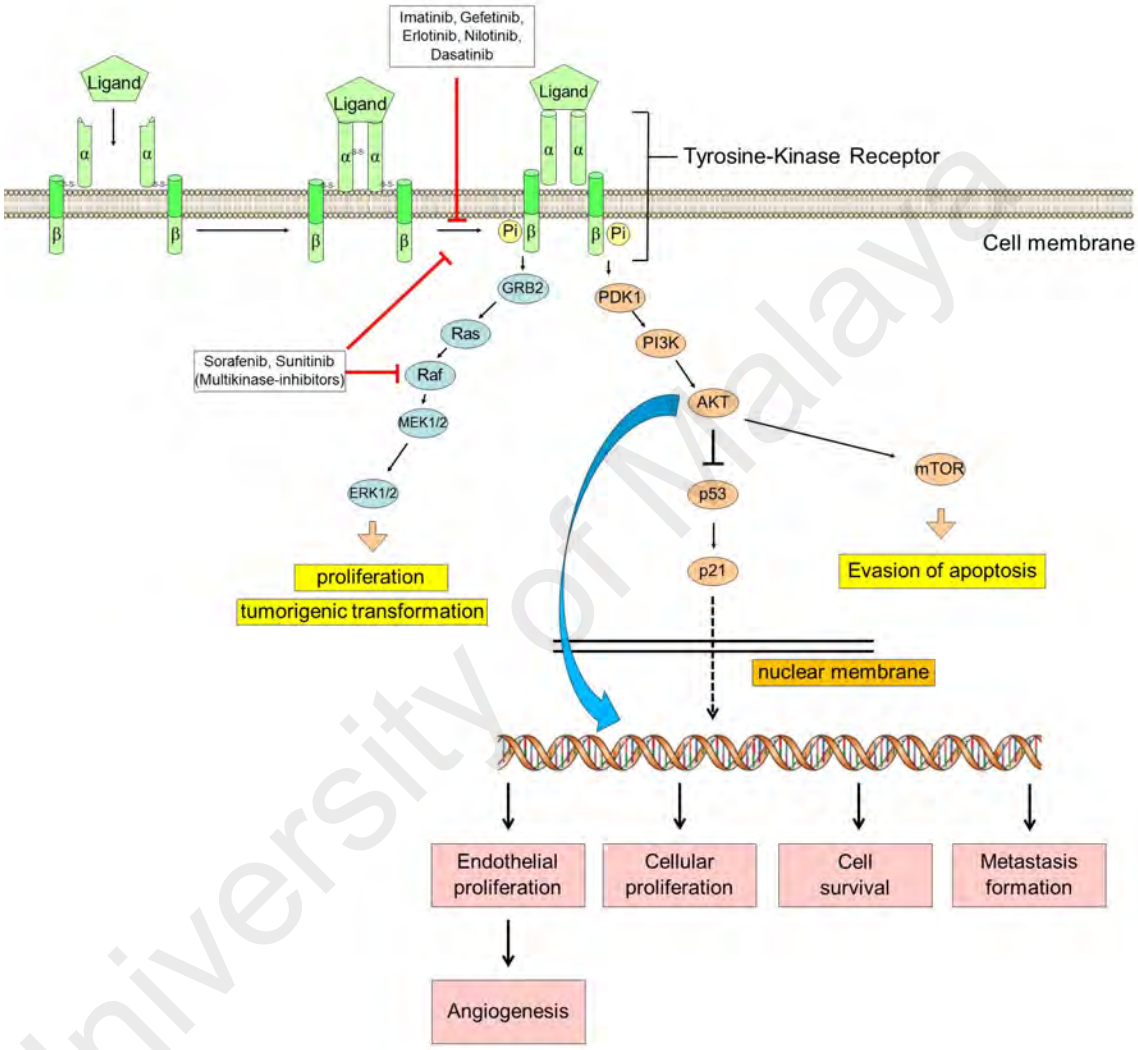

Figure 2.4: Schematic diagram showing the tumorigenic signaling pathways and their inhibition by receptor tyrosine kinase inhibitor molecules. (Adapted from Eckstein et al., 2014).

A

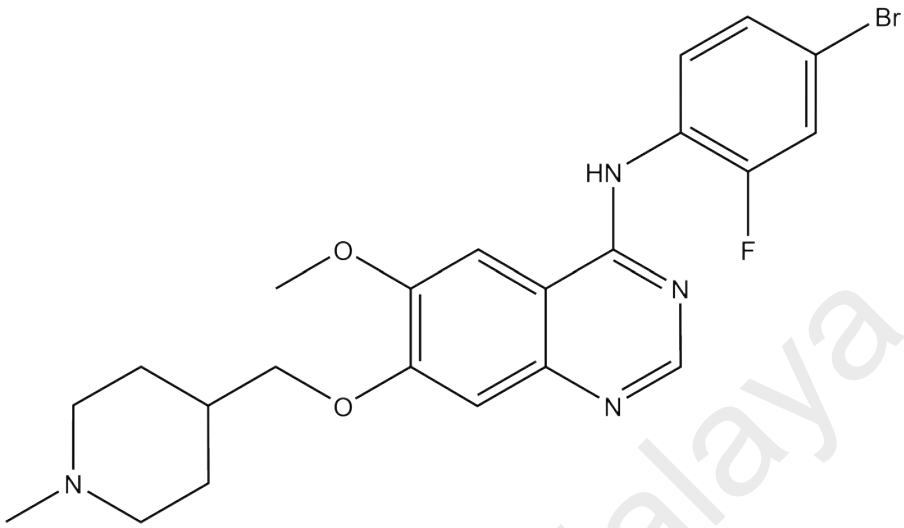

B

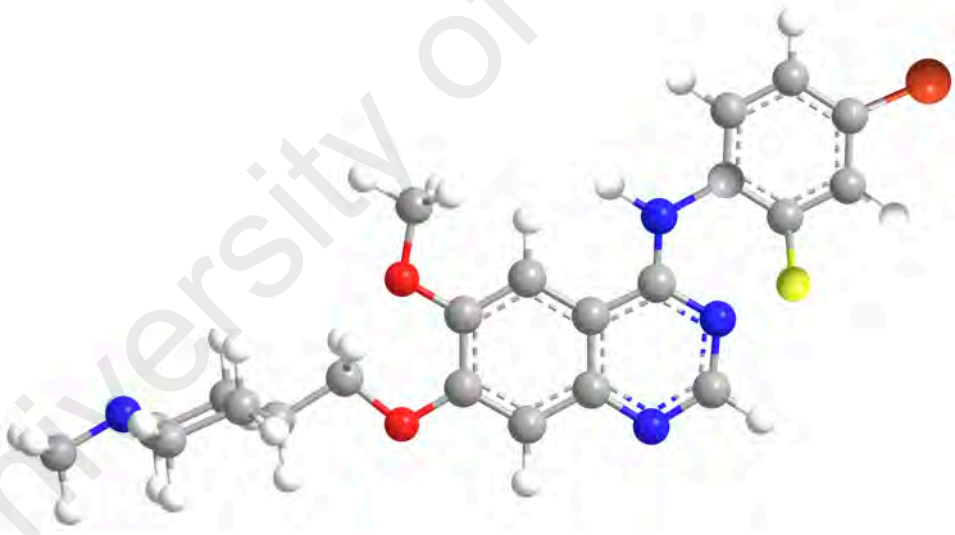

Figure 2.5: Structural representations of vandetanib. (A) Chemical structure, (B) Ball-and-stick model.

(Brassard & Rondeau, 2012). It is an orally administered drug, used for the treatment of advanced or metastatic medullary thyroid cancer due to its inhibitory action against VEGFR2 and EGFR, which are the key pathways in the development of medullary thyroid cancer (Wedge et al., 2002). It binds to the ATP binding pockets of the receptor kinases and halts the downstream signaling pathways, thus assists in preventing the growth of the medullary thyroid cancer (Brassard & Rondeau, 2012). VDB also inhibits the activity of RETRs, which are responsible for the proliferation of non-small lung cancer cells (Yoh et al., 2016). Many studies have shown impressive responses of VDB in controlling proliferation of these cancer cells (Arora & Scholar, 2005; Lin et al., 2002; Yoshikawa et al., 2009). Although, some side effects such as diarrhea, rash, fatigue, high blood pressure, headache and nausea are commonly observed in VDB therapy, majority of them are manageable by adjusting the dosages of VDB (Wells et al., 2012). Therefore, cancer treatment with VDB is well tolerated and its discontinuation rate is very low (Wells et al., 2012).

2.6.2 Lapatinib

Lapatinib (N-[3-chloro-4-[(3-fluorophenyl)methoxy]phenyl]-6-[5-[[[2-(methylsulfo-nyl)ethyl]amino]methyl]-2-furanyl]-4-quinazolinamine), whose chemical structure is shown in Figure 2.6 is one of the key promising drug molecules, approved by FDA in 2007 (Higa & Abraham, 2007). It is being used to develop a safe and effective targeted therapy against breast cancer. LAP, a small hydrophobic tyrosine kinase inhibitor, is known to suppress the abnormal activity of the human epidermal growth factor receptor 2 (HER2) and EGFR by inhibiting their phosphorylation (Arteaga et al., 2012; Tsang et al., 2011). It blocks certain signal transduction pathways that are responsible for tumour cell growth, and therefore prevents tumour growth (Arteaga et al., 2012; Tsang et al., 2011). The clinical efficacy of LAP in combination with capecitabine has been shown effective against HER2-positive breast cancer (Tevaarwerk & Kolesar, 2009).

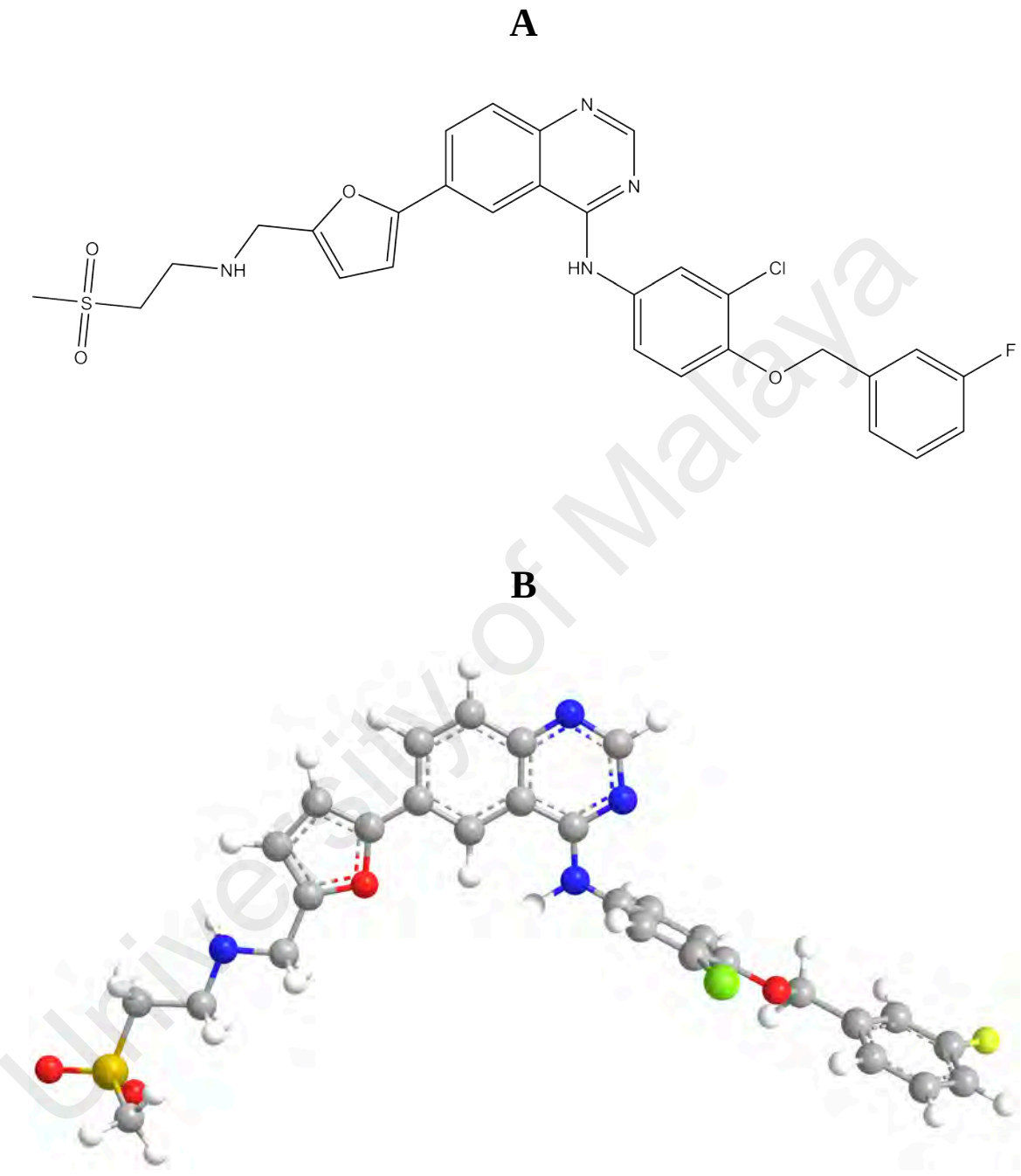

Figure 2.6: Structural representations of lapatinib. (A) Chemical structure, (B) Ball and-stick model.

Furthermore, LAP-loaded HSA nanoparticles have also been proposed to be a safe therapy against HER2-positive cells (Wan et al., 2015). A combination therapy involving LAP and other chemotherapeutic agents, *viz.*, vinorelbine and letrozole is currently being assessed in various clinical trials (Liao et al., 2010). In addition, LAP has also shown promising results in the treatment of central nervous system metastasis and is being evaluated in various clinical settings (Liao et al., 2010). This drug appears to have very low cardiotoxicity and is well tolerated in patients with diarrhea, nausea, fatigue, dry skin and rashes, being the moderate adverse effects (Liao et al., 2010; Moy & Goss, 2006).

2.6.3 Gefitinib

Among the wide variety of anticancer drugs used in clinical routine for the treatment of non-small cell lung cancer (Raymond et al., 2000; Yanase et al., 2004), gefitinib (N-(3-chloro-4-fluorophenyl)-7-methoxy-6-[3-(4-morpholinyl)propoxy]-4-quinazolina-mine) is one of the newly FDA-approved drug, whose chemical structure is shown in Figure 2.7. GEF is an orally administered, reversible tyrosine kinase inhibitor of EGFR. It competes with ATP for the ATP- binding site of the EGFR tyrosine kinase and subsequently freezes the functions of the signaling cascade of the kinase, thus prevents malignancy (Arora & Scholar, 2005). GEF may cause some adverse effects, which include diarrhea, rash, acne, dry skin, and pruritus. Acceptable tolerability profiles have not been evaluated while used in combinations with other cytotoxic drugs (Costanzo et al., 2011). However, this drug has shown safety, tolerance and therapeutic efficacy as a single drug to treat non-small cell lung cancer (Burotto et al., 2015).

2.6.4 Sunitinib

Sunitinib (N-[2-(diethylamino)ethyl]-5-[(Z)-(5-fluoro-1,2-dihydro-2-oxo-3H-indol-3-ylidene)methyl]-2,4-dimethyl-1H-pyrrole-3-carboxamide), whose chemical structure is shown in Figure 2.8 is FDA-approved multi-targeted oral drug, which possesses

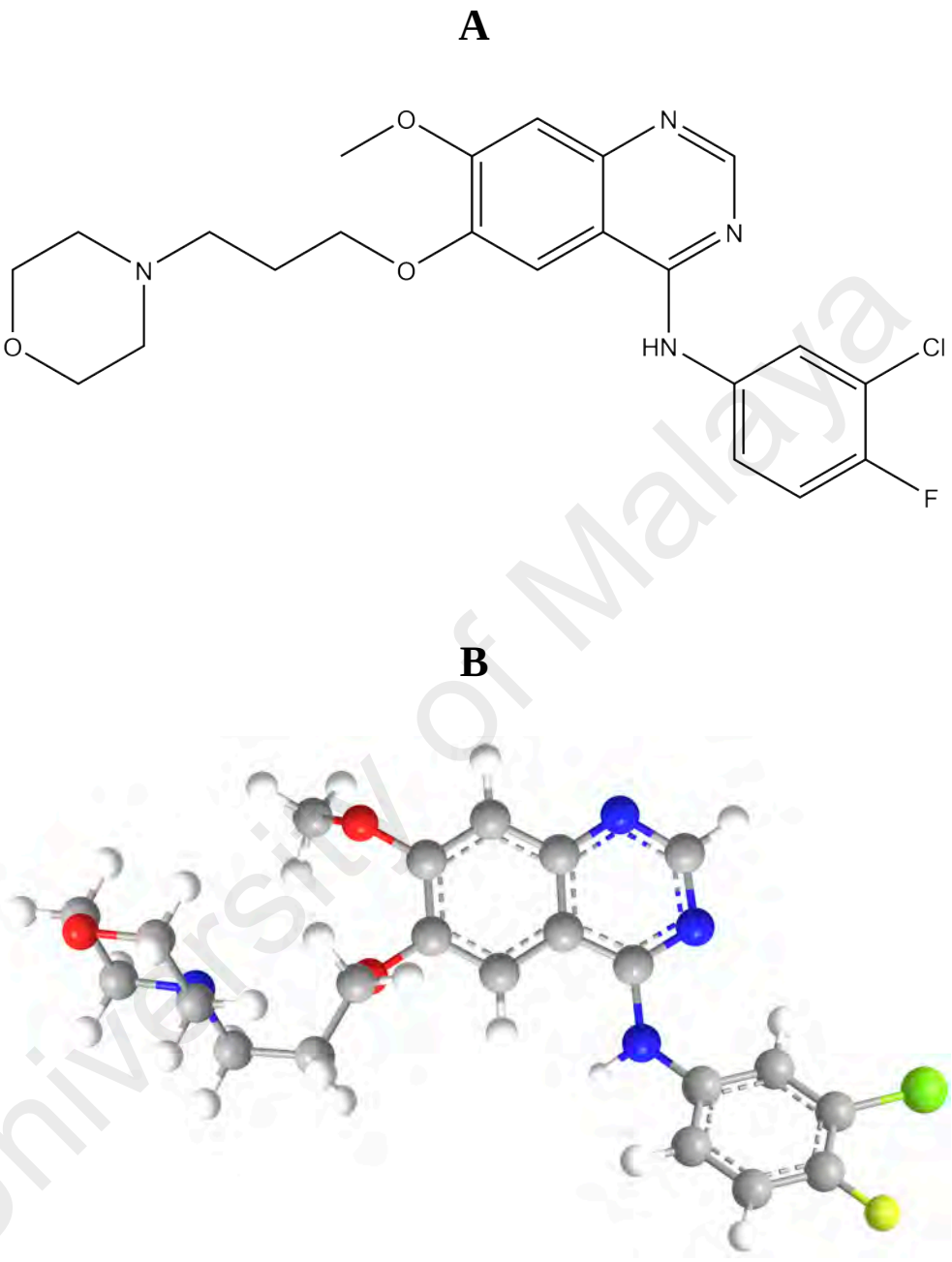

Figure 2.7: Structural representations of gefitinib. (A) Chemical structure, (B) Ball-and-stick model.

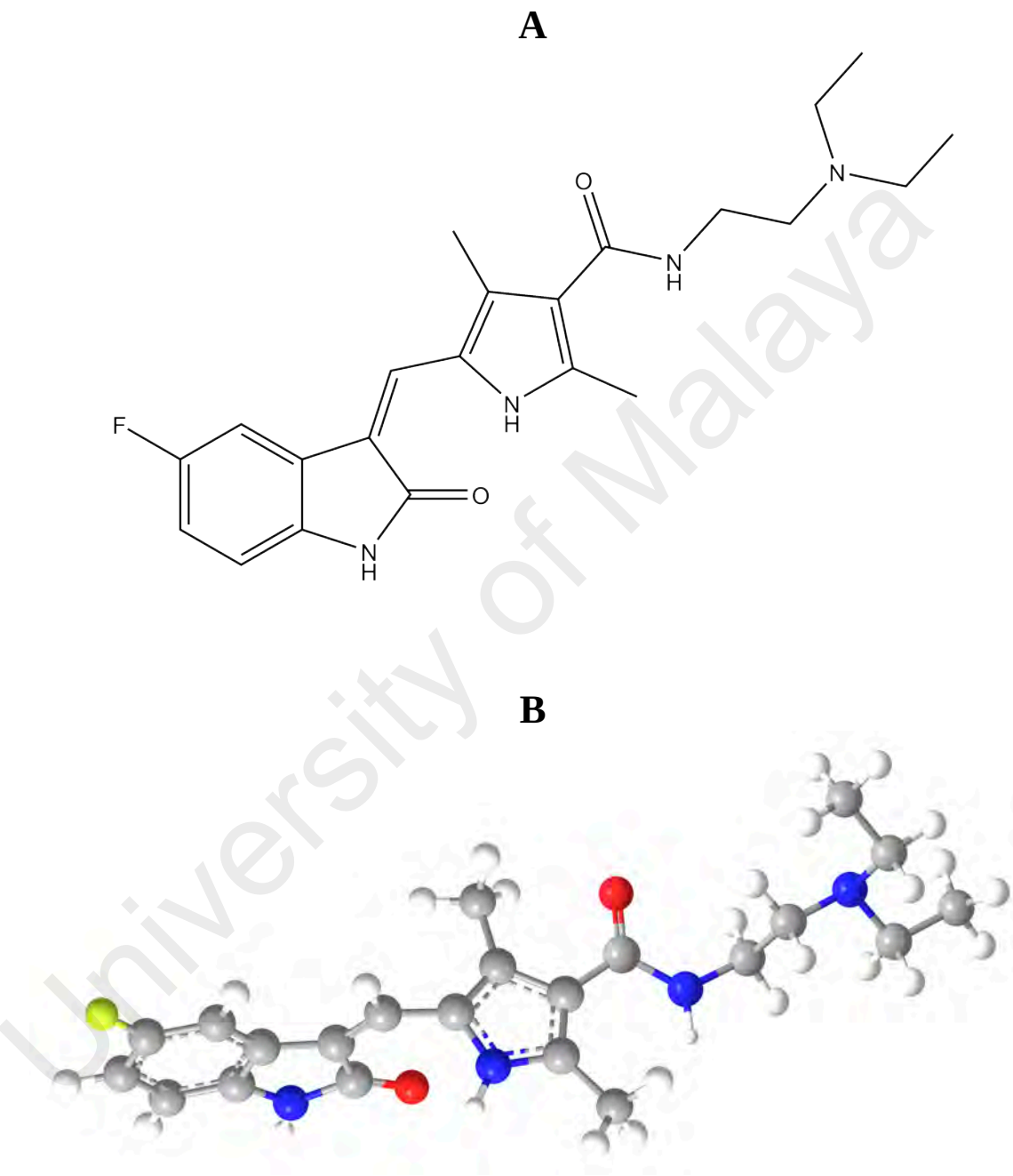

Figure 2.8: Structural representations of sunitinib. (A) Chemical structure, (B) Ball-and-stick model.

inhibitory activities against the growth of human metastatic renal cancers and gastrointestinal stromal tumors (Rini et al., 2007; Tourneau et al., 2007). It is an inhibitor of EGFR, VEGFR, PDGFR and the stem cell factor receptor C-Kit tyrosine kinases (Tourneau et al., 2007; Sulkes, 2010). SU reversibly binds to the ATP-binding site of the kinase and pauses receptor phosphorylation and activation. By inhibiting certain signal transduction pathways through various tyrosine kinases, that are responsible for diverse tumour cells growth, SU induces apoptosis of oncogenic cells and thus prevents cancer growth (Tourneau et al., 2007). Some common adverse effects in SU-treated patients included hypertension, diarrhea, skin abnormalities, fatigue and nausea (Schmid & Gore, 2016). However, cardiac safety in terms of increasing dose of SU remains unclear (Rock et al., 2007).

2.7 Transportation of therapeutic ligands in human blood circulation

Interactions between various therapeutic ligands (*e.g.*, pharmaceutical ligands, drugs etc.) and the plasma proteins are of pharmacological importance, as pharmacokinetic and pharmacodynamic properties of therapeutic ligands depend on their interactions with plasma proteins in the human body (Fasano et al., 2005; Kragh-Hansen et al., 2002; Olson & Christ, 1996). Such interactions may influence their bioavailability, distribution, metabolism and elimination processes in the body (Kragh-Hansen et al., 2002). Binding of a therapeutic ligand to plasma transport proteins and its active transport to the specific target site is vital for its therapeutic effects (Korolenko et al., 2007). These ligands can be found either in the free form or bound to plasma proteins in the circulatory system. The free ligand can be passively diffused through the barriers constituted by endothelial cells into the organs (*e.g.*, kidney and liver), where it is metabolized (Rowland & Tozer, 2010; Yamasaki et al., 2013). On the other hand, protein-bound ligand is protected from rapid metabolism by the body's detoxification system and would remain in the circulatory system for producing a longer duration of

therapeutic effects (Lindup & Orme, 1981; Smith et al., 2010). Therefore, binding of a drug to the plasma protein significantly affects the efficacy of the drug. Human serum albumin (HSA), lipoproteins and α-1-acid glycoprotein are the common carrier proteins present in the blood plasma, while HSA is unique as a major transport protein due to its ligand binding competence with high affinity (Korolenko et al., 2007; Kragh-Hansen, 1990).

2.8 Human serum albumin

HSA is a multifunctional non-glycosylated transport protein present in blood plasma with a concentration of ~ 600 μM (Peters, 1996). It is mainly synthesized in the liver and contributes more than 50% of the total plasma protein content (Quinlan et al., 2005). Molecular and structural properties of HSA are described in the following sections in detail.

2.8.1 Physicochemical properties of HSA

Various important physicochemical properties of HSA are summarized in Table 2.2. HSA is a single chain protein with a molecular mass of 66,500 Da, as calculated from its amino acid composition (Peters, 1996), which was similar to the molecular mass of 66,437 Da, obtained from matrix-assisted laser desorption / ionization-time of flight (MALDI-TOF) mass spectrometry (Amoresano et al., 1998). Values of the hydrodynamic parameters such as diffusion coefficient and sedimentation coefficient were determined as 6.1×10^{-7} cm^2 s^{-1} and 4.2 S, respectively (Hunter & McDuffie, 1959; Oncley et al., 1947). An axial ratio of 3.5 was obtained from dielectric dispersion measurements (Ferrer et al., 2001). The radius of gyration (26.7 Å) was found to be similar to the rotational hydrodynamic radius value of 26.7 Å (Carter & Ho, 1994). Based on X-ray crystallographic data of HSA, the polypeptide chain forms a heart-shaped structure with the dimensions of 80 × 80 × 30 Å (He & Carter, 1992). Values of

Table 2.2: Physicochemical properties of HSA.

Property	Value	Reference
Molecular mass		
– Amino acid composition	66,500 Da	Peters (1996)
– MALDI-TOF	66,437 Da	Amoresano et al. (1998)
Diffusion coefficient, $D_{20,W}$	6.1×10^{-7} cm^2 s^{-1}	Oncley et al. (1947)
Sedimentation coefficient, $S_{20,W}$	4.2 S	Hunter & McDuffie (1959)
Axial ratio	3.5:1	Ferrer et al. (2001)
Radius of gyration	26.7 Å	Carter & Ho (1994)
Overall dimension	80 × 80 × 30 Å	He & Carter (1992)
Frictional ratio, f/f_0	1.37:1	Hunter & McDuffie (1959)
Intrinsic viscosity, $[\eta]$	0.056 dL g^{-1}	Hunter & McDuffie (1959)
Partial specific volume, $\bar{v}_2$	0.733 cm^3 g^{-1}	Matthews (1968)
Isoelectric point		
– Native	4.7	Candiano et al. (1986)
– Defatted	5.8	Gianazza et al. (1984)
Isoionic point	5.2	Putnam (1975)
Extinction coefficient, ε	36,500 M^{-1} cm^{-1}	Painter et al. (1998)
α-Helix	67 %	Carter & Ho (1994)
β-Sheet	10 %	Carter & Ho (1994)
Net charge per molecule		
– at pH 7.4	– 19	Tanford (1950)
– Amino acid sequence	– 15	Peters (1996)

the frictional ratio (1.37:1) and the intrinsic viscosity (0.056 dL g^{-1}) of HSA suggested protein's globular structure (Hunter & McDuffie, 1959). A value of 0.733 cm^3 g^{-1} was obtained for the partial specific volume of HSA (Matthews, 1968). The protein has an isoelectric point of 4.7 in the native form (Candiano et al., 1986) and 5.8 for defatted HSA (Gianazza et al., 1984), while the isoionic point was measured as 5.2 (Putnam, 1975). A value of the extinction coefficient of 36,500 M^{-1} cm^{-1}, as determined at 280 nm for HSA reflected the presence of Trp and Tyr residues (Painter et al., 1998). The secondary structures present in HSA were distributed as 67 % α-helices, 10 % β-sheets and 23 % flexible regions (Carter & Ho, 1994). The protein net charge is –19 at physiological pH (pH 7.4) (Tanford, 1950), whereas a net change of – 15 was obtained from its amino acid sequence (Peters, 1996). The high negative charge of HSA provides high solubility to the protein in acquous environment.

2.8.2 Structural organization of HSA

2.8.2.1 Amino acid composition and primary structure

Table 2.3 shows the amino acid composition of HSA. It is a small globular protein, comprising of 585 amino acid residues with lone Trp residue. Two other amino acids, *i.e.*, Ile (8) and Met (6) were also found in smaller quantity. The protein is rich in the number of charged amino acid residues such as Lys (59), Asp (36), Glu (62) and Arg (24). The content of the hydrophobic amino acid residues was also high with the distribution as Ala (62), Val (41), Leu (61) and Phe (35). There are 35 Cys residues in the polypeptide chain.

Figure 2.9 depicts the primary structure of HSA, as determined from the amino acid sequence. The amino acid residues form nine flexible loops, arranged in a distinct pattern with eight sequential Cys-Cys pairs. The primary structure of HSA is made up of three homologous domains, namely, I, II and III, which are grouped from the nine loops. These domains are comprised of amino acid residues, 1–195 (domain I), 196–383

Table 2.3: Amino acid composition of HSA.*

Amino Acid	Three Letter Code	No. of Residues
Glycine	Gly	12
Alanine	Ala	62
Valine	Val	41
Leucine	Leu	61
Isoleucine	Ile	8
Serine	Ser	24
Threonine	Thr	28
Proline	Pro	24
Aspartic acid	Asp	36
Glutamic acid	Glu	62
Asparagine	Asn	17
Glutamine	Gln	20
Histidine	His	16
Lysine	Lys	59
Arginine	Arg	24
Phenylalanine	Phe	31
Tyrosine	Tyr	18
Tryptophan	Trp	1
Cysteine	Cys	35
Methionine	Met	6
Total		**585**

* Data were obtained from Peters (1996)

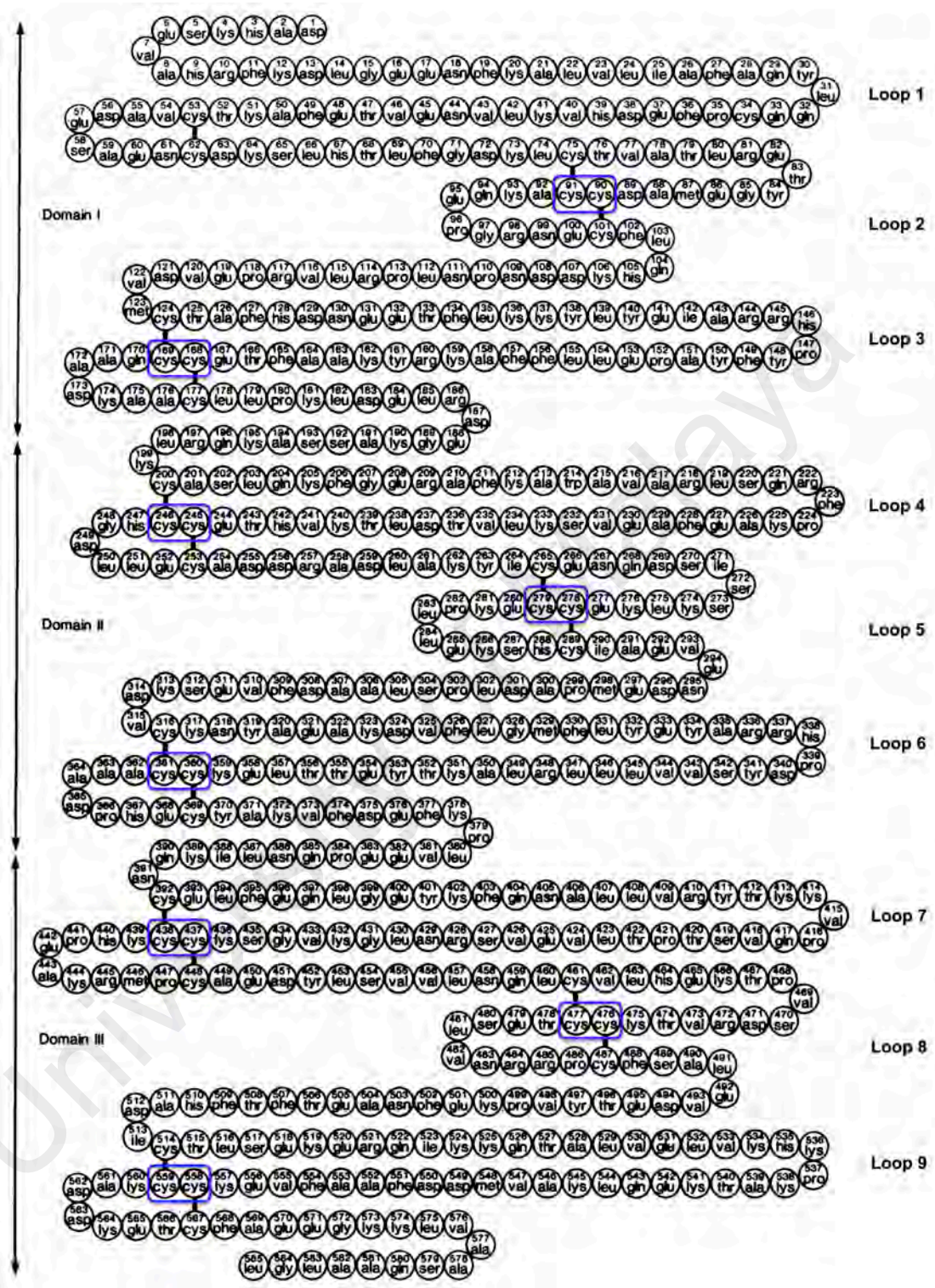

Figure 2.9: Amino acid sequence and disulfide bonding pattern of HSA. Each domain contains one short and two long loops. The blue-colored boxes show the Cys-Cys pairs.
(Adapted from Dugaiczyk et al., 1982).

(domain II) and 384–585 (domain III), which are further divided into two subdomains, A and B, respectively (Carter & Ho, 1994). Among nine long-short-long loops, first two loops within each domain form subdomain 'A' such as loops 1–2, 4–5 and 7–8 for subdomains IA, IIA and IIIA, respectively, while subdomain 'B' is formed from the third loop, *i. e.*, loops 3, 6 and 9 for subdomains IB, IIB and IIIB, respectively. (Dugaiczyk et al., 1982). The structure of HSA is stabilized by 17 intramolecular disulfide bonds, which are formed by 34 Cys out of 35 Cys residues. One Cys residue is available in free form at position number 34. The movement of subdomains from one to another is accomplished by the presence of flexible loops of Pro residues, which support the binding of a wide range of ligands (Quinlan et al., 2005).

Comparative analyses of three domains of HSA based on their structural and sequence similarities have shown 18–25 % sequence homology, which is the maximum among the long loops 3, 6 and 9 (Peters, 1996). On the other hand, serum albumins from different mammalian sources have displayed structural similarities with significant degree of sequence conservation. For instance, overall sequence similarities of serum albumins from bovine (BSA), equine (ESA) and rabbit (RSA), compared to human (HSA) are 75.6 %, 76.1 % and 74.2 %, respectively (Majorek et al., 2012).

2.8.2.2 Three-dimensional structure

Three homologous domains of HSA are further divided into a pair of subdomains, namely, 'A' and 'B', which consist of 6 and 4 α-helices (Figure 2.10), respectively (Carter & Ho, 1994). The arrangement of four helices (h1–h4) in subdomains 'A' and 'B' are identical, while two other short helices (h5 and h6) in subdomains 'A' are ordered in antiparallel fashion. These helices are connected by 17 Cys-Cys disulfide bridges. As can be seen from Figure 2.10, domains I–II and II–III are linked through extensions of helices, *viz.*, Ib-h4–IIa-h1 and IIb-h4–IIIa-h1, respectively. Such

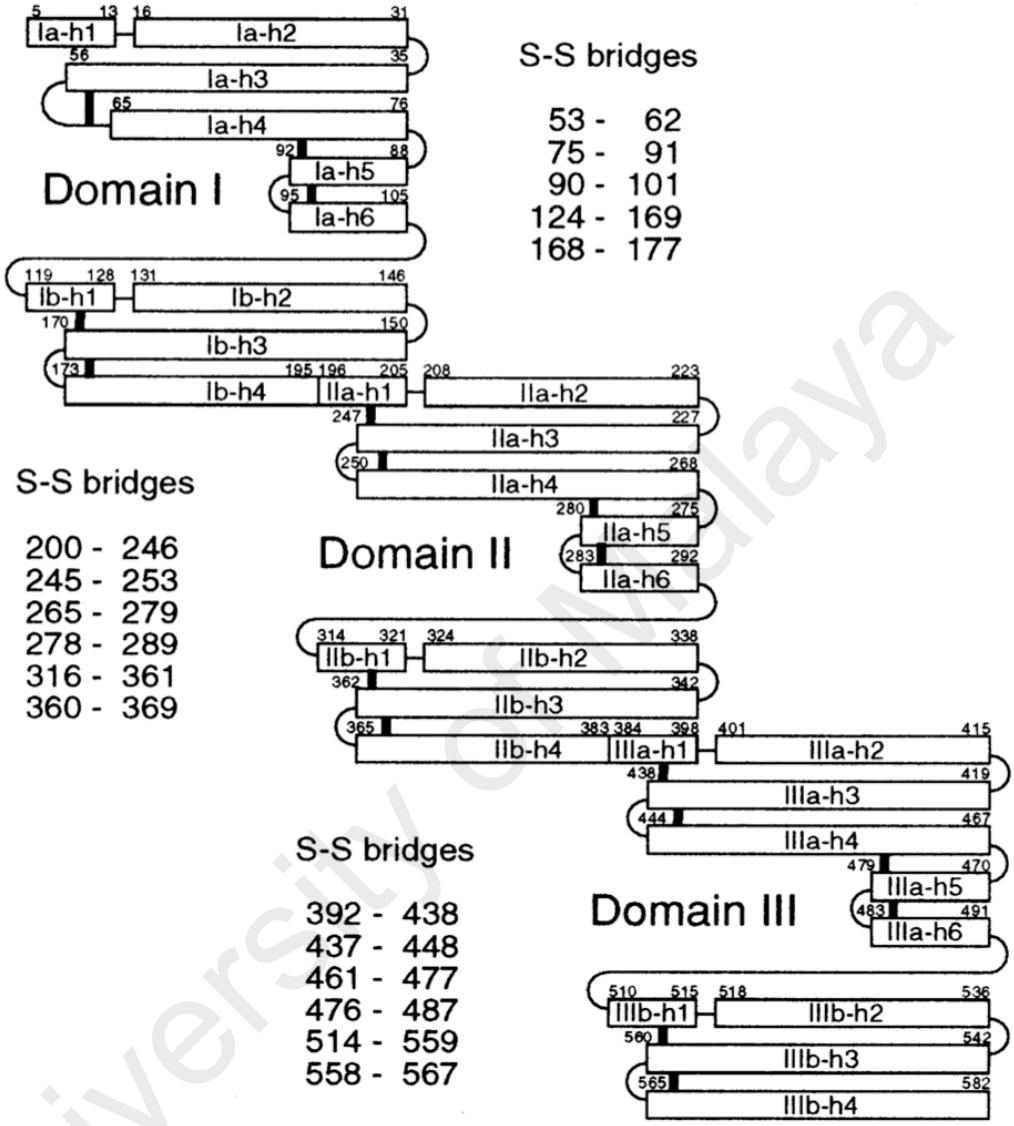

Figure 2.10: Diagram showing helices and disulfide bridges of HSA. Helices are depicted by rectangles, and loops and turns by thin lines. Disulfide bridges are represented with thick lines.
(Adapted from Sugio et al., 1999).

connections form two longest helices, which make the actual number of helices in HSA structure as 28 in total instead of 30.

The crystallographic studies on HSA have revealed a heart-shaped structure formed from three homologous domains I, II, and III along with a pair of subdomains, 'A' and 'B' (Figure 2.11) (Carter & Ho, 1994; Peters, 1996). While the three domains are structurally similar, their global configuration is relatively asymmetric. The perpendicular orientation of domain I to domain II forms a T-shaped configuration of HSA. On the other hand, formation of a Y-shaped configuration is observed due to an angle shift of 45^{o} between domains II and III. Interaction between domains such as domains I to II and domains II to III are stabilized through hydrogen bonds and hydrophobic interactions, respectively (Sugio et al., 1999). HSA subdomains are identical, which share common structural features in terms of polypeptide chain folding as well as disulfide bond topology (Sugio et al., 1999). The surface-exposed portions of HSA have high degree of flexibility, which allow the binding of a large number of small molecules to the protein (Karush, 1954). The hydrophobic cavities of subdomains IIA, IIIA and IB form three well-characterized ligand binding sites, namely, Sudlow's site I, Sudlow's site II and site III, respectively (Kragh-Hansen et al., 2002; Sudlow et al., 1975).

2.8.3 Functions of HSA

Due to the high concentration in the blood plasma, HSA is the most important protein responsible for many physiological and pharmacological functions. It plays vital roles in the body such as regulation of the colloid osmotic pressure, maintenance of the blood pH and binding of a large variety of endogenous and exogenous compounds (Figge et al., 1991; Quinlan et al., 2005). It also plays the role of an antioxidant by giving protection against reactive oxygen species. Enzymatic activity such as esterase activity has also been found associated with HSA. Furthermore, HSA is involved in

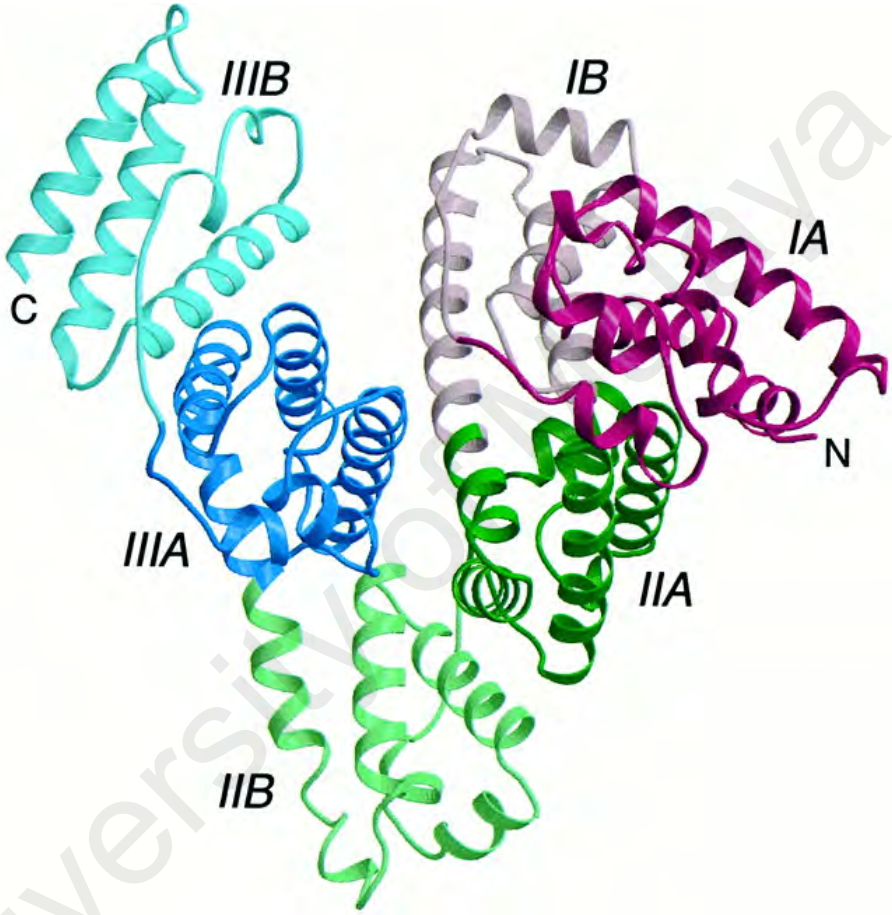

Figure 2.11: Three-dimensional structure of HSA. Various colors represent domain I (red), domain II (green), domain III (blue). Where subdomains A and B of each domain are shown in 'dark' and 'light' shades, the N- and C-termini are depicted as N and C, respectively.
(Taken from Bhattacharya et al., 2000).

blood coagulation due to its structural similarity to heparin (Nicholson et al., 2000).

Owing to the presence of three well-characterized ligand binding sites in HSA, various ligand molecules such as therapeutic drugs, hormones, toxic metabolites, fatty acids, bile acids and metal ions bind to the protein (Bal et al., 2013; Kragh-Hansen, 1985; Peters, 1996; Sudlow et al., 1975). It facilitates the transportation of numerus drugs through blood circulation and their release at the specific target sites (Kragh-Hansen et al., 2002). Besides, it also transports the key signaling molecule, nitric oxide (Stamler et al., 1992).

2.8.4 Ligand binding sites of HSA

Several high and low affinity binding sites are present in HSA to accommodate different ligands. According to Sudlow's classification, two principal ligand binding sites of HSA, *i.e.*, Sudlow's sites I and II are well characterized for their high adaptability to bind different molecules (Kragh-Hansen et al., 2002; Sudlow et al., 1975). In addition, a third site, *i.e.*, site III of HSA is also known as the preferred binding site for few ligands such as digitoxin and hemin (Kragh-Hansen, 1985). These binding sites are located in the hydrophobic cavities of subdomains IIA (Sudlow's sites I), IIIA (Sudlow's sites II) and IB (site III) in HSA (Figure 2.12). Various ligands that have been shown to bind with higher affinity to HSA, including their preferences to sites I / II / III are listed in Table 2.4. Besides these ligand binding sites, few ligands are also known to bind at their secondary binding sites in HSA. As can be seen from Figure 2.12, diflunisal, halothane and ibuprofen also bind at the interface between subdomains IIA-IIB, while oxyphenbutazone and propofol are bound in subdomain IIIB (Ghuman et al., 2005). Furthermore, HSA has the ability to bind different metal ions such as Mg^{2+}, K^{+}, Ca^{2+}, Mn^{2+}, Cu^{2+}, Zn^{2+} and Ba^{2+} (Bal et al., 2013; Quinlan et al., 2005; Carter and Ho, 1994). Four metal binding sites of HSA, namely, the N-terminal site (subdomain IA), Cys34 residue (subdomain IA), multi-metal binding site A (domain II) and site B

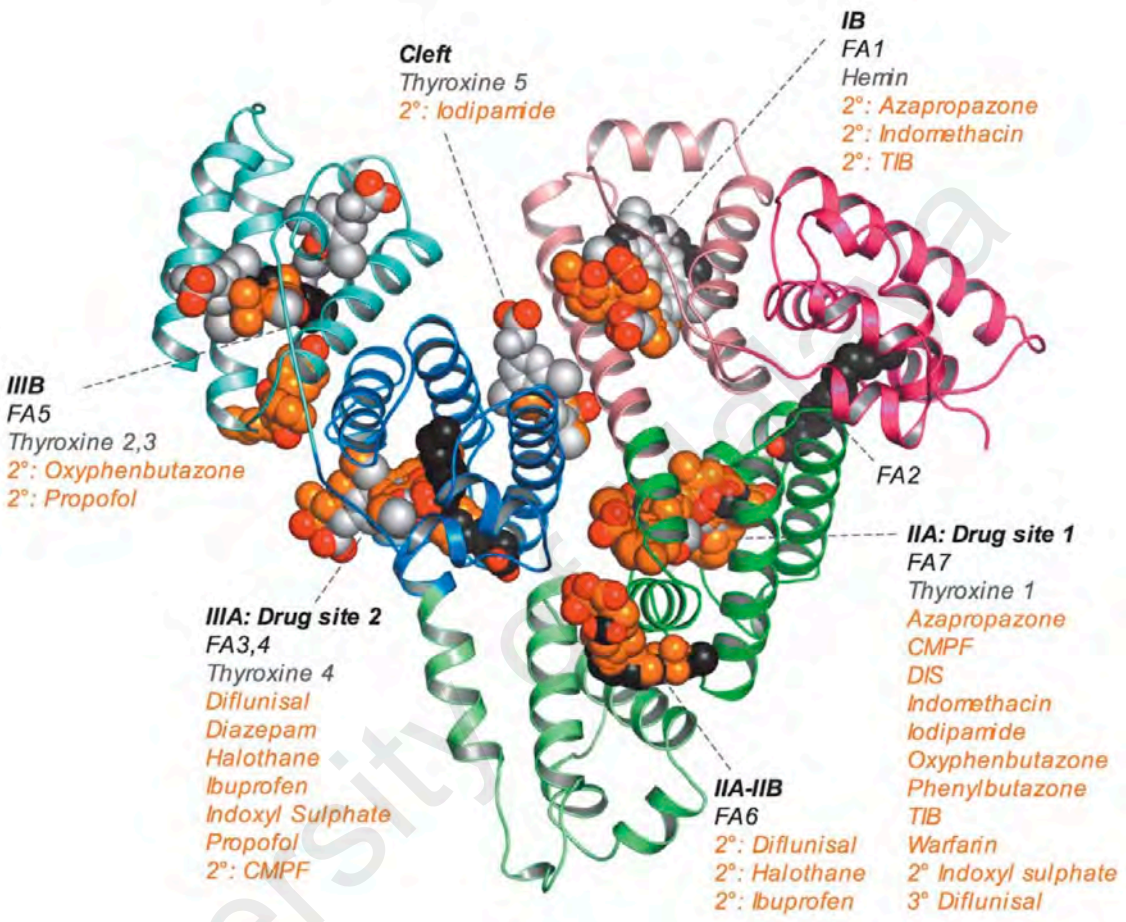

Figure 2.12: Diagram showing ligand binding sites of HSA. Individual subdomains are colored differently and ligands are displayed as space-filling models. Oxygen atoms are shown in red. All other atoms in fatty acids (black), other endogenous ligands (hemin and thyroxine) (grey) and drugs (orange) are also marked.
(Taken from Ghuman et al., 2005).

Table 2.4: Binding properties of some ligands to HSA.

Ligand	K_a (M^{-1})	Reference
Site I		
Azapropazone	2.8×10^5	Kragh-Hansen (1988)
Balofloxacin	3.9×10^6	Ma et al. (2015)
Baicalin	1.3×10^6	Dufour & Dangles (2005)
Bilirubin	9.5×10^7	Brodersen (1982)
Carbenoxolone	2.0×10^7	Zsila (2013)
Celecoxib	1.1×10^6	Zsila (2013)
Iodipamide	9.9×10^6	Yamasaki et al. (1996)
Iophenoxate	7.7×10^7	Mudge et al. (1978)
Indomethacin	1.4×10^6	Montero et al. (1986)
Indometacin	1.1×10^6	Yang et al. (2012)
Osthole	1.7×10^6	Bijari et al. (2013)
Oxyphenbutazone	3.5×10^5	Elbary et al. (1982)
Phenylbutazone	1.5×10^6	Yamasaki et al. (1996)
Propofol	1.3×10^6	Sun et al. (2016)
Suramin	2.2×10^6	Zsila (2013)
Warfarin	3.4×10^6	Yamasaki et al. (1996)

Table 2.4: continued.

Ligand	K_a (M^{-1})	Reference
Site II		
Crocetin	2.4×10^6	Zsila (2013)
Diazepam	3.8×10^5	Kragh-Hansen (1991)
Diclofenac	3.3×10^6	Yamasaki et al. (2000)
Diflunisal	5.0×10^5	Horone & Brodersen (1984)
Ethacrynic acid	1.7×10^6	Bertucci et al. (1998)
Gemfibrozil	5.1×10^5	Zsila (2013)
Ibuprofen	2.7×10^6	Kragh-Hansen (1981)
Iopanoate	6.7×10^6	Mudge et al. (1978)
Ketoprofen	2.5×10^6	Rahman et al. (1993a)
Naproxen	3.7×10^6	Bischer et al. (1995)
Sulindac	7.6×10^6	Russeva et al. (1994)
Site III		
Digitoxin	9.6×10^4	Lukas & Martino (1969)
Fusidic acid	1.5×10^5	Zsila (2013)
Hemin	2.1×10^6	Zsila (2013)
lidocaine	1.3×10^5	Hein et al. (2010)
Phycocyanobilin	2.2×10^6	Minic et al. (2015)

(non-localized) have shown specificity to different metal ions (Bal et al., 2013). However, crystallographic studies have not yet characterized these sites to reveal the molecular details of their metal ion binding. The details of ligand binding sites I, II and III are described in the following subsections.

2.8.4.1 Site I

Crystallographic studies have shown that Sudlow's site I is one of the major recognized sites available for high-affinity binding of various ligands to HSA (Kragh-Hansen et al., 2002). It is characterized as hydrophobic ligand binding pocket, surrounded by positively-charged residues at the entrance, thus favoring the binding of bulky heterocyclic molecules, possessing negatively-charged groups (Kragh-Hansen et al., 2002). Sudlow's site I is a multi-chamber cavity, which comprises of six helices of the subdomain IIA as well as a loop-helix feature of subdomain IB (Ghuman et al., 2005). The interior of the binding pocket is found to be deep inside the protein structure and mostly placed in a hydrophobic cleft, which is enveloped by amino acid residues: Trp-214, Leu-219, Phe-223, Leu-238, His-242, Leu-260, Ile-264, Ser-287, Ile-290 and Ala-291 (Yang et al., 2014). However, site I also contains two clusters with polar residues, an inner cluster at the bottom of the pocket, formed by Tyr-150, His-242 and Arg-257 residues and an outer cluster at the entrance of the pocket, comprised of Lys-195, Lys-199, Arg-218, and Arg-222 residues (Ghuman et al., 2005).

Binding site I is more flexible, wider and greater compared to other sites, thus the larger molecules generally prefer to bind to site I (Kragh-Hansen et al., 2002). Several studies have shown the binding locus of various ligands in site I with high affinity (Table 2.4). As can be seen from the Figure 2.12, ligands such as warfarin, azapropazone, indomethacin and phenylbutazone are found to fit at the location of the binding site I (Ghuman et al., 2005). Site I contains two overlapping binding sites (warfarin-azapropazone binding area) for warfarin and azapropazone binding and the

single Trp (Trp-24) residue in the non-overlapping region of the warfarin site (Fehske et al., 1982). Although, different studies have anticipated the existence of two independent binding regions within site I (Kragh-Hansen, 1985, 1988), Yamasaki and his colleges suggested the presence of three binding regions, *viz.*, Ia, Ib and Ic within this site for the binding of warfarin, azapropazone and butamben, respectively (Yamasaki et al., 1996).

2.8.4.2 Site II

Various ligands such as diazepam, ibuprofen, iopanoate and ketoprofen (Table 2.4) prefer to bind in the cavity of binding site II (subdomain IIIA). It is smaller and less flexible compared to site I and thus, large molecules are rarely bound to the binding pockets of site II (Kragh-Hansen et al., 2002). This site is favored by the binding of aromatic carboxylic acids with a negative charged group at one end of the molecule away from a hydrophobic center (Kragh-Hansen et al., 2002). The binding preference of larger molecules to this site is infrequent due to the absence of any overlapping binding regions as well as the effect of steroselectivity. For example, L-Trp shows 100 times higher affinity to site II compared to D-isomer (Ghuman et al., 2005). However, it has a degree of structural adaptability for the binding of two molecules of long chain fatty acids concurrently (Curry, 2003). A slight modification, substitution of the ligands with a relatively small group may greatly affect their binding to site II. Accordingly, fluorination of diazepam was found to halt its binding to the well characterized binding site (site II) of diazepam (Chuang & Otagiri, 2001).

Site II is topologically similar to site I since it is composed of six helices of subdomain IIIA. Its structure is less complicated, as a few residues from subdomain IIB participate to its opening (Zsila et al., 2011). The interior of the binding pocket is hydrophobic, with a single dominant polar patch near to the entrance that centered around Arg-410 and Tyr-411 residues (Sugio et al., 1999). Site II-bound drugs (Figure 2.11) such as diazepam, ibuprofen and diflunisal interact with the OH group of Tyr-411,

while Arg-410 and Ser-489 also participate for the interactions with diflunisal and ibuprofen by forming salt-bridge as well as H-bond (Yamasaki et al., 2013).

2.8.4.3 Site III

Although, Sudlow's sites I and II are well known for noncovalent association of a broad spectrum of small molecules, existence of an additional drug binding site in HSA is also suggested for some ligands (Kragh-Hansen, 1985; Sjöholm et al., 1979; Sudlow et al., 1975). This binding site (termed as site III) is identified as hydrophobic D-shaped binding pocket, located in subdomain IB. Site III is considered as primary binding locus of ligands such as hemin, digitoxin, fusidic acid and lidocaine (Kragh-Hansen, 1985; Zunszain *et al.*, 2008). It also houses secondary binding sites for some additional ligands, *viz.*, azapropazone, warfarin and indomethacin that are preferentially known to bind at Sudlow's site I (Zsila, 2013).

The hydrophobic cavity of site III consists of three basic residues at its entrance to coordinate the two propionate groups on hemin, which helps in the interaction of ligands with this site. In the absence of ligand, the binding pocket is partly blocked by Tyr-138 and Tyr-161 residues. Binding of ligand such as hemin and fatty acid leads to a conformational change that opens the binding pocket as well as helps to fit the ligand (Zunszain et al., 2003). Based on the hydrophobicity of the binding pocket and coordination of the propionate groups by basic residues, HSA seems to have similar features to the heme binding site on myoglobin / hemoglobin (Zsila, 2013; Zunszain et al., 2003). Besides, site III is allosterically linked with Sudlow's sites, I and II (Zsila, 2013).

2.8.5 Pharmacological importance of ligand–HSA interaction

Since HSA is known to bind to neutral and acidic lipophilic compounds, it is an ideal transporter for most of the drugs in the blood circulation (Kragh-Hansen et al., 2002; Olson & Christ, 1996). Generally, binding of a drug to HSA improves its

pharmacokinetic properties. For instance, the *in vivo* half-life of a therapeutic drug is increased upon binding to HSA, which can elongate the duration of the drug's efficacy. Drug-protein interaction also improves the drug's solubility, reduces its toxicity and defends its elimination from the human body (Kragh-Hansen et al., 2002; Olson & Christ, 1996; Peters, 1996).

HSA concentration in the plasma is much higher than the concentration of administered drugs *in vivo*, thus the drug shows affinity to bind at the higher affinity binding sites on HSA (Kragh-Hansen et al., 2002). On the other hand, high affinity binding sites for drugs in HSA are limited and therefore, binding of a drug to HSA may result concurrent displacement of another drug, which may influence the therapeutic effect of both drugs. Drug displacement phenomenon resulted by drug-drug interaction can play crucial role in the efficacy of a specific administered drug, while it can either improve or being detrimental to the effect of that drug. For example, coadministration of phenylbutazone or buculome with warfarin increases the anti-coagulant activity of warfarin due to the displacement of warfarin from the plasma (Hatakeyama et al., 2010). It has been observed that concentration of HSA-bound drug can also influence drug-protein interaction. A rapid increase of endogenous HSA-bound drug may cause massive release of the bound drug from the protein, thus produces intoxication of the patient (Fasano et al., 2005).

Furthermore, certain disease conditions such as renal and liver diseases may also affect drug-protein interaction. These diseases reduce the concentration HSA from its normal level, decrease the distribution of HSA between inter- and intravascular spaces and induce the accumulation of endogenous ligands (e.g., fatty acids and uremic acid) in the plasma. Therefore, binding of a drug to HSA can be significantly affected under these conditions (Dasgupta & Havlik, 1998). In view of the above, it is important to investigate the characteristics of drug–protein interaction for understanding the

physiological action of pharmaceutical compounds at the molecular level in the human body.

Despite several reports, highlighting the pharmacological significance of four tyrosine kinase inhibitors, vandetanib (VDB), lapatinib (LAP), gefitinib (GEF) and sunitinib (SU) (Brassard & Rondeau, 2012; Burotto et al., 2015; Liao et al., 2010; Tourneau et al., 2007), their interaction with human serum albumin (HSA) need to be explored. In view of the importance of the drug-protein interaction, this study aims to reveal the characteristics of ligand–HSA interaction in terms of the binding affinity, intermolecular forces involved, effect on HSA fluorophore microenvironment as well as protein's structure and location of the binding site using fluorescence spectroscopy and molecular docking analysis.

CHAPTER 3: MATERIALS AND METHODS

3.1 Materials

3.1.1 Protein

Fatty acid and globulin free albumin from human serum (HSA) (purity ≥ 99 %; Lot # 068K7538V) was purchased from Sigma-Aldrich Co., St. Louis, MO, USA. The protein was used as such without further purification.

3.1.2 Drugs

Vandetanib (VDB) (purity ≥ 98 %; Batch # 0454075-6), lapatinib (LAP) (purity ≥ 98 %; Batch # 0452287-17) and sunitinib (SU) (purity ≥ 98 %; Batch # 0446636-17) were supplied by Cayman Chemical Company, Michigan, USA. Gefitinib (GEF) (purity ≥ 99 %; Batch # S102503) was the product of Selleckchem, Houston, TX, USA.

3.1.3 Ligands used in drug displacement studies

Phenylbutazone (PBZ) (purity ≥ 98 %; Batch # 124K1625), indomethacin (IDM) (purity ≥ 99 %; Lot # 115K0689), ketoprofen (KTN) (purity ≥ 98 %; Lot # BCBG9546V), hemin (HMN) (purity ≥ 80 %; Lot # 015K0872) and digitoxin (DGT) (purity ≥ 92 %; Lot # NOI0195) were procured from Sigma-Aldrich Co., St. Louis, MO, USA. Diazepam (DZM) (purity ≥ 98 %; Lot # 1071B02) was supplied by Lipomed AG, Arlesheim, Switzerland.

3.1.4 Miscellaneous

Sodium dihydrogen phosphate and *di*-sodium hydrogen phosphate were obtained from Systerm, Selangor, Malaysia. Standard buffers of pH 7.0 and pH 10.0 as well as various metal salts such as magnesium chloride ($MgCl_2$), potassium chloride (KCl), calcium chloride ($CaCl_2$), manganese (II) chloride ($MnCl_2$), copper (II) chloride ($CuCl_2$), zinc chloride ($ZnCl_2$) and barium chloride ($BaCl_2$) were procured from Sigma-

Aldrich Co., St. Louis, MO, USA. Dimethyl sulphoxide (DMSO) was the product of Merck Millipore, Darmstadt, Germany. Cellulose nitrate membrane filters (0.45 µm pore size) were supplied by Whatman GmbH, Dassel, Germany, whereas polyvinylidene fluoride (PVDF) membrane filters (0.45 µm pore size) were purchased from Merck Millipore, Darmstadt, Germany. All chemicals used in this study were of analytical reagent grade.

Ultrapure (Type 1) water produced by Milli-Q water purification system (Merck Millipore, Darmstadt, Germany) as well as glass distilled water was used throughout this study. All experiments were performed in 60 mM sodium phosphate buffer, pH 7.4 at 298 K, unless otherwise stated.

3.2 Methods

3.2.1 pH measurements

Measurements of pH were made on a Delta 320 pH meter (Mettler-Toledo GmbH, Greifensee, Switzerland), attached with a HA405-K2/120 combination electrode. The calibration of the pH meter was performed using standard buffers of pH 7.0 and pH 10.0 for pH measurements in the neutral and alkaline pH ranges, respectively. The least count of the pH meter was 0.01 pH unit.

3.2.2 Preparation of protein solution

The stock protein solution was prepared by dissolving a known amount of HSA crystals in a fixed volume of 60 mM sodium phosphate buffer, pH 7.4. The stock solution was filtered using syringe-driven PVDF membrane filters and the protein concentration was determined spectrophotometrically using a molar extinction coefficient of 36,500 M^{-1} cm^{-1} at 280 nm (Painter et al., 1998). The stock protein solution was stored at 4 ^{o}C and was used within a week.

3.2.3 Preparation of ligand solutions

The stock solutions (1.0 mg ml^{-1}) of various drugs, *i.e.*, VDB, LAP, GEF and SU were prepared by dissolving their crystals in DMSO. These stock solutions were diluted to the desired concentration with the above buffer for experimental use. In all experiments, the final concentration of DMSO in the incubation mixture remained less than 1 % (v/v). Such DMSO concentration has no effect on the overall conformation of HSA (Papadopoulou et al., 2005).

Preparation of the stock solutions various ligands, *i.e.*, PBZ, IDM, DZM, KTN, HMN and DGT (1.0 mg ml^{-1}) was made in the same way as described above for other drugs.

A known amount of metal salts' crystals ($MgCl_2$, KCl, $CaCl_2$, $MnCl_2$, $CuCl_2$, $ZnCl_2$ and $BaCl_2$) was dissolved in sodium phosphate buffer, pH 7.4 to prepare the stock solutions (1.0 mg ml^{-1}) of metal salts.

3.2.4 Spectral measurements

3.2.4.1 Fluorescence spectroscopy

Fluorescence spectra were recorded on a Jasco FP-6500 spectrofluorometer, equipped with a xenon lamp source and a 10 mm path length quartz cuvette. The temperature was controlled using a temperature controller, attached to a water-jacketed cell holder, which was connected to a Protech 632D circulating water bath. The excitation (λ_{ex}) and the emission (λ_{em}) bandwidths were fixed at 10 nm each, while a scanning speed of 500 nm min^{-1}, a data pitch of 1 nm, a response time of 1 s and a detector voltage of 240 V were employed throughout these studies.

For intrinsic fluorescence measurements, the protein solution was excited at 295 nm and the emission spectra were recorded in the wavelength range, 310–380 or 310–390 nm. Fluorescence spectra of free drug solutions were also obtained in the same wavelength range upon excitation at 295 nm.

Fluorescence spectrum of the buffer solution was obtained in the same wavelength range and fluorescence intensity values at each wavelength were subtracted from the fluorescence spectra of the protein or ligand–protein mixtures.

Three-dimensional (3-D) fluorescence spectra of HSA (3 μM) were obtained both in the absence and presence of ligands (VDB / LAP / GEF / SU) using the excitation wavelength range, 220–350 nm with a data pitch of 5 nm and the emission wavelength range, 220–500 nm with a data pitch of 1 nm. All other scanning parameters were kept the same as those described above for fluorescence measurements. The molar ratios between the ligand and the protein were kept as 5:1 for [VDB]:[HSA] and [GEF]:[HSA] while 1:1 and 6:1 for [LAP]:[HSA] and [SU]:[HSA], respectively. The molar ratios of [ligand]:[protein] were optimized to monitor significant quenching in the HSA fluorescence in the presence of ligands. Three-dimensional fluorescence spectra of HSA in the absence and presence of ligands were recorded to acquire information about the microenvironmental changes around Tyr and Trp residues of the protein upon ligand binding.

3.2.4.2 Absorption spectroscopy

Absorption spectral measurements were made on a double beam UV-Vis spectrophotometer (Perkin-Elmer Lambda 25), using a pair of 10 mm path length cuvettes. For the inner filter effect correction, absorption spectra of the protein (3 μM) were recorded in the presence of increasing concentrations of the ligands in the wavelength range, 295−390 nm at 298 K.

In order to monitor ligand-induced changes in the absorption spectra of HSA, spectral measurements of the protein (15 / 20 μM) and ligand–protein mixtures were made in the wavelength range, 230–380 nm. The ligand concentrations in the ligand–protein mixtures were varied as 4–20 μM with 4 μM intervals (VDB and LAP); 5–50 μM with 5 μM intervals (GEF) and 2–24 μM with 2 μM intervals (SU).

Absorption contributions of free ligand solutions were also determined by taking the absorption spectra of free ligand solutions of similar concentrations in the same wavelength range.

3.2.4.3 Circular dichroism spectroscopy

Circular dichroism (CD) spectra of the protein and ligand–protein mixtures ([ligand]:[protein] = 1:1) were recorded in the far-UV (200–250 nm) and the near-UV (250–300 nm) regions at 298 K on a Jasco J–815 spectropolarimeter, equipped with a thermostatically-controlled water-jacketed cell holder under constant nitrogen flow. The path length of the sample cuvette and the protein concentration used were 1 mm and 1 µM (VDB) / 2 µM (LAP) / 3 µM (GEF and SU) for the far-UV CD spectral measurements. On the other hand, 10 mm path length cuvette and 5 µM (VDB) / 8 µM (LAP) / 9 µM (SU) / 10 µM (GEF) protein concentration were employed for CD measurements in the near-UV region. The spectra were recorded using a scan speed of 100 nm min^{-1}, a response time of 0.5 s and a data pitch of 1 nm. The final spectrum was an average of four successive scans. The far-UV and the near-UV CD spectral measurements of HSA were made in the absence and presence of ligand (VDB / LAP / GEF / SU) to reveal ligand-induced changes (if any) in the protein's secondary and tertiary structures, respectively.

The measured ellipticity values were expressed in terms of mean residue ellipticity (MRE) in deg. cm^2. $dmol^{-1}$ according to the following equation:

$$\text{MRE} = \frac{[\theta_{\text{obs}} \times \text{MRW}]}{10 \times l \times C_p} \quad (1)$$

where θ_{obs} is the ellipticity in millidegree; MRW is the mean residue weight (molecular weight of the protein, 66,500 divided by the total number of amino acid residues, 585); l is the path length of the cuvette in mm and C_p is the protein concentration in mg ml^{-1} (Chen et al., 1972).

3.2.5 Ligand–protein interaction studies

3.2.5.1 Fluorescence quenching titration

Interactions of VDB, LAP, GEF and SU with HSA were studied using fluorescence quenching titration method according to the published procedure (Feroz et al., 2012). In short, a fixed concentration of the protein (3 µM) was titrated with increasing ligand concentrations in a total volume of 3.0 ml. The ligand concentrations used in different titrations were 5–60 µM with 5 µM intervals (VDB); 0.5–4.5 µM with 0.5 µM intervals (LAP); 5–50 µM with 5 µM intervals (GEF) and 2–24 µM with 2 µM intervals (SU). An incubation time of 1 h was used to allow the equilibrium to be established at the desired temperature. The fluorescence spectra were recorded after an additional equilibration time of 6 min in the cuvette at each temperature.

In order to investigate the quenching mechanism as well as thermodynamics of the ligand–protein interaction, the titration was performed at three different temperatures, *i.e.*, 288 K, 303 K and 318 K (VDB, LAP and GEF) or 288 K, 298 K and 308 K (SU).

3.2.5.2 Analysis of the fluorescence quenching titration data

Fluorescence quenching titration results were treated for making inner filter effect correction, investigating the quenching mechanism and determining the binding constant and thermodynamic parameters of the binding reaction. These treatments were made in the following way.

I. Inner filter effect correction

In order to eliminate the inner filter effect, the fluorescence data were corrected for the absorption of the exciting light and reabsorption of the emitted light by the ligand (VDB / LAP / GEF / SU), using the following equation (Lakowicz, 2006):

$$F_{cor} = F_{obs} 10^{(A_{ex} + A_{em})/2} \quad (2)$$

where F_{cor} and F_{obs} refer to the corrected and the observed fluorescence intensity values, while A_{ex} and A_{em} are the differences in the absorbance values of the protein, observed in the presence of ligand at the excitation wavelength (295 nm) and the emission wavelengths (310–390 nm), respectively (Lakowicz, 2006).

II. Quenching mechanism

Investigation of the quenching mechanism involved in ligand (VDB / LAP / GEF / SU)-induced quenching of HSA fluorescence was made by the temperature dependency of the fluorescence quenching. The fluorescence data were treated according to the well-known Stern-Volmer equation (Lakowicz, 2006):

$$F_0 \,/\, F = 1 + \, K_{SV} \, [Q] = \, 1 + \, k_q \, \tau_0 \, [Q] \qquad (3)$$

where F_0 and F represent the fluorescence intensity values of the protein (HSA) in the absence and presence of the quencher (ligand), respectively; K_{SV} is the Stern-Volmer quenching constant and $[Q]$ is the quencher concentration (Lakowicz, 2006).

Values of the bimolecular quenching rate constant, k_q of the fluorescence quenching process at different temperatures were obtained by substituting the value of τ_0, the average lifetime of the biomolecule in the absence of the quencher as 6.38×10^{-9} s for HSA (Abou-Zied and Al-Shihi, 2008) in the following equation:

$$k_q = K_{SV} \,/\, \tau_0 \qquad (4)$$

III. Binding constant

Values of the binding constant (K_a) for the ligand (VDB / LAP / GEF / SU)–HSA system were obtained by treating the fluorescence quenching data according to the following double logarithmic equation (Bi et al., 2004):

$$\log \left(F_0 - F\right) / F = n \log K_a - n \log \left[1 \,/\, \left([L_T] - \left(F_0 - F\right)[P_T] \,/\, F_0\right)\right] \qquad (5)$$

where n is the Hill coefficient; $[L_T]$ and $[P_T]$ are the total concentrations of the ligand and the protein, respectively.

The value of K_a was obtained by dividing the Y-axis intercept value with the slope value of the straight line plot between $\log (F_0 - F) / F$ versus $\log \left[1 / \left([L_T] - \left(F_0 - F\right)[P_T] / F_0\right)\right]$ and taking the antilog of it.

IV. Thermodynamic parameters

Thermodynamic parameters of the binding reaction are useful in characterizing the forces involved in ligand–protein complex formation. Values of the enthalpy change (ΔH) and the entropy change (ΔS) for ligand–HSA interaction were obtained from the van't Hoff plot between ln K_a and 1 / T using the following equation:

$$\ln K_a = -\Delta H/RT + \Delta S/R \quad (6)$$

where R is the gas constant (8.314 J mol^{-1} K^{-1}) and T is the absolute temperature (273 ± ^{o}C).

Values of the free energy change, ΔG of the binding reaction at different temperatures were obtained by substituting the values of ΔH and ΔS in the following equation:

$$\Delta G = \Delta H - T\Delta S \quad (7)$$

3.2.6 Thermal stability studies

In order to evaluate the effect of ligand (VDB / LAP / GEF / SU) binding on the thermal stability of the protein, fluorescence measurements were carried out on HSA in the absence and the presence of ligand in the temperature range, 298–353 K with 5 K intervals. Both HSA (3 μM) and ligand–HSA mixtures ([VDB]:[HSA] = 10:1 / [LAP]:[HSA] = 2:1 / [GEF]:[HSA] = 10:1 / [SU]:[HSA] = 4:1) were incubated at 298 K for 1 h followed by a further incubation for 10 min at each temperature for equilibrium establishment (Celej et al., 2003; Sancataldo et al., 2014). The selected molar ratios of

[ligand]:[HSA] were made to obtain ~ 40 % decrease in the fluorescence intensity of HSA upon ligand binding. All other scanning parameters were kept the same as described in the Section 3.2.4.1 and the spectra were recorded in the wavelength range, 300–400 nm upon excitation at 295 nm.

The fluorescence data were transformed into relative fluorescence intensity at 342 nm ($FI_{342\ nm}$) or 343 nm ($FI_{343\ nm}$) by taking the fluorescence intensity at 342 / 343 nm of HSA or ligand–HSA mixtures at 298 K as 100.

3.2.7 Effect of metal ions on ligand–protein interactions

The fluorescence quenching titration method (as described in Section 3.2.5.1) was used to study the effect of metal ions, such as Mg^{2+}, K^{+}, Ca^{2+}, Mn^{2+}, Cu^{2+}, Zn^{2+} and Ba^{2+} on the ligand (VDB / LAP / GEF / SU) binding affinity of HSA. The protein solution was preincubated with these metal ions for 12 h or 1 h at 298 K in separate experiments prior to titration with the ligands. The final concentrations of the protein and the metal ions in the incubation mixture were maintained as 3 μM and 30 μM (VDB) / 50 μM (LAP) / 100 μM (GEF and SU), respectively.

Values of the binding constant, K_a for ligand–HSA interactions in the absence and presence of metal ions were obtained by treating the fluorescence quenching data in the same way as described in Section 3.2.5.2.

3.2.8 Competitive ligand displacement studies

In order to investigate the location of VDB, LAP, GEF and SU binding sites on HSA, competitive ligand binding experiments were performed using different site-specific markers, *i.e.*, PBZ and IDM for Sudlow's site I, DZM and KTN for Sudlow's site II and HMN and DGT for site III (Kragh-Hansen, 1985; Kragh-Hansen et al., 2002). In these experiments, either ligand–HSA complex was titrated with site markers or site marker–HSA complex was titrated with ligands and fluorescence spectra were

recorded in the wavelength range of 300–400 nm upon excitation at 295 nm. Values of the binding constant (K_a) for LAP / GEF / SU–HSA interactions were determined in the absence and presence site markers using Equation (5). All competitive ligand displacement experiments were performed at 298 K, pH 7.4.

3.2.8.1 Investigation of the VDB binding site

In these experiments, a fixed concentration of HSA (3 μM) and VDB–HSA mixture (mixed in a molar ratio of 5:1 and preincubated for 1 h at 298 K) were titrated with increasing concentrations (0–30 μM with 5 μM intervals) of PBZ or DZM in a total volume of 3.0 ml. After incubating the mixtures for additional 1 h at 298 K, the fluorescence spectra were recorded.

3.2.8.2 Investigation of the LAP binding site

The titration experiments were performed using free HSA as well as site marker (PBZ / DZM / HMN / DGT)-bound HSA. To a fixed concentration of HSA (3 μM) and its complexes with different site markers (mixed in a [site marker]:[HSA] molar ratio of 2:1 and preincubated for 1 h at 298 K), increasing concentrations (0–6.0 μM with 0.5 μM intervals) of LAP were added in a total volume of 3.0 ml. The fluorescence spectra were recorded after 1 h incubation at 298 K.

3.2.8.3 Investigation of the GEF binding site

These experiments were performed by titrating 3 μM HSA and its equimolar (1:1) complexes with IDM / KTN / HMN with increasing GEF concentrations (0–50 μM with 5 μM intervals). Site marker–HSA mixtures were allowed to equilibrate for 1 h at 298 K before titration with GEF. Fluorescence spectra were recorded after additional 1 h incubation at 298 K upon GEF addition.

3.2.8.4 Investigation of the SU binding site

Free protein (HSA) solution (3 μM) and its mixture with PBZ / DZM (mixed in a [site marker]:[HSA] molar ratio of 1:1 and preincubated for 1 h at 298 K) were titrated with increasing SU concentrations (0–24 μM with 2 μM intervals). The fluorescence spectra were recorded after 1 h incubation at 298 K.

3.2.9 Molecular docking studies

The 3-D structures of VDB, LAP, GEF and SU were constructed and their geometries were optimized by energy minimization in MMFF94 force field (Halgren, 1996) using Avogadro Software (Hanwell et al., 2012). These structures were exported as mol2 files. Docking, visualization and rendering simulation were performed using AutoDock 4.2 (Goodsell et al., 1996) and AutoDockTools 1.5.6 at the Academic Grid Malaysia Infrastructure (Sanner, 1999). The crystal structure of HSA (PDB code: 1BM0) with resolution at 2.5 Å was downloaded from the Protein Data Bank (Berman et al., 2000). Water molecules were removed and the atomic coordinates of chain A of 1BM0 were stored in a separate file and were used as input for AutoDockTools after adding polar hydrogens, Kollman charges and solvation parameters. Merging of nonpolar hydrogens and defining rotatable bonds were made in the ligands. The molecular docking analyses were made for different ligand binding sites, *i.e.*, Sudlow's sites I and II (VDB and SU) or sites I, II and III (LAP and GEF) of HSA. For each binding site (sites I, II and III), an independent docking analysis of 100 runs (VDB, LAP and GEF) / 250 runs (SU) was performed within a grid box with 70 × 70 × 70 grid points and a grid space of 0.375 Å.

For VDB–HSA docking analysis, the 3-D coordinates of center of grid box were at x = 35.26, y = 32.41 and z = 36.46 for site I and x = 14.42, y = 23.55 and z = 23.31 for site II.

For LAP–HSA docking analysis, the 3-D coordinates of center of grid box were at x = 35.26, y = 32.41 and z = 36.46 for site I; x = 14.42, y = 23.55 and z = 23.31 for site II and x = 42.45, y = 24.47 and z = 15.28 for site III.

For GEF–HSA docking analysis, the 3-D coordinates of center of grid box were at x = 41.61, y = 33.78 and z = 30.49 for site I; x = 11.61, y = 29.78 and z = 18.49 for site II and x = 46.61, y = 22.78 and z = 14.49 for site III.

For SU–HSA docking analysis, the 3-D coordinates of center of grid box were at x = 35.61, y = 31.78 and z = 31.49 for site I and x = 14.61, y = 22.78 and z = 21.49 for site II.

Lamarckian genetic algorithm with local search was used as the search engine. In each run, a population of 150 individuals with 27 000 generations and 250 000 energy evaluations were employed. Operator weights for crossover, mutation and elitism were set at 0.8, 0.02, and 1.0, respectively. For the local search, default parameters were used. Cluster analyses were performed on docked results using a root-mean-square deviation (RMSD) tolerance of 2.0 Å. The ligand–HSA complexes were visualized using AutoDockTools (VDB and LAP) or Chimera 1.10.2 (GEF and SU) (Pettersen et al., 2004).

Besides, the docking results depicting the interactions between the ligand and its binding sites were observed using LigPlot+ (VDB, LAP and SU) (Wallace et al., 1995) and mesh surface representation (GEF).

3.2.10 Statistical analysis

The experimental results of this study are presented as an average ± standard deviation (SD) from three individual experiments. All the figures were made using the OriginPro version 8.5 software (OriginLab Corp., Northampton, MA) by fitting experimental data to their corresponding equations.

Flow chart of the research work

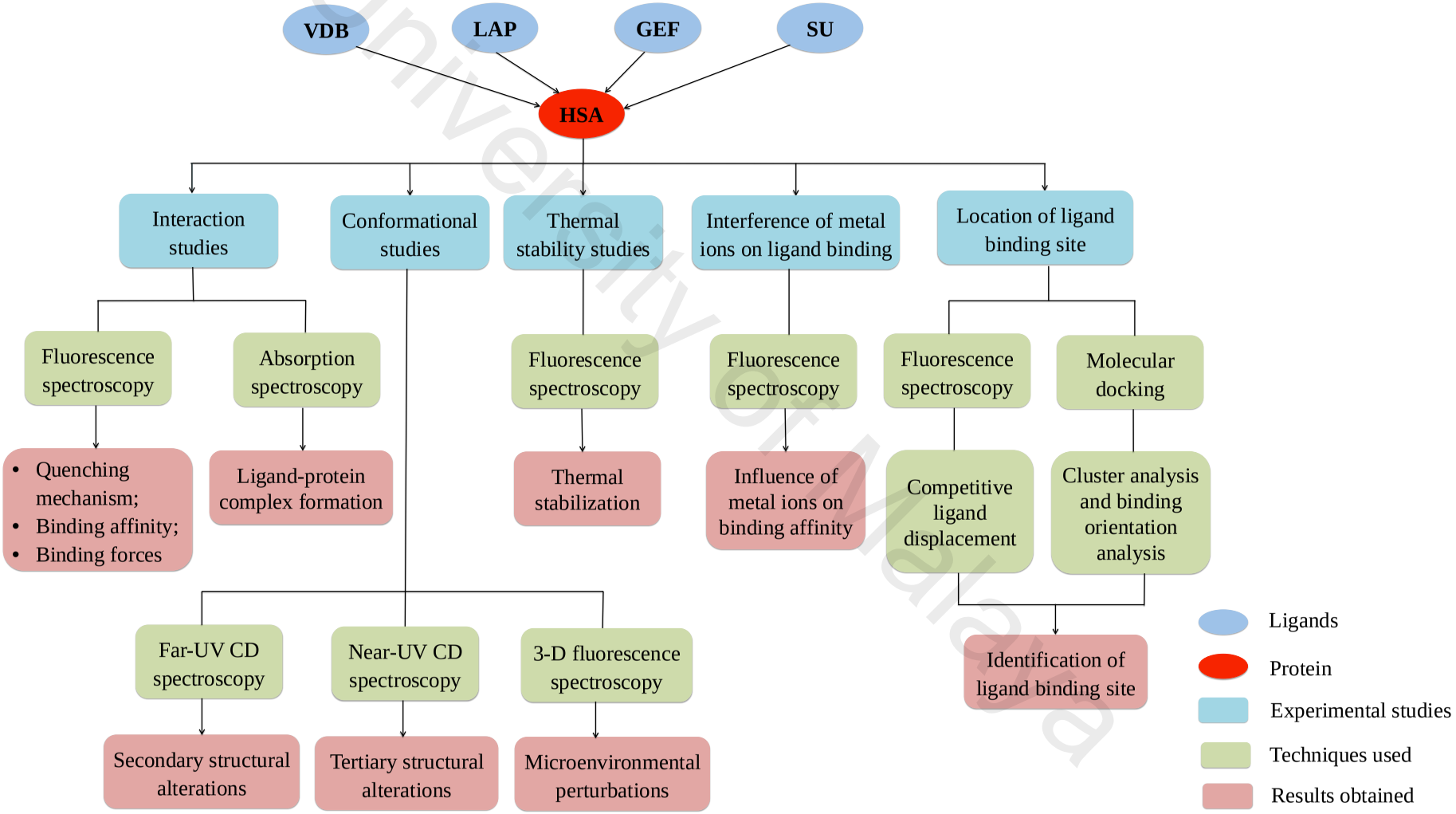

CHAPTER 4: RESULTS AND DISCUSSION

4.1 VDB–HSA interaction

Fluorescence spectroscopic method has been greatly exploited in ligand binding studies in being highly sensitive, less time consuming and easy to perform. The fluorescence measurements can provide some useful information about the binding of small molecules to protein such as binding mechanism, binding mode, binding constants and binding numbers (Bozoglan et al., 2014). Therefore, fluorescence spectroscopy was employed to study VDB–HSA interaction.

4.1.1 Fluorescence spectra

Figure 4.1 shows the fluorescence spectra of HSA in the absence and presence of increasing concentrations of VDB. The fluorescence spectrum of HSA was characterized by the presence of an emission maximum at 342 nm, which was indicative of the presence of tryptophan (Trp) in HSA (Sulkowska, 2002). A progressive decrease in the fluorescence intensity and red shift in the emission maximum were observed upon addition of VDB to HSA. About 35 % decrease in the fluorescence intensity at 342 nm (inset of Figure 4.1) and 8 nm red shift were noticed at the highest concentration (60 μM) of VDB (Figure 4.1). Free VDB did not produce any fluorescence signal within this wavelength range (Figure 4.1). Alteration in the fluorescence characteristics (fluorescence intensity and emission maximum) of HSA upon addition of VDB were suggestive of VDB binding to HSA. Similar changes in the fluorescence characteristics have been shown in many ligand binding studies (Cheng et al., 2013; Feroz et al., 2013; Li et al., 2007). It seems probable that VDB binds to a site near the single Trp residue (Trp-214) of HSA, which may account for the significant decrease in the fluorescence intensity and red shift in the emission maximum upon VDB binding. In view of the unique sensitivity of the emission maximum to

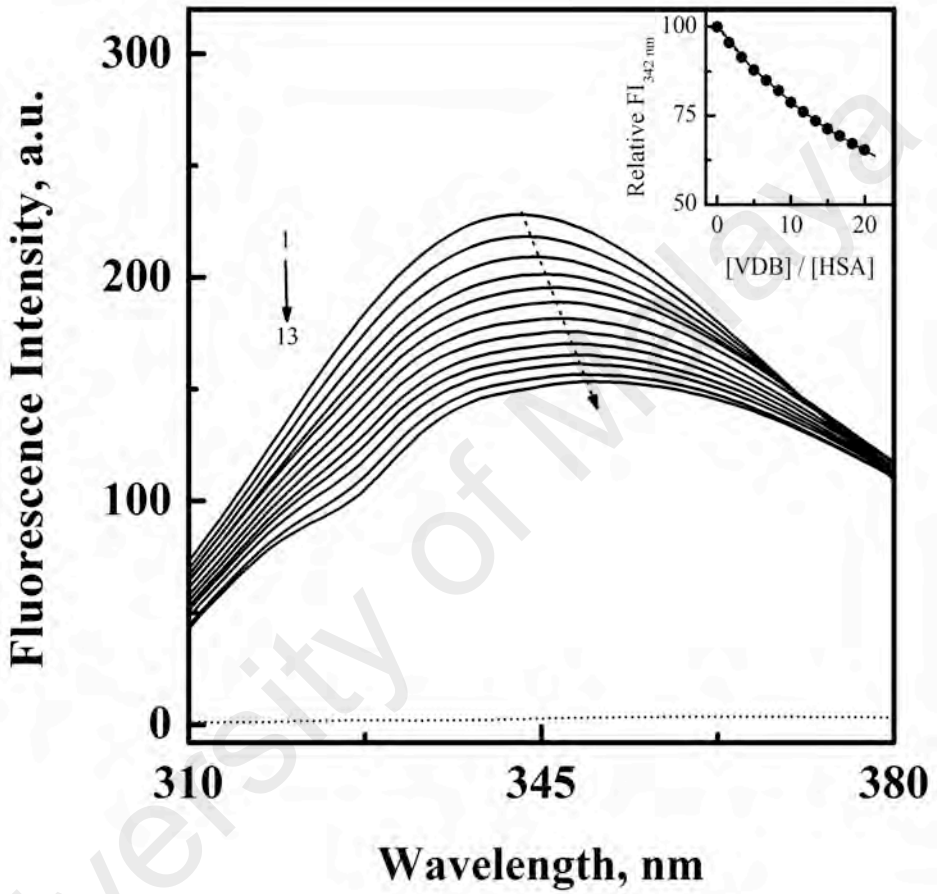

Figure 4.1: Fluorescence spectra of HSA (3 μM) in the absence (spectrum 1) and presence (spectra 2–13) of increasing VDB concentrations (5–60 μM with 5 μM intervals), obtained in 60 mM sodium phosphate buffer, pH 7.4 at 288 K upon excitation at 295 nm. The fluorescence spectrum of free VDB (60 μM) is shown with dotted line. The inset shows the decrease in the relative fluorescence intensity of HSA at 342 nm ($FI_{342\ nm}$) with increasing VDB/HSA molar ratios.

hydrophobic changes in the microenvironment around fluorophores (Lakowicz, 2006), red shift in the emission maximum observed upon VDB addition may point toward increased polarity of the microenvironment around Trp residue. This was also supported by the decrease in the fluorescence intensity of HSA in the presence of VDB, as fluorescence intensity is known to be affected by hydrophobic changes and movement of charged groups in the vicinity of the Trp residue (Lakowicz, 2006).

4.1.2 Mechanism of fluorescence quenching

The mechanism of fluorescence quenching of a protein can be classified either as static or dynamic quenching process. These two mechanisms can be distinguished by their response to temperature (Lakowicz, 2006). Higher temperatures lead to faster diffusion, thus producing a large amount of collisional quenching between the fluorophore and the quencher. Contrary to it, higher temperatures contribute to the dissociation of weakly-bound complexes, resulting in a decrease in static quenching (Lakowicz, 2006). Therefore, the quenching constant increases with temperature for dynamic quenching process and shows a decrease for static quenching (Maiti et al., 2008; Tunc et al., 2013a; Xu et al., 2013). In order to investigate the fluorescence quenching mechanism involved in VDB−HSA system, the titration experiments were carried out at three different temperatures, *i. e.*, 288 K (Figure 4.1), 303 K and 318 K (Figure 4.1S) and the fluorescence quenching data were analyzed according to the Stern-Volmer equation (Eq. (3)). The Stern-Volmer plots shown in Figure 4.2 indicated linear relationship between F_0 / F and [VDB]. Regression analysis of these plots yielded the values of the Stern-Volmer constant, K_{SV} at different temperatures, which are listed in Table 4.1. A gradual decrease in the K_{SV} value with increasing temperatures (Figure 4.2, Table 4.1) clearly demonstrated that the fluorescence quenching observed was due to the complex formation between VDB and HSA and therefore, can be characterized as static quenching. This seems understandable as increase in temperature would have

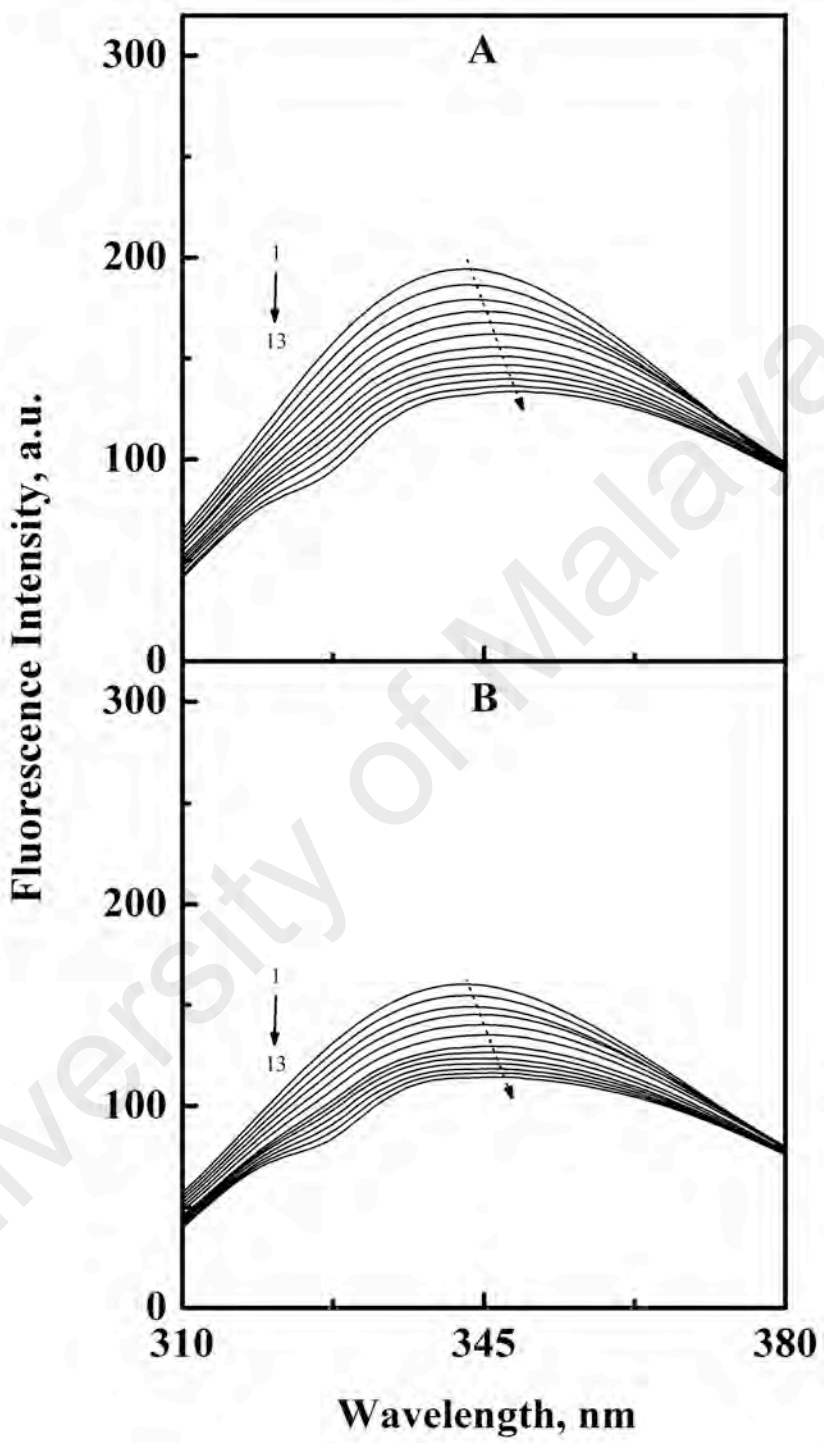

Figure 4.1 S: Fluorescence spectra of HSA (3 μM) in the absence (spectrum 1) and presence (spectra 2–13) of increasing VDB concentrations (5–60 μM with 5 μM intervals), obtained in 60 mM sodium phosphate buffer, pH 7.4 at (A) 303 K and (B) 318 K upon excitation at 295 nm.

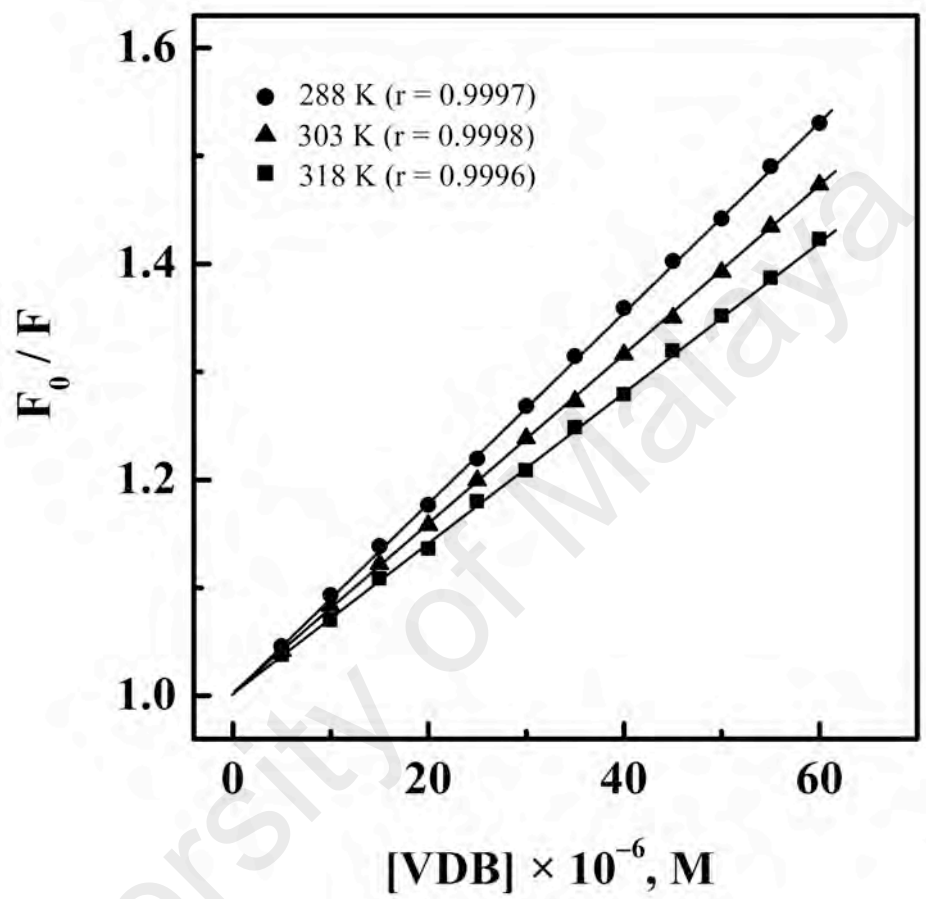

Figure 4.2: Stern-Volmer plots for the fluorescence quenching data of the VDB–HSA system, obtained at three different temperatures, *i.e.*, 288 K, 303 K and 318 K.

Table 4.1: Quenching and binding parameters for VDB–HSA interaction, studied at three different temperatures, pH 7.4.

T (K)	K_{SV} (M^{-1})	k_q ($M^{-1}\,s^{-1}$)	K_a (M^{-1})
288	$(8.77 \pm 0.15) \times 10^3$	$(1.37 \pm 0.14) \times 10^{12}$	$(8.92 \pm 0.05) \times 10^3$
303	$(7.70 \pm 0.10) \times 10^3$	$(1.20 \pm 0.12) \times 10^{12}$	$(7.63 \pm 0.17) \times 10^3$
318	$(6.90 \pm 0.17) \times 10^3$	$(1.08 \pm 0.15) \times 10^{12}$	$(6.89 \pm 0.10) \times 10^3$

weakened the forces involved in VDB–HSA complex formation. Furthermore, the calculated k_q values, using Eq. (4) for VDB–HSA system (Table 4.1) were found higher than the maximum dynamic quenching constant (2×10^{10} M^{-1} s^{-1}), reported for various quenchers of biomolecules (Ware, 1962). This has further supported the involvement of static quenching mechanism in the interaction between VDB and HSA.

4.1.3 Binding affinity

To determine the binding constant (K_a) of VDB–HSA system at different temperatures, fluorescence quenching data were analyzed using Eq. (5) and were plotted as log $(F_0 - F) / F$ versus log $[1 / ([L_T] - [(F_0 - F) [P_T] / F_0)]$, as shown in Figure 4.3. The values of K_a at three different temperatures were obtained from these plots following the method described in Section 3.2.5.2 and are listed in Table 4.1. The K_a values ($8.92–6.89 \times 10^3$ M^{-1}) reflected weak binding affinity between VDB and HSA, which is useful for efficient transport and release of VDB at the target site. Several reports have suggested the values of K_a for different ligand–protein interactions fall in the range, $3.35 \times 10^3 – 1.3 \times 10^4$ M^{-1} (Afrin et al., 2014; Li et al., 2015; Liu et al., 2009). The decreasing trend of K_a values with temperature indicated reduction in the VBD binding capacity of HSA, thus leading to less stable VDB–HSA complex (Feroz et al., 2012; Trnkova et al., 2011).

4.1.4 Interaction forces

The ligand–protein complex formation may involve various noncovalent forces such as hydrogen bonds, hydrophobic interactions, van der Walls forces and electrostatic forces. Thermodynamic parameters such as the enthalpy change (ΔH), the entropy change (ΔS) and the free energy change (ΔG) of the binding reaction can establish the binding mode between a ligand and the protein (Li et al., 2007; Olsson et al., 2008; Ross & Subramaniam, 1981). In order to examine the acting forces involved in

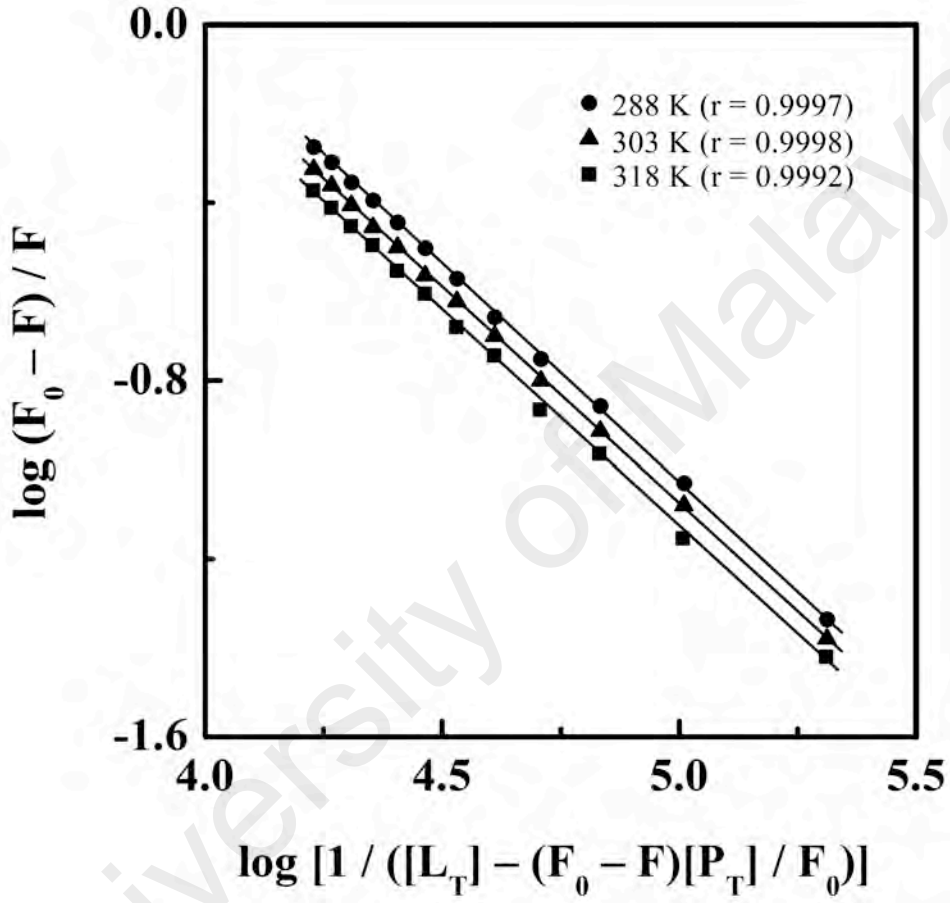

Figure 4.3: Double logarithmic plots of [log ($F_0 - F$) / F versus log [1 / ([L_T] – [(F_0 – F)[P_T] / F_0)] for the fluorescence quenching data of the VDB–HSA system, obtained at three different temperatures, *i.e.*, 288 K, 303 K and 318 K.

VDB–HSA interaction, thermodynamic parameters (ΔH and ΔS) were assessed using Eq. (6) for the van't Hoff plot between ln K_a and $1/T$, as shown in Figure 4.4. Values of ΔH and ΔS along with ΔG (obtained by using Eq. (7)) are summarized in Table 4.2. The negative values of ΔG clearly demonstrated that the binding between VDB and HSA was spontaneous at all temperatures. The negative sign of ΔH revealed exothermic nature of the binding reaction. The water molecules that were otherwise arranged in an orderly fashion around the ligand (VDB) and the protein (HSA) molecules, must have acquired a more random conformation upon VDB–HSA complex formation, thus resulting in the positive entropy change (ΔS). A positive value of ΔS obtained for ligand-protein interaction is frequently taken as an evidence for the involvement of hydrophobic interactions (Ross & Subramaniam, 1981). Meanwhile, ΔS value seems to play the major role in making the ΔG value negative for VDB−HSA interaction. (Li et al., 2007; Zhang et al., 2008). On the other hand, the large negative value of ΔH, obtained for VDB–HSA system can account for the involvement of hydrogen bonds and / or van der Walls forces (Ross & Subramaniam, 1981). Involvement of electrostatic interactions in VDB–HSA complex formation can be ruled out as the value of ΔH should be either very small or close to zero for typical electrostatic interactions (Rahman et al., 1993b; Ross & Subramanian, 1981; Zhang et al., 2008). Since VDB lacks any ionizable / charged group, it is inconceivable to suggest the involvement of electrostatic interactions in the VDB−HSA binding process.

It is not reasonable to account for the observed changes in the thermodynamic parameters using only a single binding force, as these changes reflect several intermolecular phenomena between the ligand and the protein (Li et al., 2007; Zhang et al., 2008). Therefore, hydrophobic interactions and hydrogen bonds are believed to contribute collectively for the stabilization of VDB–HSA complex. Several reports have shown the involvement of hydrophobic interactions and hydrogen bonds as the acting

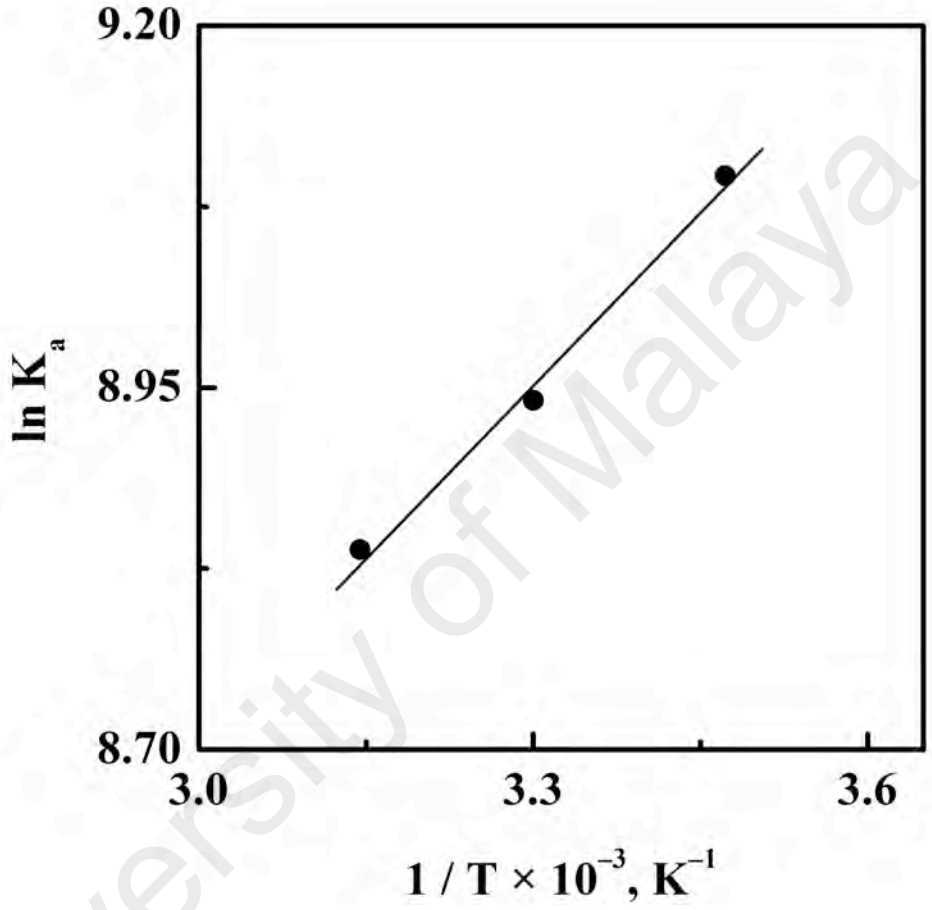

Figure 4.4: The van't Hoff plot for VDB–HSA interaction. Values of K_a were obtained from the double logarithmic plots, displayed in Figure 4.3.

Table 4.2: Thermodynamic parameters for VDB–HSA interaction, studied at three different temperatures, pH 7.4.

T (K)	ΔS (J mol^{-1} K^{-1})	ΔH (kJ mol^{-1})	ΔG (kJ mol^{-1})
288			– 21.77
303	+ 52.76	– 6.57	– 22.56
318			– 23.35

forces in drug-serum albumin interactions based on the positive value of ΔS and the negative ΔH value (Feroz et al., 2012; Feroz et al., 2015; Li et al., 2007; Li et al., 2008; Zhang et al., 2008). Our docking analysis of VDB–HSA complex also predicted the involvement of both these interactions in the complex formation as described in Section 4.1.9.2.

4.1.5 Absorption spectra

Ligand-induced perturbations in the absorption spectrum of the protein are usually seized as indicator for the complex formation between a ligand and the protein (Peters, 1996). Variations in the absorption spectrum of HSA in the presence of increasing VDB concentrations (4–20 μM with 4 μM intervals) (Figure 4.5) were attained after subtracting the absorption contribution of free VDB (Figure 4.5S(B)) from the absorption spectra of respective VDB–HSA mixture (Figure 4.5S(A)). Occurrence of the absorption peak at 280 nm in the UV-vis absorption spectrum of HSA can be ascribed to the presence of lone Trp residue (Trp-214) in HSA (Berde et al., 1979). In addition, another peak also appeared at 330 nm, whose intensity also increased with increasing VDB concentrations. The hyperchromic effect in the absorption spectrum of HSA produced by the added VDB clearly reflected VDB-induced microenvironmental changes in the vicinity of the Trp-214 due to complex formation between VDB and HSA (Peters, 1996). These results were in line with those described in Section 4.1.2, confirming VDB–HSA complex formation.

4.1.6 VDB-induced structural / microenvironmental changes in HSA

VDB-induced structural (secondary and tertiary structures) changes and microenvironmental perturbations around protein fluorophores (Trp and Tyr) in HSA were investigated using circular dichroism and 3-D fluorescence spectroscopy, respectively.

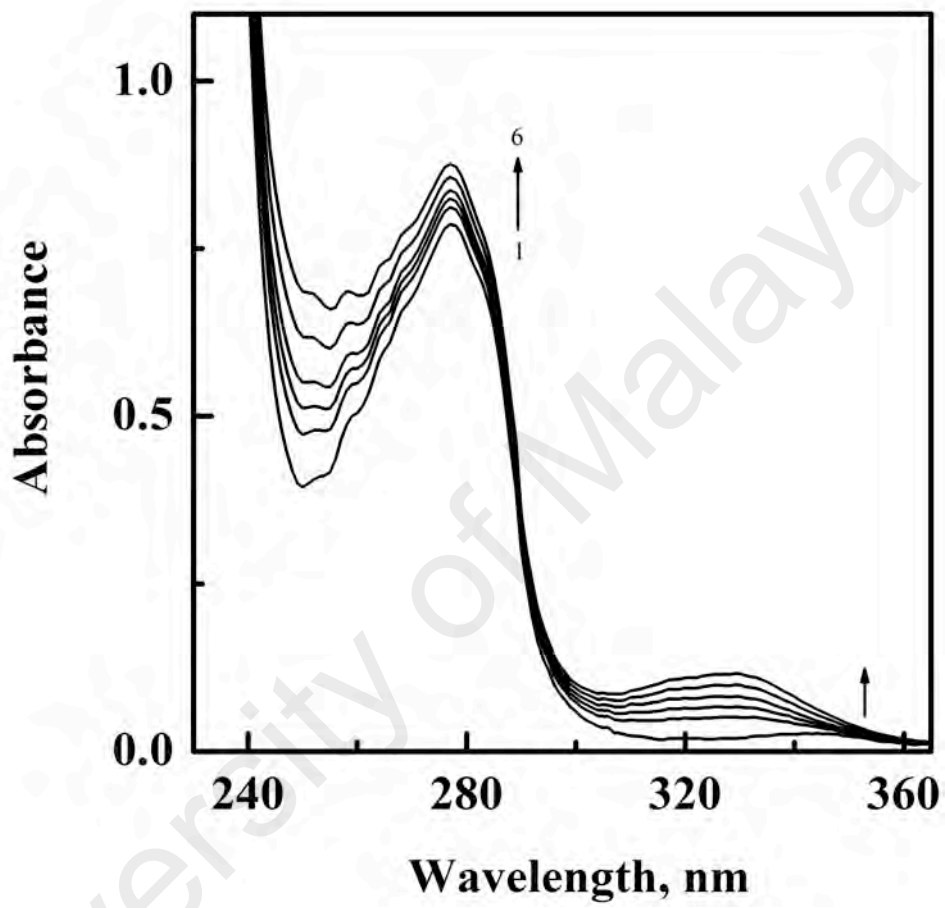

Figure 4.5: UV-vis absorption spectra of HSA (20 μM) in the absence (spectrum 1) and presence (spectra 2–6) of increasing VDB concentrations (4–20 μM with 4 μM intervals), obtained in 60 mM sodium phosphate buffer, pH 7.4 at 298 K. The spectra (2–6) were obtained by subtracting the absorption contribution of respective free VDB from the absorption spectra of VDB–HSA mixtures.

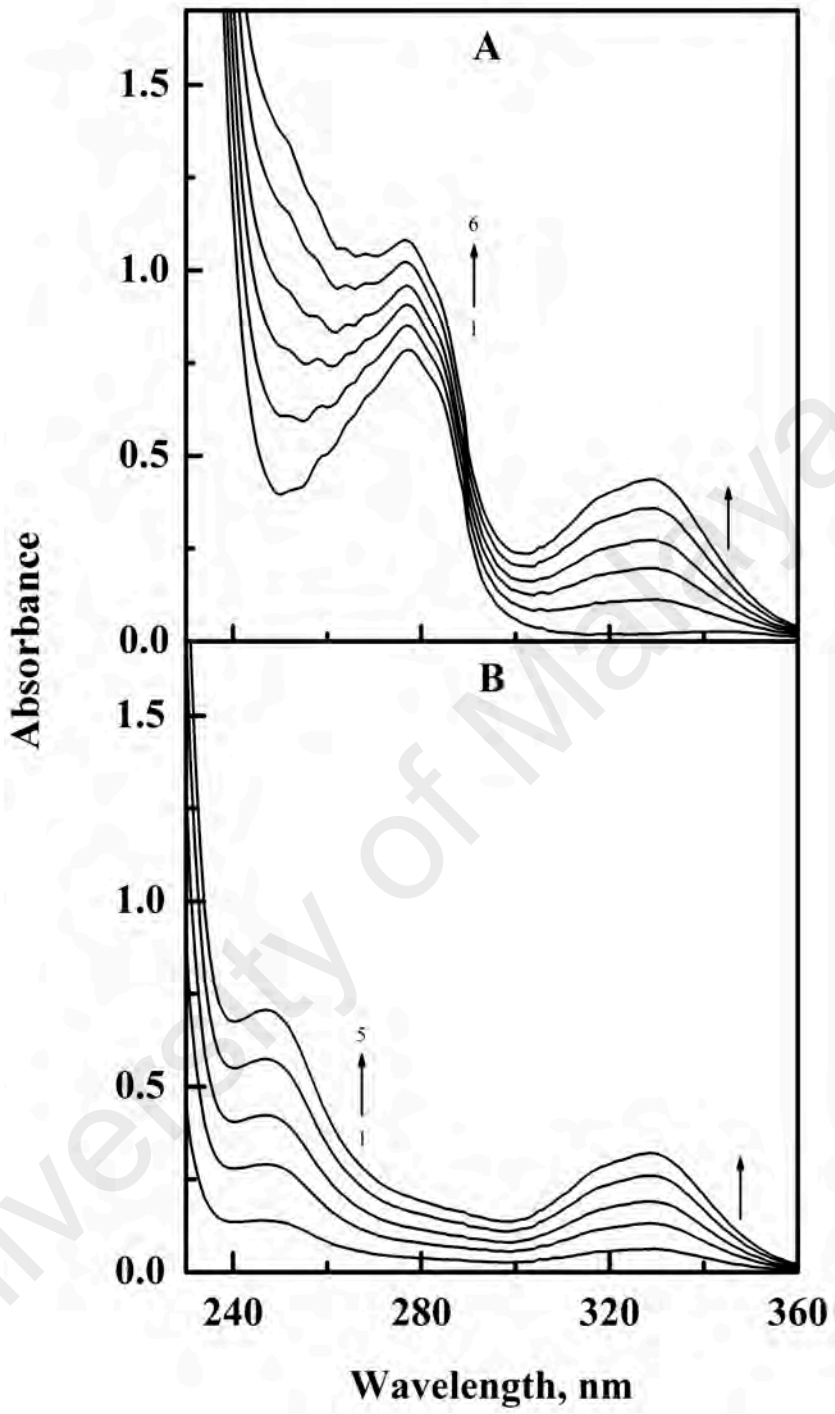

Figure 4.5 S: (A) Uncorrected UV-vis absorption spectra of HSA (20 μM) in the absence (spectrum 1) and presence (spectra 2–6) of increasing VDB concentrations (4–20 μM with 4 μM intervals), obtained in 60 mM sodium phosphate buffer, pH 7.4 at 298 K. (B) The spectra (1–5) were obtained with increasing VDB concentrations (4–20 μM with 4 μM intervals).

4.1.6.1 Far-UV and near-UV CD spectra

Figures 4.6 and 4.7 show the effect of VDB binding on the secondary and tertiary structures, respectively, of HSA at a [VDB]:[HSA] molar ratio of 1:1. The far-UV CD spectrum of HSA (Figure 4.6) was characterized by the presence of two minima at 208 nm and 222 nm, characteristics of the $\alpha-$ helical structure of the protein (Reed et al., 1975). Presence of VDB in the system produced significant alterations in the far-UV CD spectra of HSA, showing ~ 7.5 % decrease in the $MRE_{222\ nm}$ value at 1:1 VDB/HSA molar ratio. Such a decrease in the $MRE_{222\ nm}$ value was indicative of the secondary structure alteration of HSA in the presence of VDB, thus implying complex formation between VDB and HSA.

The near-UV CD spectra of HSA in the absence and presence of VDB are displayed in Figure 4.7. Presence of two minima at around 263 nm and 270 nm and shoulders around 272 nm and 284 nm characterized the near-UV CD spectrum of HSA. These spectral features were similar to those reported earlier and characterized the presence of the disulfide bonds and aromatic chromophores in the protein (Lee et al., 1992; Uversky et al., 1997). A significant reduction in the CD spectral signals was observed in the presence of VDB, suggesting perturbations around the Trp residue and disulfide bonds due to tertiary structural change.

In view of the above, it can be concluded that VDB binding to HSA produced both secondary and tertiary structural alterations in HSA. Similar CD spectral changes of HSA have been reported in the presence of various other ligands (Chatterjee et al., 2012; Dockal et al., 1999; Lee et al., 1992).

4.1.6.2 Three-dimensional fluorescence spectra

Knowledge of VDB-induced microenvironmental changes around aromatic fluorophores (Trp and Tyr) is particularly important as one of the ligand binding sites *i.e.*, Sudlow's site I is located in the vicinity of Trp-214 of HSA (Sudlow et al., 1975).

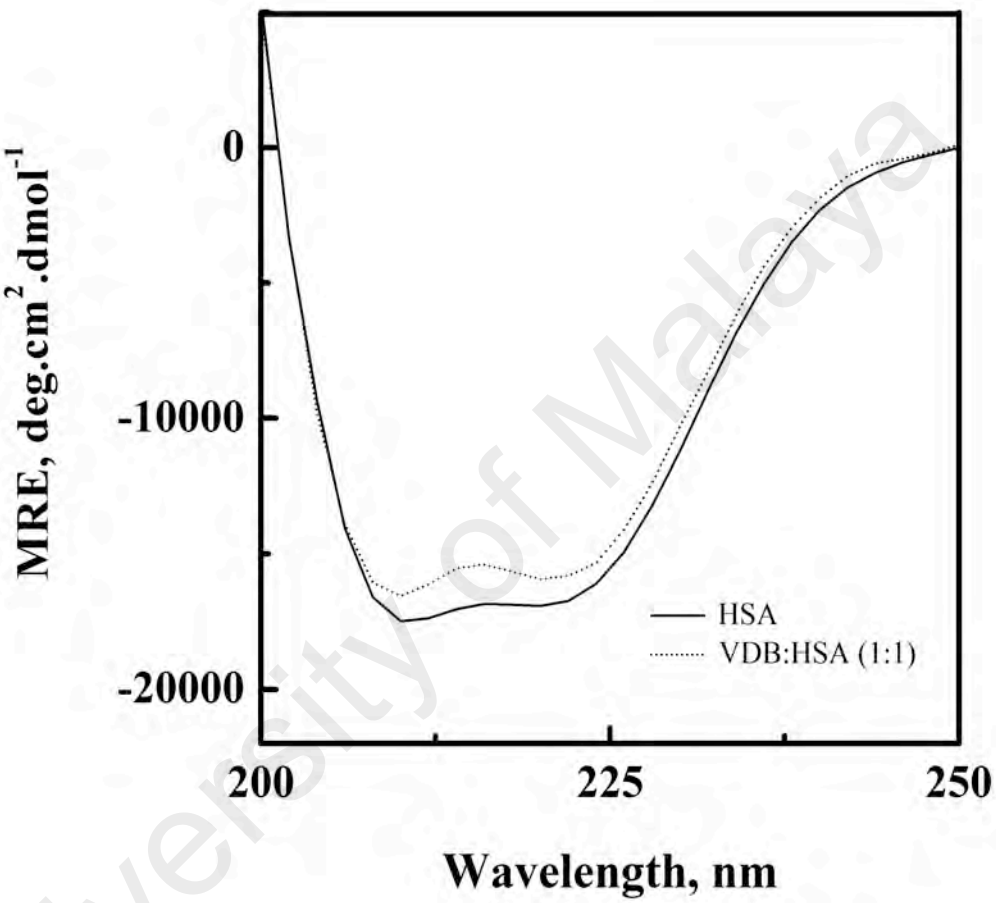

Figure 4.6: Far-UV CD spectra of HSA (1 μM) and VDB–HSA (1:1) mixture. The CD spectra were recorded using a 1 mm path length cuvette, in 60 mM sodium phosphate buffer, pH 7.4 at 298 K.

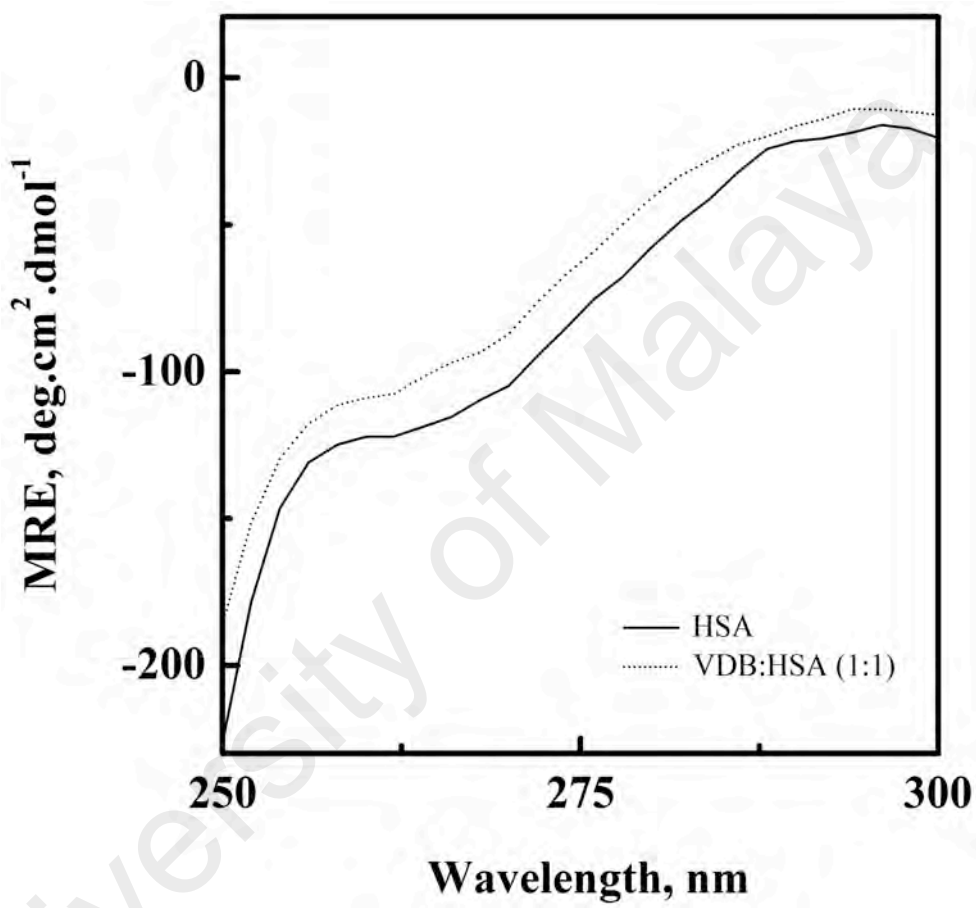

Figure 4.7: Near-UV CD spectra of HSA (5 μM) and VDB–HSA (1:1) mixture. The CD spectra were recorded using a 10 mm path length cuvette, in 60 mM sodium phosphate buffer, pH 7.4 at 298 K.

Three-dimensional fluorescence spectra and corresponding contour maps of free HSA (A) and [VDB]:[HSA] (5:1) mixture (B) are shown in Figure 4.8. The fluorescence characteristics, such as peak position (λ_{ex} / λ_{em}) and intensity of the peaks are listed in Table 4.3. As shown in Figure 4.8, peaks 'a' and 'b', which are known as Rayleigh scattering peak ($\lambda_{ex} = \lambda_{em}$) and the second order scattering peak ($2\lambda_{ex} = \lambda_{em}$), respectively, are common in 3-D fluorescence spectra (Cheng et al., 2013; Feroz et al., 2013; Lu et al., 2009). In addition to these peaks, two other fluorescence peaks, namely, '1' (λ_{ex} = 280 nm) and '2' (λ_{ex} = 230 nm) were also observed, which were due to the presence of Trp and Tyr residues in the protein (Feroz et al., 2015). Presence of VDB in the incubation mixture produced significant change in the spectral characteristics. Whereas peak '1' showed a red shift of 11 nm and ~ 36 % decrease in the fluorescence intensity, 13 nm red shift and ~ 80 % decrease in the fluorescence intensity were noticed in peak '2' upon VDB addition to HSA (Table 4.3). These results suggested microenvironmental perturbation around Trp-214 upon VDB binding. Due to the presence of the lone tryptophan (Trp-214) in domain II of HSA (Peters, 1996), it seems that domain II might have undergone significant structural perturbation upon VDB binding.

4.1.7 Thermal stabilization of HSA

Several earlier reports have shown relatively greater thermostability of HSA in the presence of ligands, which are known to bind to HSA (Feroz et al., 2013; Sancataldo et al., 2014; Watanabe et al., 2001). In view of it, we also checked the thermostability of HSA in the presence of VDB ([VDB]:[HSA] = 10:1), by monitoring the change in the protein's fluorescence with increasing temperatures. Temperature-induced variations in the protein's fluorescence intensity in the absence and upon addition of VDB are depicted in Figure 4.9. As can be noticed from the figure, significantly lesser decease in the intensity value was observed in the presence of VDB within the temperature range,

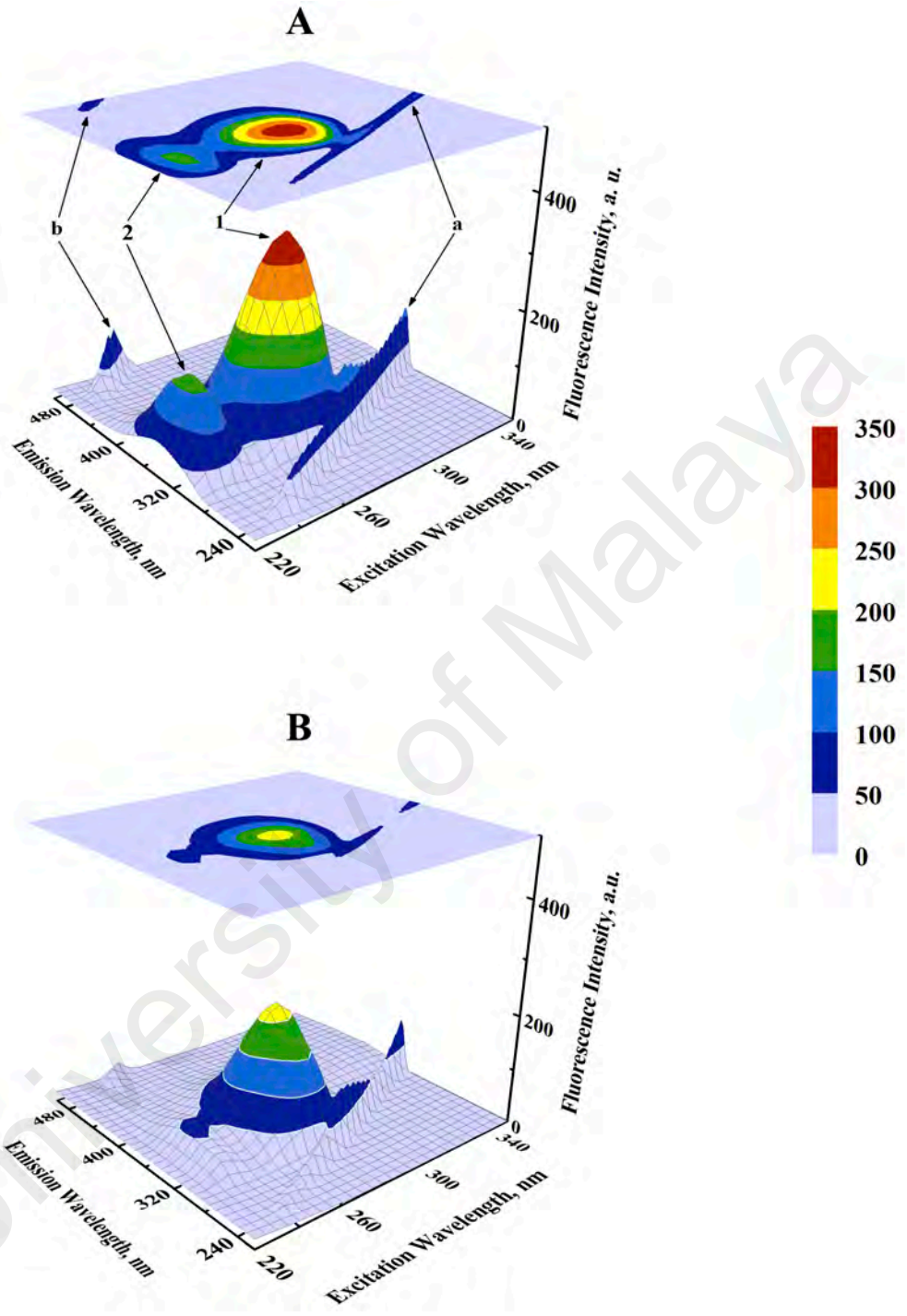

Figure 4.8: Three-dimensional fluorescence spectra and corresponding contour maps of (A) HSA (3 μM) and (B) VDB–HSA (5:1) mixture. The spectra were recorded in 60 mM sodium phosphate buffer, pH 7.4 at 298 K.

Table 4.3: Three-dimensional fluorescence spectral characteristics of HSA (3 μM) and VDB–HSA system at 298 K, pH 7.4.

System	Peak	Peak Position [λ_{ex} / λ_{em} (nm/nm)]	Intensity
HSA	a	230/230→350/350	17.91→113.91
	b	250/500	93.97
	1	280/338	342.62
	2	230/335	161.63
[VDB]:[HSA] = 5:1	a	230/230→350/350	14.53→95.82
	b	250/500	32.87
	1	280/349	221.10
	2	230/348	31.64

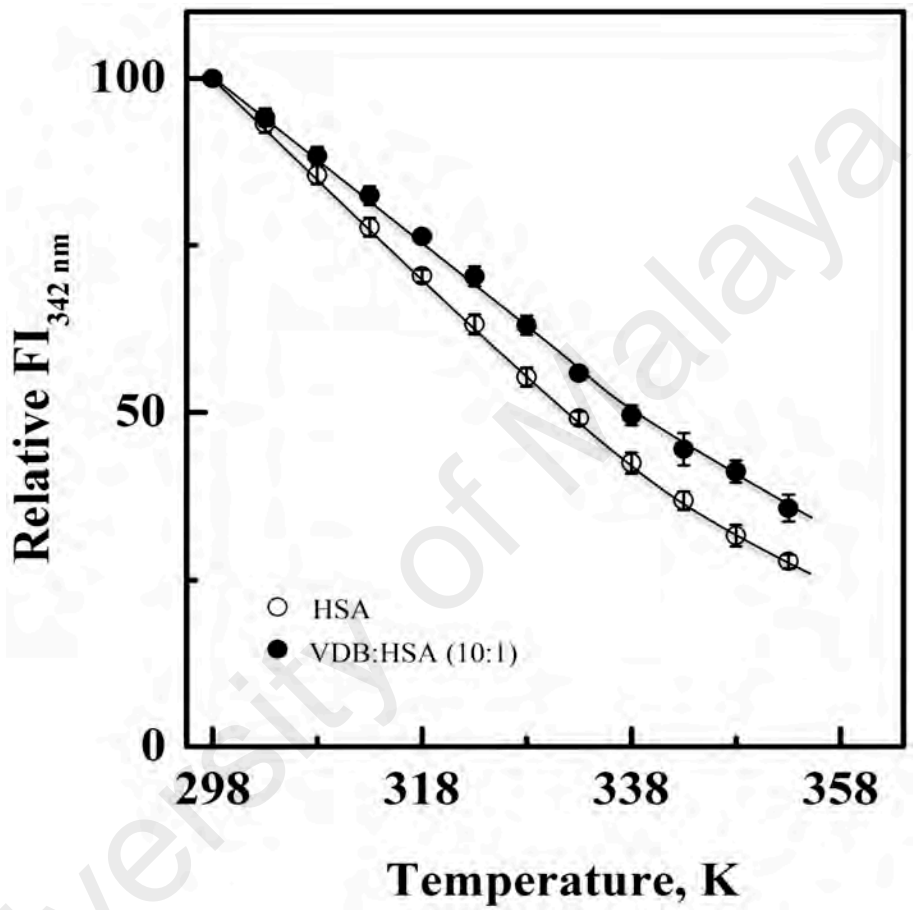

Figure 4.9: Thermal stability profiles of HSA (3 μM) and VDB–HSA (10:1) mixture in the temperature range, 298–353 K with a regular increments of 5 K, as monitored by fluorescence intensity measurements at 342 nm ($FI_{342\ nm}$), in 60 mM sodium phosphate buffer, pH 7.4.

308–353 K compared to that evident with HSA alone. Such difference was more pronounced at higher temperatures. Quantitatively, ~ 64 % loss in the fluorescence intensity value of the protein was marked at 353 K with addition of VDB against ~ 72 % decrease noticed with HSA alone. Such improvement in the fluorescence intensity displayed by VDB–HSA mixture at higher temperatures clearly suggested thermal stabilization of HSA offered by VDB binding. This seems understandable as higher temperatures might be needed to destabilize the noncovalent forces involved in the VDB–HSA complexation (Stickle et al., 1992).

4.1.8 Influence of metal ions on VDB–HSA interaction

Metal ions are vital for various biochemical processes and some of these are present in low concentrations in blood plasma (Guidotti et al., 2008). The influence of some common metal ions such as Ca^{2+}, Zn^{2+}, Cu^{2+}, Ba^{2+}, Mg^{2+} and Mn^{2+} on VDB–HSA interaction was investigated at pH 7.4, 298 K by determining the binding constant (K_a) of VDB–HSA complex in the absence and presence of these metal ions (30 μM). As can be seen from Table 4.4, the K_a value of VDB–HSA complex showed smaller but significant decrease in the presence of Mg^{2+}, Zn^{2+}, Ba^{2+} and Cu^{2+} while a smaller but significant increase in K_a value was noticed in the presence of Mn^{2+}. These results suggested metal ions' interference with VDB–HSA complex formation due to change in the binding affinity in the presence of metal ions. Such interference may shorten or prolong the storage time of drug in blood plasma that could weaken or enhance the effectiveness of the drug (Cheng et al., 2013; Cui et al., 2004). Therefore, presence of metal ions in blood plasma could affect the pharmacokinetics of VDB in blood circulation.

Table 4.4: K_a values of VDB–HSA interaction in the absence and presence of different metal ions (30 μM) at 298 K, pH 7.4.

Metal Ion	K_a ($\times 10^3$ M^{-1})
-	8.09 ± 0.15
Mg^{2+}	7.36 ± 0.20
Ca^{2+}	7.87 ± 0.21
Mn^{2+}	9.00 ± 0.15
Cu^{2+}	7.27 ± 0.07
Zn^{2+}	6.82 ± 0.03
Ba^{2+}	7.22 ± 0.16

4.1.9 Location of VDB binding site

Identification of VDB binding site on HSA was made using competitive ligand displacement studies with site markers as well as molecular docking.

4.1.9.1 Site marker-induced VDB displacement

According to Sudlow et al. (1975), a large number of common ligands as well as drugs interact with HSA at two different binding sites, namely, site I and site II, that are resided in sub-domains IIA and IIIA, respectively (Peters, 1996). Site I shows affinity for several specific markers such as warfarin, PBZ and IDM, whereas DZM, KTN and ibuprofen are well known markers for site II (Kragh-Hansen et al., 2002). In order to identify the location of the VDB binding site on HSA, competitive ligand displacement experiments were performed with PBZ (site I marker) and DZM (site II marker) using fluorescence spectroscopy. Figures 4.10 and 4.11 show titration results of HSA and VDB–HSA mixture ([VDB]:[HSA] = 5:1) with increasing concentrations of PBZ and DZM, respectively. As can be seen from the figures, a progressive decrease in the fluorescence intensity at 342 nm ($FI_{342\ nm}$) of HSA was noticed upon addition of PBZ or DZM, which was indicative of their binding to HSA. Interestingly, presence of VDB in VDB–HSA mixture offered significant protection against PBZ-induced decrease in the spectral signal, but lesser effect was noticed in the presence of DZM. These results clearly suggested preference of site I of HSA for VDB binding compared to site II. Furthermore, these results were in line with our 3-D fluorescence spectral results, suggesting structural perturbation around protein fluorophores upon VDB binding. Since site I contains Trp-214 in it, its microenvironment might have been changed upon VDB binding to this site to produce spectral shift and decrease in fluorescence intensity.

4.1.9.2 Molecular docking analysis

A molecular docking study was made to predict the binding site of VDB in HSA and

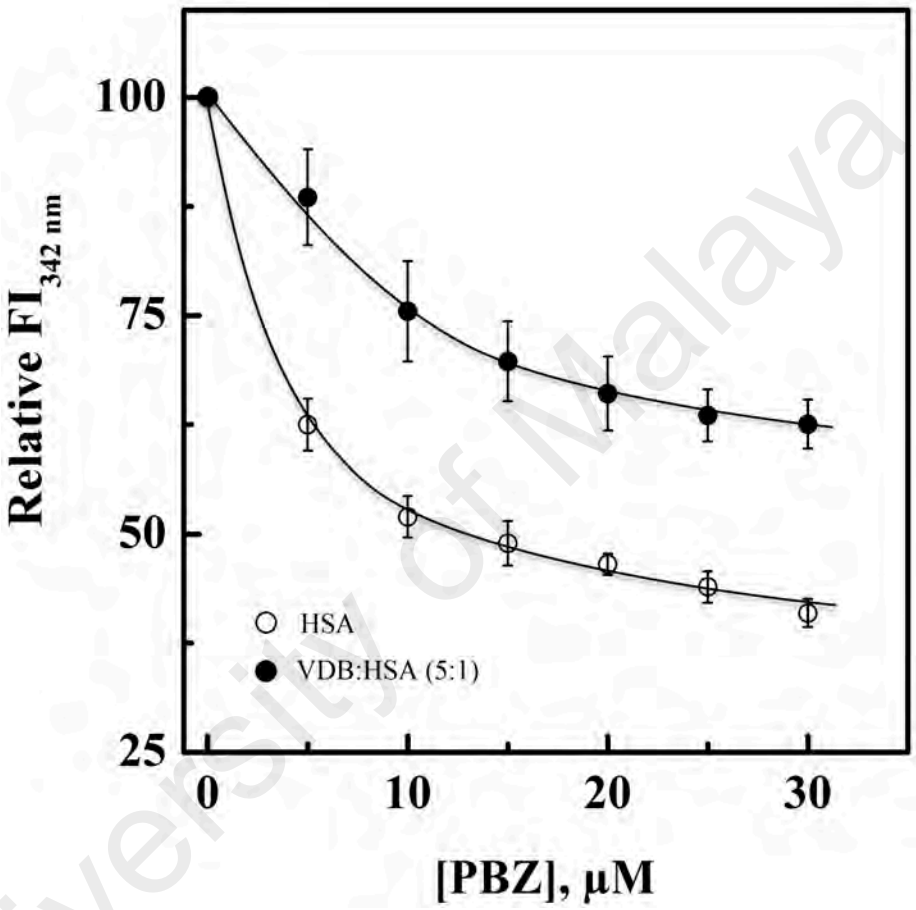

Figure 4.10: Plots showing the decrease in the relative fluorescence intensity at 342 nm ($FI_{342\ nm}$) of HSA (3 μM) and VDB–HSA (5:1) mixture with increasing concentrations (0–30 μM with 5 μM intervals) of PBZ. The experiments were carried out in 60 mM sodium phosphate buffer, pH 7.4 at 298 K.

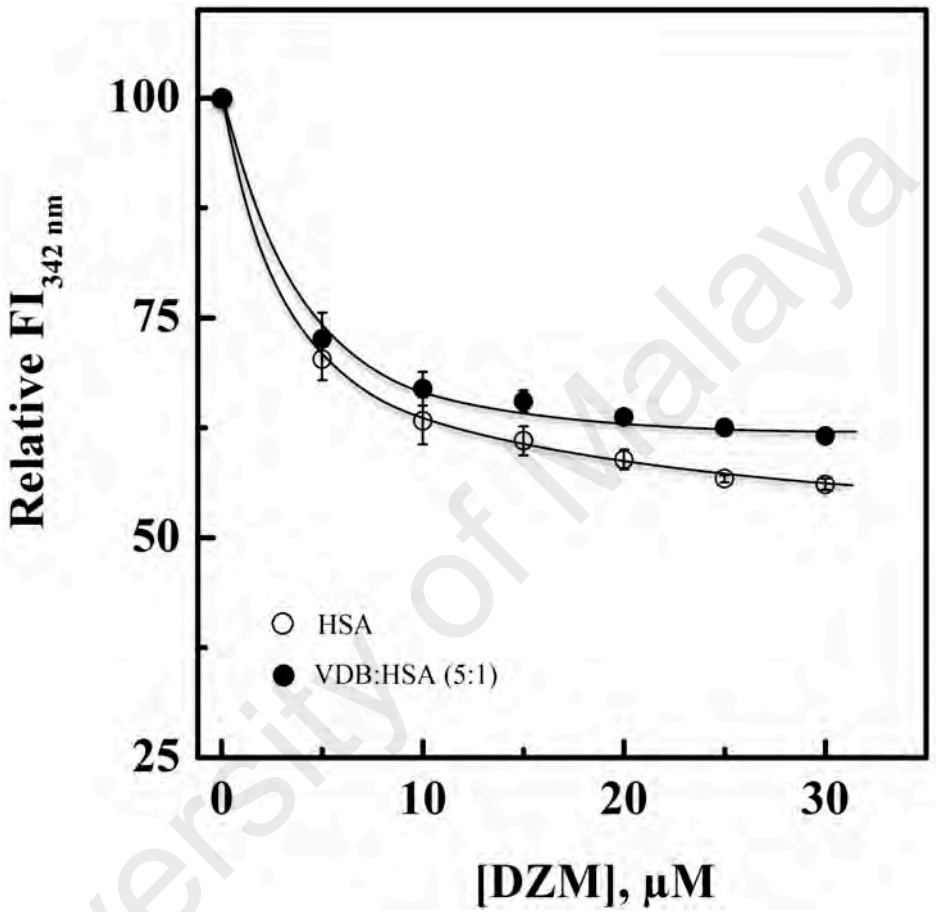

Figure 4.11: Plots showing the decrease in the relative fluorescence intensity at 342 nm ($FI_{342\ nm}$) of HSA (3 μM) and VDB–HSA (5:1) mixture with increasing concentrations (0–30 μM with 5 μM intervals) of DZM. The experiments were carried out in 60 mM sodium phosphate buffer, pH 7.4 at 298 K.

to support the results of the competitive ligand displacement experiments described above. Site marker-induced VDB displacement results (Section 4.1.9.1) suggested Sudlow's site I (subdomain IIA) as the preferred binding site of VDB on HSA. Therefore, we selected site-specific areas (Sudlow's site I and site II of HSA) for docking studies to confirm the experimental results. Cluster analysis for the binding site I using RMSD tolerance of 2.0 Å yielded a total of 10 multimember conformational clusters from 100 docking runs with the lowest mean binding energy of – 36.11 kJ mol^{-1}. The highest populated cluster had 27 out of 100 conformations. However, the conformation with the lowest binding energy (– 37.24 kJ mol^{-1}) was not a member of the highest populated cluster (Figure 4.12). On the other hand, at the binding site II, 12 multimember conformational clusters, possessing the lowest mean binding energy of – 23.53 kJ mol^{-1} were identified, with the highest populated cluster possessing 26 members out of 100 conformations (Figure 4.12). As the docking energy of the most favorable docking conformation in site II was higher than the one in site I, it suggested the binding preference of VDB for the drug binding site I (subdomain IIA) of HSA.

The results of these docking studies were in good agreement with the displacement experiments discussed above. The predicted binding model with the lowest docking energy (– 37.24 kJ mol^{-1}) was then used for binding orientation analysis (Figure 4.13). The binding site (defined by the amino acid residues within 5 Å distance to the ligand) was found to be deep inside the protein structure and mostly located in a hydrophobic cleft, lined by the following amino acid residues: Tyr-150, Glu-153, Lys-195, Gln-196, Leu-198, Lys-199, Trp-214, Arg-218, Leu-219, Arg-222, Leu-238, His-242, Arg-257, Leu-260, Ala-261, Ile-264, Ser-287, His-288, Ile-290, Ala-291, Glu-292, Val-343, Asp-451, Ser-454 and Val-455. Presence of hydrophobic amino acid residues at the binding site of HSA might have contributed toward the stability of the VDB–HSA complex through hydrophobic interactions, as illustrated in red in the LigPlot+ diagram shown in

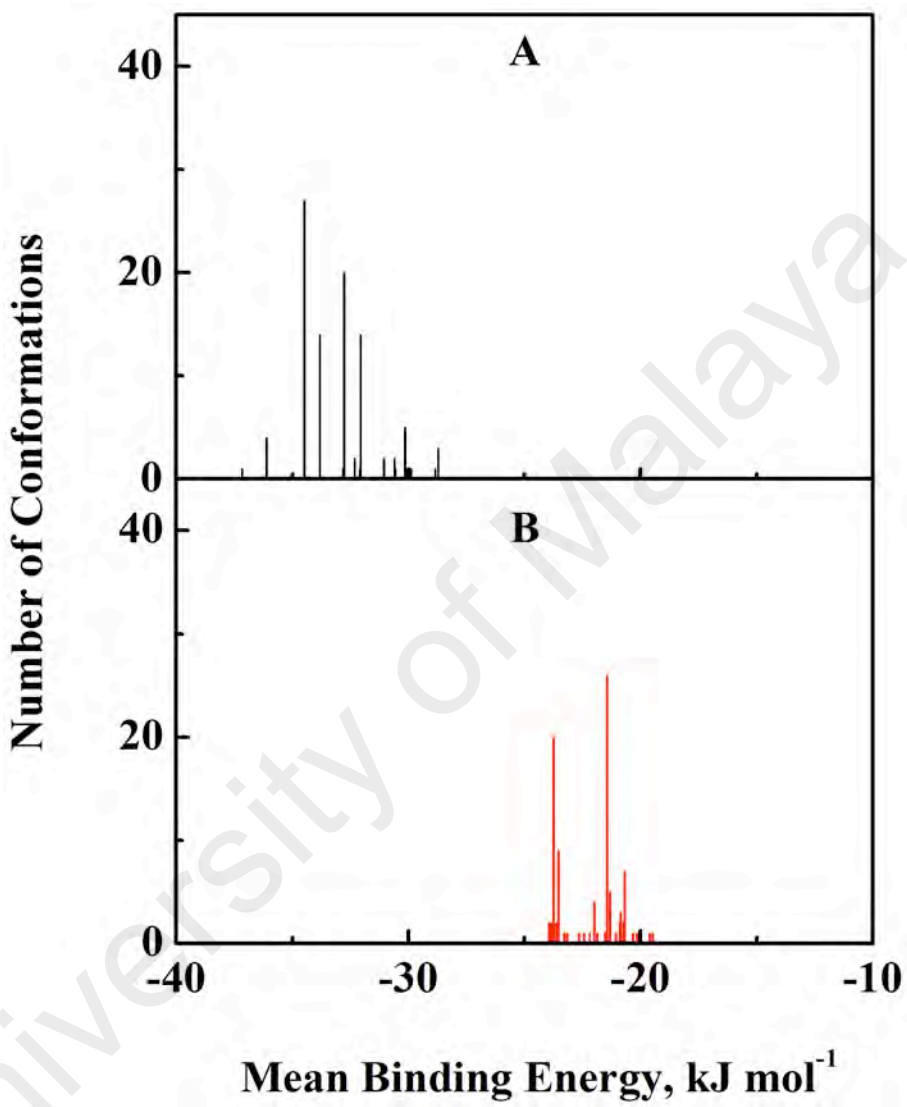

Figure 4.12: Cluster analysis of the docking of VDB to Sudlow's sites I (A) and II (B) of HSA crystal structure (1BM0). The results were obtained from a total of 100 runs for each binding site.

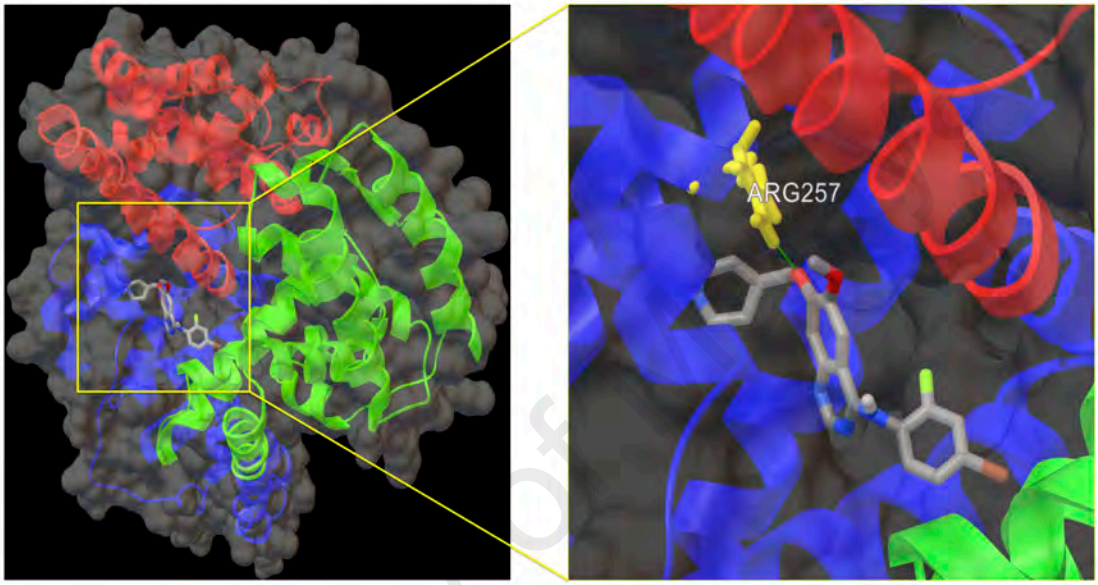

Figure 4.13: Predicted binding orientation of the lowest docking energy conformation of VDB (ball-and-stick rendered) in the Sudlow's site I (subdomain IIA) of HSA (1BM0). Different domains of HSA, namely, I, II and III are shown in red, blue and green, respectively. The enlarged view shows the hydrogen bond (green line) formed between VDB and side chain of Arg–257 (colored yellow).

Figure 4.14. Several reports have shown the involvement of hydrophobic interactions and hydrogen bonding in stabilizing the drug-serum albumin complexes based on LigPlot+ diagram (Ebrahimi et al., 2015; Taghavi et al., 2013; Yeggoni et al., 2015). As can also be seen from the figure, VDB orientates itself at site I such that its electronegative atoms (fluorine and bromine) are facing the Trp-214 residue of HSA and thus create a more polar environment around the Trp residue. However, presence of several polar amino acid residues within the proximity of the bound ligand indicated that the interaction between VDB and HSA at site I (Figure 4.14) cannot be exclusively hydrophobic. Furthermore, in the VDB–HSA complex docking conformation at the site I, one hydrogen bond was predicted involving the hydrogen atom of Arg-257 and the ethereal oxygen atom of VDB. Thus results obtained from the docking analysis also suggested that both hydrophobic interactions and hydrogen bonding collectively contribute towards VDB–HSA complex formation. These results were in line with our thermodynamic analysis of the binding reaction, suggesting involvement of both hydrophobic interactions and hydrogen bonding in VDB–HSA complex formation.

In summary, VDB quenched the intrinsic fluorescence of HSA through static quenching mechanism, thus suggesting formation of VDB–HSA complex. Thermodynamic and molecular docking data suggested the involvement of both hydrophobic interactions and hydrogen bonding in VBD–HSA complex formation at site I of HSA, located in subdomain IIA. VDB-induced alteration in both secondary and tertiary structures of HSA was evident from the far–UV and the near–UV CD spectral results. Metal ions were found to affect the binding affinity of VDB–HSA to a smaller extent.

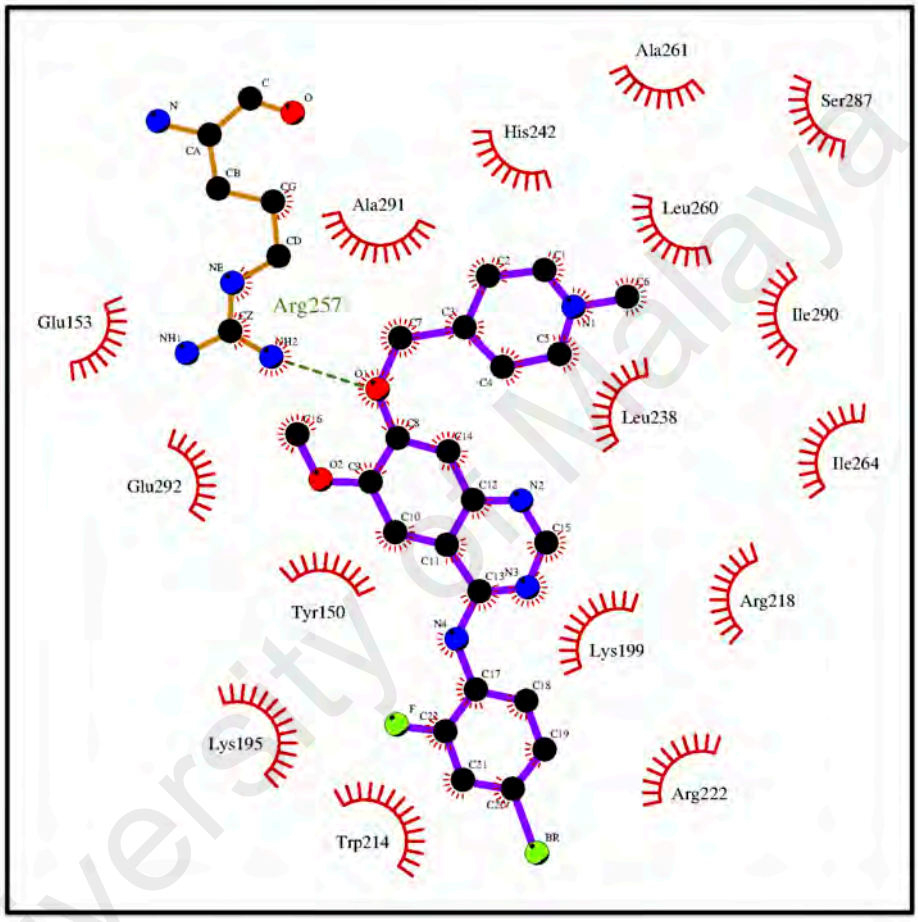

Figure 4.14: LigPlot+ diagram of VDB (purple lines) and the amino acid residues of HSA at site I. The residues indicate the presence of hydrophobic interactions with VDB. Hydrogen bond of VDB and HSA is rendered with dashed green line.

4.2 LAP–HSA interaction

Similar to VDB–HSA interaction studies described in the Section 4.1, binding of another tyrosine kinase inhibitor, LAP to HSA was also investigated using fluorescence spectroscopy.

4.2.1 Fluorescence spectra

The fluorescence spectra of HSA (3 μM), obtained in the absence and presence of increasing LAP concentrations (0.5–4.5 μM) at pH 7.4 are shown in Figure 4.15. The fluorescence spectrum of HSA produced an emission maximum at 343 nm due to the presence of sole tryptophan (Trp-214) residue (Peters, 1996). Addition of LAP to HSA resulted in a gradual decrease in the fluorescence intensity at 343 nm, producing ~ 35 % quenching at the highest (4.5 μM) LAP concentration (inset of Figure 4.15). However, no shift in the emission maximum was noticed upon LAP addition to HSA. Such quenching in the fluorescence intensity clearly indicated the binding of LAP to HSA. Free LAP did not produce any significant fluorescence in the selected wavelength range (Figure 4.15). In the absence of any shift in the emission maximum, polarity changes in the microenvironment around Trp residue might be responsible for the observed quenching of the fluorescence intensity (Lakowicz, 2006). Several earlier reports have shown quenching of HSA fluorescence upon ligand binding without affecting the emission maximum (Feroz et al., 2015; Neamtu et al., 2013; Shahabadi et al., 2015).

4.2.2 Mechanism of fluorescence quenching

In order to verify the quenching mechanism, titration of HSA with increasing LAP concentrations was studied at three different temperatures, *i.e.*, 288 K (Figure 4.15), 303 K and 318 K (Figure 4.15S). The fluorescence quenching data were treated according to the Stern-Volmer equation (Eq. (3)). Figure 4.16 shows the Stern-Volmer plots for LAP–HSA system, obtained at three different temperatures. Although the plots showed linearity up to 3.5 μM LAP concentration, deviations were observed at higher

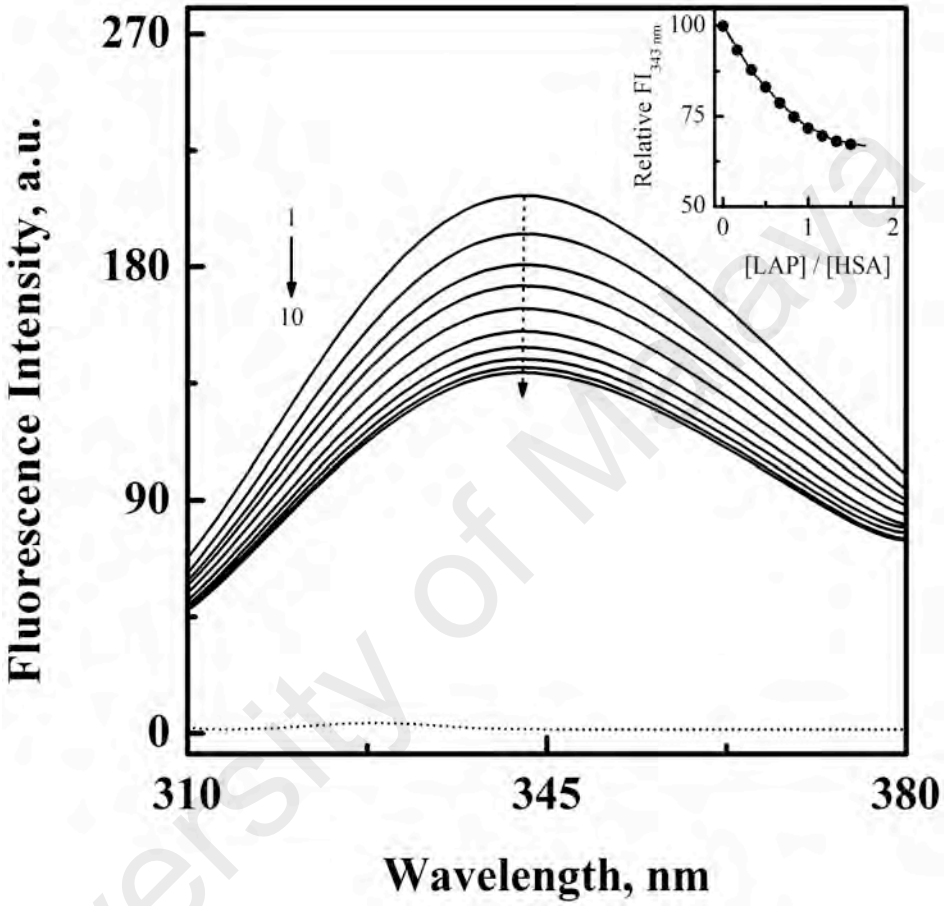

Figure 4.15: Fluorescence spectra of HSA (3 μM) in the absence (spectrum 1) and presence (spectra 2–10) of increasing LAP concentrations (0.5–4.5 μM with 0.5 μM intervals), obtained in 60 mM sodium phosphate buffer, pH 7.4 at 288 K upon excitation at 295 nm. The fluorescence spectrum of free LAP (4.5 μM) is shown with dotted line. The inset shows the decrease in the relative fluorescence intensity of HSA at 343 nm ($FI_{343\ nm}$) with increasing LAP/HSA molar ratios.

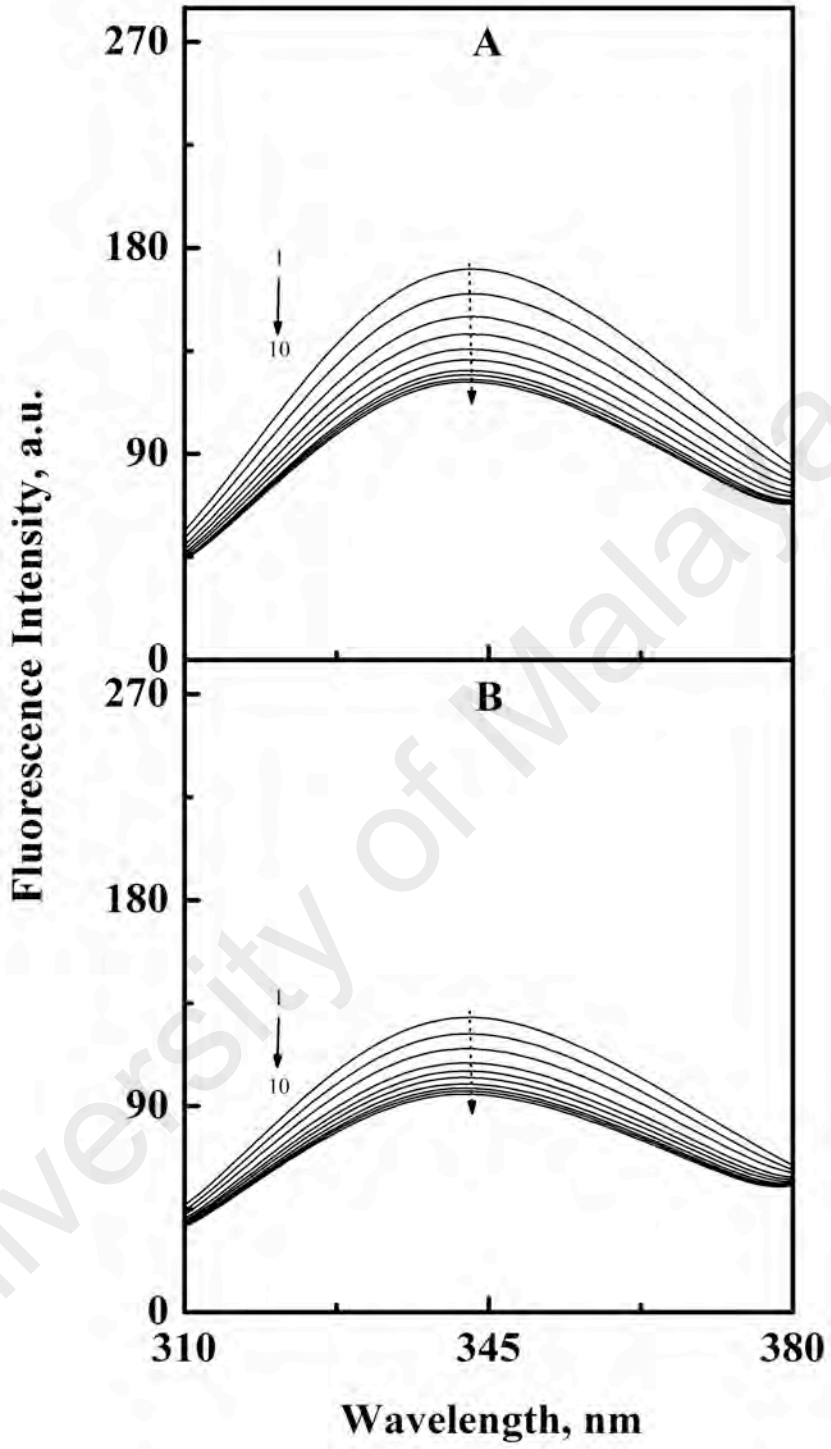

Figure 4.15 S: Fluorescence spectra of HSA (3 μM) in the absence (spectrum 1) and presence (spectra 2–10) of increasing LAP concentrations (0.5–4.5 μM with 0.5 μM intervals), obtained in 60 mM sodium phosphate buffer, pH 7.4 at (A) 303 K and (B) 318 K upon excitation at 295 nm.

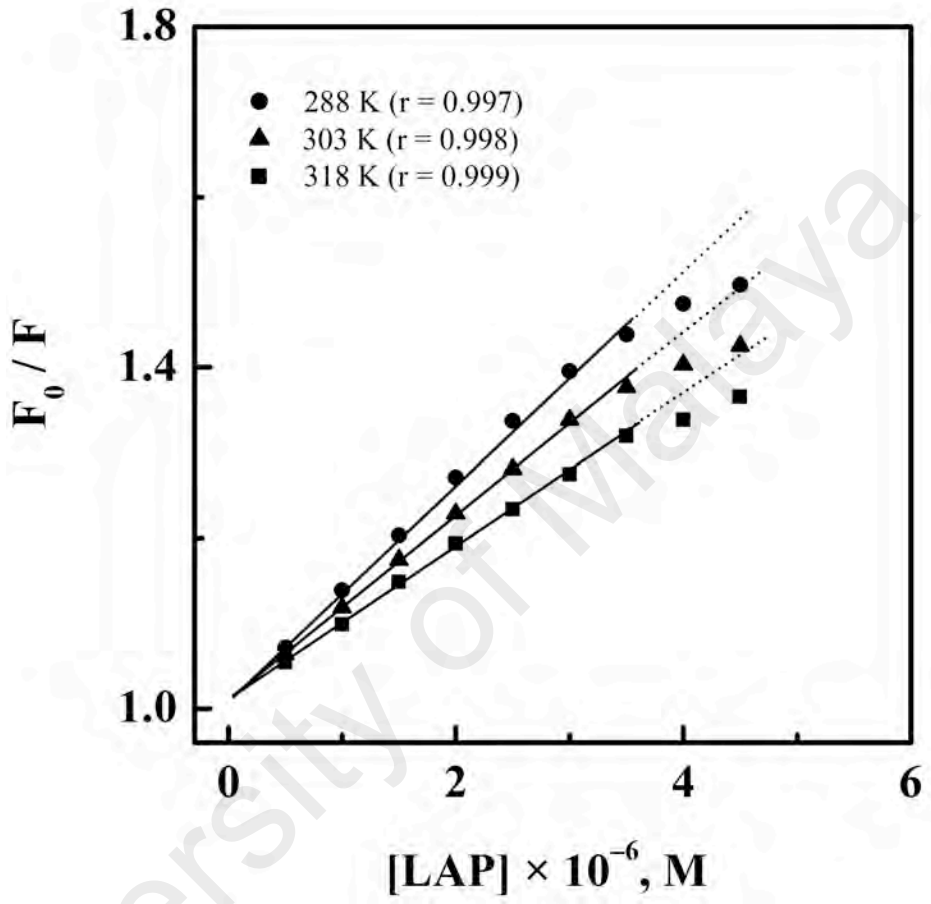

Figure 4.16: Stern-Volmer plots for the fluorescence quenching data of the LAP–HSA system, obtained at three different temperatures, *i.e.*, 288 K, 303 K and 318 K.

LAP concentrations. Such deviations at higher ligand concentrations were not uncommon and have been reported earlier (Ma et al., 2012; Molina-Boliver et al., 2015; Silva et al., 2013). Values of the Stern-Volmer constant, K_{SV} (Table 4.5) were obtained by regression analysis of the linear parts of the Stern-Volmer plots. An inverse correlation between K_{SV} and the temperature was indicative of the involvement of static quenching mechanism due to the LAP–HSA complex formation. Additionally, higher magnitude of the k_q values (Table 4.5), obtained using Eq. (4) for the LAP–HSA system in comparison to a diffusion-controlled process (2.0×10^{10} $M^{-1} s^{-1}$), also supported the complex formation involving static quenching mechanism (Ware, 1962).

4.2.3 Binding affinity

Treatment of the fluorescence quenching data according to the Eq. (5) yielded the double logarithmic plots between log $(F_0 - F) / F$ and log $[1 / ([L_T] - [(F_0 - F)[P_T] / F_0)]$, as shown in Figure 4.17. The K_a values at three different temperatures were obtained in the same way as described in the Section 3.2.5.2 and are listed in Table 4.5. Being fallen in the order of 10^5, K_a values suggested the nature of the binding affinity between LAP and HSA as intermediate / moderate (Dufour & Dangles, 2005). Based on intermediate binding affinity, transport of LAP in the bloodstream as well as its release at the specific target site seems to be a feasible process. Many drugs have been reported to bind to HSA with an intermediate binding affinity (Duman et al., 2013; Feroz et al., 2013; Neamtu et al., 2013). A progressive decrease in the K_a value with increase in temperature (Table 4.5) was suggestive of weaker interactions between LAP and HSA at higher temperatures (Feroz et al., 2015; Wang et al., 2011).

4.2.4 Interaction forces

The linear van't Hoff plot between ln K_a and $1/T$ (Figure 4.18) allowed determination of ΔH and ΔS values for LAP–HSA interaction while the values of ΔG at different

Table 4.5: Quenching and binding parameters for LAP–HSA interaction, studied at three different temperatures, pH 7.4.

T (K)	K_{SV} (M^{-1})	k_q (M^{-1} s^{-1})	K_a (M^{-1})
288	$(1.24 \pm 0.03) \times 10^5$	$(1.94 \pm 0.11) \times 10^{13}$	$(1.49 \pm 0.08) \times 10^5$
303	$(1.07 \pm 0.03) \times 10^5$	$(1.68 \pm 0.09) \times 10^{13}$	$(1.24 \pm 0.06) \times 10^5$
318	$(0.88 \pm 0.01) \times 10^5$	$(1.38 \pm 0.08) \times 10^{13}$	$(1.01 \pm 0.06) \times 10^5$

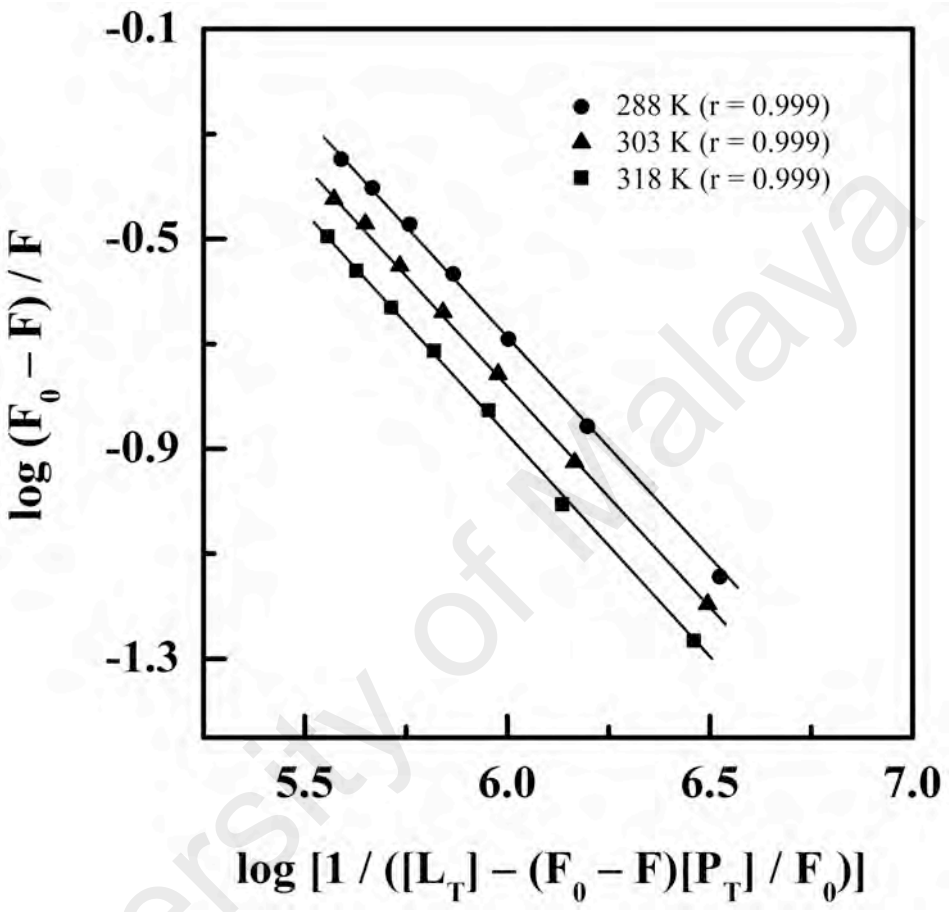

Figure 4.17: Double logarithmic plots of [log ($F_0 - F$) / F versus log [1 / ([L_T] – [(F_0 – F)[P_T] / F_0)] for the fluorescence quenching data of the LAP–HSA system, obtained at three different temperatures, *i.e.,* 288 K, 303 K and 318 K.

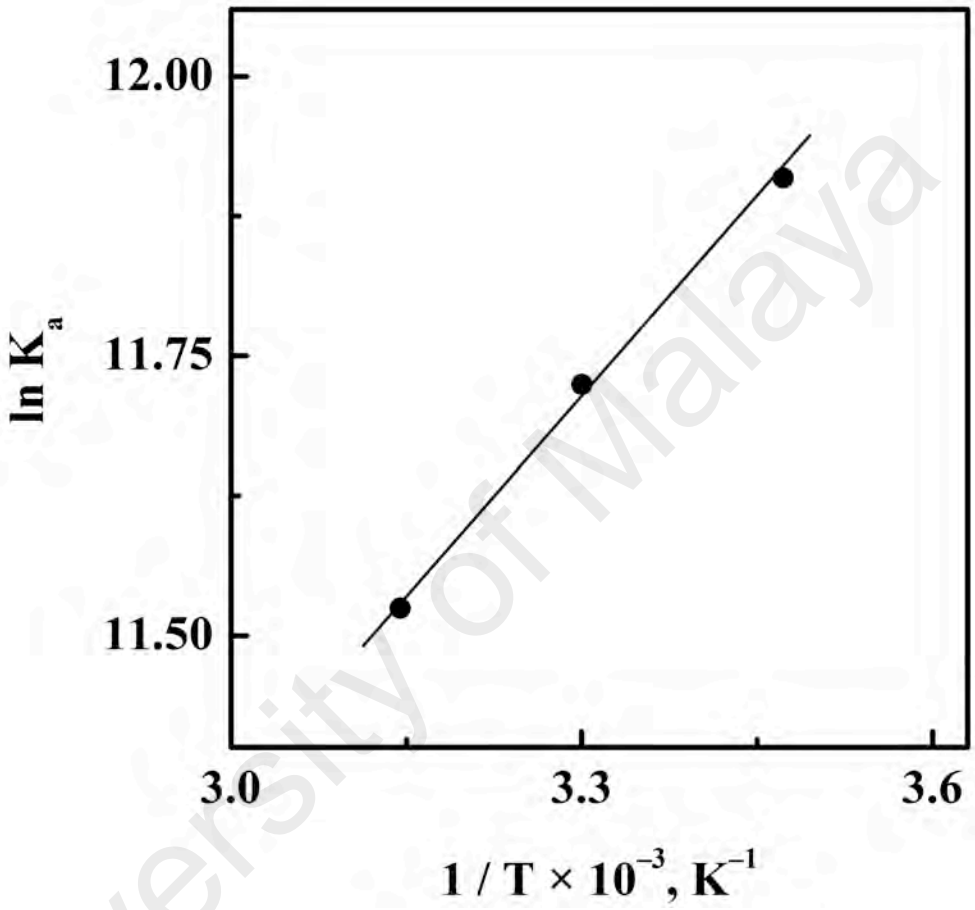

Figure 4.18: The van't Hoff plot for LAP–HSA interaction. Values of K_a were obtained from the double logarithmic plots, displayed in Figure 4.17.

temperatures were obtained from Eq. (7). Table 4.6 shows the values of Δ*H*, Δ*S* and Δ*G* of the LAP–HSA system. As evident from Table 4.6, the negative values of Δ*G* affirmed that the binding process was spontaneous at all temperatures. Furthermore, the binding reaction was accompanied by a positive entropy change and the release of heat as shown by the negative sign of Δ*H*. Since hydrophobic interactions are accompanied by a positive entropy change and a large negative Δ*H* value generally accounts for the hydrogen bonding and van der Waals interactions (Ross & Subramanian, 1981), it appears that all these interactions, *i.e.*, hydrophobic and van der Waals interactions as well as hydrogen bonds facilitated the formation of LAP–HSA complex. Disruption of the ordered water layers around the protein (HSA) and the ligand (LAP) molecules in free states might have contributed a large increase in entropy upon LAP–HSA complex formation. Involvement of a number of forces seems plausible to stabilize LAP–HSA complex. Our results (thermodynamic data) showing the involvement of hydrophobic along with van der Waals interactions as well as hydrogen bonds were well supported by docking analysis as described in Section 4.2.9.2.

4.2.5 Absorption spectra

Figure 4.19 shows the UV-vis absorption spectra of HSA in the absence and presence of increasing LAP concentrations (4–20 μM with 4 μM intervals). The spectra were obtained by subtracting the absorption spectra of pure LAP solutions (Figure 4.19S(B)) from the absorption spectra of respective LAP–HSA mixtures (Figure 4.19S(A)). Presence of the absorption maximum of HSA around 280 nm characterized the absorption peak of protein chromophores (Barreca et al., 2013). As can be seen from Figure 4.19, the absorption peak of the protein showed hyperchromism without any shift in the absorption maximum in the presence of increasing LAP concentrations. Such changes in the absorbance of HSA upon LAP addition clearly indicated microenvironmental alterations around protein chromophores due to LAP–HSA

Table 4.6: Thermodynamic parameters for LAP–HSA interaction, studied at three different temperatures, pH 7.4.

T (K)	ΔS (J mol^{-1} K^{-1})	ΔH (kJ mol^{-1})	ΔG (kJ mol^{-1})
288			– 28.53
303	+ 65.21	– 9.75	– 29.51
318			– 30.49

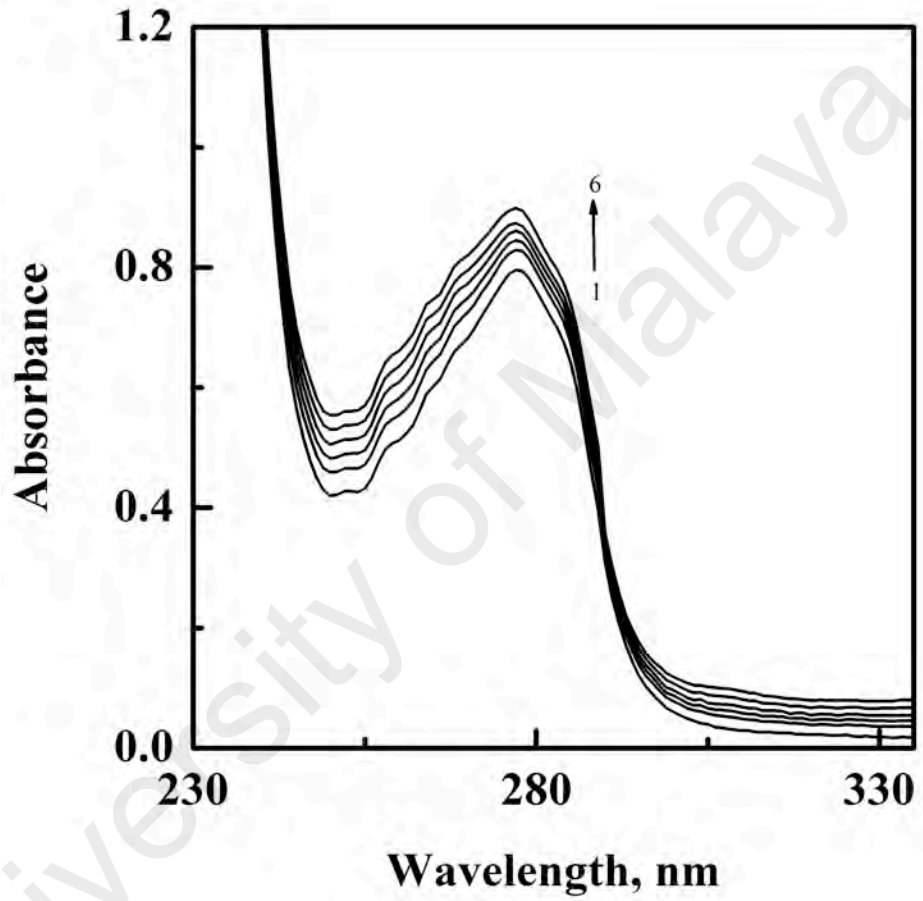

Figure 4.19: UV-vis absorption spectra of HSA (20 μM) in the absence (spectrum 1) and presence (spectra 2–6) of increasing LAP concentrations (4–20 μM with 4 μM intervals), obtained in 60 mM sodium phosphate buffer, pH 7.4 at 298 K. The spectra (2–6) were obtained by subtracting the absorption contribution of respective free LAP from the absorption spectra of LAP–HSA mixtures.

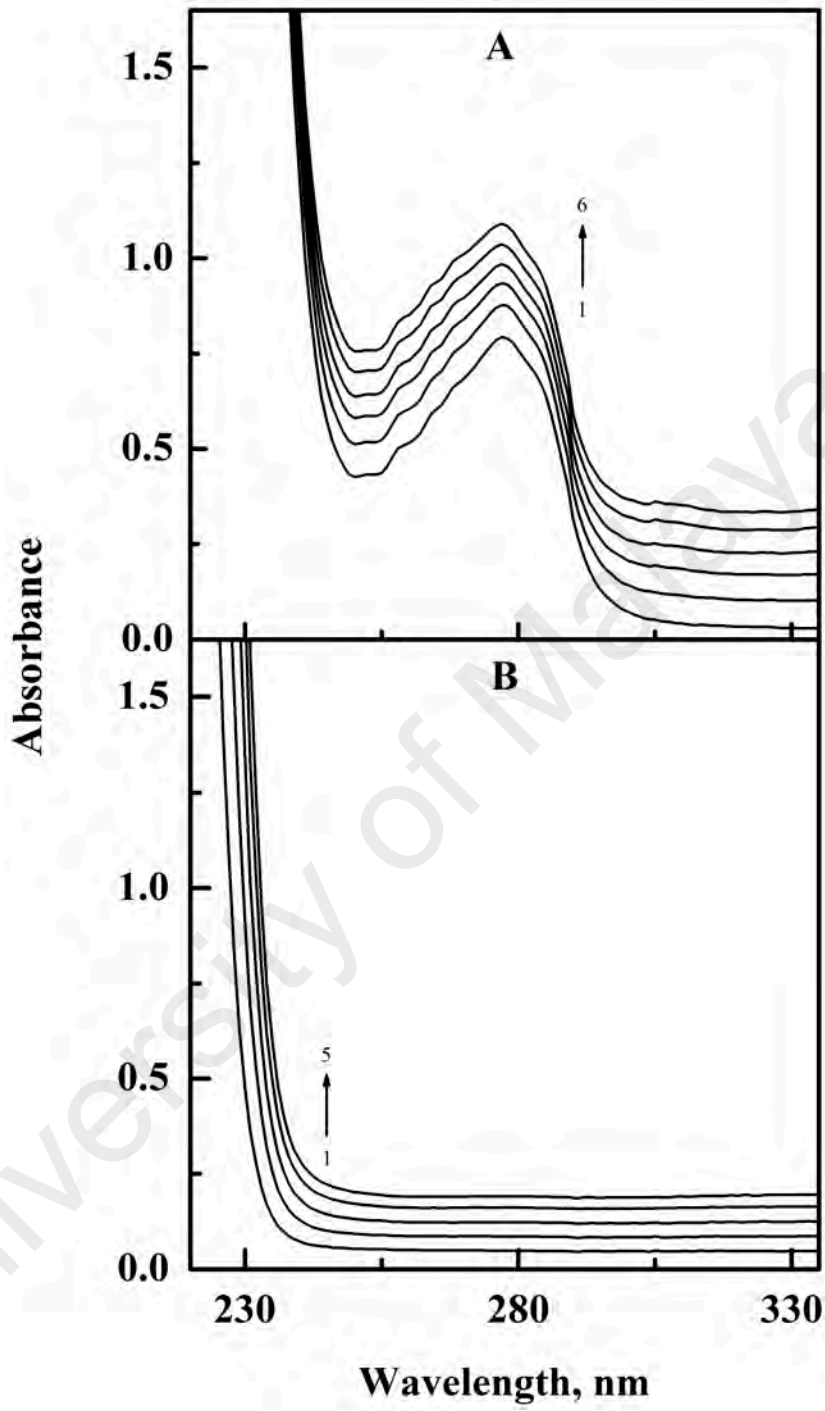

Figure 4.19 S: (A) Uncorrected UV-vis absorption spectra of HSA (20 μM) in the absence (spectrum 1) and presence (spectra 2–6) of increasing LAP concentrations (4–20 μM with 4 μM intervals), obtained in 60 mM sodium phosphate buffer, pH 7.4 at 298 K. (B) The spectra (1–5) were obtained with increasing LAP concentrations (4–20 μM with 4 μM intervals).

complex formation. Therefore, involvement of static quenching mechanism can be confirmed by the change in the absorption spectrum of HSA upon LAP addition, which suggested the formation of LAP–HSA complex.

4.2.6 LAP-induced structural / microenvironmental changes in HSA

Similar to VDB–HSA system, structural (secondary and tertiary structures) alterations and microenvironmental perturbations around Trp and Tyr residues in HSA upon LAP binding were studied using circular dichroism and 3-D fluorescence spectroscopy, respectively.

4.2.6.1 Far-UV and near-UV CD spectra

Figures 4.20 and 4.21 show the influence of LAP binding on the far-UV and the near-UV CD spectra of HSA, respectively. As can be seen from Figure 4.20, presence of LAP in the incubation mixture produced significant alteration in the far-UV CD spectrum of HSA, which was characterized by the presence of two minima at 208 nm and 222 nm, spectral signals for α–helical structure (Reed et al., 1975). Quantitatively, about 13.5 % decrease in the $MRE_{222\ nm}$ value was noticed at 1:1 [LAP]:[HSA] molar ratio, suggesting alteration in protein's helical content due to LAP–HSA complex formation.

Similar to the far-UV CD spectra, the near-UV CD spectra also showed significant variation in the presence of LAP (Figure 4.21). Significant reduction in the spectral signals at 262 nm, 268 nm, 278 nm and 292 nm, occurring due to aromatic chromophores (Dockel et al., 2000) clearly suggested alteration in the protein's tertiary structure in the presence of LAP, thus implying LAP-HSA complex formation.

4.2.6.2 Three-dimensional fluorescence spectra

Figure 4.22 shows 3-D fluorescence spectra and corresponding contour maps of free HSA (A) and [LAP]:[HSA] (1:1) mixture (B). The fluorescence spectral characteristics

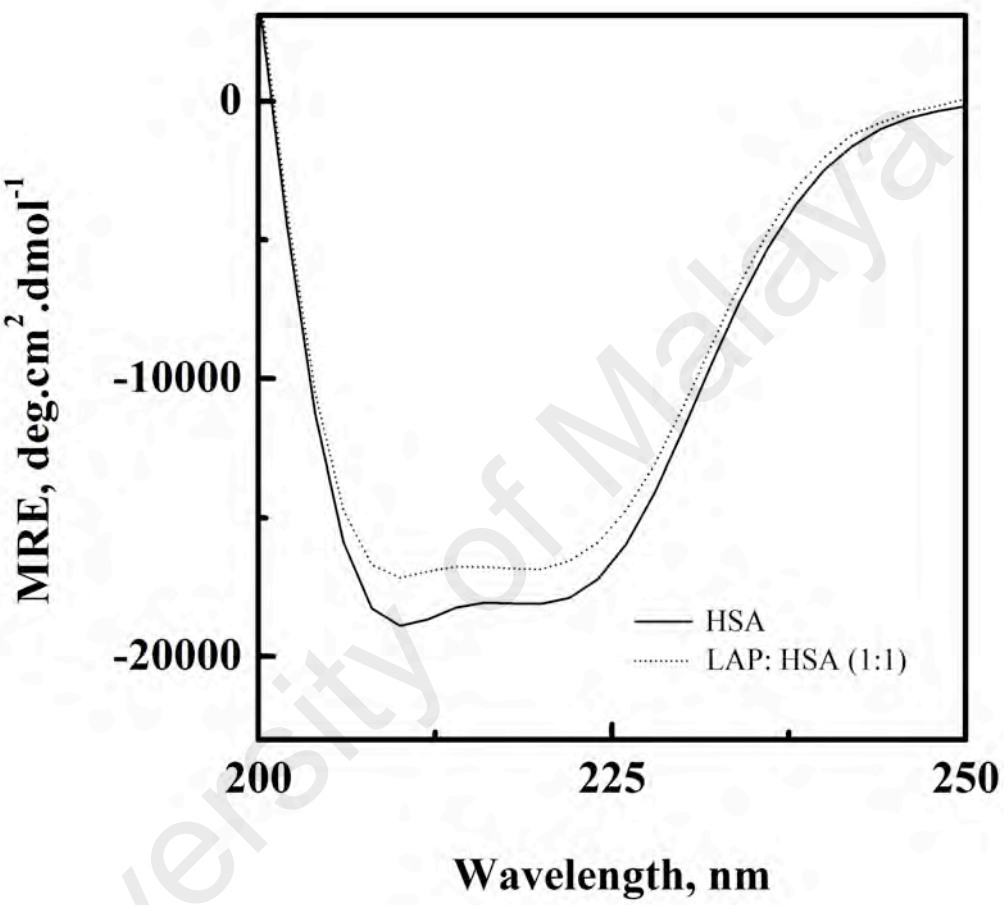

Figure 4.20: Far-UV CD spectra of HSA (2 μM) and LAP–HSA (1:1) mixture. The CD spectra were recorded using a 1 mm path length cuvette, in 60 mM sodium phosphate buffer, pH 7.4 at 298 K.

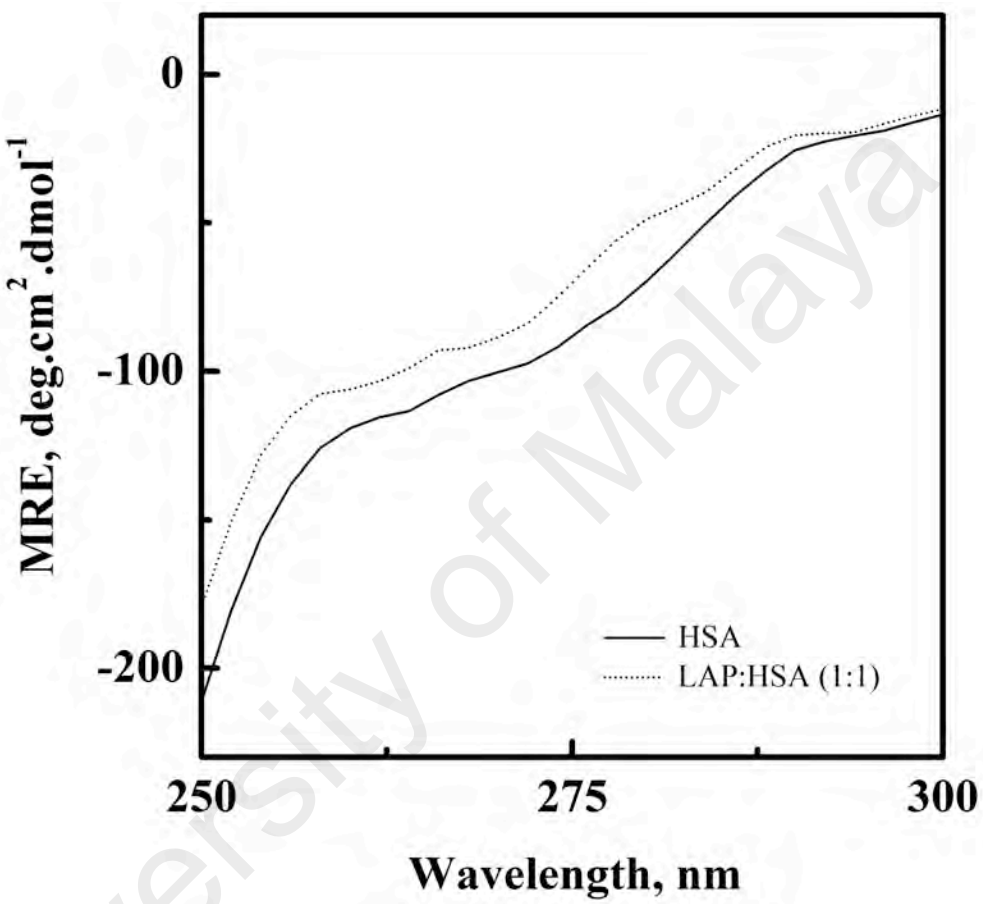

Figure 4.21: Near-UV CD spectra of HSA (8 μM) and LAP–HSA (1:1) mixture. The CD spectra were recorded using a 10 mm path length cuvette, in 60 mM sodium phosphate buffer, pH 7.4 at 298 K.

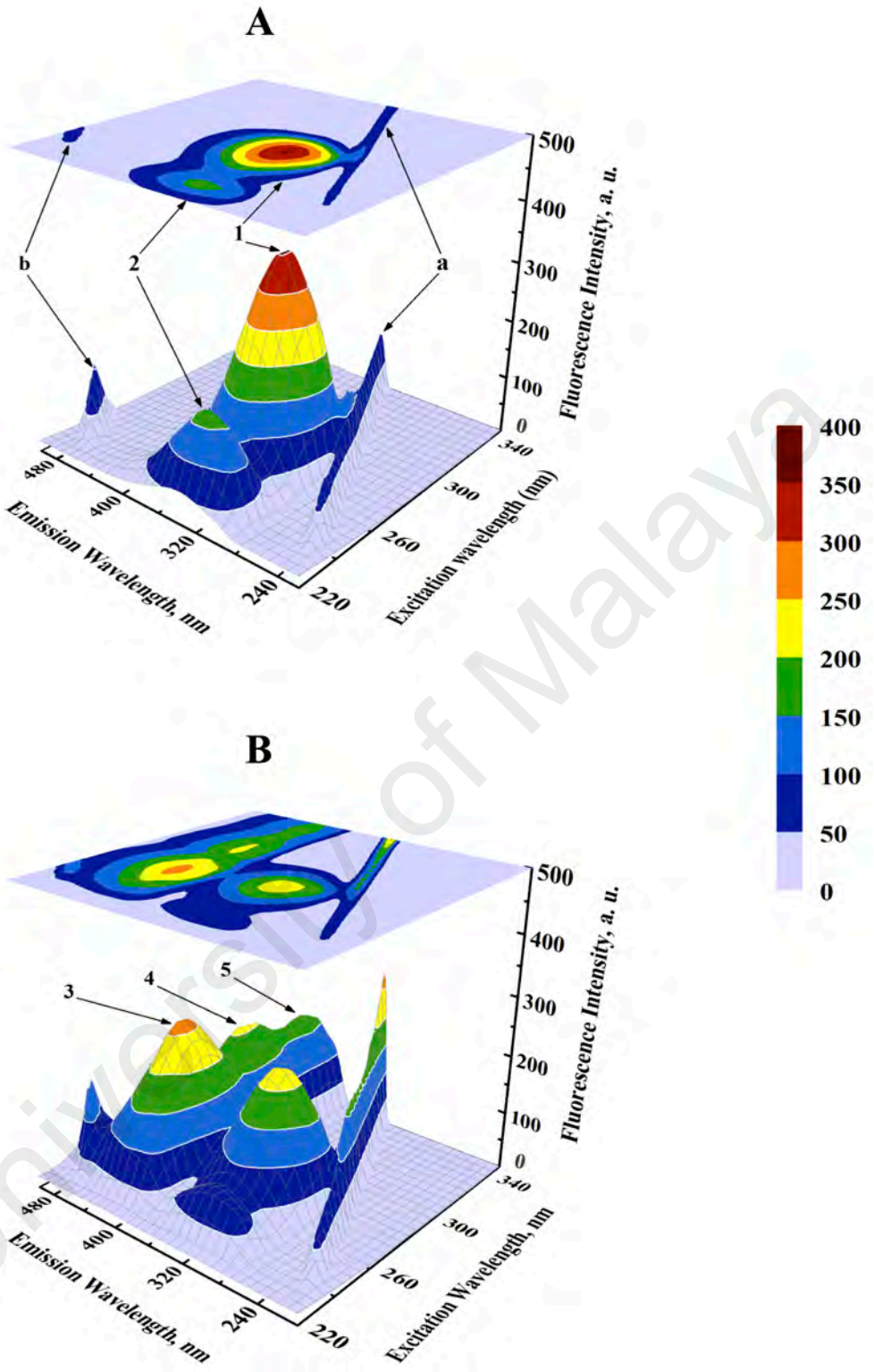

Figure 4.22: Three-dimensional fluorescence spectra and corresponding contour maps of (A) HSA (3 μM) and (B) LAP–HSA (1:1) mixture. The spectra were recorded in 60 mM sodium phosphate buffer, pH 7.4 at 298 K.

i.e., peak position (λ_{ex} / λ_{em}) and peak intensity are summarized in Table 4.7. Peaks 'a' and 'b' arise due to the first order Rayleigh scattering ($\lambda_{ex} = \lambda_{em}$) and the second order scattering ($2\lambda_{ex} = \lambda_{em}$), respectively (Lakowicz, 2006) and are commonly observed in the 3-D fluorescence spectra of HSA (Feroz et al., 2013; Madrakian et al., 2014). Besides these scattering peaks, two additional peaks ('1' and '2') were noticed in the 3-D fluorescence spectra of HSA. On the other hand, 3-D florescence spectra of LAP–HSA system showed three (3–5) additional peaks. Peaks '1' (λ_{ex} = 280 nm) and '2' (λ_{ex} = 230 nm) mainly revealed the spectral characteristics of Trp and Tyr residues and provided information about the tertiary structure of HSA. Appearance of peaks '3' (λ_{ex} = 260 nm), '4' (λ_{ex} = 300 nm) and '5' (λ_{ex} = 340 nm) in the 3-D fluorescence spectra of the LAP–HSA system can be ascribed to the fluorescence characteristics of LAP–HSA complex. A significant decrease in the fluorescence intensity along with a shift in the emission maximum of peaks '1' (~ 38 %, 2 nm blue shift) and '2' (~ 64 %, 5 nm blue shift), observed in the presence of LAP clearly suggested microenvironmental changes around Trp and Tyr residues of HSA due to LAP binding.

4.2.7 Thermal stabilization of HSA

In order to study the effect of LAP binding on the thermal stability of HSA, temperature-dependent titrations were performed in the temperature range, 298–353 K with 5 K intervals in the absence and presence of LAP. Figure 4.23 shows the influence of temperature on the fluorescence intensity of free as well as ligand-bound HSA ([LAP]:[HSA] = 2:1) at 343 nm. Increase in temperature led to a linear decrease in the fluorescence intensity at 343 nm of HSA up to 338 K and sloped off thereafter. No significant difference was noticed in the fluorescence spectral signals of HSA and LAP–HSA complex up to 328 K, beyond which presence of LAP in the incubation mixture improved the relative fluorescence intensity of HSA by showing lesser change in the fluorescence intensity with temperature compared to that observed with free

Table 4.7: Three-dimensional fluorescence spectral characteristics of HSA (3 μM) and LAP–HSA system at 298 K, pH 7.4.

System	Peak	Peak Position [λ_{ex} / λ_{em} (nm/nm)]	Intensity
HSA	a	230/230→350/350	18.51→100.81
	b	250/500	107.12
	1	280/338	350.41
	2	230/334	154.59
[LAP]:[HSA] = 1:1	a	230/230→350/350	16.81→274.12
	b	250/500	142.93
	1	280/336	215.47
	2	230/329	55.99
	3	260/424	252.12
	4	300/424	208.33
	5	340/424	175.05

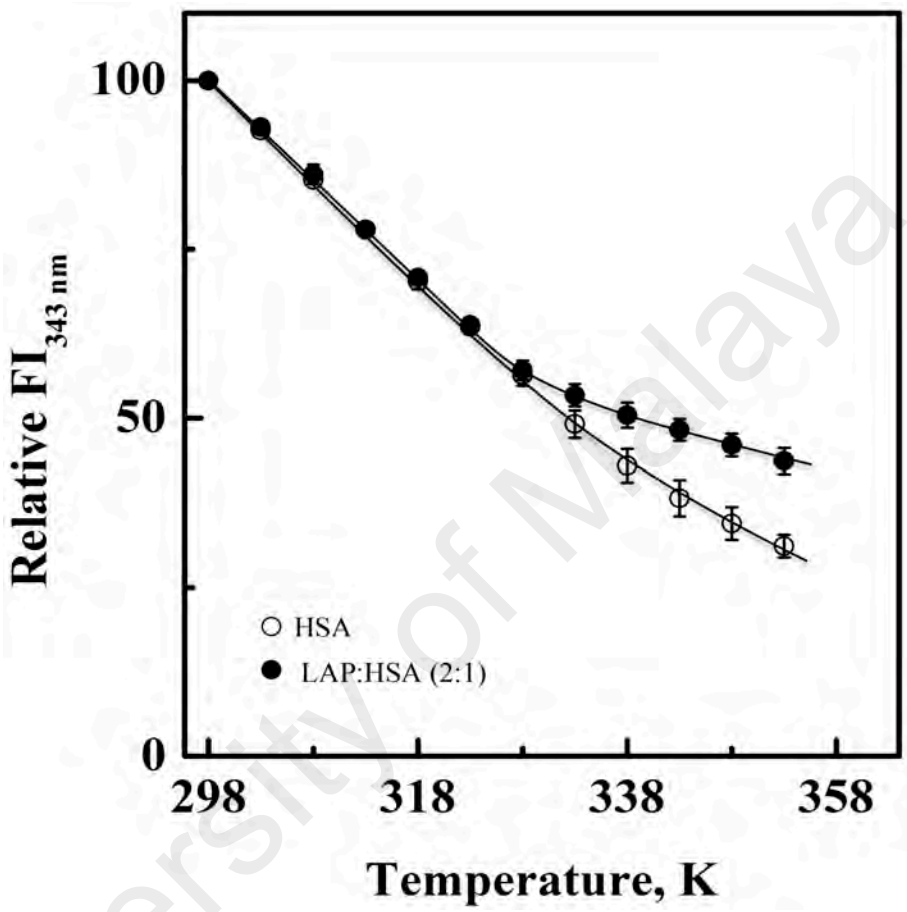

Figure 4.23: Thermal stability profiles of HSA (3 μM) and LAP–HSA (2:1) mixture in the temperature range, 298–353 K with a regular increments of 5 K, as monitored by fluorescence intensity measurements at 343 nm ($FI_{343\ nm}$), in 60 mM sodium phosphate buffer, pH 7.4.

HSA. These results suggested LAP-induced thermal stabilization of HSA through LAP–HSA complex formation due to the coupling of binding and unfolding equilibria (Celej et al., 2003; Shrake & Ross, 1988).

4.2.8 Influence of metal ions on LAP–HSA interaction

The study on the interference of metal ions with LAP–HSA interaction is crucial as metal ions are able to interact with the protein and may affect the interaction of LAP with HSA (Cheng et al., 2013; Lin et al., 2014). Therefore, LAP–HSA titration experiments were carried out in the absence and the presence of a fixed concentration (50 μM) of Ca^{2+}, Mg^{2+}, Zn^{2+}, Cu^{2+}, Ba^{2+} and Mn^{2+} and the binding constant, K_a values were determined (Table 4.8). Presence of these metal ions showed smaller but significant decrease in the binding constant of LAP–HSA complex, being more significant in the presence of Mn^{2+} and Ba^{2+}, suggesting conformational perturbation in the vicinity of the drug binding site on HSA. Such decrease in the K_a value would shorten the storage time of the drug in the blood plasma and weaken the maximum effectiveness of the drug (Cui et al., 2004; Kalanur et al., 2010; Wang et al., 2011).

4.2.9 Location of LAP binding site

Identification of the binding locus of LAP on HSA was made using competitive ligand displacement experiments with site markers and molecular docking analysis.

4.2.9.1 LAP-induced site marker displacement

The binding site specificity of LAP on HSA was investigated using marker ligands for these sites, *viz.*, PBZ (site I), DZM (site II), HMN and DGT (site III). Figures 4.24–4.27 show titration results obtained with free as well as site marker-bound HSA with increasing LAP concentrations. Although a gradual decrease in the fluorescence intensity at 343 nm ($FI_{343\ nm}$) of HSA and site marker-HSA complexes was noticed with increasing LAP concentrations, the decrease was less pronounced with site marker-

Table 4.8: K_a values of LAP–HSA interaction in the absence and presence of different metal ions (50 μM) at 298 K, pH 7.4.

Metal Ions	K_a ($\times 10^5$ M^{-1})
–	1.29 ± 0.05
Mg^{2+}	1.07 ± 0.11
Ca^{2+}	1.08 ± 0.07
Mn^{2+}	0.86 ± 0.17
Cu^{2+}	1.10 ± 0.08
Zn^{2+}	1.03 ± 0.10
Ba^{2+}	0.96 ± 0.14

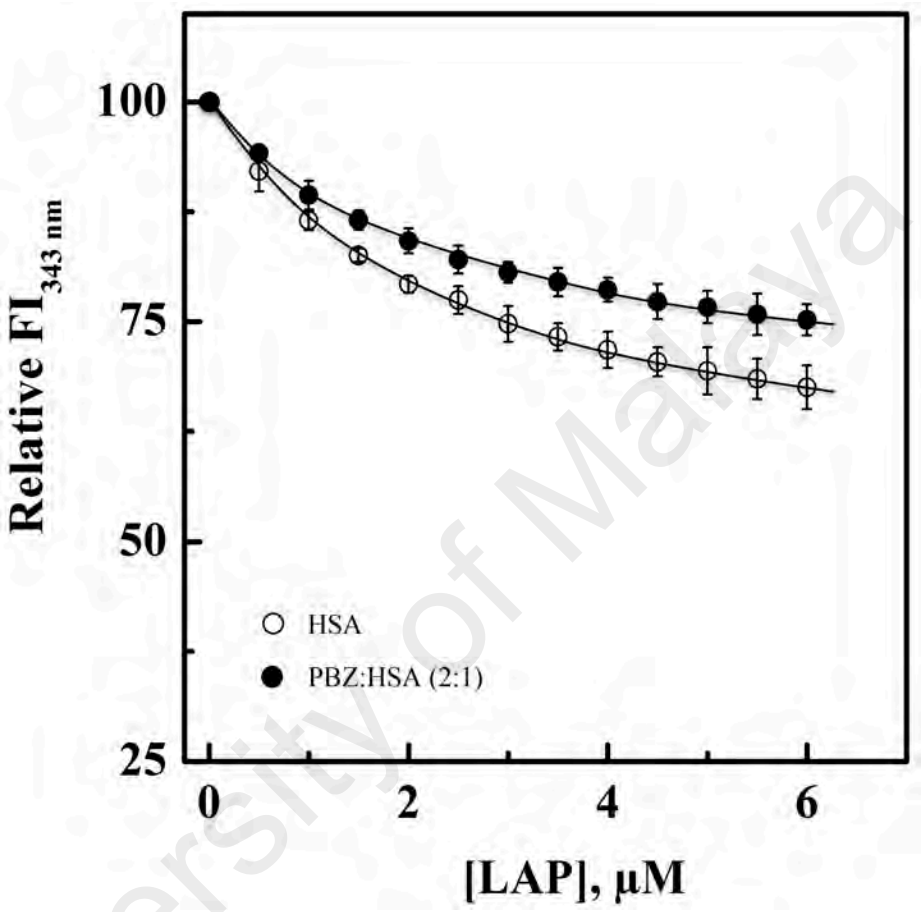

Figure 4.24: Plots showing the decrease in the relative fluorescence intensity at 343 nm ($FI_{343\ nm}$) of HSA (3 μM) and PBZ–HSA (2:1) mixture with increasing concentrations (0–6.0 μM with 0.5 μM intervals) of LAP. The experiments were carried out in 60 mM sodium phosphate buffer, pH 7.4 at 298 K.

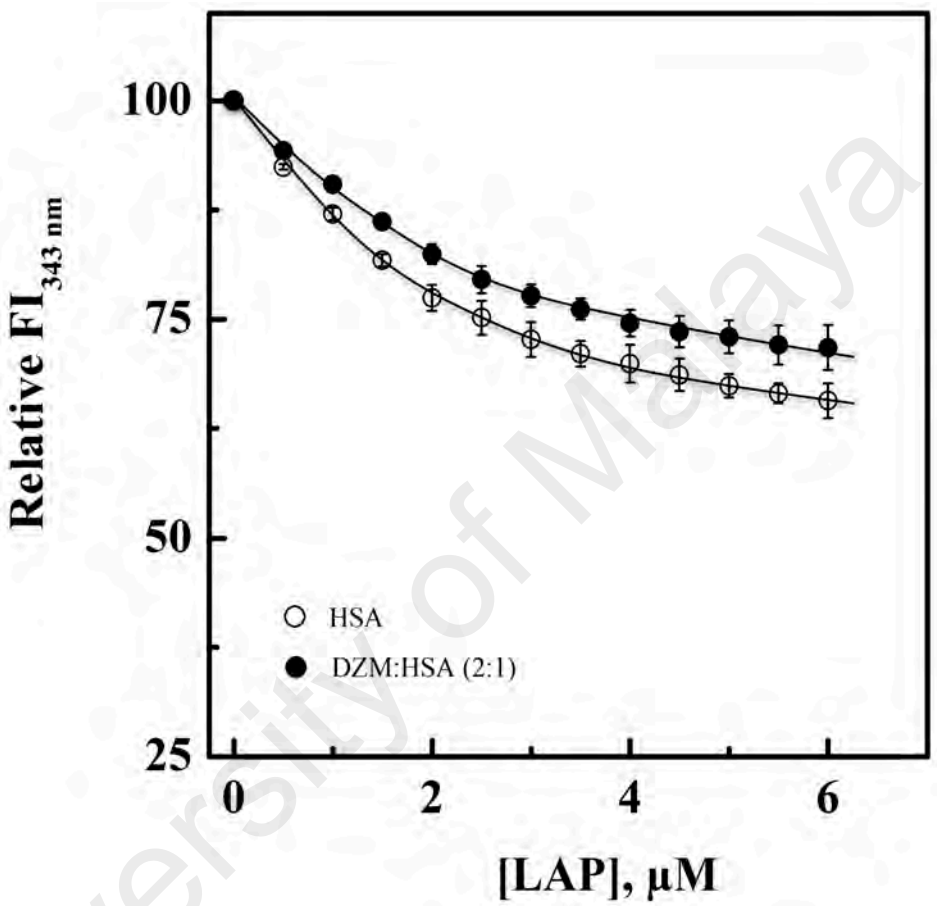

Figure 4.25: Plots showing the decrease in the relative fluorescence intensity at 343 nm ($FI_{343\ nm}$) of HSA (3 μM) and DZM–HSA (2:1) mixture with increasing concentrations (0–6.0 μM with 0.5 μM intervals) of LAP. The experiments were carried out in 60 mM sodium phosphate buffer, pH 7.4 at 298 K.

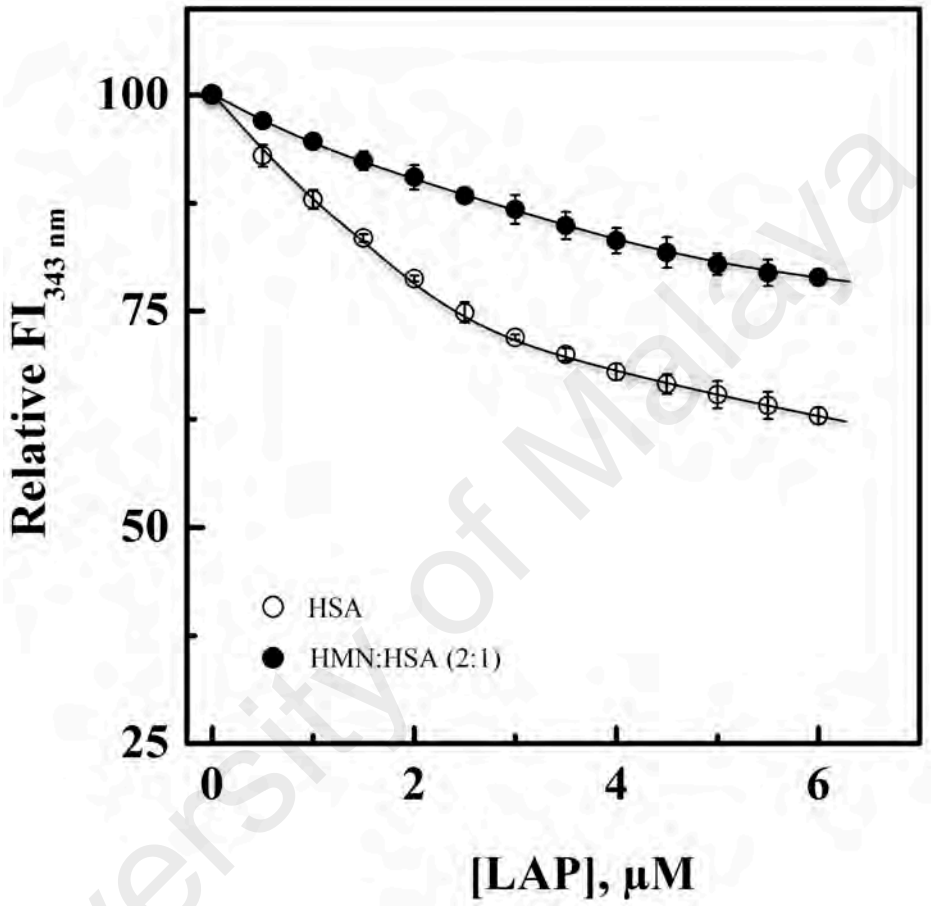

Figure 4.26: Plots showing the decrease in the relative fluorescence intensity at 343 nm ($FI_{343\ nm}$) of HSA (3 μM) and HMN–HSA (2:1) mixture with increasing concentrations (0–6.0 μM with 0.5 μM intervals) of LAP. The experiments were carried out in 60 mM sodium phosphate buffer, pH 7.4 at 298 K.

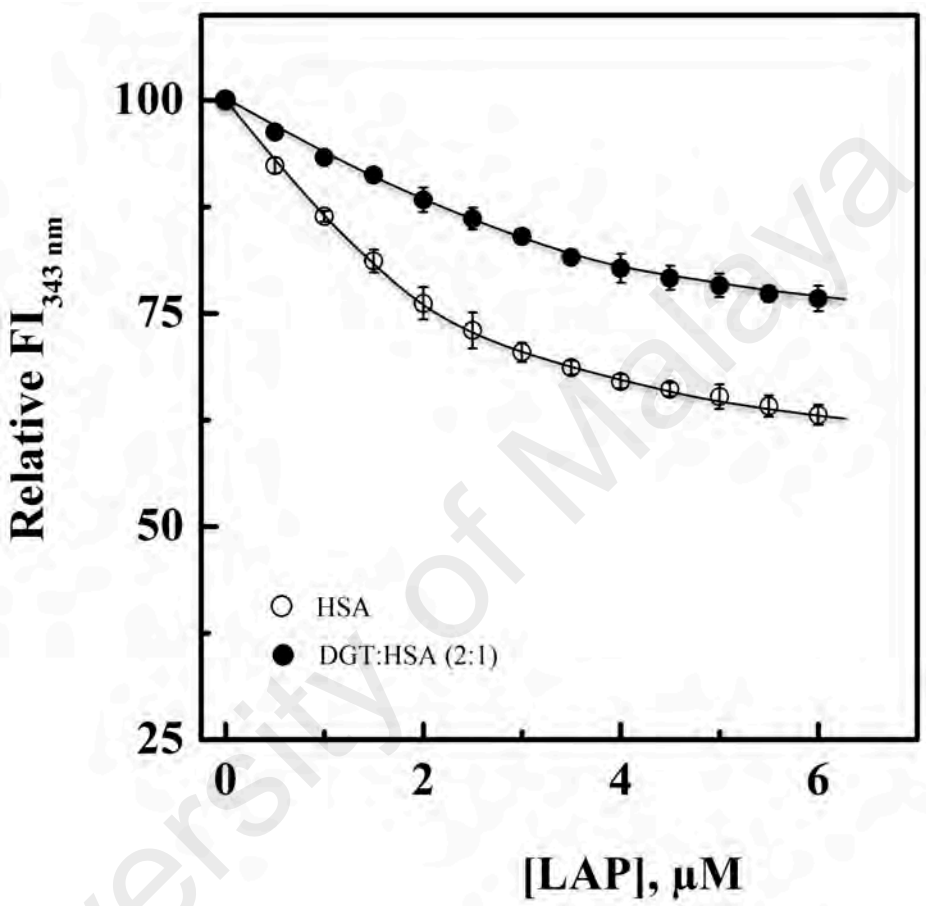

Figure 4.27: Plots showing the decrease in the relative fluorescence intensity at 343 nm ($FI_{343\ nm}$) of HSA (3 μM) and DGT–HSA (2:1) mixture with increasing concentrations (0–6.0 μM with 0.5 μM intervals) of LAP. The experiments were carried out in 60 mM sodium phosphate buffer, pH 7.4 at 298 K.

bound HSA compared to HSA alone. A comparison of the differences in the fluorescence intensity values, observed between free HSA and site marker-bound HSA shows major distinctions with HMN- (Figure 4.26) and DGT- (Figure 4.27) bound systems. In view of these results, it seems that HMN or DGT offered significant protection against LAP binding to HSA, suggesting a common binding site for these ligands. In other words, binding site III, located in subdomain IB appears to be the preferable LAP binding site on HSA. Since a lesser difference in the fluorescence intensity was noticed with both PBZ- (Figure 4.24) and DZM- (Figure 4.25) bound systems, binding of LAP to Sudlow's site I and site II cannot be completely ruled out.

Furthermore, data obtained from Figures 4.24–4.27 were treated according to Eq. (5) and double logarithmic plots, thus obtained with HSA and site marker–HSA complexes are shown in Figure 4.28. Values of the binding constant (K_a) for LAP–HSA system in the absence and presence of site markers, as determined from the double logarithmic plots (Figure 4.28) are summarized in Table 4.9. A comparison of these values with the K_a value ($1.30 \pm 0.07 \times 10^5$ M^{-1}), obtained in the absence of PBZ, DZM, HMN and DGT clearly suggested significant decrease in the K_a value (Table 4.9) in the presence of HMN or DGT than that observed in the presence of PBZ or DZM. These results further manifested competition between LAP and HMN or DGT for the same binding site on HSA. Therefore, site III is supposed to be the favored LAP binding locus in HSA. Our competitive ligand displacement results were well supported by the molecular docking analysis.

4.2.9.2 Molecular docking analysis

Since LAP showed a binding preference for the binding site III (subdomain IB) of HSA as described in the section 4.2.9.1, a site-specific molecular docking analysis was made to validate the results of the competitive ligand displacement experiments. The binding mode of LAP was predicted for the three drug binding sites, namely, sites I, II

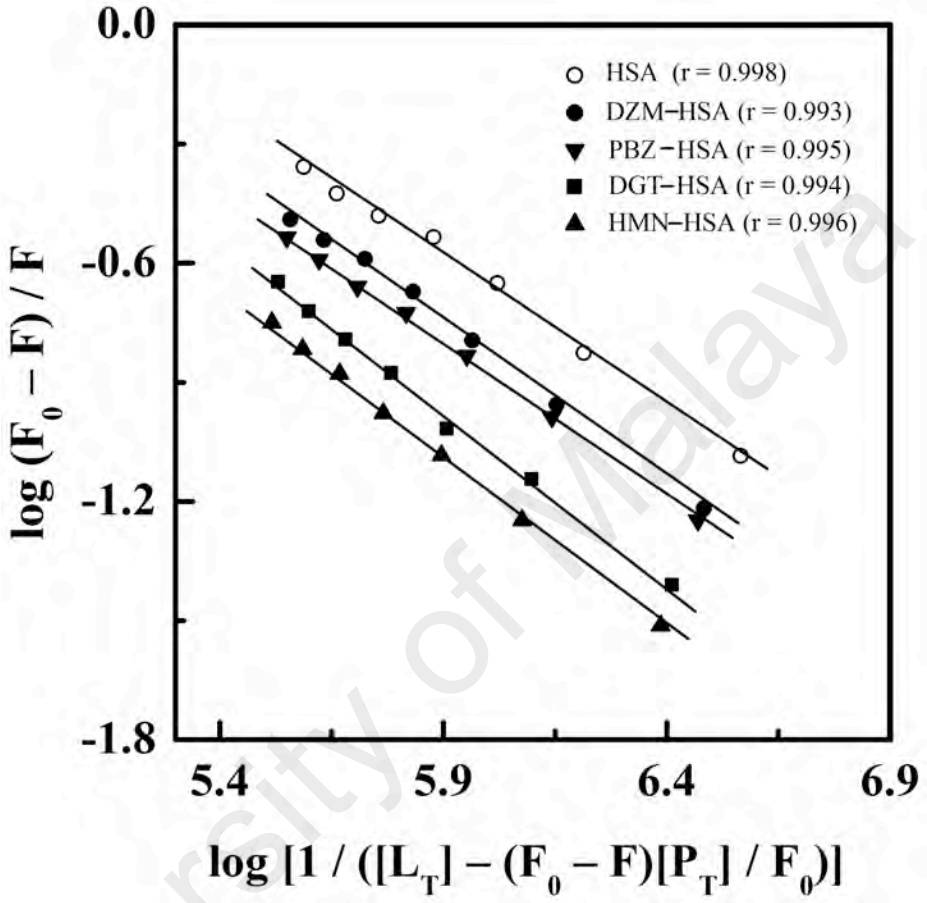

Figure 4.28: Double logarithmic plots of [log ($F_0 - F$) / F versus log [1 / ([L_T] – [(F_0 – F)[P_T] / F_0)] for the fluorescence quenching data of the LAP–HSA system in the absence and presence of different site markers, *i.e.*, PBZ, DZM, HMN and DGT, obtained in 60 mM sodium phosphate buffer, pH 7.4 at 298 K (Figures 4.24–4.27).

Table 4.9: K_a values of LAP–HSA interaction in the absence and presence of site markers, obtained at 298 K, pH 7.4.

Site Marker	K_a ($\times 10^5$ M^{-1})
–	1.30 ± 0.07
PBZ	0.73 ± 0.08
DZM	0.93 ± 0.05
HMN	0.45 ± 0.09
DGT	0.57 ± 0.04

and III, which are located at subdomains IIA, IIIA (Sudlow et al., 1975) and IB (Kragh-Hansan, 1985), respectively, of HSA. Cluster analysis, performed for all the three binding sites (Figure 4.29) using a RMSD tolerance of 2.0 Å yielded a total of 93, 93 and 79 multimember conformational clusters from 100 docking runs for binding sites I, II and III, respectively. The lowest binding energy was found with site III at a value of – 40.03 kJ mol^{-1}, while the values of the lowest binding energy with site I and site II were calculated as –30.50 and –22.18 kJ mol^{-1}, respectively. The highest populated clusters for site I and site II had 3 members each out of 100 conformations, whereas a 6 member cluster was found with site III. Nevertheless, the highest populated cluster with any of the sites was not the most energetically (– 40.03 kJ mol^{-1}) favorable cluster (Figure 4.29). Docking results revealed that LAP showed a binding preference for the drug binding site III of HSA with more favorable docking conformer than the one in either site I or site II. Hence, site-specific marker displacement results discussed in Section 4.2.9.1 were well supported by the docking analysis.

In view of the large chemical structure of LAP, the predicted binding model with the lowest docking energy for the binding sites I, II and III was then used for binding orientation analysis (Figure 4.30). The binding site (defined by the amino acid residues within 5 Å distance to the ligand) I was found to be deep inside the protein structure and was mostly located in a hydrophobic cleft, lined by the following amino acid residues: Tyr-150, Glu-153, Lys-195, Gln-196, Lys-199, Trp-214, Arg-218, Leu-219, Arg-222, Phe-223, Leu-238, Val-241, His-242, Ile-290, Ala-291 and Glu-292. The LAP-HSA complex formation at binding site II involved 12 amino acid residues, namely, Gln-390, Ala-406, Val-409, Arg-410, Tyr-411, Lys-413, Lys-414, Leu-491, Glu-492, Val-493, Asp-494 and Thr-540. Interestingly, formation of LAP–HSA complex at site III engaged 25 amino acid residues, *viz.*, Asn-109, Pro-110, Asn-111, Leu-112, Pro-113, Arg-114, Leu-115, Val-116, Arg-117, Met-123, Phe-134, Lys-137, Thr-138, Glu-141,

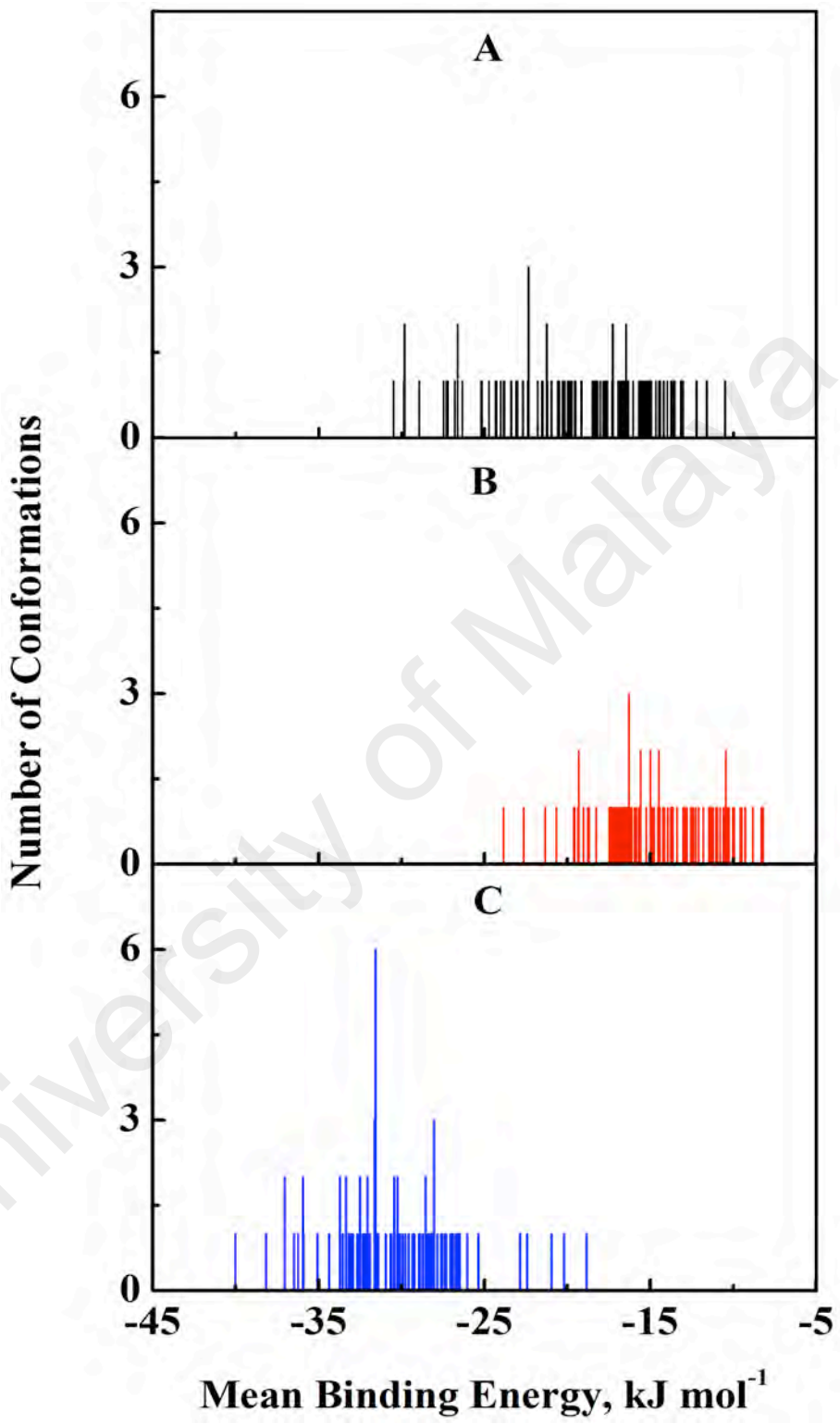

Figure 4.29: Cluster analysis of the docking of LAP to three different binding sites, *viz.*, I (A), II (B) and III (C) of HSA crystal structure (1BM0). The results were obtained from a total of 100 runs for each binding site.

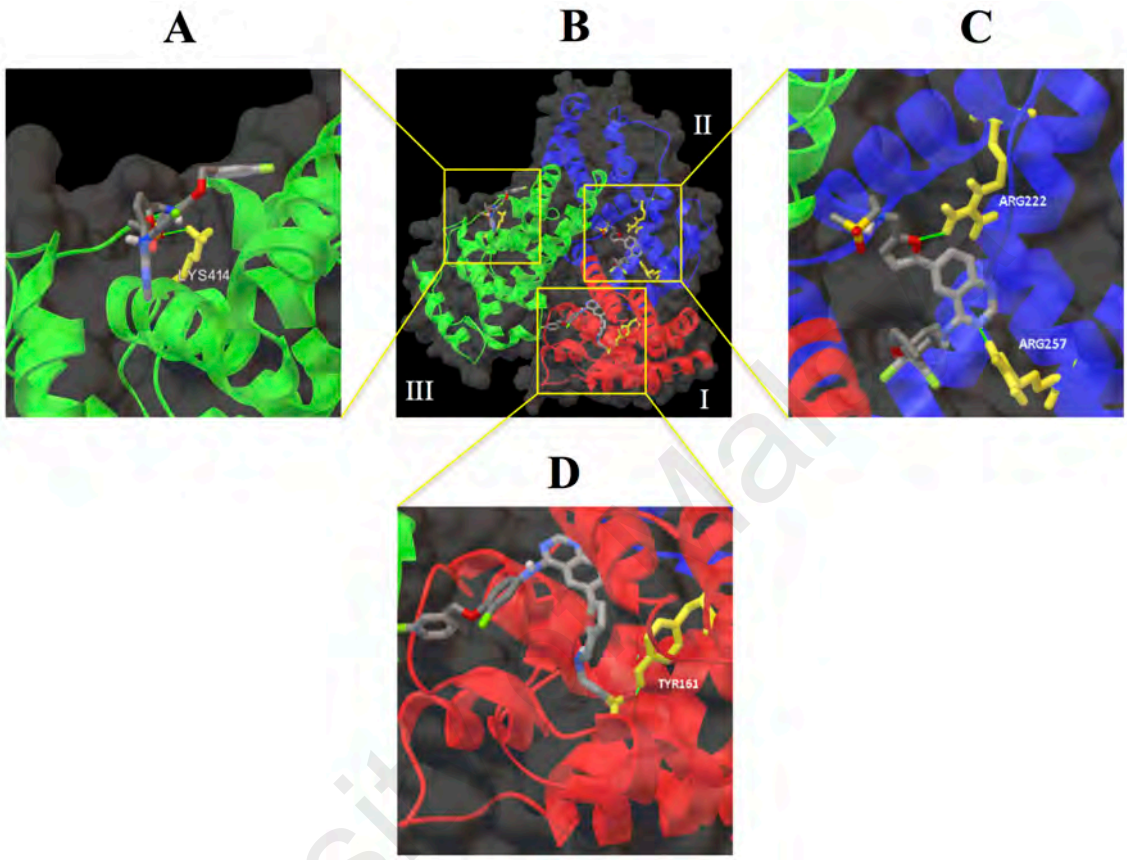

Figure 4.30: Predicted binding orientation of the lowest docking energy conformation of LAP (ball-and-stick rendered) in the binding sites I (subdomain IIA), II (subdomain IIIA) and III (subdomain IB) of HSA (1BM0) (B). Different domains of HSA, namely, I, II and III are shown in red, blue and green, respectively. The enlarged views show the hydrogen bonds (green lines) formed between amino acid residues (rendered in yellow ball and stick) and LAP in the binding site I (C), II (A) and III (D) of HSA.

Ile-142, Arg-145, His-146, Phe-149, Phe-157, Tyr-161, Leu-182, Leu-185, Arg-186, Gly-189 and Lys-190.

As illustrated in red in the LigPlot+ diagrams (Figure 4.31), hydrophobic amino acid residues mostly encompassed the three binding sites of HSA and they might have contributed towards the stability of the ligand–HSA complex through hydrophobic interactions. However, presence of several polar amino acid residues within the proximity of the bound ligand indicated that the interactions between the LAP and HSA at these sites cannot be presumed to be exclusively hydrophobic in nature. Furthermore, in the LAP–HSA complex docking conformation at site III, one hydrogen bond was predicted involving the hydrogen atom of Tyr-161 and the oxygen atom of LAP (Figure 4.30; Table 4.10). On the other hand, at the binding sites I and II, two and one hydrogen bonds, respectively, were also formed (Figure 4.30; Table 4.10). Hence, it can be concluded that LAP binds preferably to the hemin binding site, located in subdomain IB involving both hydrophobic interactions and hydrogen bonding. These docking results were in line with our thermodynamic analysis of the binding reaction, implying involvement of both hydrophobic interactions and hydrogen bonding in LAP–HSA complex formation.

In conclusion, the results obtained from the LAP–HSA interaction studies demonstrated intermediate binding affinity and the involvement of hydrophobic interactions as well as hydrogen bonding in the binding reaction. Both secondary and tertiary structural changes in HSA along with increased thermal stability were noticed upon LAP binding. Presence of metal ions was found to decrease the binding affinity between LAP and HSA. Site III, located in subdomain 1B of HSA was suggested as the preferred LAP binding site on HSA.

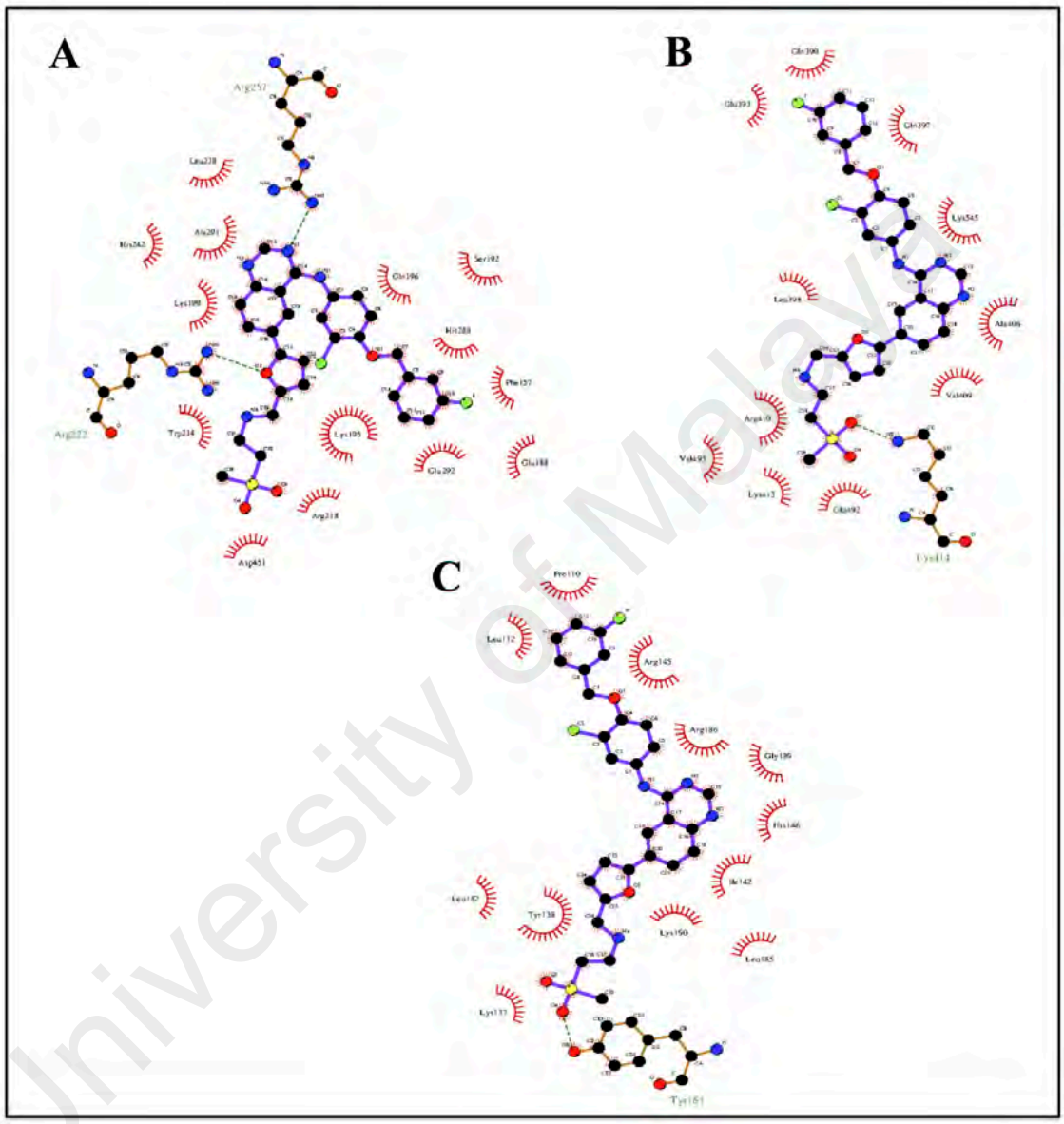

Figure 4.31: LigPlot+ diagram of LAP (purple lines) and the amino acid residues of HSA at three different binding sites I (A), II (B) and III (C). The residues indicate the presence of hydrophobic interactions with LAP. Hydrogen bonds of LAP and HSA are rendered with dashed green lines.

Table 4.10: Predicted hydrogen bonds between interacting atoms of the amino acid residues of HSA (1BM0) and LAP at sites I, II and III.

HSA Binding Site	HSA Atom	LAP Atom	Distance (Å)
Site I	Arg222:HH2	O (Oxacyclopentane)	2.170
	Arg257:HH2	N (Pyrimidine)	2.241
Site II	Lys414:HZ3	O (Sulfonyl)	2.119
Site III	Tyr161:HH	O (Sulfonyl)	1.721

4.3 GEF–HSA interaction

Interaction between GEF, a tyrosine kinase inhibitor and HSA was also studied using fluorescence spectroscopy.

4.3.1 Fluorescence spectra

The fluorescence spectra of HSA in the absence and presence of increasing GEF concentrations are displayed in Figure 4.32. The fluorescence spectrum of HSA showed an emission maximum at 343 nm due to the presence of the lone Trp-214 residue at subdomain IIA of HSA (Sulkowska, 2002). Addition of increasing GEF concentrations led to significant quenching in the protein's fluorescence along with red shift in the emission maximum in a concentration dependent manner (Figure 4.32). It is important to note that free GEF did not produce any fluorescence in this wavelength range (Figure 4.32). About 45 % quenching in the fluorescence intensity at 343 nm (inset of Figure 4.32) and 15 nm red shift in the emission maximum, observed at the highest GEF concentration (50 μM) clearly suggested the binding of GEF to HSA. Occurrence of the red shift in the emission maximum can be ascribed to the change in the microenvironment around lone Trp residue from nonpolar to polar (Il'ichev et al., 2002). On the other hand, a variety of molecular processes such as excited-state reactions, molecular rearrangements, energy transfer, ground-state complex formation and collisional quenching may be responsible for the observed quenching of the protein fluorescence upon ligand binding (Lakowicz, 2006). Several earlier reports have shown quenching of HSA fluorescence upon drug binding with red shift in the emission maximum (Saeidifar et al., 2015; Trnkova et al., 2011; Tu et al., 2015).

4.3.2 Mechanism of fluorescence quenching

Titration of HSA with increasing concentrations of GEF was performed at three different temperatures, *i. e.*, 288 K (Figure 4.32), 303 K and 318 K (Figure 4.32S). Analysis of the fluorescence quenching data obtained at three different temperatures

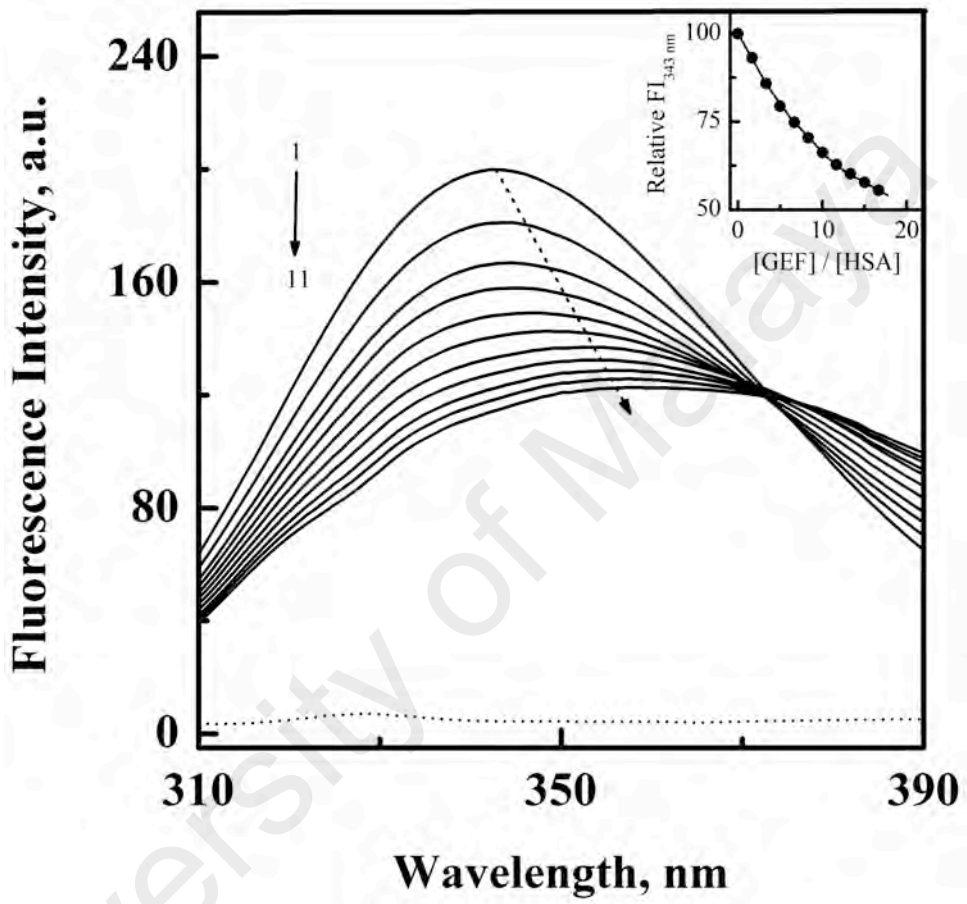

Figure 4.32: Fluorescence spectra of HSA (3 μM) in the absence (spectrum 1) and presence (spectra 2–11) of increasing GEF concentrations (5–50 μM with 5 μM intervals), obtained in 60 mM sodium phosphate buffer, pH 7.4 at 288 K upon excitation at 295 nm. The fluorescence spectrum of free GEF (50 μM) is shown with dotted line. The inset shows the decrease in the relative fluorescence intensity of HSA at 343 nm ($FI_{343\ nm}$) with increasing GEF/HSA molar ratios.

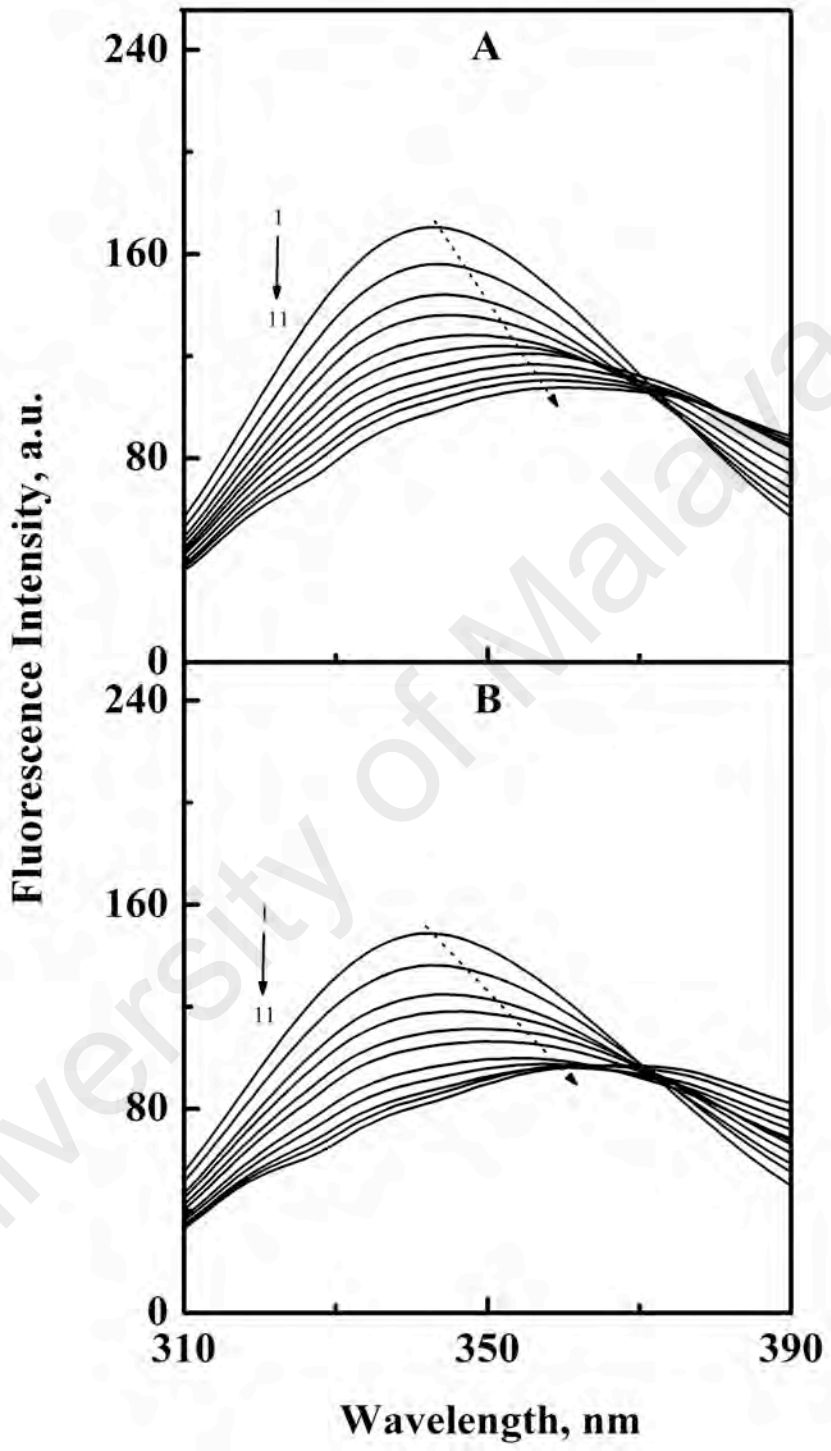

Figure 4.32 S: Fluorescence spectra of HSA (3 μM) in the absence (spectrum 1) and presence (spectra 2–11) of increasing GEF concentrations (5–50 μM with 5 μM intervals), obtained in 60 mM sodium phosphate buffer, pH 7.4 at (A) 303 K and (B) 318 K upon excitation at 295 nm.

according to Eq. (3) yielded the Stern-Volmer plots, as shown in Figure 4.33. These plots exhibited good linearity with a correlation coefficient (r) ≥ 0.997 throughout the GEF concentrations used. Values of the Stern-Volmer constant, K_{SV} were obtained from the linear regression analysis of the above plots and are listed in Table 4.11. The quenching constant, K_{SV} is expected to decrease with increasing temperature for static quenching, while the reverse trend characterizes dynamic quenching (Lakowicz, 2006). As can be seen from the Table 4.11, value of K_{SV} significantly decreased with increasing temperature, thus indicating the characteristic of static quenching. Therefore, the observed quenching in the protein's fluorescence upon GEF addition seems to be the result of GEF–HSA complex formation. Furthermore, k_q values (Table 4.11), obtained at three different temperatures using Eq. (4) for the GEF–HSA system were significantly higher than the value of 2×10^{10} M^{-1} s^{-1}, reported for the maximum dynamic quenching constant for the association of various quenchers and the fluorophore in a bimolecular complex (Ware, 1972). Therefore, it can be concluded that the quenching mechanism involved in the GEF–HSA system was initiated by static rather than dynamic quenching process.

4.3.3 Binding affinity

Figure 4.34 shows double logarithmic plots for the binding of GEF to HSA at different temperatures, as obtained after treatment of the fluorescence quenching data according to Eq. (5). The values K_a for the GEF–HSA system at three different temperatures, as retrieved from these plots are included in Table 4.11. Since the K_a value for the GEF–HSA system was found to remain in the range of 1.70–1.25 × 10^4 M^{-1}, it indicated a moderate binding affinity between GEF and HSA. Such moderate binding affinity is beneficial for the efficient transport of the drug and its subsequent release at its target site. As can be seen from Table 4.11, K_a value of the GEF–HSA system showed a decreasing trend with increasing temperature due to decomposition of

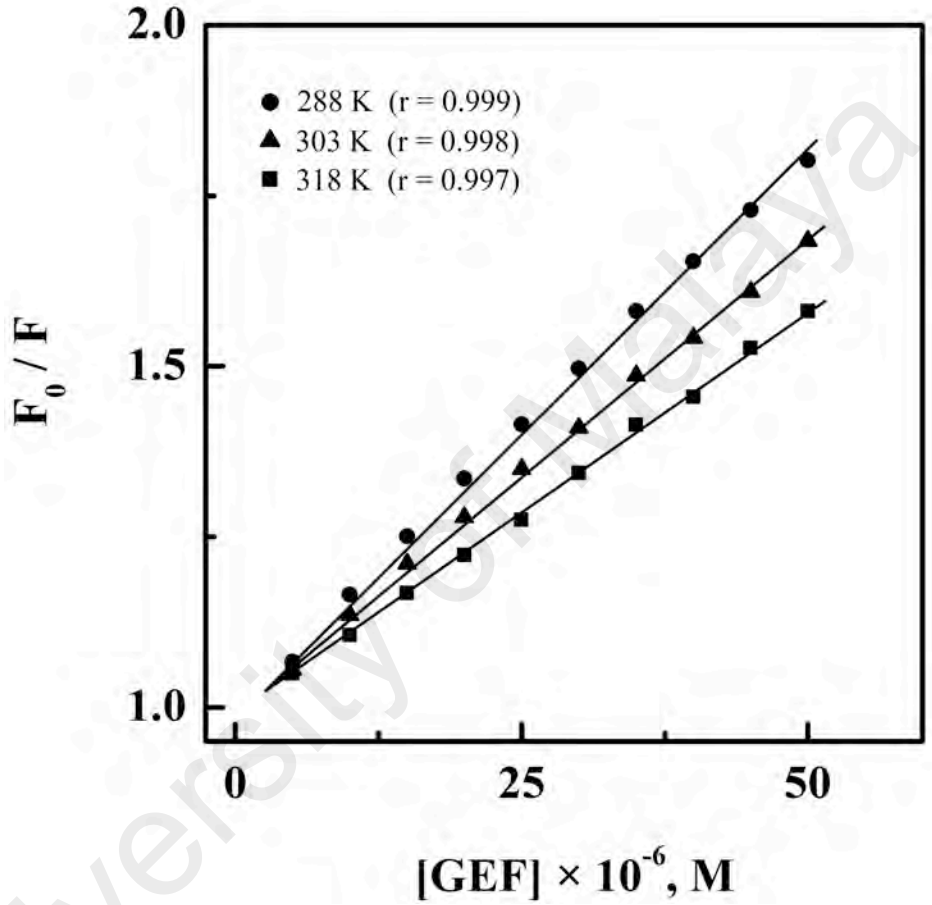

Figure 4.33: Stern-Volmer plots for the fluorescence quenching data of the GEF–HSA system, obtained at three different temperatures, *i.e.,* 288 K, 303 K and 318 K.

Table 4.11: Quenching and binding parameters for GEF–HSA interaction, studied at three different temperatures, pH 7.4.

T (K)	K_{SV} (M^{-1})	k_q (M^{-1} s^{-1})	K_a (M^{-1})
288	$(1.60 \pm 0.03) \times 10^4$	$(2.51 \pm 0.09) \times 10^{12}$	$(1.70 \pm 0.07) \times 10^4$
303	$(1.36 \pm 0.07) \times 10^4$	$(2.13 \pm 0.06) \times 10^{12}$	$(1.43 \pm 0.04) \times 10^4$
318	$(1.19 \pm 0.06) \times 10^4$	$(1.87 \pm 0.08) \times 10^{12}$	$(1.25 \pm 0.08) \times 10^4$

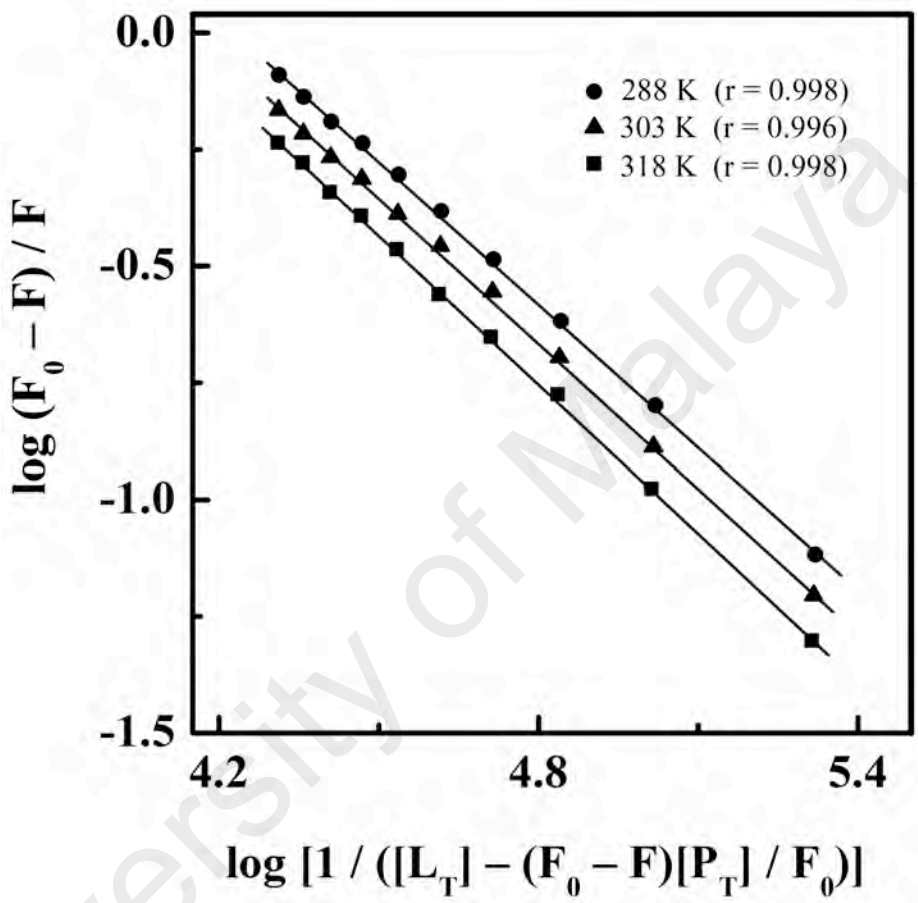

Figure 4.34: Double logarithmic plots of [log ($F_0 - F$) / F versus log [1 / ([L_T] – [(F_0 – F)[P_T] / F_0)] for the fluorescence quenching data of the GEF–HSA system, obtained at three different temperatures, *i.e.*, 288 K, 303 K and 318 K.

the GEF–HSA complex at higher temperatures. Several published reports on the binding of various drugs to HSA have shown moderate affinity (Shahabadi et al., 2016; Tunc et al., 2013b; Wang et al., 2015).

4.3.4 Interaction forces

In view of the temperature dependence of the binding constant, ligand-protein interaction seems to be a thermodynamic process (Wang et al., 2011). Figure 4.35 shows linear van't Hoff plot for GEF–HSA interaction. Values of ΔH and ΔS, as obtained from the slope and the intercept, respectively, of the van't Hoff plot along with the ΔG values at three different temperatures are listed in Table 4.12. Whereas, the negative sign of ΔG value showed spontaneous nature of the binding reaction at all temperatures, negative value of ΔH revealed that formation of GEF–HSA complex was an exothermic process. In view of the positive ΔS value and negative ΔH value, obtained for GEF–HSA system, hydrophobic interactions along with hydrogen bonds and van der Waals forces seem to favor the stabilization of GEF–HSA complex (Li et al., 2007; Ross & Subramanian, 1981). Absence of charged group in the GEF molecule and the negative ΔH value, obtained in this study excluded the participation of electrostatic interactions in the stabilization of GEF–HSA complex (Ross & Subramanian, 1981). It is feasible to account more than one intermolecular binding forces for ligand–protein interactions (Ross & Subramanian, 1981). Thus, thermodynamic data clearly revealed hydrophobic interactions, van der Waals interactions and hydrogen bonds as the major stabilizing forces in the GEF–HSA complex formation. This was further supported by our molecular docking results, as described in Section 4.3.9.2.

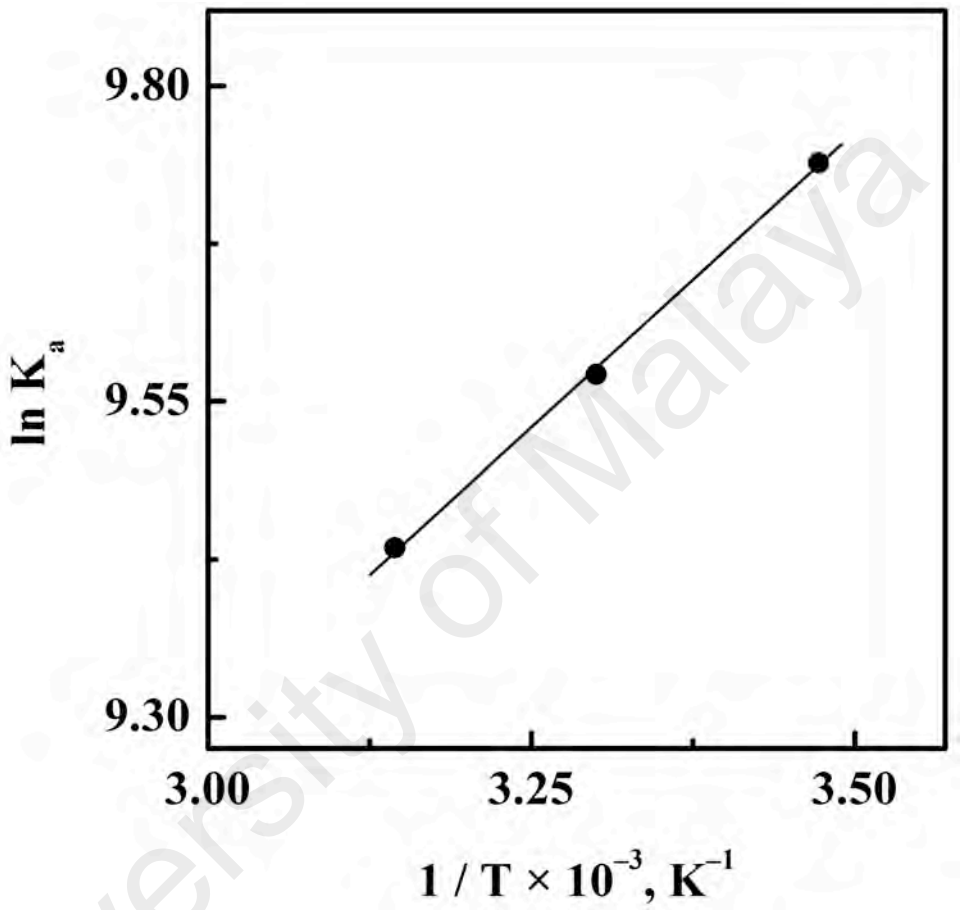

Figure 4.35: The van't Hoff plot for GEF–HSA interaction. Values of K_a were obtained from the double logarithmic plots, displayed in Figure 4.34.

Table 4.12: Thermodynamic parameters for GEF–HSA interaction, studied at three different temperatures, pH 7.4.

T (K)	ΔS (J mol^{-1} K^{-1})	ΔH (kJ mol^{-1})	ΔG (kJ mol^{-1})
288			– 23.32
303	+ 54.06	– 7.74	– 24.13
318			– 24.94

4.3.5 Absorption spectra

In order to confirm the complex formation between GEF and HSA, UV-vis absorption spectra of HSA were studied in the absence (spectrum 1) and presence (spectra 2–11) of increasing (5–50 μM with 5 μM intervals) GEF concentrations (Figure 4.36). These changes in the UV absorption spectra of the protein at respective GEF concentrations were obtained by subtracting the spectra of the pure GEF solutions (Figure 4.36S(B)) from the spectra of GEF–HSA mixtures (Figure 4.36S(A)). Significant change in the absorbance value of HSA at 280 nm upon GEF addition suggested microenvironmental perturbations around the protein chromophores due to the complex formation between GEF and HSA. Absorption spectrum of free GEF was characterized by the presence of a peak at 332 nm (Figure 4.36S). Increase in the absorbance value at 332 nm with increasing GEF concentrations was also noticed, which was suggestive of the complex formation between GEF and HSA. Such changes in the absorption spectrum of HSA in the presence of GEF supported the involvement of static quenching mechanism in GEF–HSA system.

4.3.6 GEF-induced structural / microenvironmental changes in HSA

Circular dichroism and 3-D fluorescence spectroscopy were employed to study GEF-induced structural (secondary and tertiary structures) alterations and microenvironmental perturbations around Trp and Tyr residues, respectively, in HSA.

4.3.6.1 Far-UV and near-UV CD spectra

Alterations in the secondary and the tertiary structures of HSA in the presence of GEF were evident from the far-UV CD (Figure 4.37) and the near-UV CD (Figure 4.38) spectra of the protein, respectively. Presence of the α–helical structure in HSA was reflected from the appearance of two minima at 208 nm and 222 nm in the far-UV CD spectrum (Reed et al., 1975), as shown in Figure 4.37. Binding of GEF to HSA in 1:1

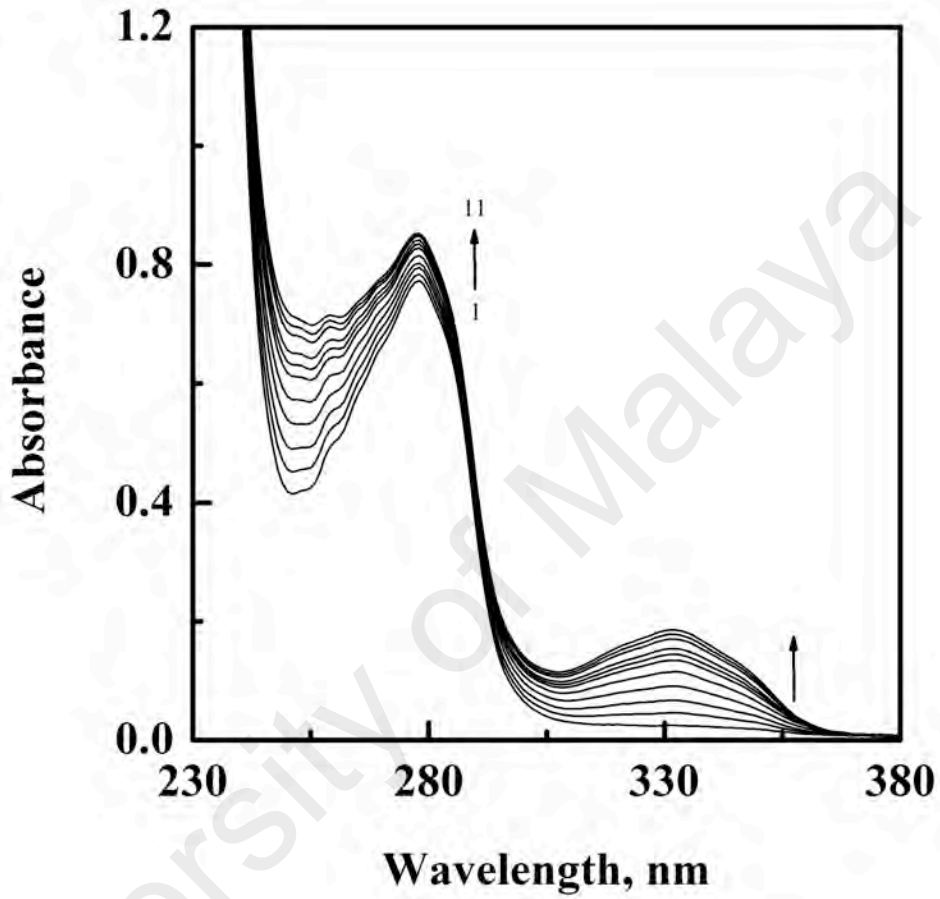

Figure 4.36: UV-vis absorption spectra of HSA (15 μM) in the absence (spectrum 1) and presence (spectra 2–11) of increasing GEF concentrations (5–50 μM with 5 μM intervals), obtained in 60 mM sodium phosphate buffer, pH 7.4 at 298 K. The spectra (2–11) were obtained by subtracting the absorption contribution of respective free GEF from the absorption spectra of GEF–HSA mixtures.

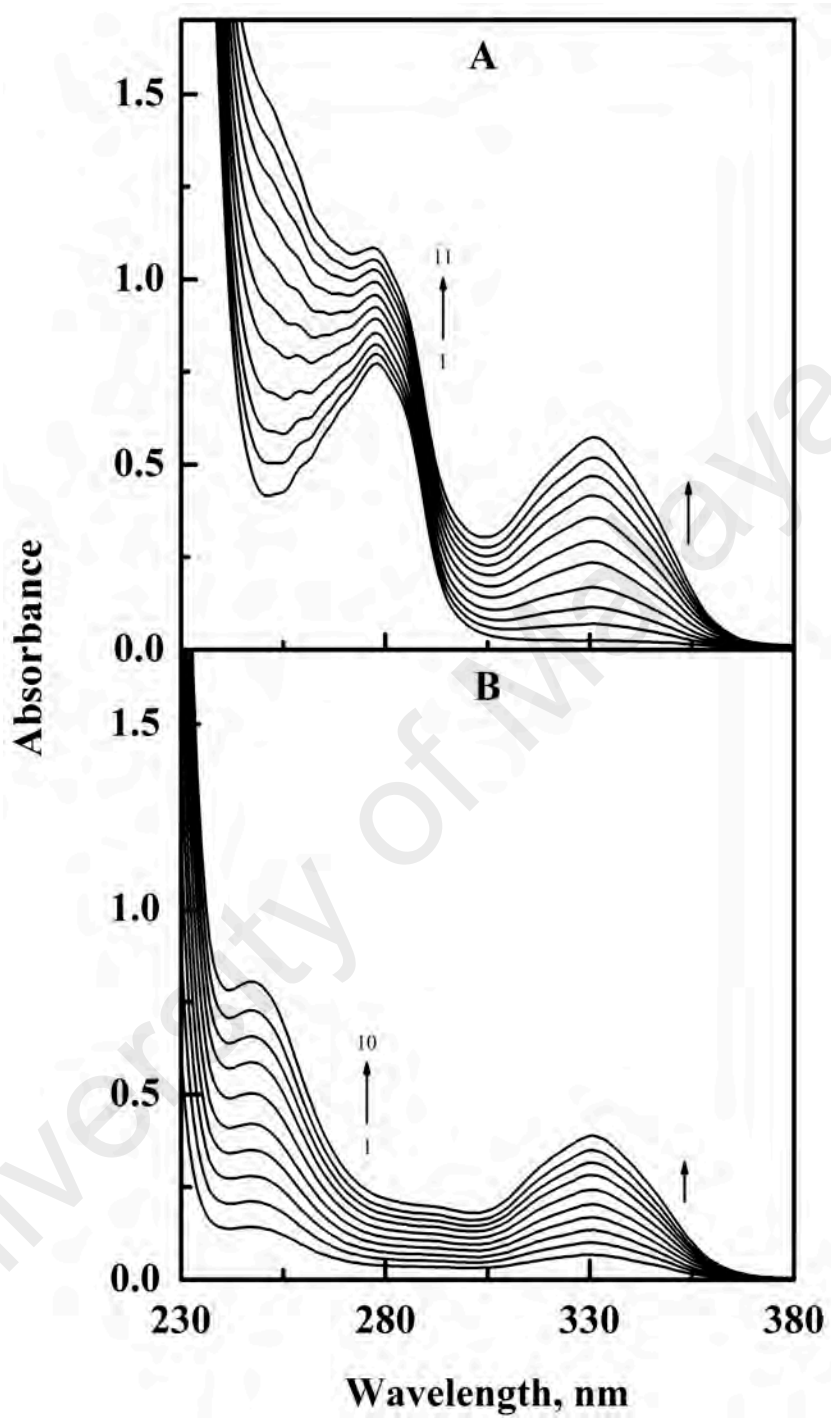

Figure 4.36 S: (A) Uncorrected UV-vis absorption spectra of HSA (15 μM) in the absence (spectrum 1) and presence (spectra 2–11) of increasing GEF concentrations (5–50 μM with 5 μM intervals), obtained in 60 mM sodium phosphate buffer, pH 7.4 at 298 K. (B) The spectra (1–10) were obtained with increasing GEF concentrations (5–50 μM with 5 μM intervals).

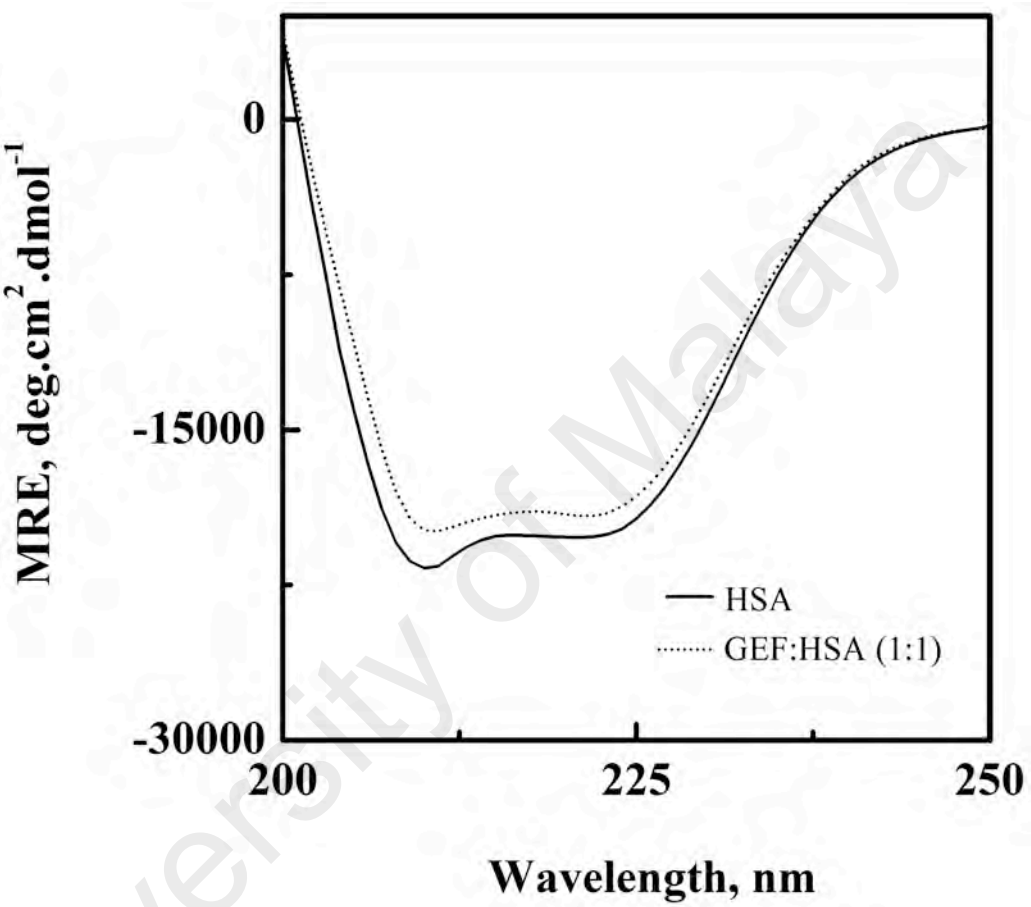

Figure 4.37: Far-UV CD spectra of HSA (3 μM) and GEF–HSA (1:1) mixture. The CD spectra were recorded using a 1 mm path length cuvette, in 60 mM sodium phosphate buffer, pH 7.4 at 298 K.

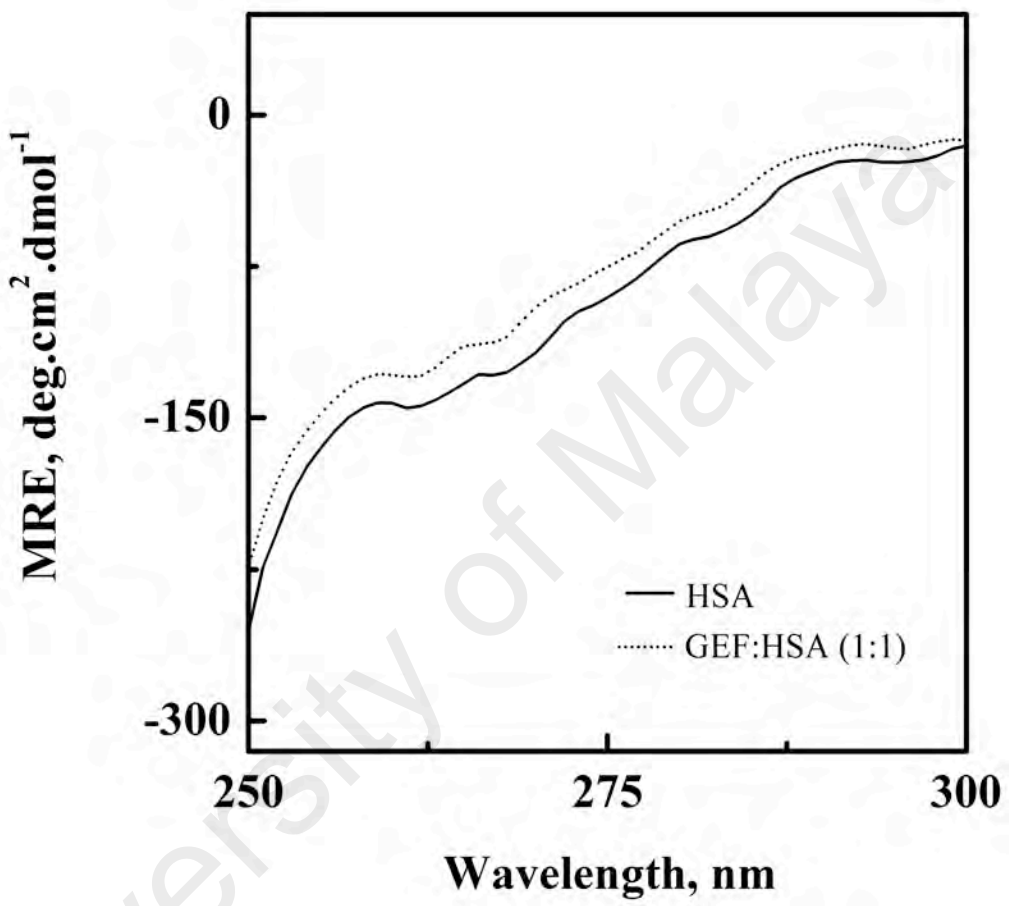

Figure 4.38: Near-UV CD spectra of HSA (10 μM) and GEF–HSA (1:1) mixture. The CD spectra were recorded using a 10 mm path length cuvette, in 60 mM sodium phosphate buffer, pH 7.4 at 298 K.

molar ratio induced significant change in the far-UV CD spectrum of HSA (Figure 4.37), thus suggesting secondary structural changes in the protein.

The near-UV CD spectrum of HSA (Figure 4.38) was characterized by the spectral features due to aromatic chromophores and disulfide bonds present in the protein (Lee & Hirose, 1992). Appearance of two minima around 263 nm and 269 nm and shoulders around 282 nm and 291 nm characterized the near-UV CD spectrum of HSA (Figure 4.38). Significant alteration in the near-UV CD spectrum of HSA was observed in the presence of GEF, suggesting tertiary structural changes in HSA due to GEF binding.

4.3.6.2 Three-dimensional fluorescence spectra

Although knowledge of GEF-induced microenvironmental perturbations around Trp-214 was evident from the fluorescence spectra (Figure 4.32), greater insights about these changes can be achieved by studying the 3-D fluorescence spectra of HSA in the presence of GEF. The 3-D fluorescence spectra and corresponding contour maps of HSA (A) and GEF–HSA mixture ([GEF]:[HSA] = 5:1) (B) are shown in Figure 4.39, while spectral characteristics are listed in Table 4.13. Besides two small scattering peaks, *i.e.*, peak 'a' and peak 'b', two strong fluorescence peaks, *viz.*, peaks '1' and '2', due to Tyr and Trp residues of the protein, as discussed in Section 4.1.6.2 and 4.2.6.2 were present in the 3-D fluorescence spectra of HSA (Figure 4.39). A comparison of the 3-D fluorescence spectral characteristics of HSA in the absence and presence of GEF (5 molar excess) showed ~ 28 % reduction in the intensity along with 16 nm red shift in the emission maximum of peak '1' and ~ 76 % reduction in the intensity along with 12 nm red shift in peak '2' (Table 4.13). Such changes in the fluorescence spectral characteristics clearly indicated microenvironmental perturbation (from nonpolar to polar) around Trp and Tyr residues of HSA.

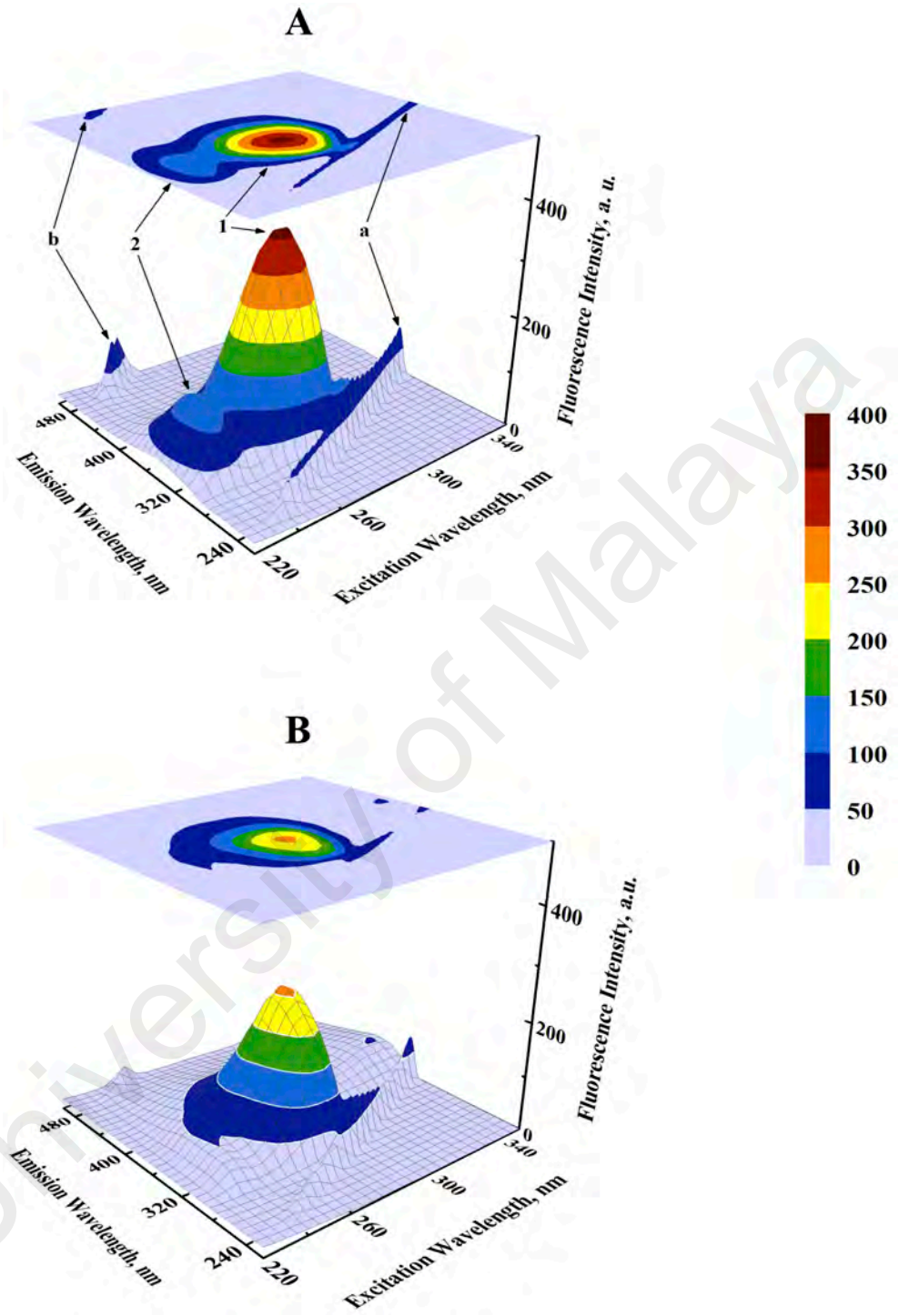

Figure 4.39: Three-dimensional fluorescence spectra and corresponding contour maps of (A) HSA (3 μM) and (B) GEF–HSA (5:1) mixture. The spectra were recorded in 60 mM sodium phosphate buffer, pH 7.4 at 298 K.

Table 4.13: Three-dimensional fluorescence spectral characteristics of HSA (3 μM) and GEF–HSA system at 298 K, pH 7.4.

System	Peak	Peak Position [λ_{ex} / λ_{em} (nm/nm)]	Intensity
HSA	a	230/230→350/350	16.44→88.91
	b	250/500	89.28
	1	280/337	361.02
	2	230/335	114.41
[GEF]:[HSA] = 5:1	a	230/230→350/350	14.70→75.92
	b	250/500	40.55
	1	280/353	261.10
	2	230/347	27.74

4.3.7 Thermal stabilization of HSA

Figure 4.40 shows the influence of temperature on the fluorescence intensity at 343 nm ($FI_{343\ nm}$) of HSA as well as [GEF]:[HSA] (10:1) mixture in the temperature range, 298–353 K. HSA showed a gradual decrease in $FI_{343\ nm}$ with the increase in temperature. Interestingly, lesser decrease in the $FI_{343\ nm}$ was noticed in the presence of GEF at higher temperatures (> 318 K) compared to that observed in its absence. These results clearly suggested significant protection of HSA against temperature-induced structural changes at higher temperatures. Such changes in the fluorescence intensity can be explained by coupling of binding and unfolding equilibria (Celej et al., 2003; Shrake & Ross, 1988). Several earlier reports have shown ligand-induced thermal stabilization of HSA (Ajloo et al., 2007; Pico, 1997).

4.3.8 Influence of metal ions on GEF–HSA interaction

Presence of some common metal ions, *viz*., Ba^{2+}, Cu^{2+}, Mn^{2+}, Zn^{2+}, Ca^{2+}, K^{+} and Mg^{2+} in the blood plasma might affect the binding of a drug to the protein (Sancataldo et al., 2014). The interference of these common ions with GEF–HSA interaction was investigated by determining the K_a values of GEF–HSA binding reaction in the absence and presence of these metal ions (100 µM). As shown in Table 4.14, both increase and decrease in the K_a value was noticed in the presence of these metal ions. Whereas, K^{+} and Mg^{2+} produced slight increase in the K_a value, decrease in the K_a was observed in the presence of Ba^{2+}, Cu^{2+}, Mn^{2+} and Zn^{2+} ions. These results clearly suggested some influence of metal ions on the binding of GEF to HSA, which may prolong and / or weaken the storage time of the drug in plasma. Therefore, it is important to adapt the dose of the drug in the presence of these ions to achieve the desired therapeutic effect (Cheng et al., 2013; Wang et al., 2011).

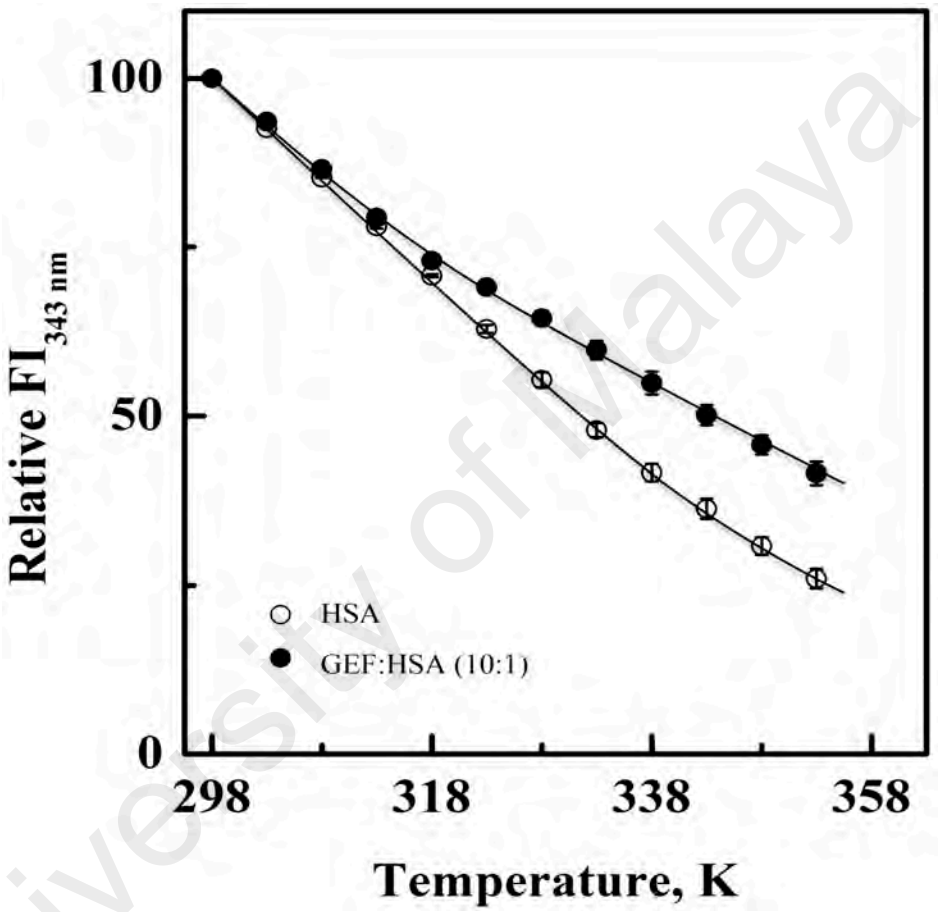

Figure 4.40: Thermal stability profiles of HSA (3 μM) and GEF–HSA (10:1) mixture in the temperature range, 298–353 K with a regular increments of 5 K, as monitored by fluorescence intensity measurements at 343 nm ($FI_{343\ nm}$), in 60 mM sodium phosphate buffer, pH 7.4.

Table 4.14: K_a values of GEF–HSA interaction in the absence and presence of different metal ions (100 μM) at 298 K, pH 7.4.

Metal Ion	K_a ($\times 10^4$ M^{-1})
–	1.53 ± 0.04
Mg^{2+}	2.10 ± 0.17
K^{+}	1.91 ± 0.13
Ca^{2+}	1.69 ± 0.08
Mn^{2+}	1.08 ± 0.09
Cu^{2+}	1.02 ± 0.07
Zn^{2+}	1.16 ± 0.10
Ba^{2+}	0.79 ± 0.08

4.3.9 Location of GEF binding site

Both competitive ligand displacement experiments with site markers and molecular docking analysis were employed to probe the preferred location of the GEF binding site on HSA.

4.3.9.1 GEF-induced site marker displacement

Three site markers, used to investigate the preferred location of the GEF binding site on HSA were IDM, KTN and HMN for sites I, II and III, respectively. The titration results of HSA and site marker (IDM / KTN / HMN)–HSA (1:1) mixture with increasing concentrations (0–50 μM with 5 μM intervals) of GEF are shown in Figures 4.41–4.43. Whereas, a gradual decrease in the fluorescence intensity at 343 nm ($FI_{343\ nm}$) of HSA and site marker-HSA mixtures was observed with increasing concentrations of GEF, relatively lesser decrease was noticed with site marker-bound HSA compared to free HSA. A comparison of the quenching patterns observed with site marker–HSA mixtures showed greater difference in between the extents of GEF-induced quenching in the fluorescence intensity of HSA and HMN–HSA mixture (Figure 4.43), compared to that produced by IDM–HSA (Figure 4.41) or KTN–HSA (Figure 4.42) mixtures. Therefore, HMN appeared to offer significant resistance against GEF-induced quenching of HSA fluorescence (Figure 4.43), thus, implying site III as the preferred binding locus of GEF on HSA.

Treatment of the fluorescence quenching titration results of HSA and its complexes with different site markers with increasing GEF concentrations (Figures 4.41–4.43) according to Eq. (5) yielded the double logarithmic plots, as shown in Figure 4.44. In order to compare the influence of site markers on the binding of GEF to HSA, values of K_a, obtained in the absence and presence of site markers (IDM / KTN / HMN) were determined. As can be seen from the Table 4.15, decrease in the K_a value for GEF–HSA interaction was significantly higher in the presence of HMN, compared to that observed

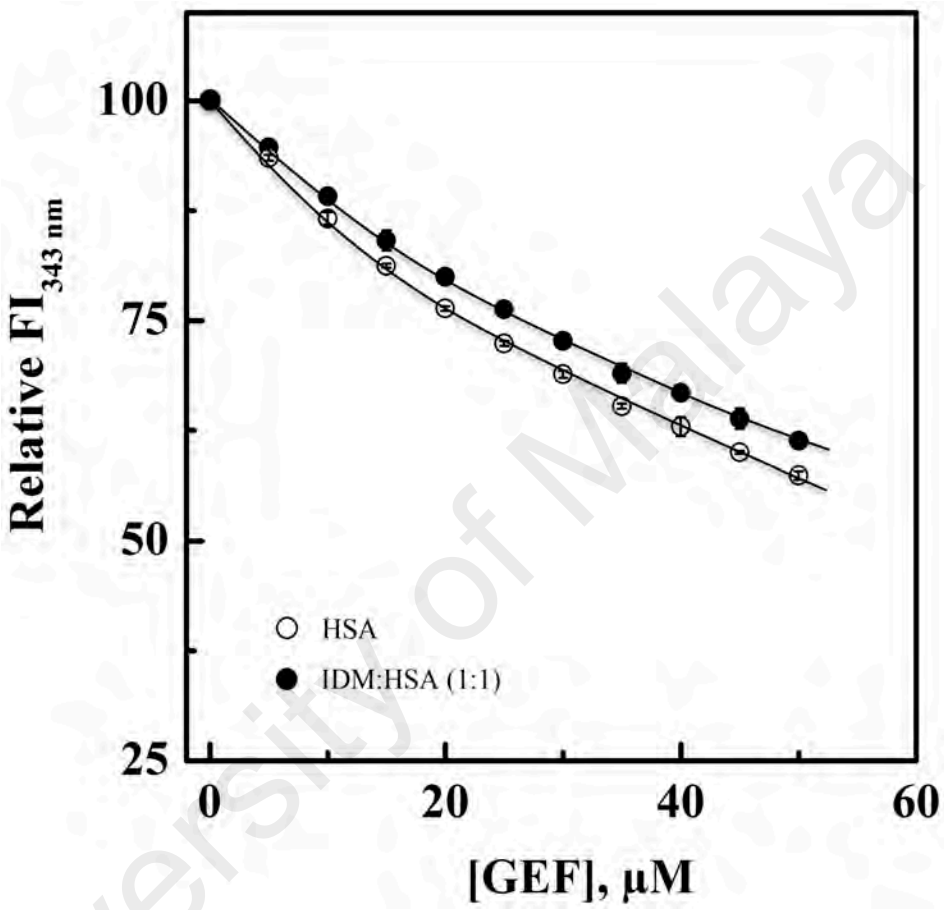

Figure 4.41: Plots showing the decrease in the relative fluorescence intensity at 343 nm ($FI_{343\ nm}$) of HSA (3 μM) and IDM–HSA (1:1) mixture with increasing concentrations (0–50 μM with 5 μM intervals) of GEF. The experiments were carried out in 60 mM sodium phosphate buffer, pH 7.4 at 298 K.

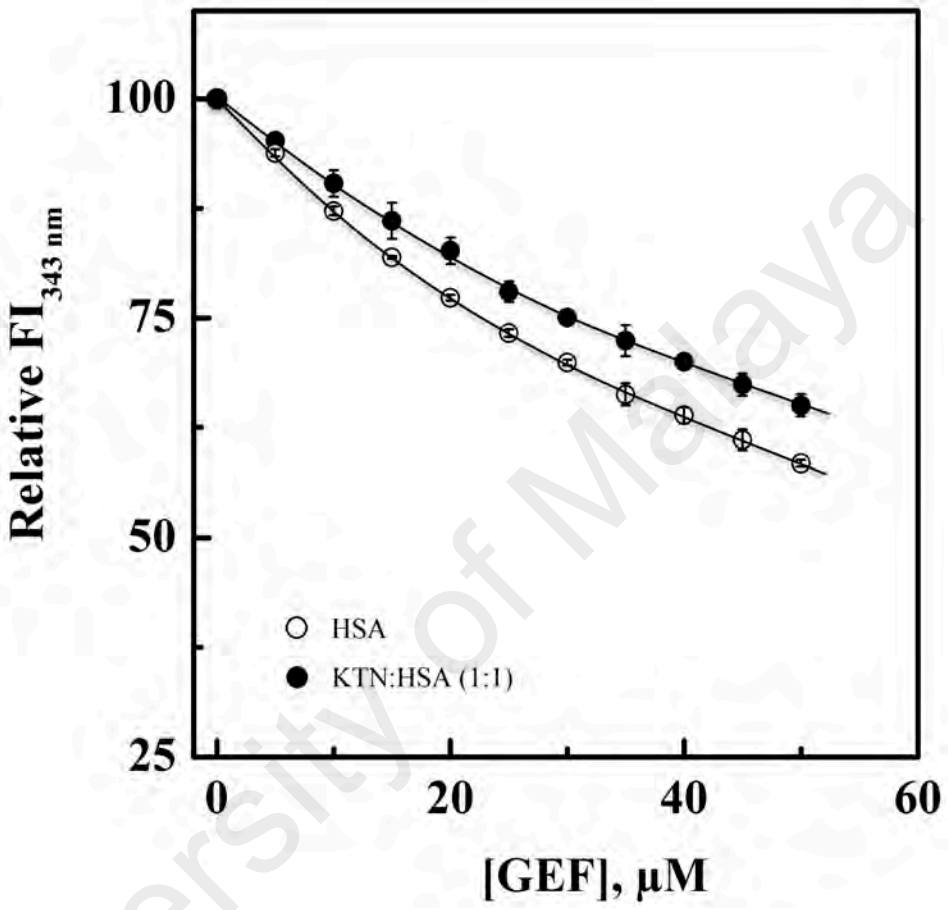

Figure 4.42: Plots showing the decrease in the relative fluorescence intensity at 343 nm ($FI_{343\ nm}$) of HSA (3 μM) and KTN–HSA (1:1) mixture with increasing concentrations (0–50 μM with 5 μM intervals) of GEF. The experiments were carried out in 60 mM sodium phosphate buffer, pH 7.4 at 298 K.

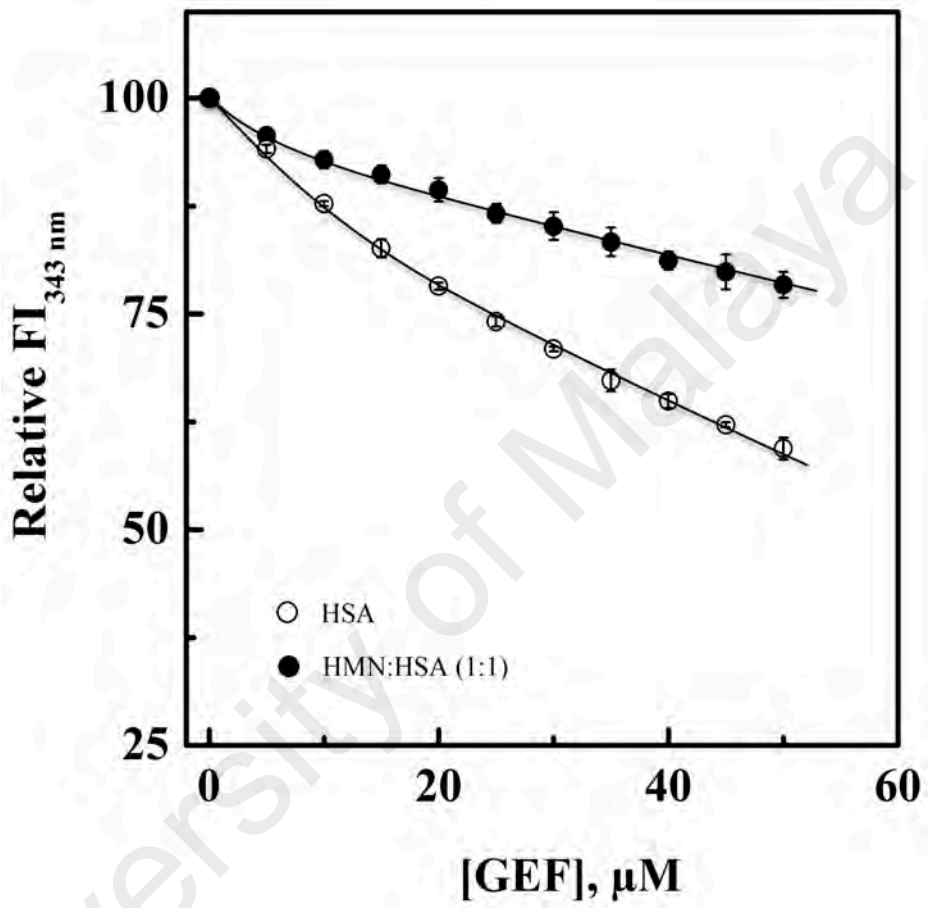

Figure 4.43: Plots showing the decrease in the relative fluorescence intensity at 343 nm ($FI_{343\ nm}$) of HSA (3 μM) and HMN–HSA (1:1) mixture with increasing concentrations (0–50 μM with 5 μM intervals) of GEF. The experiments were carried out in 60 mM sodium phosphate buffer, pH 7.4 at 298 K.

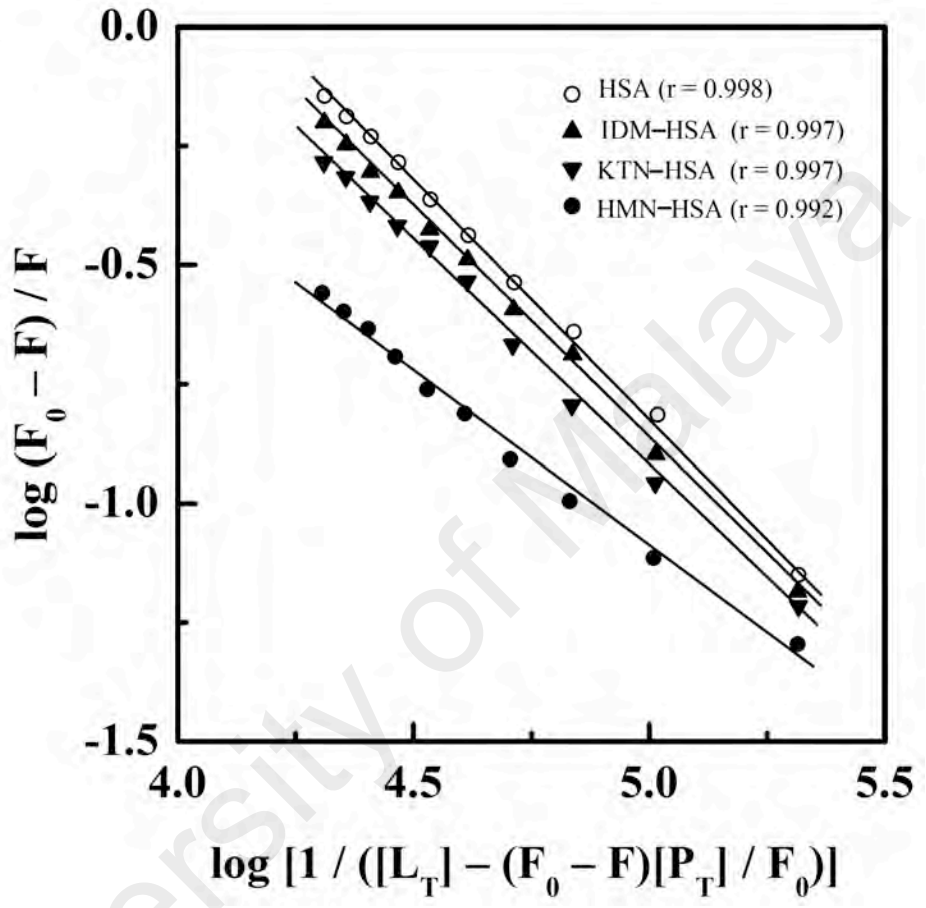

Figure 4.44: Double logarithmic plots of [log ($F_0 - F$) / F versus log [1 / ([L_T] – [(F_0 – F)[P_T] / F_0)] for the fluorescence quenching data of the GEF–HSA system in the absence and presence of different site markers, *i.e.*, IDM, KTN and HMN, obtained in 60 mM sodium phosphate buffer, pH 7.4 at 298 K (Figures 4.41–4.43).

Table 4.15: K_a values of GEF–HSA interaction in the absence and presence of site markers, obtained at 298 K, pH 7.4.

Site Marker	K_a ($\times 10^4$ M^{-1})
–	1.53 ± 0.04
IDM	1.35 ± 0.08
KTN	1.10 ± 0.07
HMN	0.29 ± 0.03

with KTN / IDM-bound HSA. In other words, presence of HMN, which is known to bind to site III, located in subdomain IB, significantly affected the binding of GEF to HSA. These results clearly suggested site III as the preferred GEF binding site on HSA. Furthermore, these results were in line with our molecular docking analysis, as discussed in the Section 4.3.9.2.

4.3.9.2 Molecular docking analysis

Computational modeling analysis allows elucidation of the most favored binding mode of the ligand to the binding site at atomic resolution. In docking analysis, GEF was set to be flexible with 8 torsional degrees of freedom due to rotatable bonds. Estimated free energy of binding was computed for each binding mode based on a semi-empirical force field with evaluated energy terms such as electrostatic interaction, torsional entropy, hydrophobic interaction and others. A comparison of the binding modes in three binding sites showed more favorable binding of GEF to site III (Figure 4.45). As shown in Figure 4.45, 10 clusters constituted by 40 out of 100 binding modes exhibited mean binding energy lower than – 29.3 kJ mol^{-1} in binding site III. However, most of the binding mode clusters in binding sites I and II possessed mean binding energy > – 29.3 kJ mol^{-1}. Therefore, the binding site III of HSA was the preferred binding site of GEF, as suggested by cluster analysis.

The best-scored binding mode from the cluster with the lowest binding energy in the binding site III was selected for subsequent analyses (Figure 4.46). The binding energy of the GEF docked to the binding site III was computed to be at – 36.4 kJ mol^{-1}. At the binding site III, GEF docked to a hydrophobic pocket walled by 21 amino acid residues within 5 Å: Leu-115, Val-116, Arg-117, Pro-118, Met-123, Phe-134, Lys-137, Tyr-138, Glu-141, Ile-142, His-146, Phe-149, Phe-157, Tyr-161, Lys-181, Leu-182, Asp-183, Leu-185, Arg-186, Gly-189 and Lys-190. Hydrophobic interactions would be a major factor that stabilize the complex of GEF–HSA through Phe-134, Tyr-138, Leu-182 and

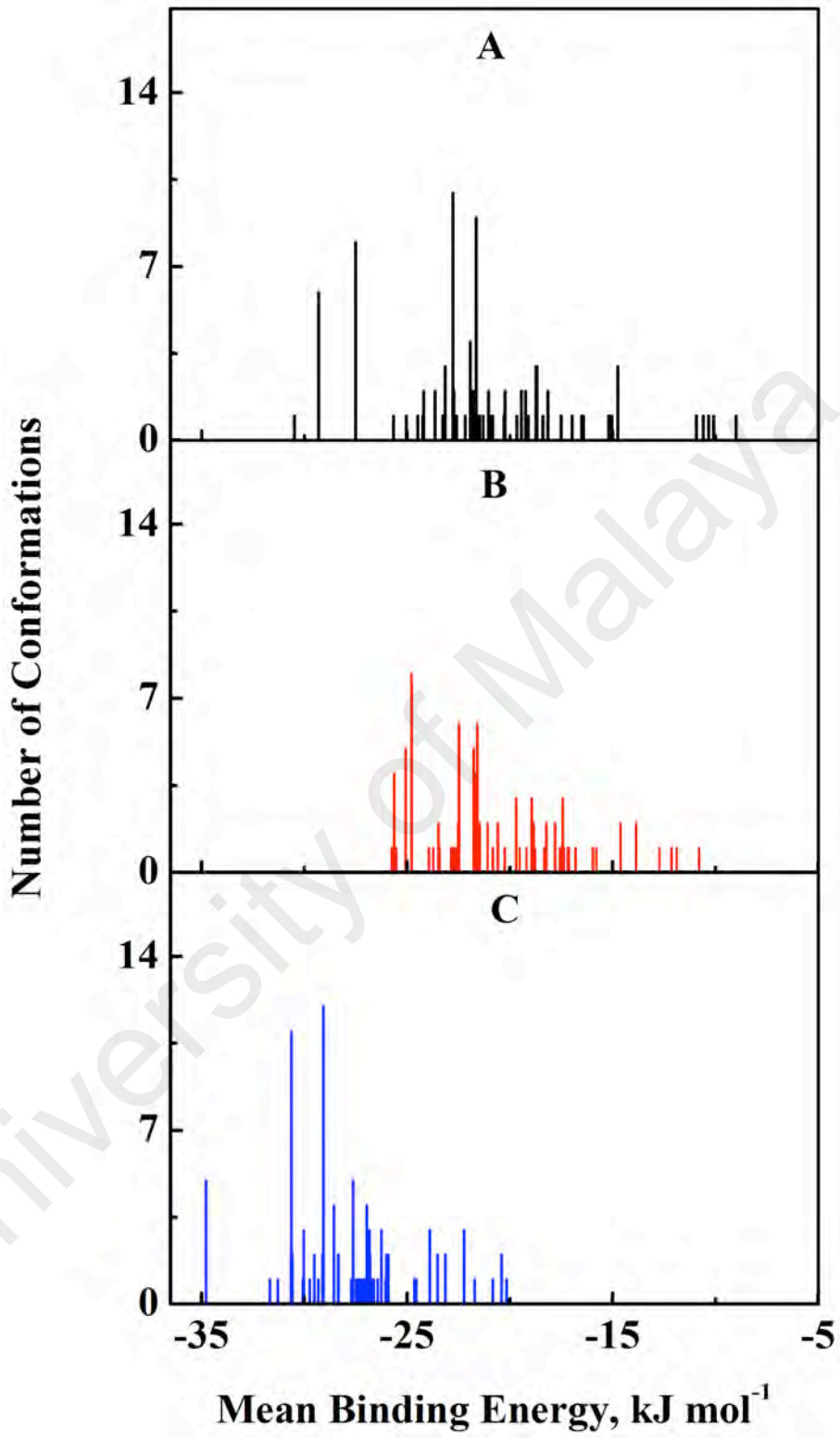

Figure 4.45: Cluster analysis of the docking of GEF to three different binding sites, *viz.*, I (A), II (B) and III (C) of HSA crystal structure (1BM0). The results were obtained from a total of 100 runs for each binding site.

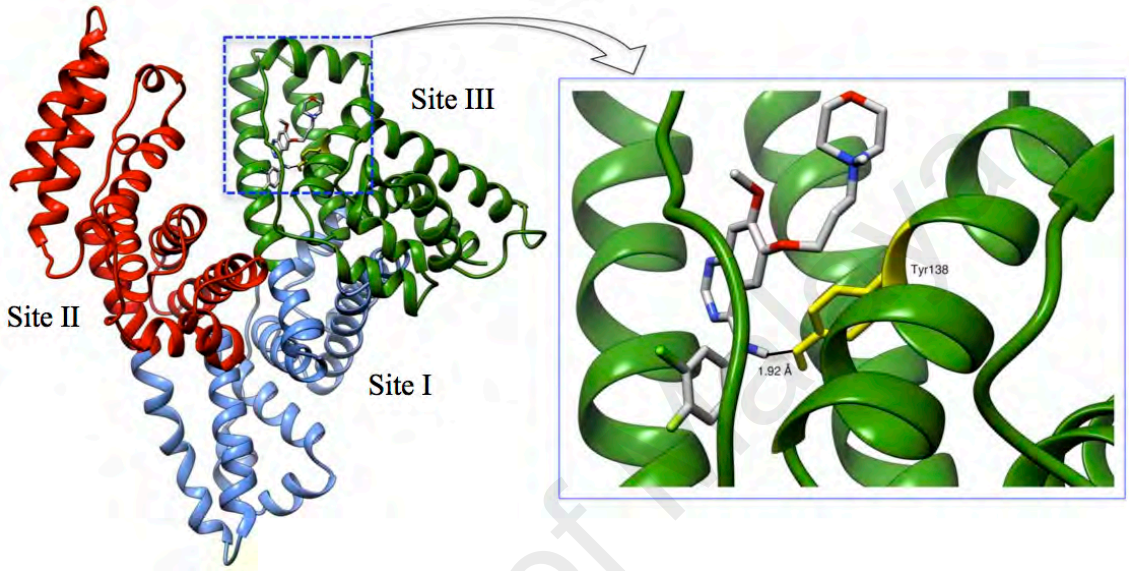

Figure 4.46: Predicted binding orientation of the lowest docking energy conformation of GEF (rendered in sticks) in the binding site III (subdomain IB) of HSA (1BM0). Different domains of HSA, namely, I, II and III are shown in green, sky blue and red, respectively. The enlarged view shows the hydrogen bond (black line) formed between GEF and side chain of Tyr-138 (rendered in yellow stick).

Leu-185 in proximity (Figure 4.47). However, the interaction between GEF and HSA cannot be presumed to be exclusively hydrophobic in nature; as there were several polar residues in the proximity of the bound ligand that may participate in polar interactions with the hydrophilic groups of GEF. One hydrogen bond was predicted between hydroxyl group of Tyr-138 and amine group of GEF with bond distance of 1.92 Å (Figure 4.46). Therefore, our docking simulation predicted the binding preference of GEF for the binding site III, located in subdomain IB of HSA, involving both hydrophobic interactions and hydrogen bonds in the GEF–HSA complex formation. Some of the molecular modeling results are not comprehensively visible using LigPlot+. Therefore, mesh surface representation of GEF and amino acid residues of HSA are presented for GEF–HSA interaction. These docking results were consistent with our competitive site marker displacement results as shown in Section 4.3.9.1.

In conclusion, molecular characterization of the binding of GEF to HSA was made in terms of the binding affinity (K_a = 1.43 × 10^4 M^{-1} at 25 ^oC), thermodynamic data (ΔH = –7.74 kJ mol^{-1} and ΔS = +54.06 J mol^{-1} K^{-1}), interaction forces involved (hydrophobic interactions and hydrogen bonds), change in the protein's secondary and tertiary structures as well as microenvironmental perturbations around protein fluorophores upon drug binding. GEF binding to HSA improved thermal stability of the protein and site III (subdomain IB) was identified as the GEF binding site on HSA. A few common ions were also found to interfere with the GEF–HSA interaction.

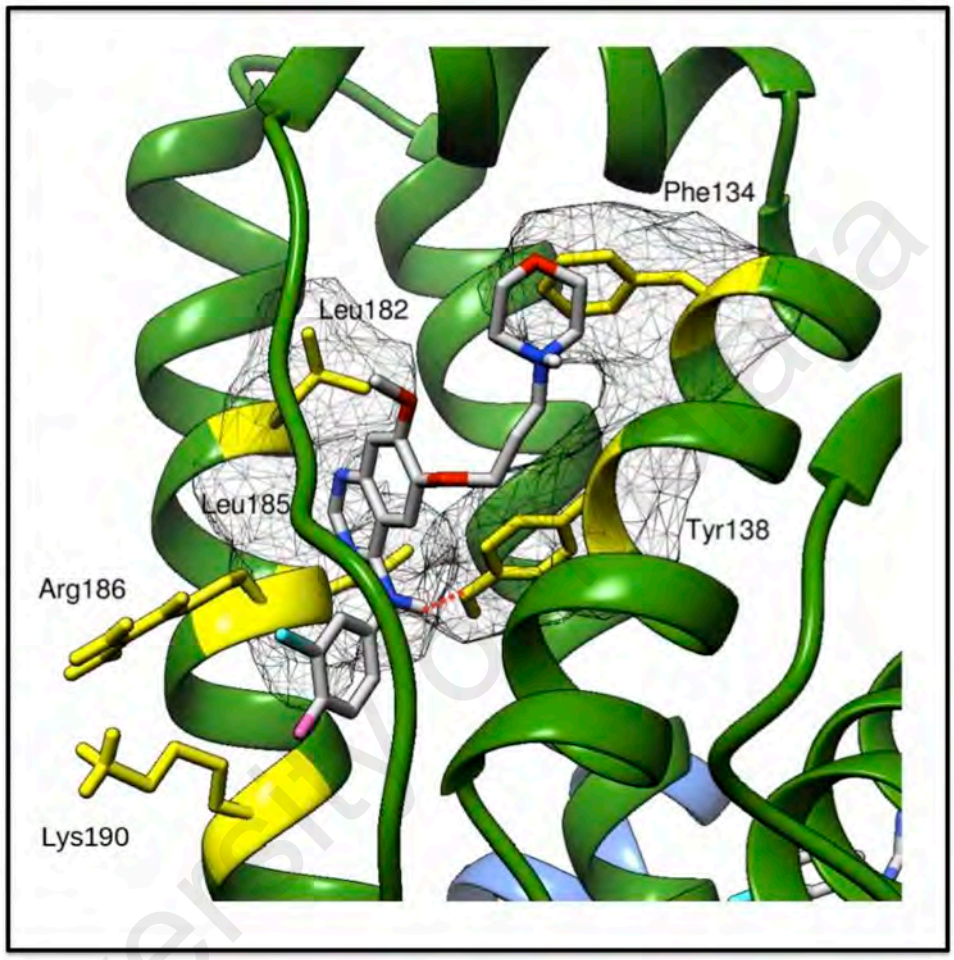

Figure 4.47: Mesh surface representation of GEF and the amino acid residues of HSA with their molecular surface at binding site III. The residues indicate the presence of hydrophobic interactions with GEF (colored in yellow). Hydrogen bond of GEF and HSA is rendered with dashed red line.

4.4 SU–HSA interaction

Fluorescence spectroscopy was also employed to study the binding of another tyrosine kinase inhibitor, SU to HSA.

4.4.1 Fluorescence spectra

Figure 4.48 shows the fluorescence spectra of HSA in the absence and presence of increasing SU concentrations. Appearance of the emission maximum at 343 nm in the fluorescence spectrum of HSA due to Trp-214 and gradual loss in the fluorescence intensity at 343 nm upon addition of increasing SU concentrations characterized the titration results. No significant shift in the emission maximum was noticed throughout the titration. Such decrease in the fluorescence intensity of HSA upon SU addition might be occurred as a result of microenvironmental perturbations around Trp-214, which seems possible due to SU–HSA complexation. Similar to GEF–HSA titration results, ~ 45 % quenching in the fluorescence intensity at 343 nm was observed at 24 μM SU (inset of Figure 4.48). Free SU did not produce any significant fluorescence in this wavelength range (Figure 4.48). Several earlier reports have shown similar fluorescence characteristics of HSA upon drug binding (Lv et al., 2013; Matei & Hillebrand, 2010).

4.4.2 Mechanism of fluorescence quenching

The quenching mechanism involved in the SU–HSA system was probed by treating the fluorescence quenching data, obtained at three different temperatures, *i.e.*, 288 K (Figure 4.48), 298 K and 308 K (Figure 4.48S) with the help of the Stern-Volmer equation (Eq. (3)). The plots of F_0 / F and SU concentrations for SU–HSA system, thus obtained, exhibited good linearity with a correlation coefficient (r) of ≥ 0.997 (Figure 4.49). Table 4.16 summarizes the K_{SV} values at different temperatures, as obtained from the slope of the Stern–Volmer plots. Involvement of the static quenching mechanism in SU–HSA system was evident from the decrease in the K_{SV} value with increasing

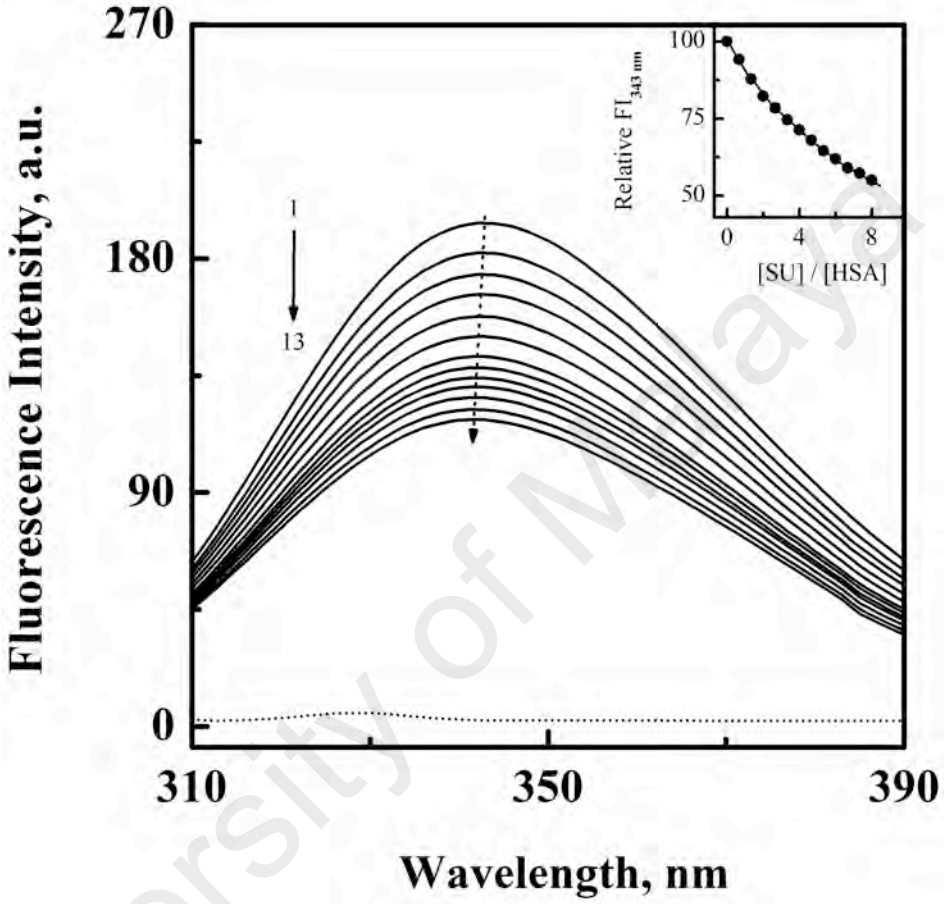

Figure 4.48: Fluorescence spectra of HSA (3 μM) in the absence (spectrum 1) and presence (spectra 2–13) of increasing SU concentrations (2–24 μM with 2 μM intervals), obtained in 60 mM sodium phosphate buffer, pH 7.4 at 288 K upon excitation at 295 nm. The fluorescence spectrum of free SU (24 μM) is shown with dotted line. The inset shows the decrease in the relative fluorescence intensity of HSA at 343 nm ($FI_{343\ nm}$) with increasing SU/HSA molar ratios.

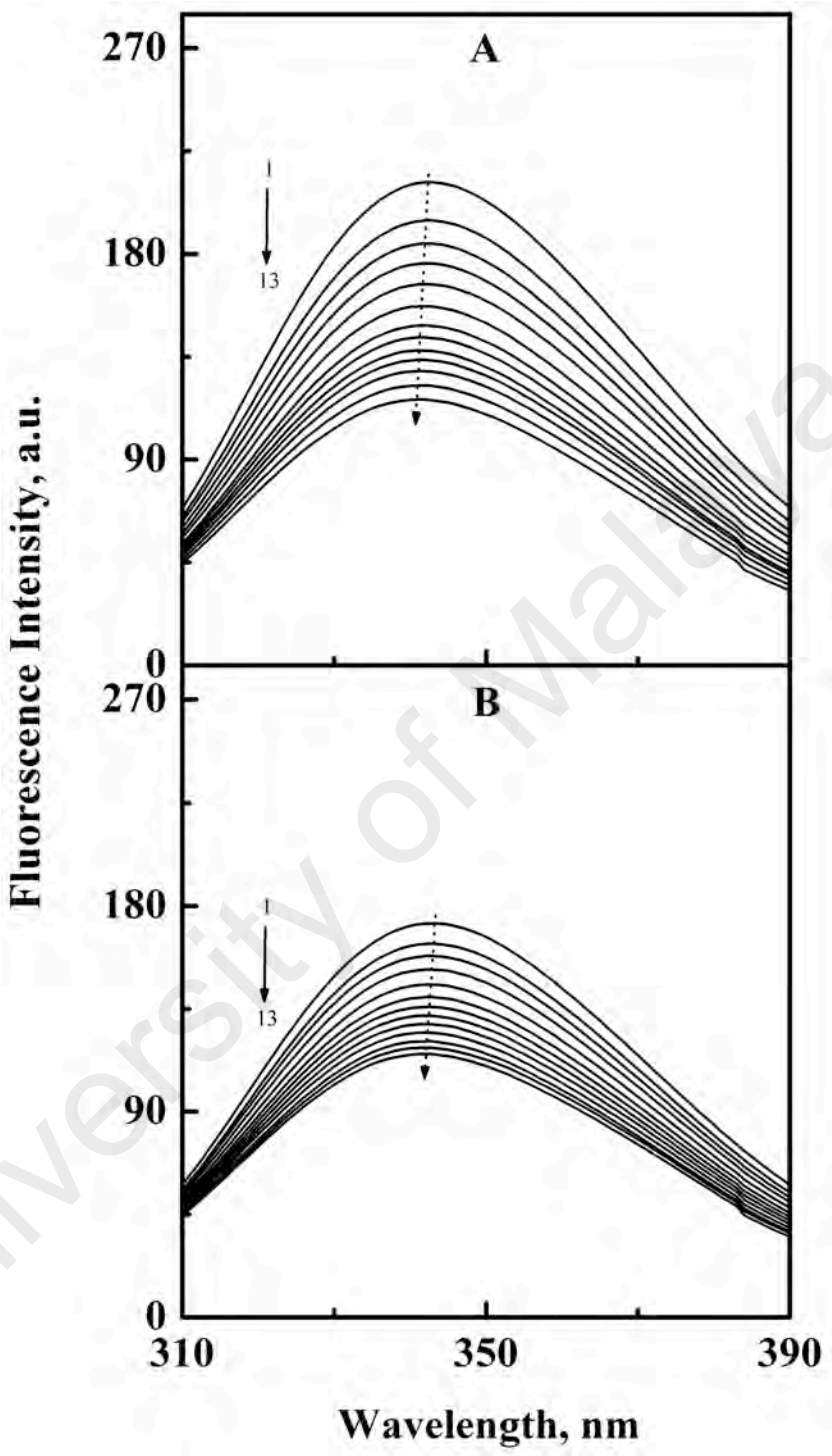

Figure 4.48 S: Fluorescence spectra of HSA (3 μM) in the absence (spectrum 1) and presence (spectra 2–13) of increasing SU concentrations (2–24 μM with 2 μM intervals), obtained in 60 mM sodium phosphate buffer, pH 7.4 at (A) 298 K and (B) 308 K upon excitation at 295 nm.

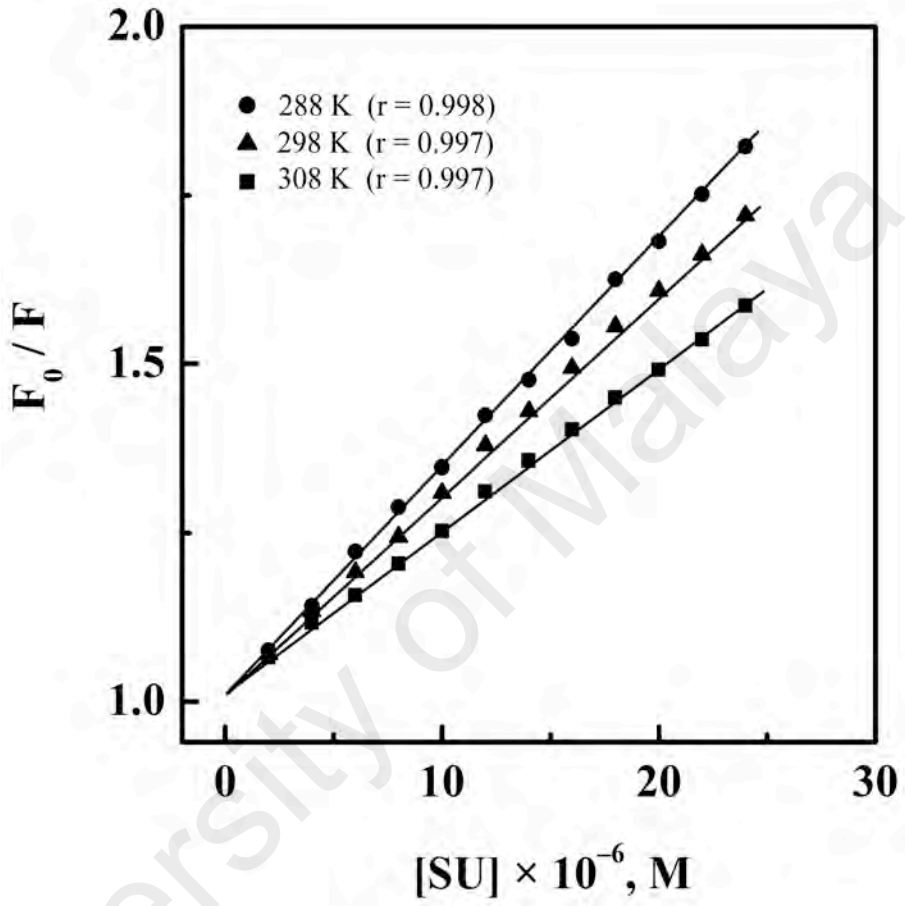

Figure 4.49: Stern-Volmer plots for the fluorescence quenching data of the SU–HSA system, obtained at three different temperatures, *i.e.*, 288 K, 298 K and 308 K.

Table 4.16: Quenching and binding parameters for SU–HSA interaction, studied at three different temperatures, pH 7.4.

T (K)	K_{SV} (M^{-1})	k_q (M^{-1} s^{-1})	K_a (M^{-1})
288	$(3.35 \pm 0.06) \times 10^4$	$(5.25 \pm 0.13) \times 10^{12}$	$(3.53 \pm 0.12) \times 10^4$
298	$(2.94 \pm 0.03) \times 10^4$	$(4.61 \pm 0.09) \times 10^{12}$	$(3.04 \pm 0.08) \times 10^4$
308	$(2.37 \pm 0.05) \times 10^4$	$(3.71 \pm 0.12) \times 10^{12}$	$(2.41 \pm 0.10) \times 10^4$

temperature (Table 4.16) and therefore, suggested complex formation between SU and HSA. Besides, calculation of k_q (obtained at three different temperatures using Eq. (4) for SU–HSA system) from the K_{SV} values also supported the formation of SU–HSA complex, as the k_q values had fallen in the order of 10^{12} (Table 4.16). These values of k_q (Table 4.16) were higher than the value of the maximum dynamic quenching constant (2×10^{10} M^{-1} s^{-1}) reported for various quencher–fluorophore systems (Ware, 1962). Several earlier reports have characterized the ligand-induced quenching of HSA fluorescence as the static quenching mechanism (He et al., 2016; Tunc et al., 2014; Amina et al., 2016).

4.4.3 Binding affinity

Analysis of the fluorescence quenching data for SU–HSA system was made according to Eq. (5) and the resulting plots between $log\ (F_0 - F) / F$ and $log\ [1 / ([L_T] - [(F_0 - F)[P_T] / F_0)]$ for SU–HSA system at three different temperatures are displayed in Figure 4.50. Values of K_a, as obtained from these plots at three different temperatures are given in the last column of Table 4.16. A moderate binding affinity between SU and HSA was reflected from the K_a values, which were found to be in the range, 3.53–2.41 $\times$ 10^4 M^{-1}. Such binding affinity seems relevant for the efficient transfer of the drug to its specific target site through blood circulation. Several published reports have shown moderate binding affinity between various drugs and HSA (Bourassa et al., 2011; Liu et al., 2015; Rastegari et al., 2016). The decrease in the K_a value with increasing temperature (Table 4.16) seems understandable, as higher temperature might have weakened noncovalent interactions, required for the stabilization of SU–HSA complex (Stickle et al., 1992).

4.4.4 Interaction forces

Values of the thermodynamic parameters, ΔH and ΔS for SU–HSA interaction were

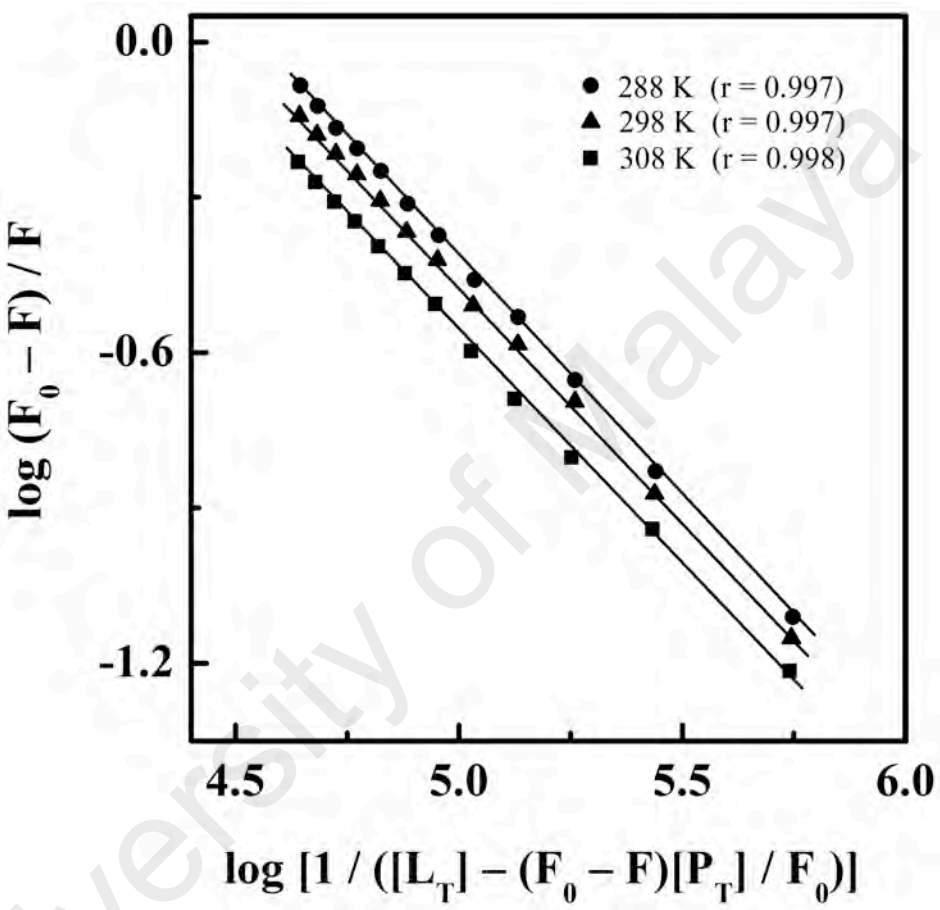

Figure 4.50: Double logarithmic plots of [log ($F_0 - F$) / F versus log [1 / ([L_T] – [(F_0 – F)[P_T] / F_0)] for the fluorescence quenching data of the SU–HSA system, obtained at three different temperatures, *i.e.*, 288 K, 298 K and 308 K.

determined from the van't Hoff plot between *ln Ka* and *1/T* (Figure 4.51), while the values of Δ*G* at three different temperatures were calculated by substituting these values into Eq. (7). Table 4.17 shows the values of thermodynamic parameters, thus obtained for SU–HSA interaction. The complex formation between SU and HSA was found to be an exothermic and feasible process, as reflected from the negative values of Δ*H* and Δ*G*, respectively (Ross & Subramanian, 1981). Since both hydrophobic and electrostatic interactions are drivened by entropy effect (Ross & Subramanian, 1981), a positive value of Δ*S* for SU–HSA system (Table 4.17) was suggestive of the involvement of hydrophobic interactions, as absence of any charged group in SU excluded the contribution of electrostatic interactions in SU–HSA complexation. The negative Δ*H* value (Table 4.17) pointed towards the participation of hydrogen bonds and van der Waals interactions in the SU–HSA complex formation (Ross & Subramanian, 1981). It seems reasonable to believe the participation of hydrophobic and van der Waals interactions along with hydrogen bonds in the binding of SU to HSA, as SU contains both polar groups (–NH and O) and hydrophobic groups (Figure 2.8).

4.4.5 Absorption spectra

UV-vis absorption spectral characteristics of HSA in the absence and presence of increasing SU concentrations were studied to probe the formation of the complex between SU and HSA. The UV-vis absorption spectra of HSA in the presence of increasing concentrations (2–24 μM with 2 μM intervals) of SU (Figure 4.52) were obtained after subtracting the absorption contribution of the pure SU solutions (Figure 4.52S(B)) from the spectra of respective SU–HSA mixtures (Figure 4.52S(A)). Whereas absorption spectrum of HSA (spectrum 1) was characterized by the absorption maximum at 278 nm, an increase in the absorbance at 278 nm was noted with subsequent addition of SU (spectra 2–13). Such increase in the absorbance value clearly

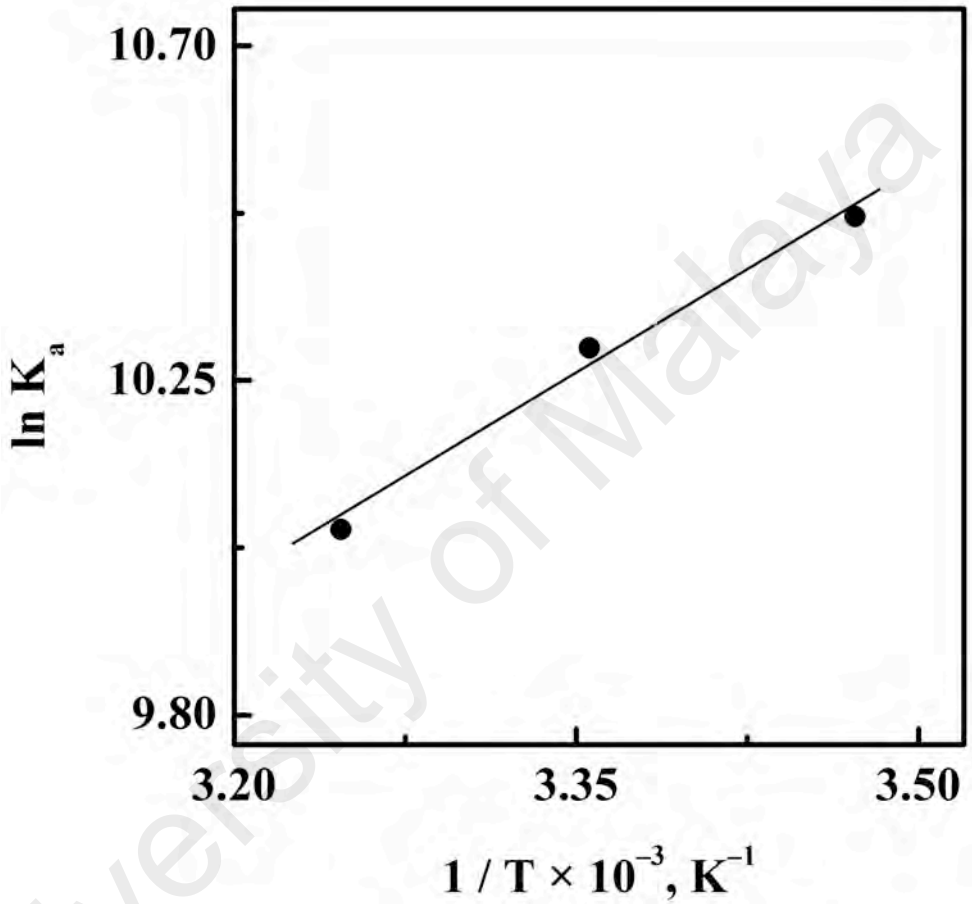

Figure 4.51: The van't Hoff plot for SU–HSA interaction. Values of K_a were obtained from the double logarithmic plots, displayed in Figure 4.50.

Table 4.17: Thermodynamic parameters for SU–HSA interaction, studied at three different temperatures, pH 7.4.

T (K)	ΔS (J mol^{-1} K^{-1})	ΔH (kJ mol^{-1})	ΔG (kJ mol^{-1})
288			– 25.13
298	+ 33.63	– 15.44	– 25.46
308			– 25.80

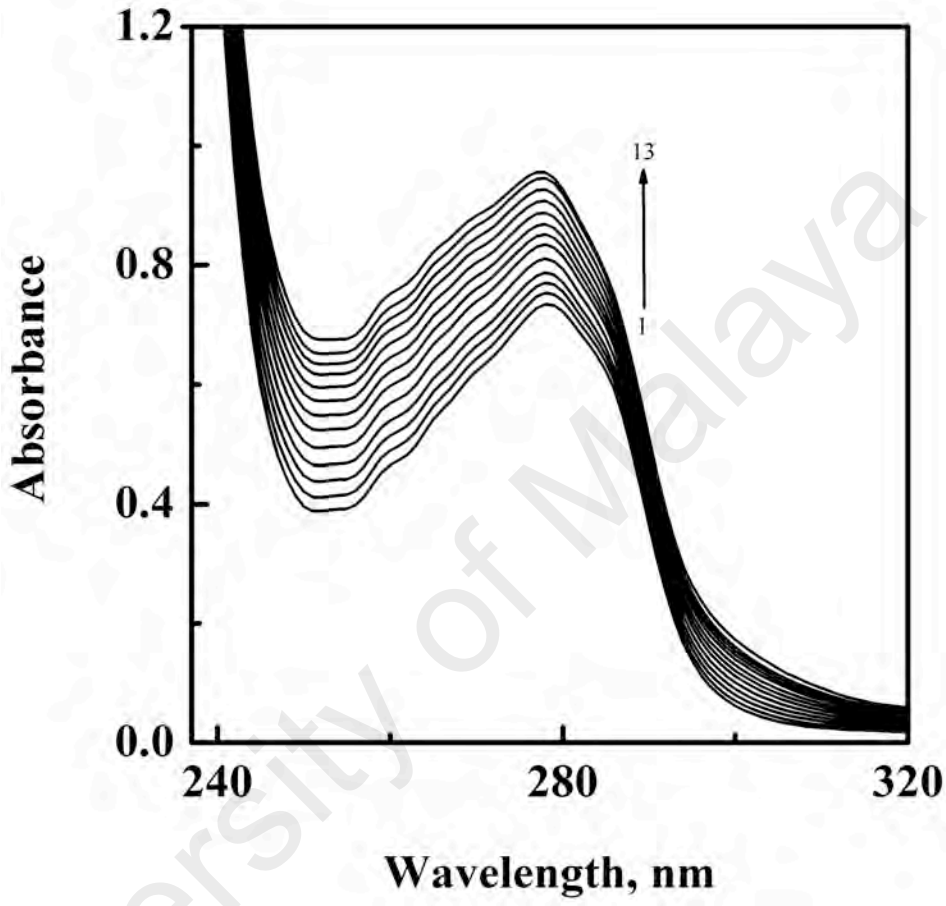

Figure 4.52: UV-vis absorption spectra of HSA (20 μM) in the absence (spectrum 1) and presence (spectra 2–13) of increasing SU concentrations (2–24 μM with 2 μM intervals), obtained in 60 mM sodium phosphate buffer, pH 7.4 at 298 K. The spectra (2–13) were obtained by subtracting the absorption contribution of respective free SU from the absorption spectra of SU–HSA mixtures.

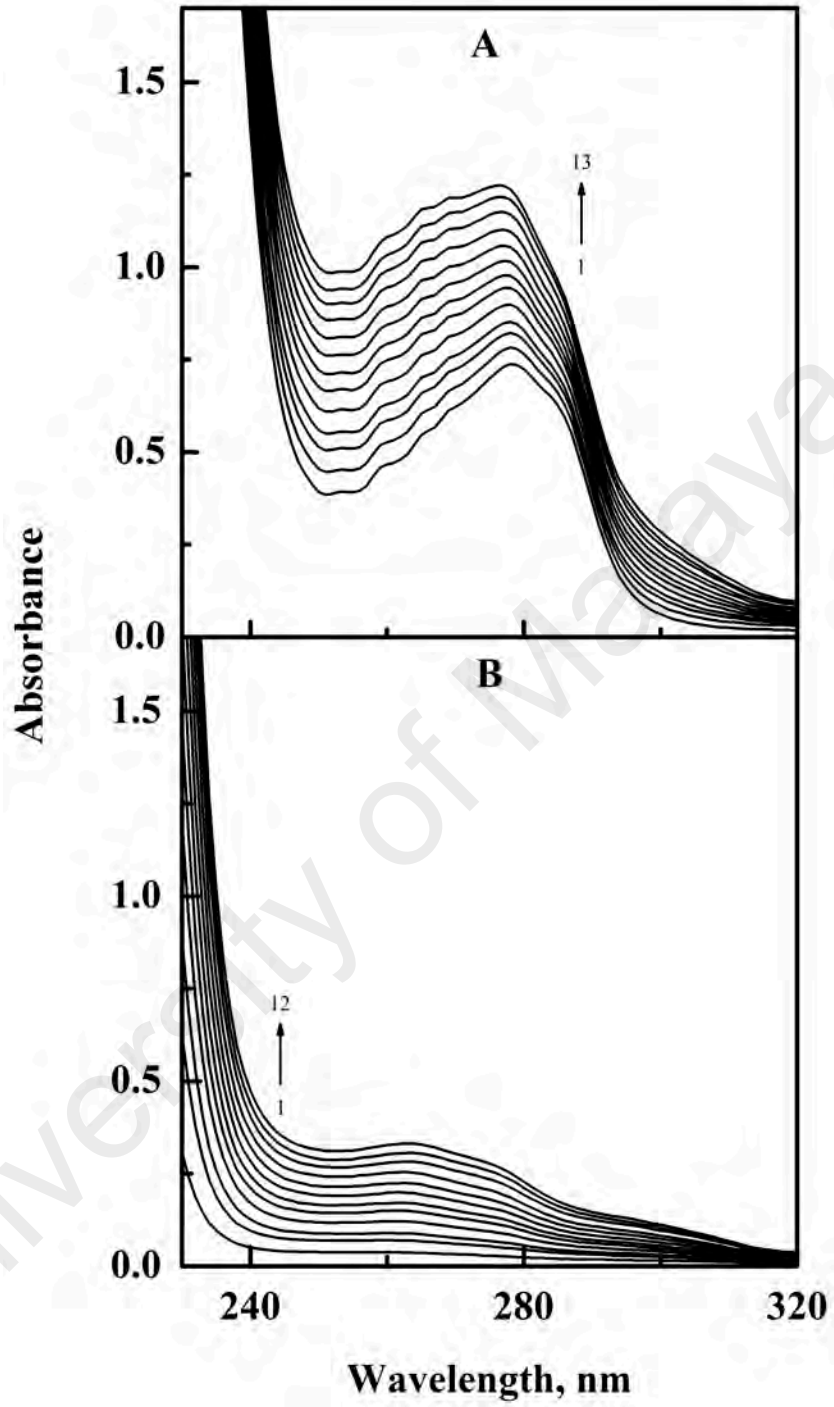

Figure 4.52 S: (A) Uncorrected UV-vis absorption spectra of HSA (20 μM) in the absence (spectrum 1) and presence (spectra 2–13) of increasing SU concentrations (2–24 μM with 2 μM intervals), obtained in 60 mM sodium phosphate buffer, pH 7.4 at 298 K. (B) The spectra (1–12) were obtained with increasing SU concentrations (2–24 μM with 2 μM intervals).

indicated perturbations in the microenvironment around protein chromophores, which seems possible upon binding of SU to HSA. Therefore, UV-vis results clearly suggested complex formation between SU and HSA and supported the fluorescence results, described above in Section 4.4.2.

4.4.6 SU-induced structural / microenvironmental changes in HSA

The possible effects of SU binding on the secondary and tertiary structures of HSA were studied using far-UV and near-UV CD spectra, respectively. On the other hand, microenvironmental perturbations around HSA fluorophores (Trp and Tyr) upon SU binding were probed by 3-D fluorescence spectra.

4.4.6.1 Far-UV and near-UV CD spectra

SU-induced alterations in the secondary and tertiary structures of the protein were checked from the far-UV and the near-UV CD spectral analysis of HSA, both in the absence and presence of SU ([SU]:[HSA] = 1:1). Presence of two minima at 208 nm and 222 nm in the far-UV CD spectrum of HSA and lower magnitude of MRE values at these wavelengths in the presence of SU (Figure 4.53) clearly reflected decrease in the α-helical content of the protein upon SU binding (Goormaghtigh et al., 1990; Bozoglan et al., 2014). Therefore, SU–HSA complex formation seems to induce secondary structural alterations in the protein.

The near-UV CD spectrum of HSA (Figure 4.54) was characterized by the presence of two negative bands at ~ 263 nm and ~ 268 nm and two shoulders at ~ 279 nm and ~ 291 nm due to the presence of aromatic chromophores and disulfide bonds (Lee & Hirose, 1992). Presence of SU in the mixture altered the near-UV CD spectra, thus reflected changes in the tertiary structure of HSA.

Therefore, SU binding to HSA produced alterations in both secondary and tertiary structures of the protein.

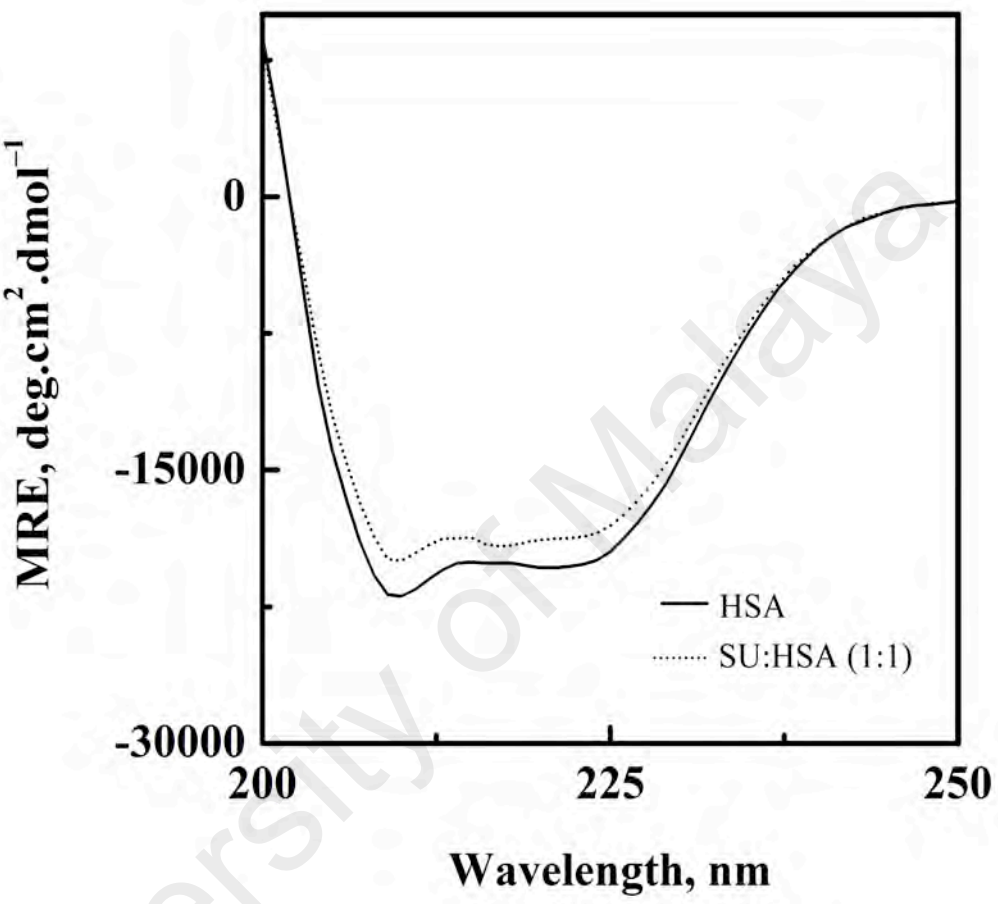

Figure 4.53: Far-UV CD spectra of HSA (3 μM) and SU–HSA (1:1) mixture. The CD spectra were recorded using a 1 mm path length cuvette, in 60 mM sodium phosphate buffer, pH 7.4 at 298 K.

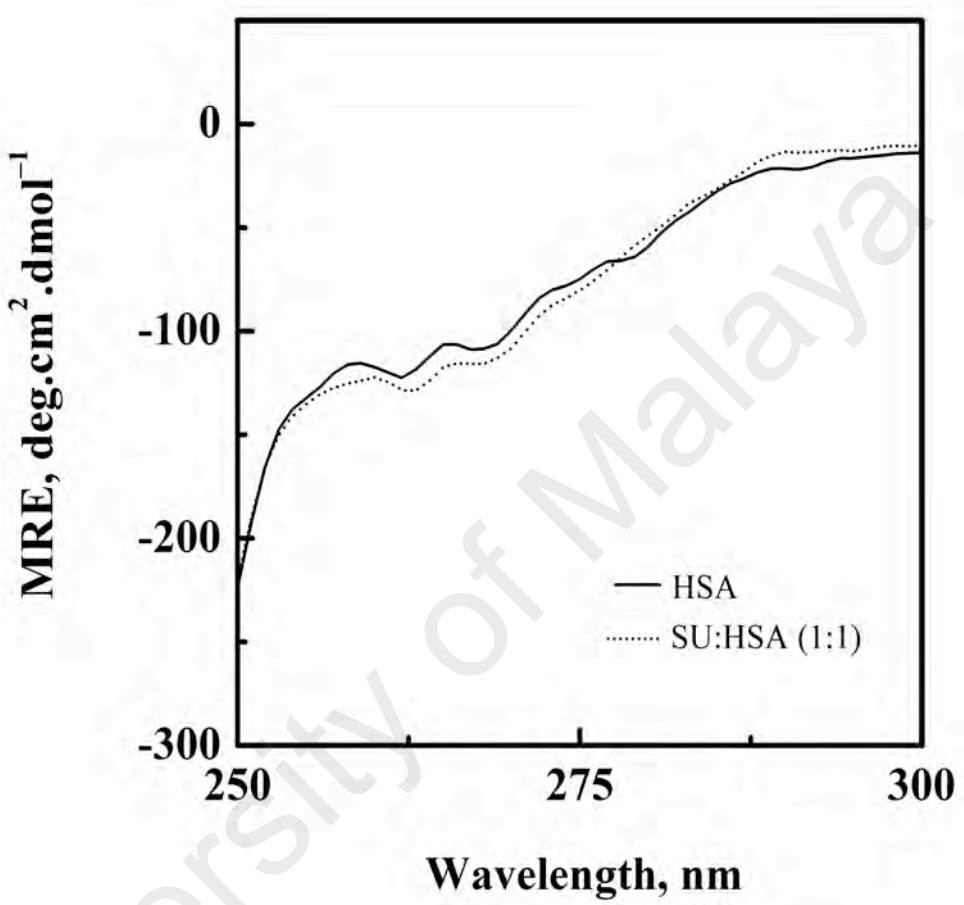

Figure 4.54: Near-UV CD spectra of HSA (9 μM) and SU–HSA (1:1) mixture. The CD spectra were recorded using a 10 mm path length cuvette, in 60 mM sodium phosphate buffer, pH 7.4 at 298 K.

4.4.6.2 Three-dimensional fluorescence spectra

In order to further explore the microenvironmental changes around protein's Tyr and Trp residues upon SU binding, 3-D fluorescence spectra of HSA were analyzed in the absence and presence of SU. Whereas, Figure 4.55 depicts the 3-D fluorescence spectra of HSA (A) and SU–HSA mixture ([SU]:[HSA] = 6:1) (B), their spectral characteristics are summarized in Table 4.18. As described in the Sections 4.1.6.2 and 4.2.6.2, in addition to two scattering peaks, namely, peak 'a' and peak 'b', two other peaks, marked as '1' and '2' represented the fluorescence spectral characteristics of Trp and Tyr residues of HSA. Quantitative evaluation of these peaks suggested ~ 48 % and ~ 83 % reduction in the fluorescence intensity of peaks '1' and '2', respectively, in the presence of SU (Table 4.18). Furthermore, 6 nm (peak '1') and 14 nm (peak '2') blue shifts were also noticed upon SU addition (Table 4.18). SU-induced micro-environmental perturbations around protein fluorophores were clearly seen from the spectral changes of these peaks, thus confirming SU–HSA complex formation.

4.4.7 Thermal stabilization of HSA

In view of the increased thermostability of proteins in the presence of their ligands (Celej et al., 2003; Flora et al., 1998; Pico, 1997), thermal stability of HSA was checked in SU–HSA mixture ([SU]:[HSA] = 4:1) in the temperature range, 298–353 K with 5 K intervals. Figure 4.56 shows thermal stability results of HSA in the absence and presence of SU, as monitored by fluorescence measurements at 343 nm. As can be seen from the figure, SU–HSA mixture produced higher fluorescence intensity at 343 nm, compared to HSA at each temperature, which suggested protein stabilization due to ligand binding. The difference in the fluorescence intensity of HSA and SU–HSA mixture became more marked at higher temperatures. Such stabilization of HSA might be ascribed to the additional forces, involved in SU–HSA complex formation as well as coupling between the binding and unfolding equilibria (Watanabe et al., 2001).

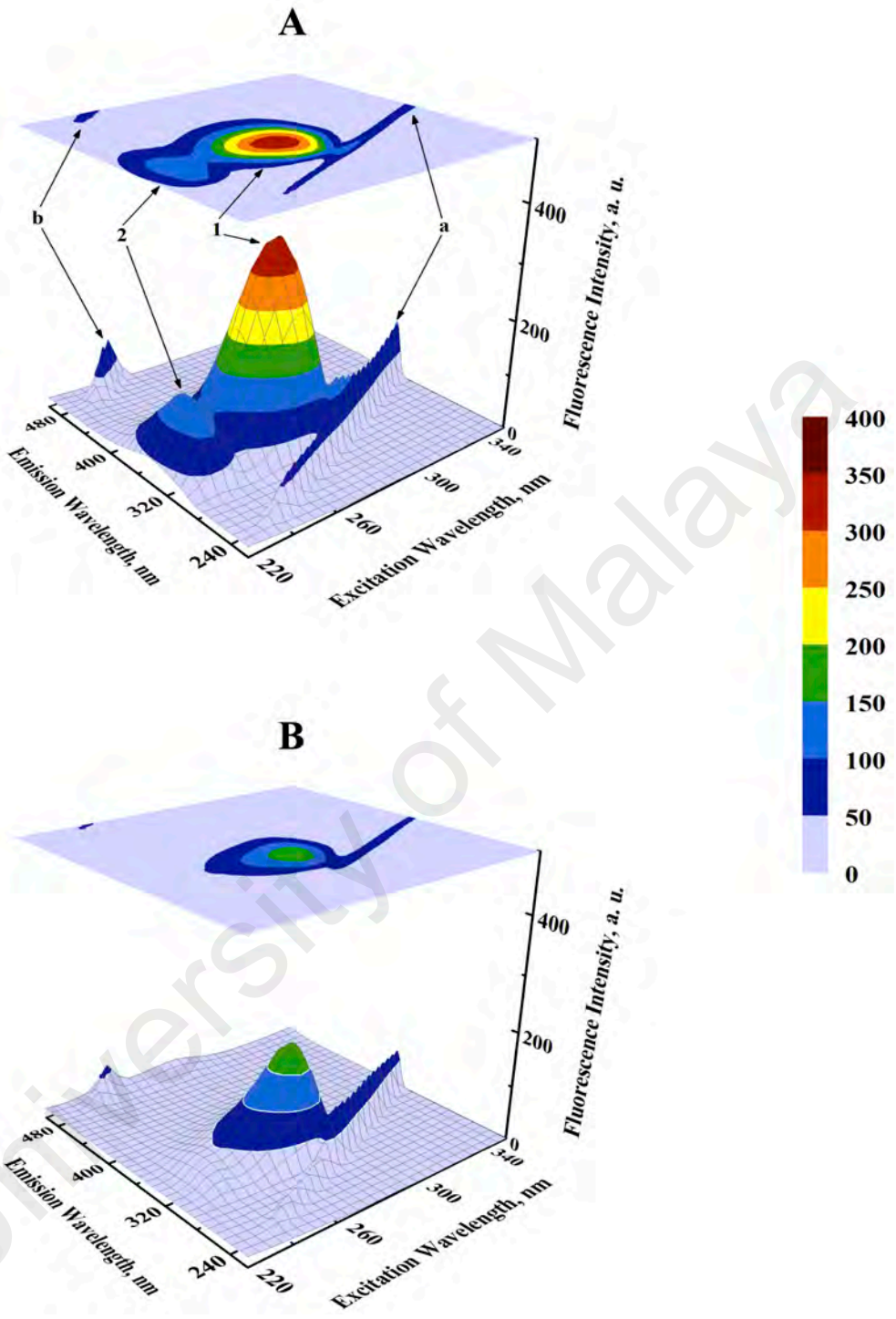

Figure 4.55: Three-dimensional fluorescence spectra and corresponding contour maps of (A) HSA (3 μM) and (B) SU–HSA (6:1) mixture. The spectra were recorded in 60 mM sodium phosphate buffer, pH 7.4 at 298 K.

Table 4.18: Three-dimensional fluorescence spectral characteristics of HSA (3 μM) and SU–HSA system at 298 K, pH 7.4.

System	Peak	Peak Position [λ_{ex} / λ_{em} (nm/nm)]	Intensity
HSA	a	230/230→350/350	17.7→105.6
	b	250/500	91.4
	1	280/337	351.7
	2	230/335	129.8
[SU]:[HSA] = 6:1	a	230/230→350/350	15.0→68.8
	b	250/500	62.7
	1	280/331	182.6
	2	230/321	22.7

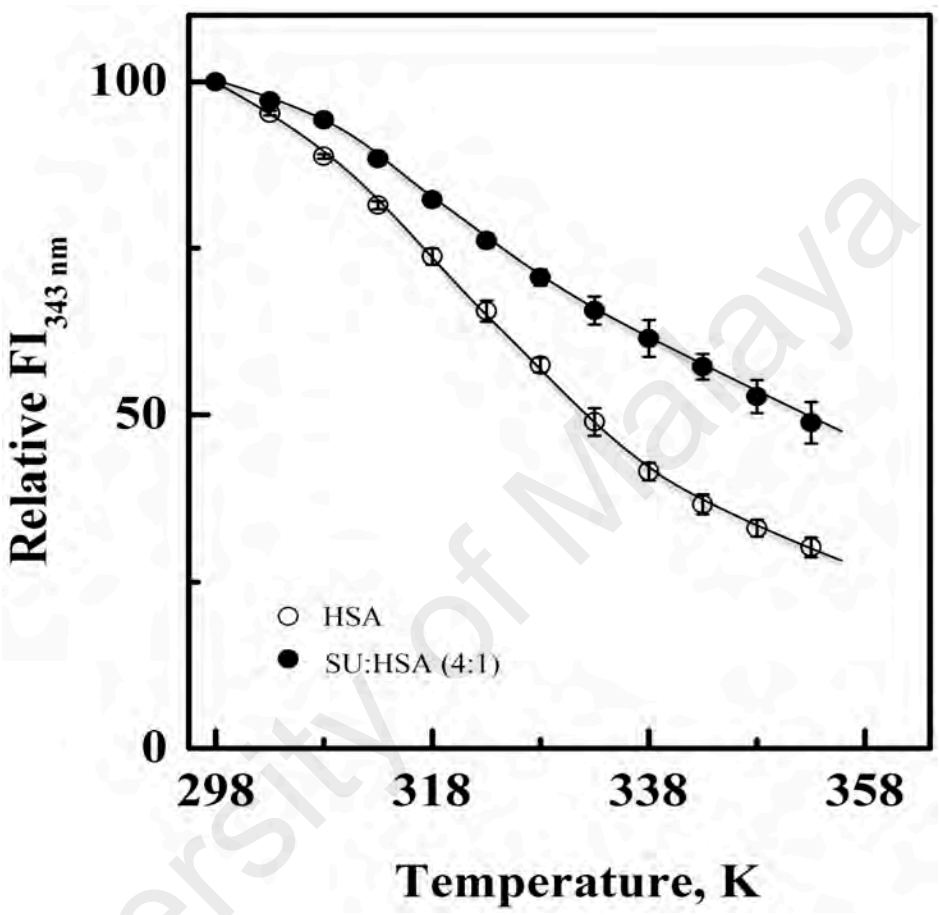

Figure 4.56: Thermal stability profiles of HSA (3 μM) and SU–HSA (4:1) mixture in the temperature range, 298–353 K with a regular increments of 5 K, as monitored by fluorescence intensity measurements at 343 nm ($FI_{343\ nm}$), in 60 mM sodium phosphate buffer, pH 7.4.

4.4.8 Influence of metal ions on SU–HSA interaction

The effect of common ions such as, K^+, Mg^{2+}, Ca^{2+}, Mn^{2+}, Cu^{2+}, Zn^{2+} and Ba^{2+} on SU–HSA interaction was investigated at 298 K by determining the binding constant, K_a of SU–HSA system in the presence of these ions (100 μM). As can be seen from Table 4.19, K_a value of SU–HSA system was significantly affected in the presence of Mn^{2+}, Ca^{2+} and Zn^{2+}. Whereas a decrease in the binding constant was noticed in the presence of Mn^{2+} and Ca^{2+}, presence of Zn^{2+} in the incubation mixture produced a significant increase in the binding constant. In view of the distant location of the four known metal binding sites from the lone Trp-214 of HSA (Bal et al., 2013), changes observed in the fluorescence characteristics of SU–HSA system in the presence of metal ions seem unlikely due to direct metal ion binding to the protein. However, formation of metal ion–drug complex and its interaction with the SU binding site on HSA may produce alteration in the fluorescence characteristics. Owing to the presence of carbonyl group in the SU structure (Figure 2.7), Mn^{2+}, Ca^{2+}, and Zn^{2+} seem to bind the drug with higher affinity (Glusker et al., 1999; Krezel & Maret, 2016). However, different geometries of metal ion–drug complexes might be responsible for producing differential effects in the fluorescence spectra of SU–HSA system, used for binding constant determination. Such changes in the binding constant of SU–HSA system might influence the half-life of the drug in blood plasma. Therefore, it is imposed to readjust the dose of the drug in the presence of these common ions.

4.4.9 Location of SU binding site

To search the binding locus of SU on HSA, competitive ligand displacement experiments using site markers and molecular docking analysis were performed.

4.4.9.1 SU-induced site marker displacement

Majority of drugs bind to one of the two well-characterized ligand binding sites

Table 4.19: K_a values of SU–HSA interaction in the absence and presence of different metal ions (100 μM) at 298 K, pH 7.4.

Metal Ion	K_a ($\times 10^4$ M^{-1})
–	3.04 ± 0.08
Mg^{2+}	2.82 ± 0.13
K^{+}	3.19 ± 0.11
Ca^{2+}	2.79 ± 0.09
Mn^{2+}	2.68 ± 0.12
Cu^{2+}	3.01 ± 0.07
Zn^{2+}	3.43 ± 0.15
Ba^{2+}	2.93 ± 0.09

(Sudlow's sites I and II) of HSA, which are placed in subdomains IIA and IIIA, respectively (Sudlow et al., 1975). In order to identify SU binding site on HSA, competitive ligand displacement experiments were carried out using different site markers, such as PBZ (site I marker) and DZM (site II marker) (Kragh-Hansen et al., 2002). Figures 4.57 and 4.58 show the titration results of HSA and site marker (PBZ / DZM)–HSA mixture ([site marker]:[HSA] = 1:1) with increasing SU concentrations. A comparison of the titration results showed marked variation in the SU-induced quenching of protein fluorescence in the absence and presence of PBZ (Figure 4.57). On the other hand, smaller changes in the quenching patterns were noticed between HSA and DZM–HSA complex (Figure 4.58).

Treatment of the quenching data (Figures 4.57 and 4.58) according to Eq. (5) produced linear plots (Figure 4.59). The K_a values for SU–HSA interaction in the absence and presence of PBZ and DZM, as obtained from the linear plots are given in Table 4.20. The K_a value of the SU–HSA system was significantly reduced in the presence of PBZ while presence of DZM showed little influence on the K_a value (Table 4.20). Hence, competitive displacement results clearly suggested the preference of SU binding at site I (subdomain IIA) of HSA.

4.4.9.2 Molecular docking analysis

Site-specific computational docking analysis was performed to predict the favorable binding mode of SU in between Sudlow's site I and site II on HSA as well as to validate the results described in Section 4.4.9.1. In docking analysis, energy terms of hydrophobic interaction, electrostatic interaction, torsional entropy and other parameters were evaluated in 250 iterations for each binding site. From the predicted binding modes, estimated free energies of the binding of SU to different binding sites were compared. As shown by cluster analysis (Figure 4.60), the largest cluster consisted of 97 out of 250 modes with the lowest binding energies for site I, whereas for site II, 46

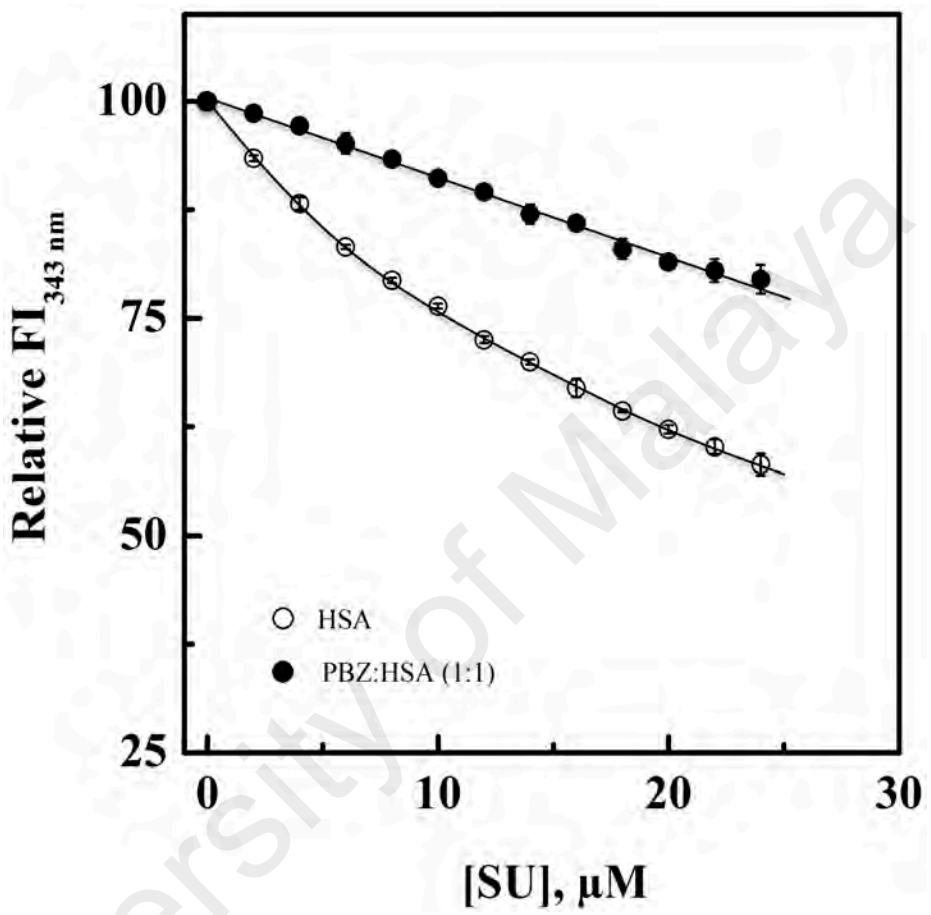

Figure 4.57: Plots showing the decrease in the relative fluorescence intensity at 343 nm ($FI_{343\ nm}$) of HSA (3 μM) and PBZ–HSA (1:1) mixture with increasing concentrations (0–24 μM with 2 μM intervals) of SU. The experiments were carried out in 60 mM sodium phosphate buffer, pH 7.4 at 298 K.

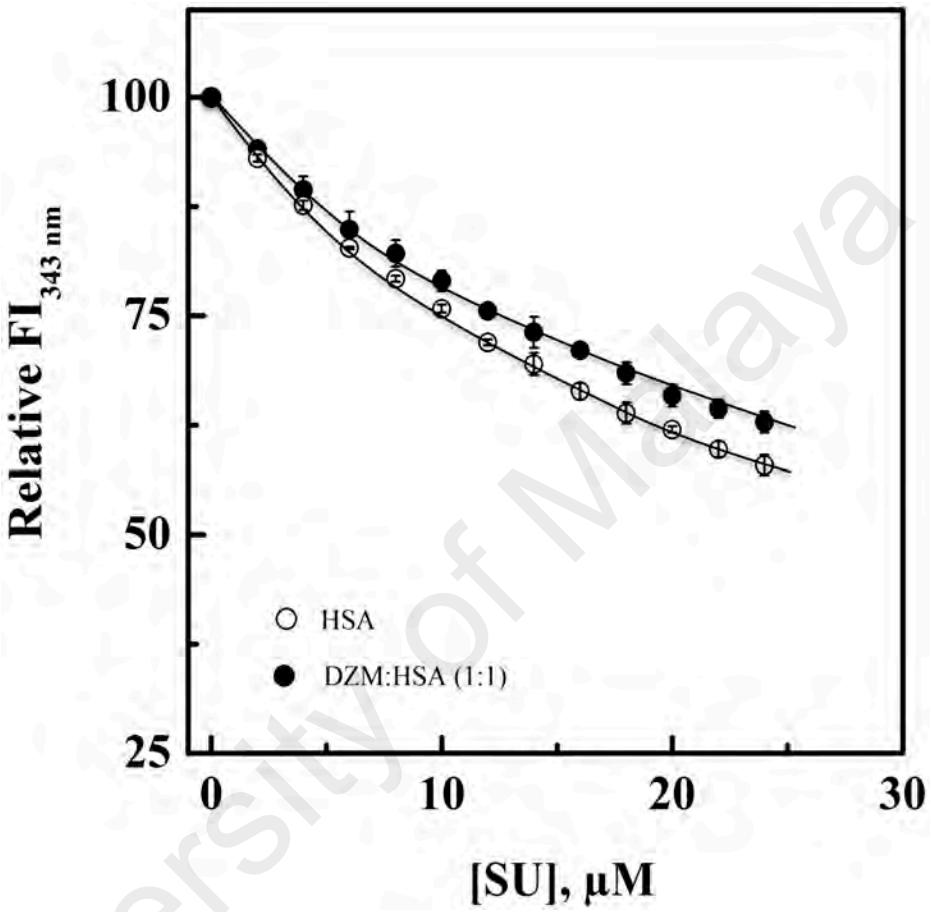

Figure 4.58: Plots showing the decrease in the relative fluorescence intensity at 343 nm ($FI_{343\ nm}$) of HSA (3 μM) and DZM–HSA (1:1) mixture with increasing concentrations (0–24 μM with 2 μM intervals) of SU. The experiments were carried out in 60 mM sodium phosphate buffer, pH 7.4 at 298 K.

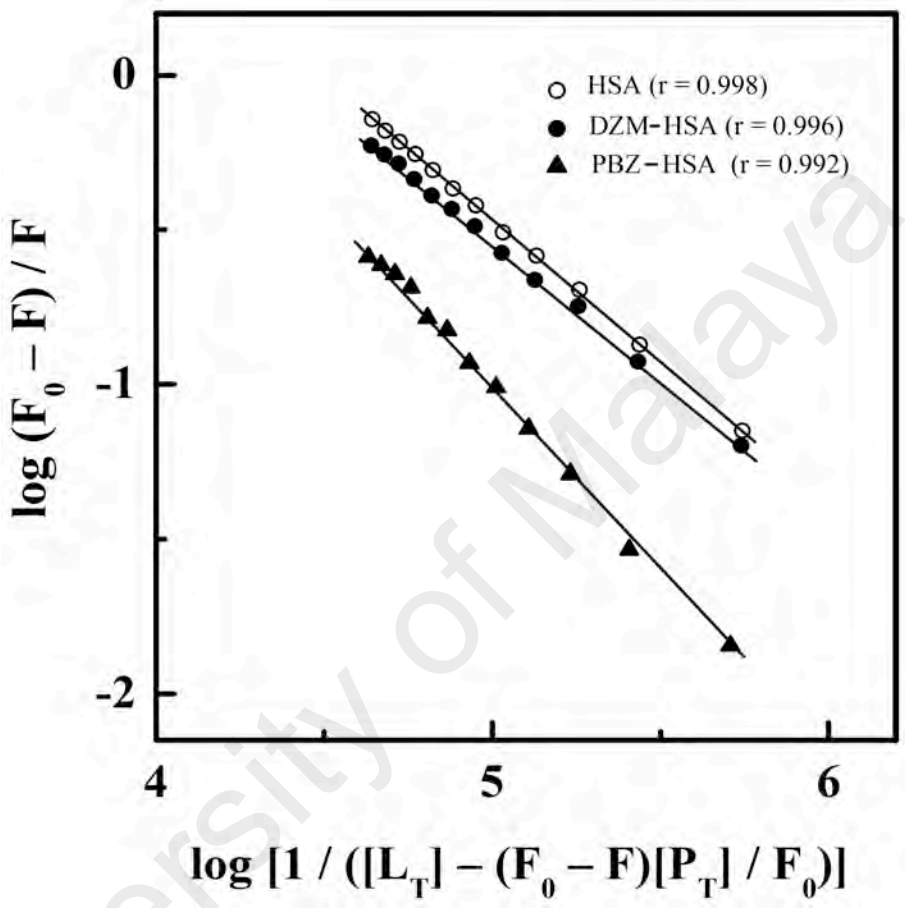

Figure 4.59: Double logarithmic plots of [log ($F_0 - F$) / F versus log [1 / ([L_T] – [(F_0 – F)[P_T] / F_0)] for the fluorescence quenching data of the SU–HSA system in the absence and presence of different site markers, *i.e.*, PBZ and DZM, obtained in 60 mM sodium phosphate buffer, pH 7.4 at 298 K (Figures 4.57 and 4.58).

Table 4.20: K_a values of SU–HSA interaction in the absence and presence of site markers, obtained at 298 K, pH 7.4.

Site Marker	K_a ($\times 10^4$ M^{-1})
–	3.04 ± 0.08
DZM	2.45 ± 0.06
PBZ	1.47 ± 0.10

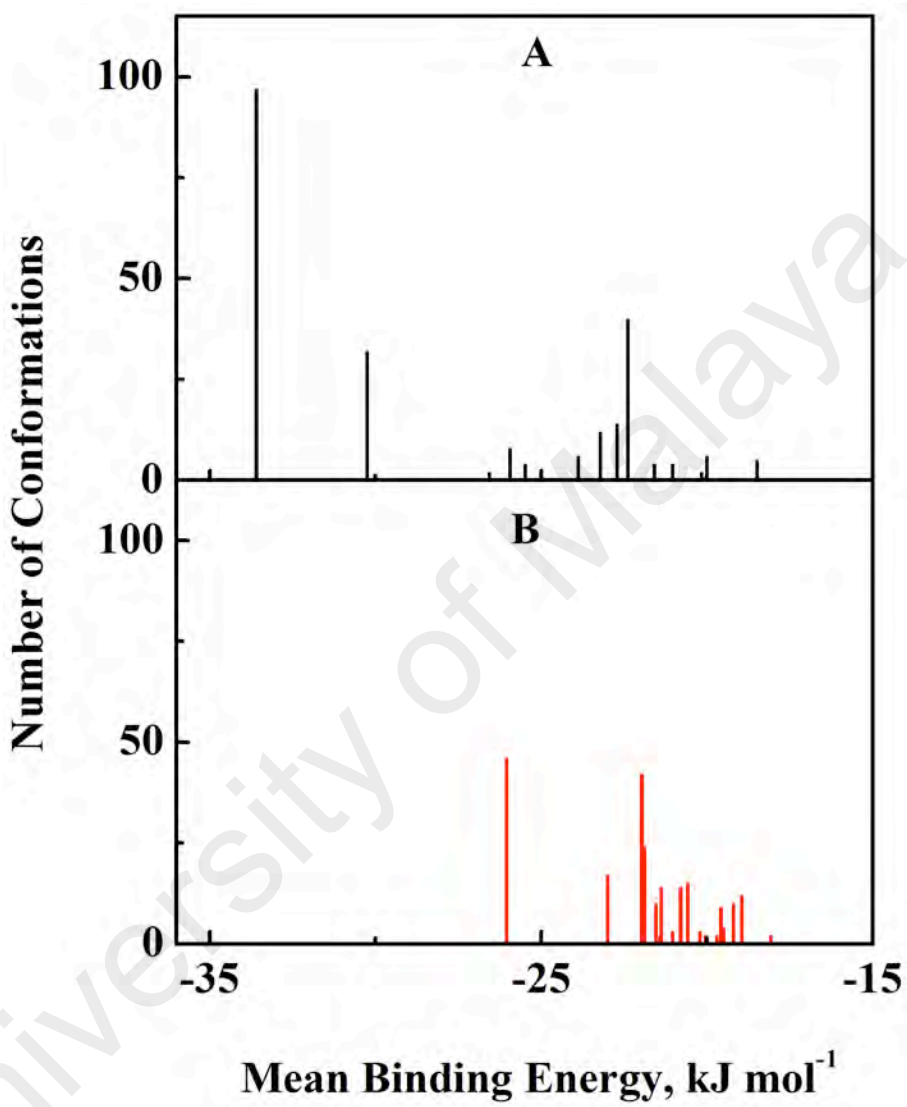

Figure 4.60: Cluster analysis of the docking of SU to Sudlow's sites I (A) and II (B) of HSA crystal structure (1BM0). The results were obtained from a total of 100 runs for each binding site.

modes with the lowest binding energies formed the largest cluster. However, the mean binding energy of the largest cluster (–26.15 kJ mol^{-1}) in site II was higher than that (–33.60 kJ mol^{-1}) in site I (Figure 4.60). Furthermore, the lowest binding energy for sites I and II were found to be –36.94 kJ mol^{-1} and –26.15 kJ mol^{-1}, respectively. Based on the lowest binding energy results, SU seems to have a binding preference for Sudlow's site I with more favorable docking conformer than Sudlow's site II of HSA.

Subsequently, the SU binding mode of the lowest binding energy to Sudlow's site I was selected for further analyses. Visualization (Figure 4.61) showed that SU docked to a cavity, mainly formed by the charged and polar residues. These 16 residues, *viz.*, Tyr-150, Glu-153, Arg-160, Glu-188, Ser-192, Lys-195, Gln-196, Lys-199, Trp-214, Arg-218, Leu-219, Arg-222, His-242, Arg-257, His-288 and Glu-292 were located within 5 Å distance from SU. On the other hand, two and one hydrogen bonds were formed at the binding sites I and II, respectively, in SU–HSA complex docking analysis (Table 4.21). Furthermore, the binding site I of HSA was surrounded by hydrophobic amino acid residues and they might be involved in the stabilization of SU–HSA complex through hydrophobic interactions (Figure 4.62). Therefore, inspection on molecular interactions showed that both hydrogen bonds and hydrophobic interactions are the major forces towards the stability of SU–HSA complex.

In summary, the results of SU–HSA interaction study showed moderate binding affinity between SU and HSA and the binding reaction was mediated by the participation of hydrophobic and van der Waals interactions along with hydrogen bonds. Secondary and tertiary structural alterations, microenvironmental perturbations around Tyr and Trp residues and improvement in thermal stability of the protein were noticed upon SU binding. Besides, subdomain IIA (Sudlow's site I) of HSA was identified as the preferred binding locus of SU. The influence of a few common ions on SU–HSA interaction was also noticed. Since SU has potential drug value, its interaction

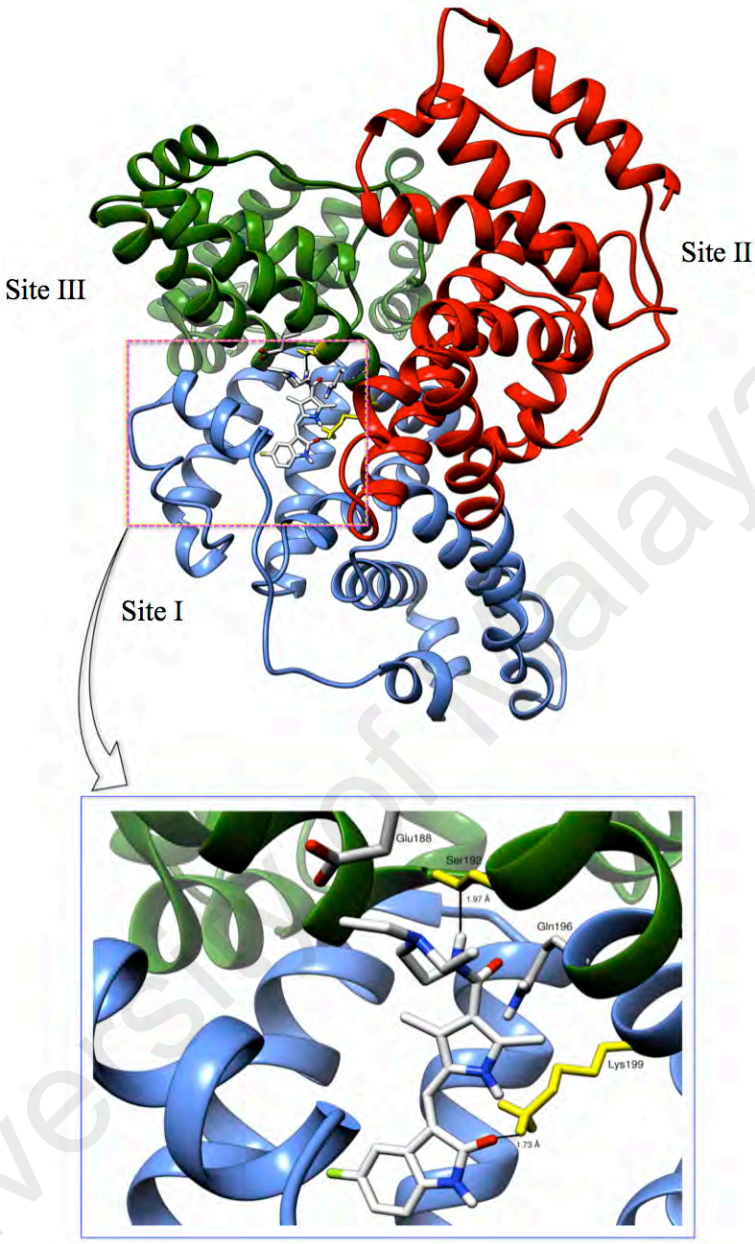

Figure 4.61: Predicted binding orientation of the lowest docking energy conformation of SU (rendered in sticks) in the Sudlow's site I (subdomain IIA) of HSA (1BM0). Different domains of HSA, namely, I, II and III are shown in green, sky blue and red, respectively. The enlarged view shows the hydrogen bond (black line) formed between SU and amino acid residues of HSA (rendered in yellow stick).

Table 4.21: Predicted hydrogen bonds between interacting atoms of the amino acid residues of HSA (1BM0) and SU at Sudlow's sites I and II.

HSA Binding Site	HSA Atom	SU Atom	Distance (Å)
Site I	Ser192:OG	H (Nitro)	1.97
	Lys199:HZ1	O (Carbonyl)	1.73
Site II	Lys413:HZ3	O (Carbonyl)	2.07

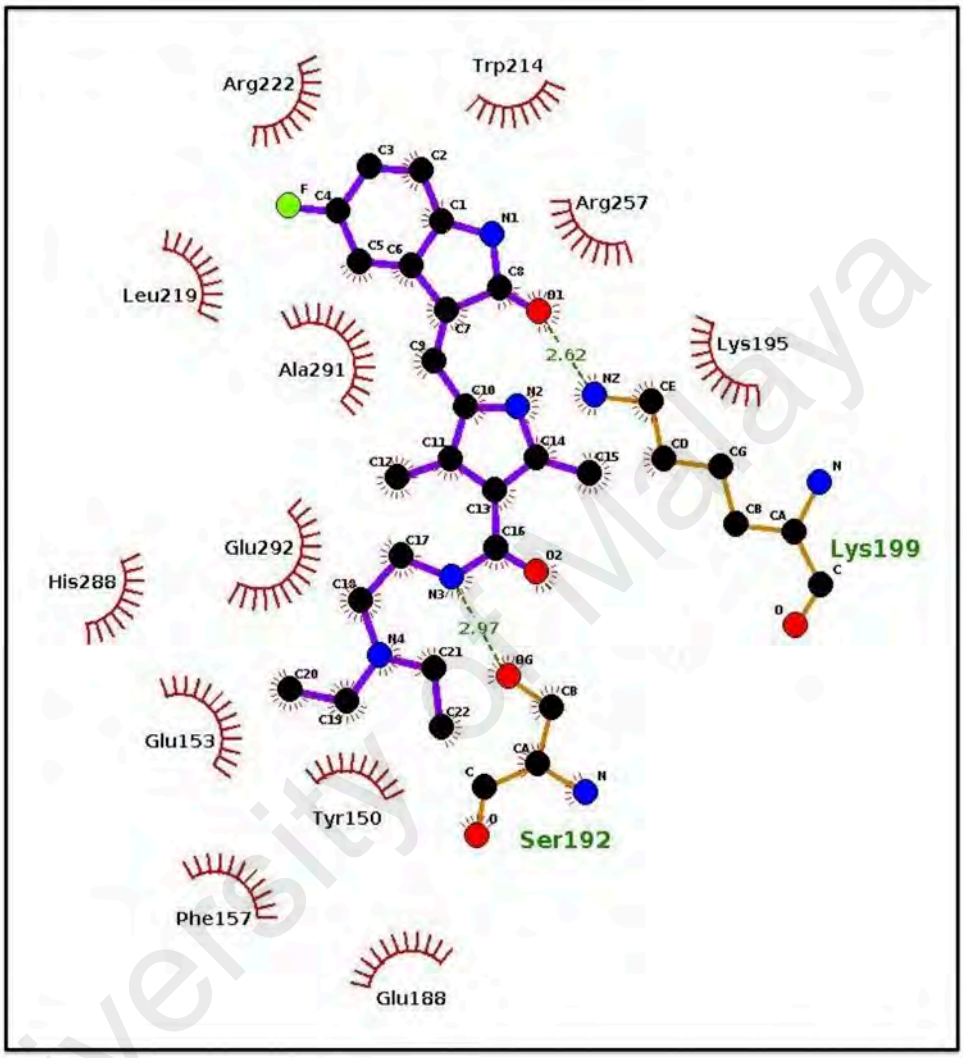

Figure 4.62: LigPlot+ diagram of SU (purple lines) and the amino acid residues of HSA at site I. The residues indicate the presence of hydrophobic interactions with SU. Hydrogen bonds of SU and HSA are rendered with dashed green lines.

study with HSA might be important for understanding its transport in the human body. Therefore, these results may be vital for selecting SU as a therapeutic drug in future.

CHAPTER 5: CONCLUSIONS

This research study provides a detailed description of the binding of four tyrosine kinase inhibitors, *i.e.*, VDB, LAP, GEF and SU to HSA in terms of binding affinity, forces involved, effects on protein conformation and thermal stability as well as identification of the binding site. The binding characteristics of these ligands were found to be more or less similar and comparable to many other ligands / drugs. While LAP, GEF and SU showed a moderate binding affinity towards HSA, relatively weaker binding affinity was observed for VDB. Ligand-induced quenching was characterized as static quenching based on fluorescence quenching results, obtained with these ligands and suggested ligand–protein complex formation. Hydrophobic and van der Waals interactions along with hydrogen bonds seemed to stabilize these complexes based on thermodynamic data. Although microenvironmental perturbation around protein fluorophores and changes in protein's secondary and tertiary structures were noticed upon addition of these ligands, thermal stability of the protein was improved upon ligand binding. Whereas, VDB and SU exhibited a clear binding preference for site I (subdomain IIA) of HSA, LAP and GEF were shown to bind to site III (subdomain IB). Presence of a few metal ions, *i.e.*, Mg^{2+}, K^{+}, Ca^{2+}, Mn^{2+}, Cu^{2+}, Zn^{2+} and Ba^{2+} were found to affect the stability of the ligand–protein complex. These findings can be helpful in understanding the pharmacokinetics of these drugs, as drug–protein interaction increases drug's efficacy, solubility and *in vivo* half-life, while defending its elimination from the body and reducing its toxicity.

REFERENCES

Abdelhameed, A. S., Alanazi, A. M., Bakheit, A. H., Darwish, H. W., Ghabbour, H. A., & Darwish, I. A. (2017). Fluorescence spectroscopic and molecular modeling studies of the binding interaction between the new anaplastic lymphoma kinase inhibitor crizotinib and bovine serum albumin. *Spectrochimica Acta Part A: Molecular and Biomolecular Spectroscopy*, *171*, 174–182.

Abou-Zied, O. K., & Al-Shihi, O. I. (2008). Characterization of subdomain IIA binding site of human serum albumin in its native, unfolded, and refolded states using small molecular probes. *Journal of the American Chemical Society*, *130*, 10793–10801.

Afrin, S., Riyazuddeen, Rabbani, G., & Khan, R. H. (2014). Spectroscopic and calorimetric studies of interaction of methimazole with human serum albumin. *Journal of Luminescence*, *151*, 219–223.

Ajloo, D., Behnam, H., Saboury, A. A., Mohamadi-Zonoz, F., Ranjbar, B., Moosavi-Movahedi, A. A., Hasani, Z., Alizadeh, K., Gharanfoli, M., & Amani, M. (2007). Thermodynamic and structural studies on the human serum albumin in the presence of a polyoxometalate. *Bulletin of the Korean Chemical Society*, *28*, 730–736.

Ajmal, M. R., Abdelhameed, A. S., Alam, P., & Khan, R. H. (2016). Interaction of new kinase inhibitors cabozantinib and tofacitinib with human serum alpha-1-acid glycoprotein. A comprehensive spectroscopic and molecular docking approach. *Spectrochimica Acta Part A: Molecular and Biomolecular Spectroscopy*, *159*, 199–208.

Allen, L. F., Lenehan, P. F., Eiseman, I. A., Elliott, W. L., & Fry, D. W. (2002). Potential benefits of the irreversible pan-erbB inhibitor, CI-1033, in the treatment of breast cancer. *Seminars in Oncology*, *29*, 11–21.

Amina, M., Ali, M. S., Al-Musayeib, N. M., & Al-Lohedan, H. A. (2016). Biophysical characterization of the interaction of bovine serum albumin with anticancer sipholane triterpenoid from the Red Sea sponge. *Journal of Molecular Liquids*, *220*, 931–938.

Amoresano, A., Andolfo, A., Siciliano, R. A., Cozzolino, R., Minchiotti, L., Galliano, M., & Pucci, P. (1998). Analysis of human serum albumin variants by mass spectrometric procedures. *Biochimica et Biophysica Acta – Protein Structure and Molecular Enzymology*, *1384*, 79–92.

Arora, A., & Scholar, E. M. (2005). Role of tyrosine kinase inhibitors in cancer therapy. *Journal of Pharmacology and Experimental Therapeutics*, *315*, 971–979.

Arteaga, C. L. (2001). The epidermal growth factor receptor: From mutant oncogene in nonhuman cancers to therapeutic target in human neoplasia. *Journal of Clinical Oncology*, *19*, 32–40.

Arteaga, C. L., Sliwkowski, M. X., Osborne, C. K., Perez, E. A., Puglisi, F., & Gianni, L. (2012). Treatment of HER2-positive breast cancer: Current status and future perspectives. *Nature Reviews. Clinical Oncology, 9,* 16–32.

Ayranci, E., & Duman, O. (2004). Binding of lead ion to bovine serum albumin studied by ion selective electrode. *Protein and Peptide Letters, 11,* 331–337.

Bal, W., Sokolowska, M., Kurowska, E., & Faller, P. (2013). Binding of transition metal ions to albumin: Sites, affinities and rates. *Biochimica et Biophysica Acta – General Subjects, 1830,* 5444–5455.

Barok, M., Joensuu, H., & Isola, J. (2014). Trastuzumab emtansine: Mechanisms of action and drug resistance. *Breast Cancer Research, 16,* 209–220.

Barre, J., Chamouard, J. M., Houin, G., & Tillement, J. P. (1985). Equilibrium dialysis, ultrafiltration, and ultracentrifugation compared for determining the plasma-protein-binding characteristics of valproic acid. *Clinical Chemistry, 31,* 60–64.

Barreca, D., Lagana, G., Bruno, G., Magazu, S., & Bellocco, E. (2013). Diosmin binding to human serum albumin and its preventive action against degradation due to oxidative injuries. *Biochimie, 95,* 2042–2049.

Bennasroune, A., Gardin, A., Aunis, D., Crémel, G., & Hubert, P. (2004). Tyrosine kinase receptors as attractive targets of cancer therapy. *Critical Reviews in Oncology/Hematology, 50,* 23–38.

Bergsland, E. K. (2004). Vascular endothelial growth factor as a therapeutic target in cancer. *American Journal of Health-System Pharmacy, 61,* 4–11.

Berman, H. M., Westbrook, J., Feng, Z., Gilliland, G., Bhat, T. N., Weissig, H., Shindyalov, I. N., & Bourne, P. E. (2000). The protein data bank. *Nucleic Acids Research, 28,* 235–242.

Bertucci, C., Nanni, B., Raffaelli, A., & Salvadori, P. (1998). Chemical modification of human albumin at Cys-34 by ethacrynic acid: Structural characterisation and binding properties. *Journal of Pharmaceutical and Biomedical Analysis, 18,* 127–136.

Bhattacharya, A. A., Curry, S., & Franks, N. P. (2000). Binding of the general anesthetics propofol and halothane to human serum albumin. High resolution crystal structures. *The Journal of Biological Chemistry, 275,* 38731–38738.

Bi, S., Ding, L., Tian, Y., Song, D., Zhou, X., Liu, X., & Zhang, H. (2004). Investigation of the interaction between flavonoids and human serum albumin. *Journal of Molecular Structure, 703,* 37–45.

Bijari, N., Shokoohinia, Y., Ashrafi-Kooshk, M. R., Ranjbar, S., Parvaneh, S., Moieni-Arya, M., & Khodarahmi, R. (2013). Spectroscopic study of interaction between osthole and human serum albumin: Identification of possible binding site of the compound. *Journal of Luminescence, 143,* 328–336.

Bischer, A., Zia-Amirhosseini, P., Iwaki, M., McDonagh, A. F., & Benet, L. Z. (1995). Stereoselective binding properties of naproxen glucuronide diastereomers to proteins. *Journal of Pharmacokinetics and Pharmacodynamics, 23,* 379–395.

Bode, A. M., & Dong, Z. (2005). Signal transduction pathways in cancer development and as targets for cancer prevention. *Progress in Nucleic Acid Research and Molecular Biology, 79,* 237–297.

Boettner, B., & Aelst, L. V. (2002). The role of Rho GTPases in disease development. *Gene, 286,* 155–174.

Bourassa, P., Dubeau, S., Maharvi, G. M., Fauq, A. H., Thomas, T. J., & Tajmir-Riahi, H. A. (2011). Binding of antitumor tamoxifen and its metabolites 4-hydroxytamoxifen and endoxifen to human serum albumin. *Biochimie, 93,* 1089–1101.

Bozoglan, B. K., Tunc, S., & Duman, O. (2014). Investigation of neohesperidin dihydrochalcone binding to human serum albumin by spectroscopic methods. *Journal of Luminescence, 155,* 198–204.

Brassard, M., & Rondeau, G. (2012). Role of vandetanib in the management of medullary thyroid cancer. *Biologics: Targets and Therapy, 6,* 59–66.

Brodersen, R. (1982). *Bilirubin, Volume I. Chemistry.* Florida: CRC Press.

Burotto, M., Manasanch, E. E., Wilkerson, J., & Fojo, T. (2015). Gefitinib and erlotinib in metastatic non-small cell lung cancer: A meta-analysis of toxicity and efficacy of randomized clinical trials. *The Oncologist, 20,* 400–410.

Candiano, G., Ghiggeri, G. M., Delfino, G., & Queirolo, C. (1986). Isoelectric focusing in low-denaturing media: Visualization in renal disease of variation of the isoelectric point of albumin not related to a remarkable conformational variation. *Journal of Chromatography, 374,* 279−288.

Carter, D. C., & Ho, J. X. (1994). Structure of serum albumin. *Advances in Protein Chemistry, 45,* 153–203.

Celej, M. S., Montich, G. G., & Fidelio, G. D. (2003). Protein stability induced by ligand binding correlates with changes in protein flexibility. *Protein Science, 12,* 1496–1506.

Chatterjee, T., Pal, A., Dey, S., Chatterjee, B. K., & Chakrabarti, P. (2012). Interaction of virstatin with human serum albumin: Spectroscopic analysis and molecular modeling. *PLoS ONE, 7,* e37468.

Chen, Y. H., Yang, J. T., & Martinez, H. M. (1972). Determination of the secondary structures of proteins by circular dichroism and optical rotatory dispersion. *Biochemistry, 11,* 4120–4131.

Chen, X., Qian, K., & Chen, Q. (2015). Comparison between loureirin A and cochinchinenin C on the interaction with human serum albumin. *European Journal of Medicinal Chemistry, 93,* 492–500.

Cheng, Z., Liu, R., & Jiang, X. (2013). Spectroscopic studies on the interaction between tetrandrine and two serum albumins by chemometrics methods. *Spectrochimica Acta Part A: Molecular and Biomolecular Spectroscopy*, *115*, 92–105.

Chuang, V. T., & Otagiri, M. (2001). Flunitrazepam, a 7-nitro-1,4-benzodiazepine that is unable to bind to the indole-benzodiazepine site of human serum albumin. *Biochimica et Biophysica Acta – Protein Structure and Molecular Enzymology*, *1546*, 337–345.

Colmenarejo, G. (2003). *In silico* prediction of drug-binding strengths to human serum albumin. *Medicinal Research Reviews*, *23*, 275–301.

Cortes, J. E., Kantarjian, H. M., Brümmendorf, T. H., Kim, D. W., Turkina, A. G., Shen, Z. X., Pasquini, R., Khoury, H. J., Arkin, S., Volkert, A., Besson, N., Abbas, R., Wang, J., Leip, E., & Gambacorti-Passerini, C. (2011). Safety and efficacy of bosutinib (SKI-606) in chronic phase Philadelphia chromosome–positive chronic myeloid leukemia patients with resistance or intolerance to imatinib. *Blood*, *118*, 4567−4576.

Costanzo, R., Piccirillo, M. C., Sandomenico, C., Carillio, G., Montanino, A., Daniele, G., Giordano, P., Bryce, J., Feo, G. D., Maio, M. D., Rocco, G., Normanno, N., Perrone, F., & Morabito, A. (2011). Gefitinib in non small cell lung cancer. *Journal of Biomedicine and Biotechnology*, *2011*, 1–14.

Cui, F. L., Fan, J., Li, J. P., & Hu, Z. (2004). Interactions between 1-benzoyl-4-p-chlorophenyl thiosemicarbazide and serum albumin: Investigation by fluorescence spectroscopy. *Bioorganic and Medicinal Chemistry*, *12*, 151–157.

Curry, S. (2009). Lessons from the crystallographic analysis of small molecule binding to human serum albumin. *Drug Metabolism and Pharmacokinetics*, *24*, 342–357.

Dangkoob, F., Housaindokht, M. R., Asoodeh, A., Rajabi, O., Zaeri, Z. R., & Doghaei, A. V. (2015). Spectroscopic and molecular modeling study on the separate and simultaneous bindings of alprazolam and fluoxetine hydrochloride to human serum albumin (HSA): With the aim of the drug interactions probing. *Spectrochimica Acta Part A: Molecular and Biomolecular Spectroscopy*, *137*, 1106–1119.

Das, A., & Kumar, G. S., (2014). Binding studies of aristololactam-β-D-glucoside and daunomycin to human serum albumin. *RSC Advances*, *4*, 33082–33090.

Dasgupta, A., & Havlik, D. (1998). Elevated free fosphenytoin concentrations in uremic sera: Uremic toxins hippuric acid and indoxyl sulfate do not account for the impaired protein binding of fosphenytoin. *Therapeutic Drug Monitoring*, *20*, 658−662.

Demain, A. L., & Vaishnav, P. (2011). Natural products for cancer chemotherapy. *Microbial Biotechnology*, *4*, 687–699.

Dockal, M., Carter, D. C., & Ruker, F. (1999). The three recombinant domains of human serum albumin: Structural characterization and ligand binding properties. *The Journal of Biological Chemistry, 274,* 29303–29310.

Dockal, M., Chang, M., Carter, D. C., & Rüker, F. (2000). Five recombinant fragments of human serum albumin–Tools for the characterization of the warfarin binding site. *Protein Science, 9,* 1455–1465.

Dufour, C., & Dangles, O. (2005). Flavonoid–serum albumin complexation: Determination of binding constants and binding sites by fluorescence spectroscopy. *Biochimica et Biophysica Acta – General Subjects, 1721,* 164–173.

Dugaiczyk, A., Law, S. W., & Dennison, O. E. (1982). Nucleotide sequence and the encoded amino acids of human serum albumin mRNA. *Proceedings of the National Academy of Sciences, USA, 79,* 71−75.

Duman, O., Tunc, S. & Bozoglan, B. K. (2013). Characterization of the binding of metoprolol tartrate and guaifenesin drugs to human serum albumin and human hemoglobin proteins by fluorescence and circular dichroism spectroscopy. *Journal of Fluorescence, 23,* 659–669.

Ebrahimi, M., Khayamian, T., Hadadzadeh, H., Tabatabaei, B. E. S., Jannesari, Z., & Khaksar, G. (2015). Spectroscopic, biological, and molecular modeling studies on the interactions of [Fe(III)-meloxicam] with G-quadruplex DNA and investigation of its release from bovine serum albumin (BSA) nanoparticles. *Journal of Biomolecular Structure and Dynamics, 33,* 2316–2329.

Echavarria, I., López-Tarruella, S., Márquez-Rodas, I., Jerez, Y., & Martin, M. (2017). Neratinib for the treatment of HER2-positive early stage breast cancer. *Expert Review of Anticancer Therapy, 17,* 669–679.

Eckstein, N., Röper, L., Haas, B., Potthast, H., Hermes, U., Unkrig, C., Naumann-Winter, F., & Enzmann, H. (2014). Clinical pharmacology of tyrosine kinase inhibitors becoming generic drugs: The regulatory perspective. *Journal of Experimental and Clinical Cancer Research, 33,* 1–10.

Elbary, A. A., Vallner, J. J., & Whitworth, C. W. (1982). Effect of albumin conformation on the binding of phenylbutazone and oxyphenbutazone to human serum albumin. *Journal of Pharmaceutical Sciences, 71,* 241–244.

Eskens, F. (2004). Angiogenesis inhibitors in clinical development; Where are we now and where are we going? *British Journal of Cancer, 90,* 1–7.

Evelyn, C. R., Wade, S. M., Wang, Q., Wu, M., Iniguez-Lluhi, J. A., Merajver, S. D., & Neubig, R. R. (2007). CCG-1423: A small-molecule inhibitor of RhoA transcriptional signaling. *Molecular Cancer Therapeutics, 6,* 2249–2260.

Fabbro, D., Parkinson, D., & Matter, A. (2002). Protein tyrosine kinase inhibitors: New treatment modalities? *Current Opinion in Pharmacology, 2,* 374–381.

Fasano, M., Curry, S., Terreno, E., Galliano, M., Fanali, G., Narciso, P., Notari, S., & Ascenzi, P. (2005). The extraordinary ligand binding properties of human serum albumin. *IUBMB Life, 57,* 787–796.

Fauvel, B., & Yasri, A. (2014). Antibodies directed against receptor tyrosine kinases: Current and future strategies to fight cancer. *Landes Bioscience, 6,* 838–851.

Fehske, K. J., Schlafer, U., Wollert, U., & Muller, W. E. (1982). Characterization of an important drug binding area on human serum albumin including the high-affinity binding sites of warfarin and azapropazone. *Molecular Pharmacology, 21,* 387–393.

Feroz, S. R., Mohamad, S. B., Bujang, N., Malek, S. N. A., & Tayyab, S. (2012). Multispectroscopic and molecular modeling approach to investigate the interaction of flavokawain B with human serum albumin. *Journal of Agricultural and Food Chemistry, 60,* 5899–5908.

Feroz, S. R., Mohamad, S. B., Bakri, Z. S. D., Malek, S. N. A., & Tayyab, S. (2013). Probing the interaction of a therapeutic flavonoid, pinostrobin with human serum albumin: Multiple spectroscopic and molecular modeling investigations. *PLoS ONE, 8,* e76067.

Feroz, S. R., Mohamad, S. B., Lee, G. S., Malek, S. N. A., & Tayyab, S. (2015). Supramolecular interaction of 6-shogaol, a therapeutic agent of *Zingiber officinale* with human serum albumin as elucidated by spectroscopic, calorimetric and molecular docking methods. *Phytomedicine, 22,* 621–630.

Feroz, S. R., Teoh, Y. J., Mohamad, S. B., Hong, S. L., Malek, S. N. A., & Tayyab, S. (2015). Interaction of flavokawain B with lysozyme: A photophysical and molecular simulation study. *Journal of Luminescence, 160,* 101–109.

Ferrer, M. L., Duchowicz, R., Carrasco, B., Torre, J. G., & Acuna, A. U. (2001). The conformation of serum albumin in solution: A combined phosphorescence depolarization-hydrodynamic modeling study. *Biophysical Journal, 80,* 2422–2430.

Fiedler, W., Mesters, R., Tinnefeld, H., Loges, S., Staib, P,. Duhrsen, U., Flasshove, M., Ottmann, O. G., Jung, W., & Cavalli, F. (2003). A phase 2 clinical study of SU5416 in patients with refractory acute myeloid leukemia. *Blood, 102,* 2763–2767.

Figge, J., Rossing, T. H., & Fencl, V. (1991). The role of serum proteins in acid-base equilibria. *Journal of Laboratory and Clinical Medicine, 117,* 453–467.

Finn, R. S., Dering, J., Conklin, D., Kalous, O., Cohen, D. J., Desai, A. J., Ginther, C., Atefi, M., Los, G., & Slamon, D. J. (2009). PD 0332991, a selective cyclin D kinase 4/6 inhibitor, preferentially inhibits proliferation of luminal estrogen receptor-positive human breast cancer cell lines *in vitro*. *Breast Cancer Research, 11,* 1–13.

Furugaki, K., Moriya, Y., Iwai, T., Yorozu, K., Yanagisawa, M., Kondoh, K., Fujimoto-Ohuchi, K., & Mori, K. (2011). Erlotinib inhibits osteolytic bone invasion of

human non-small-cell lung cancer cell line NCI-H292. *Clinical and Experimental Metastasis, 28,* 649–659.

Ghuman, J., Zunszain, P. A., Petitpas, I., Bhattacharya, A. A., Otagiri, M., & Curry, S. (2005). Structural basis of the drug-binding specificity of human serum albumin. *Journal of Molecular Biology, 353,* 38–52.

Gianazza, E., Frigerio, A., Astrua-Testori, S., & Righetti, P. G. (1984). The behavior of serum albumin upon isoelectric focusing on immobilized pH gradients. *Electrophoresis 5,* 310−312.

Gibney, G. T., & Zager, J. S. (2013). Clinical development of dabrafenib in BRAF mutant melanoma and other malignancies. *Expert Opinion on Drug Metabolism and Toxicology, 9,* 893–899.

Gibson, T. B., Ranganathan, A., & Grothey, A. (2006). Randomized phase III trial results of panitumumab, a fully human anti-epidermal growth factor receptor monoclonal antibody, in metastatic colorectal cancer. *Clinical Colorectal Cancer, 6,* 29–31.

Glusker, J. P., Katz, A. K., & Bock, C. W. (1999). Metal ions in biological systems. *Rigaku Journal, 16,* 8–17.

Gocek, E., Moulas, A. N., & Studzinski, G. P. (2014). Non-receptor protein tyrosine kinases signaling pathways in normal and cancer cells. *Critical Reviews in Clinical Laboratory Sciences, 51,* 125–137.

Gonzalez, M., Bagatolli, L. A., Echabe, I., Arrondo, J. L. R., Argarana, C. E., Cantor, C. R., & Fidelio, G. D. (1997). Interaction of biotin with streptavidin. Thermostability and conformational changes upon binding. *The Journal of Biological Chemistry, 272,* 11288–11294.

Goodsell, D. S., Morris, G. M., & Olson, A. J. (1996). Automated docking of flexible ligands: Applications of autodock. *Journal of Molecular Recognition, 9,* 1–5.

Goormaghtigh, E., Cabiaux, V., & Ruysschaert, J. M. (1990). Secondary structure and dosage of soluble and membrane proteins by attenuated total reflection Fourier-transform infrared spectroscopy on hydrated films. *European Journal of Biochemistry, 193,* 409–420.

Goss, G., Shepherd, F. A., Laurie, S., Gauthier, I., Leighl, N., Chen, E., Feld, R., Powers, J., & Seymour, L. (2009). A phase I and pharmacokinetic study of daily oral cediranib, an inhibitor of vascular endothelial growth factor tyrosine kinases, in combination with cisplatin and gemcitabine in patients with advanced non-small cell lung cancer: A study of the National Cancer Institute of Canada Clinical Trials Group. *European Journal of Cancer, 45,* 782–788.

Gross-Goupil, M., François, L., Quivy, A., & Ravaud, A. (2013). Axitinib: A review of its safety and efficacy in the treatment of adults with advanced renal cell carcinoma. *Clinical Medicine Insights: Oncology, 7,* 269–277.

Guercia, E., Forzato, C., Navarini, L., & Berti, F. (2016). Interaction of coffee

compounds with serum albumins. Part II: Diterpenes. *Food Chemistry, 199,* 502–508.

Guidotti, T. L., McNamara, J., & Moses, M. S. (2008). The interpretation of trace element analysis in body fluids. *Indian Journal of Medical Research, 128,* 524–532.

Halgren, T. A. (1996). Merck molecular force field. I. Basis, form, scope, parameterization, and performance of MMFF94. *Journal of Computational Chemistry, 17,* 490–519.

Hall, M. L., Jorgensen, W. L., & Whitehead, L. (2013). Automated ligand- and structure-based protocol for *in silico* prediction of human serum albumin binding. *Journal of Chemical Information and Modeling, 53,* 907−922.

Hanwell, M. D., Curtis, D. E., Lonie, D. C., Vandermeersch, T., Zurek, E., & Hutchison, G. R. (2012). Avogadro: An advanced semantic chemical editor, visualization, and analysis platform. *Journal of Cheminformatics, 4,* 1–17.

He, X. M., & Carter, D. C. (1992). Atomic structure and chemistry of human serum albumin. *Nature, 358,* 209–215.

He, J., Wu, D., Zhai, Y., Wang, Q., Ma, X., Yang, H., & Li, H. (2016). Interaction of inosine with human serum albumin as determined by NMR relaxation data and fluorescence methodology. *Journal of Molecular Liquids, 219,* 547–553.

Hein, K. L., Kragh-Hansen, U., Morth, J. P., Jeppesen, M. D., Otzen, D., Moller, J. V., & Nissen, P. (2010). Crystallographic analysis reveals a unique lidocaine binding site on human serum albumin. *Journal of Structural Biology, 171,* 353−360.

Higa, G. M., & Abraham, J. (2007). Lapatinib in the treatment of breast cancer. *Expert Review of Anticancer Therapy, 7,* 1183–1192.

Horone, B., & Brodersen, R. (1982). Albumin binding of anti-inflammatory drugs. Utility of a site-oriented versus a stoichiometric analysis. *Molecular Pharmacology, 25,* 137–150.

Huang, B. X., Kim, H. Y., & Dass, C. (2004). Probing there-dimensional structure of bovine serum albumin by chemical cross-linked and mass spectrometry. *Journal of the American Society for Mass Spectrometry, 15,* 1237–1247.

Huang, W. S., Liu, S., Zou, D., Thomas, M., Wang, Y., Zhou, T., Romero, J., Kohlmann, A., & Li, F. (2016). Discovery of brigatinib (AP26113), a phosphine oxide-containing, potent, orally active inhibitor of anaplastic lymphoma kinase. *Journal of Medicinal Chemistry, 59,* 4948–4964.

Hubbard, S. R., & Till, J. H. (2000). Protein tyrosine kinase structure and function. *Annual Review of Biochemistry, 69,* 373–398.

Hunter, M. J., & Mcduffie, F. C. (1959). Molecular weight studies on human serum albumin after reduction and alkylation of disulfide bonds. *Journal of the American Chemical Society, 81*, 1400–1406.

Huynh, H., Ngo, V. C., Fargnoli, J., Ayers, M., Soo, K. C., Koong, H. N., Thng, C. H., Ong, H. S., & Tran, E. (2008). Brivanib alaninate, a dual inhibitor of vascular endothelial growth factor receptor and fibroblast growth factor receptor tyrosine kinases, induces growth inhibition in mouse models of human hepatocellular carcinoma. *Clinical Cancer Research, 14*, 6146–6153.

Il'ichev, Y. V., Perry, J. L., & Simon, J. D. (2002). Interaction of ochratoxin A with human serum albumin. A common binding site of ochratoxin A and warfarin in subdomain IIA. *The Journal of Physical Chemistry B, 106*, 460–465.

Kabir, M. Z., Tee, W. V., Mohamad, S. B., Alias, Z., & Tayyab, S. (2016). Interaction of an anticancer drug, gefitinib with human serum albumin: Insights from fluorescence spectroscopy and computational modeling analysis. *RSC Advances, 6*, 91756–91767.

Karush, F. (1954). The interaction of optically isomeric dyes with human serum albumin. *Journal of the American Chemical Society, 76*, 5536–5542.

Kaur, V., & Swami, A. (2017). Ibrutinib in CLL: A focus on adverse events, resistance and novel approaches beyond ibrutinib. *Annals of Hematology, 96*, 1175–1184.

Keskin, D., Sadri, S., & Eskazan, A. E. (2016). Dasatinib for the treatment of chronic myeloid leukemia: Patient selection and special considerations. *Drug Design, Development and Therapy, 10*, 3355–3361.

Khan, S. N., Islam, B., Yennamalli, R., Sultan, A., Subbarao, N., & Khan, A. U. (2008). Interaction of mitoxantrone with human serum albumin: Spectroscopic and molecular modeling studies. *European Journal of Pharmaceutical Sciences, 35*, 371–382.

Klotz, I. M. (1973). Physicochemical aspects of drug–protein interactions: A general perspective. *Annals of the New York Academy of Sciences, 226*, 18–35.

Ko, Y. J., Small, E. J., Kabbinavar, F., Chachoua, A., Taneja, S., Reese, D., DePaoli, A., Hannah, A., Balk, S. P., & Bubley, G. J. (2001). A multi-institutional phase II study of SU101, a platelet-derived growth factor receptor inhibitor, for patients with hormone-refractory prostate cancer. *Clinical Cancer Resserch, 4*, 800–805.

Korolenko, E. A., Korolik, E. V., Korolik, A. K., & Kirkovskii, V. V. (2007). Estimation of the binding ability of main transport proteins of blood plasma with liver cirrhosis by the fluorescent probe method. *Journal of Applied Spectroscopy, 74*, 561–566.

Kragh-Hansen U. (1981). Molecular aspects of ligand binding to serum albumin. *Pharmacological Reviews, 33*, 17–53.

Kragh-Hansen, U. (1985). Relations between high-affinity binding sites of markers for binding regions on human serum albumin. *Biochemical Journal, 225,* 629–638.

Kragh-Hansen, U. (1988). Evidence for a large and flexible region of human serum albumin possessing high affinity binding sites for salicylate, warfarin, and other ligands. *Molecular Pharmacology, 34,* 160–171.

Kragh-Hansen, U. (1990). Structure and ligand binding properties of human serum albumin. *Danish Medicinal Bulletin, 37,* 57–84.

Kragh-Hansen, U., Chuang, V. T. G., & Otagiri, M. (2002). Practical aspects of the ligand-binding and enzymatic properties of human serum albumin. *Biological and Pharmaceutical Bulletin, 25,* 695–704.

Kragh-Hansen, U. (2013). Molecular and practical aspects of the enzymatic properties of human serum albumin and of albumin-ligand complexes. *Biochimica et Biophysica Acta – General Subjects, 1830,* 5535–5544.

Kratz, F. (2008). Albumin as a drug carrier: Design of prodrugs, drug conjugates and nanoparticles. *Journal of Controlled Release, 132,* 171–183.

Krezel, A., & Maret, W. (2016). The biological inorganic chemistry of zinc ions. *Archives of Biochemistry and Biophysics, 611,* 3–19.

Lakowicz, J. R. (2006). *Principles of Fluorescence Spectroscopy* (3rd ed.). New York: Plenum Press.

Larkin, J., Ascierto, P. A., Dréno, B., Atkinson, V., Choong, N., Hack, S. P., McArthur, G. A., & Ribas, A. (2014). Combined vemurafenib and cobimetinib in BRAF-mutated melanoma. *The New England Journal of Medicine, 371,* 1867–1876.

Laurie, S. A., & Goss, G. D. (2013). Role of epidermal growth factor receptor inhibitors in epidermal growth factor receptor wild-type non-small-cell lung cancer. *Journal of Clinical Oncology, 31,* 1061–1069.

Lazaro, E., Lowe, P. J., Briand, X., & Faller, B. (2008). New approach to measure protein binding based on a parallel artificial membrane assay and human serum albumin. *Journal of Medicinal Chemistry, 51,* 2009–2017.

Lee, Y. J., & Hirose, M. (1992). Partially folded state of the disulfide-reduced form of human serum albumin as an intermediate for reversible denaturation. *The Journal of Biological Chemistry, 267,* 14753–14758.

Lee, R. J., & Smith, M. R. (2014). Cabozantinib and prostate cancer: Inhibiting seed and disrupting soil. *Clinical Cancer Research, 20,* 525–527.

Li, D. J., Zhu, J. F., Jin, J., & Yao, X. J. (2007). Studies on the binding of nevadensin to human serum albumin by molecular spectroscopy and modeling. *Journal of Molecular Structure, 846,* 34–41.

Li, J., Ren, C., Zhang, Y., Liu, X., Yao, X., & Hu, Z. (2008). Spectroscopic studies on binding of puerarin to human serum albumin. *Journal of Molecular Structure, 885*, 64–69.

Li, X. & Wang, S. (2015). Study on the interaction of (+)-catechin with human serum albumin using isothermal titration calorimetry and spectroscopic techniques. *New Journal of Chemistry, 39*, 386–395.

Liao, J., Gallas, M., Pegram, M., & Slingerland, J. (2010). Lapatinib: New opportunities for management of breast cancer. *Breast Cancer: Targets and Therapy, 2*, 79–91.

Lin, B., Podar, K., Gupta, D., Tai, Y. T., Li, S., Weller, E., & Li, C. (2002). The vascular endothelial growth factor receptor tyrosine kinase inhibitor PTK787/ZK222584 inhibits growth and migration of multiple myeloma cells in the bone marrow microenvironment. *Cancer Research, 62*, 5019–5026.

Lin, C. Z., Hu, M., Wu, A. Z., & Zhu, C. C. (2014). Investigation on the differences of four flavonoids with similar structure binding to human serum albumin. *Journal of Pharmaceutical Analysis, 4*, 392–398.

Lindup, W. E., & Orme, M. C. (1981). Clinical pharmacology: Plasma protein binding of drugs. *British Medical Journal, 282*, 212–214.

Liu, Z., Zheng, X., Yang, X., Wang, E., & Wang, J. (2009). Affinity and specificity of levamlodipine-human serum albumin interactions: Insights into its carrier function. *Biophysical Journal, 96*, 3917–3925.

Liu, B. M., Zhang, J., Bai, C. L., Wang, X., Qiu, X. Z., Wang, X. L., Ji, H., & Liu, B. (2015). Spectroscopic study on flavonoid-drug interactions: Competitive binding for human serum albumin between three flavonoid compounds and ticagrelor, a new antiplatelet drug. *Journal of Luminescence, 168*, 69–76.

Lu, X. L., Fan, J. J., Liu, Y., & Hou, A. X. (2009). Characterization of the interaction between cationic Erbium (III)–porphyrin complex with bovine serum albumin. *Journal of Molecular Structure, 934*, 1–8.

Lukas, D. S., & DeMayimno, A. G. (1969). Binding of digitoxin and some related cardenolides to human plasma proteins. *The Journal of Clinical Investigation, 48*, 1041–1053.

Lv, W., Chen, Y., Li, D., Chen, X., & Leszczynski, J. (2013). Methyl-triclosan binding to human serum albumin: Multi-spectroscopic study and visualized molecular simulation. *Chemosphere, 93*, 1125–1130.

Ma, J., Liu, Y., Chen, L., Xie, Y., Wang, L. Y., & Xie, M. X. (2012). Spectroscopic investigation on the interaction of 3,7-dihydroxyflavone with different isomers of human serum albumin. *Food Chemistry, 132*, 663–670.

Ma, X., Yan, J., Wang, Q., Wu, D., & Li , H. (2015). Spectroscopy study and co-administration effect on the interaction of mycophenolic acid and human serum albumin. *International Journal of Biological Macromolecules, 77*, 280–286.

Madrakian, T., Bagheri, H., Afkhami, A., & Soleimani, M. (2014). Spectroscopic and molecular docking techniques study of the interaction between oxymetholone and human serum albumin. *Journal of Luminescence, 155,* 218–225.

Maiti, T. K., Ghosh, K. S., Samanta, A., & Dasgupta, S. (2008). The interaction of silibinin with human serum albumin: A spectroscopic investigation. *Journal of Photochemistry and Photobiology A: Chemistry, 194,* 297–307.

Majorek, K. A., Porebski, P. J., Dayal, A., Zimmerman, M. D., Jablonska, K., Stewart, A. J., Chruszcz, M., & Minor, W. (2012). Structural and immunologic characterization of bovine, horse, and rabbit serum albumins. *Molecular Immunology, 52,* 174–182.

Mano, H. (1999). Tec family of protein-tyrosine kinases: An overview of their structure and function. *Cytokine and Growth Factor Reviews, 10,* 267–280.

Matei, I., & Hillebrand, M. (2010). Interaction of kaempferol with human serum albumin: A fluorescence and circular dichroism study. *Journal of Pharmaceutical and Biomedical Analysis, 51,* 768–773.

Matsui, J., Funahashi, Y., Uenaka, T., Watanabe, T., Tsuruoka, A., & Asada, M. (2008). Multi-kinase inhibitor E7080 suppresses lymph node and lung metastases of human mammary breast tumor MDA-MB-231 via inhibition of vascular endothelial growth factor-receptor (VEGF-R) 2 and VEGF-R3 kinase. *Clinical Cancer Research, 14,* 5459–5465.

Mathew, P., Yang, J., Kim, S. J., Fidler, I., Bucana, C., Troncoso, P., Wang, X., & Thall, C. (2004). Inhibition of functional osteoblasts with the platelet-derived growth factor receptor (PDGFR) inhibitor imatinib mesylate in androgen-independent prostate cancer (PCa). *Journal of Clinical Oncology, 22,* 4625–4625.

Matthews, B. W. (1986). Solvent content of protein crystals. *Journal of Molecular Biology, 33,* 491−497.

McKeage, K. (2015). Alectinib: A review of its use in advanced ALK-rearranged non-small cell lung cancer. *Drugs, 75,* 75−82.

Medina, P. J., & Goodin, S. (2008). Lapatinib: A dual inhibitor of human epidermal growth factor receptor tyrosine kinases. *Clinical Therapeutics, 30,* 1426–1447.

Mendel, D. B., Laird, A. D., Xin, X., Li, G., Schreck, R., Carver, J., Sukbuntherng, J., Plise, E., Kelsey, S., Scigalla, P., & Cherrington, J. (2002). Development of a preclinical pharmacokinetic/pharmacodynamic relationship for the angiogenesis inhibitor SU11248, a selective inhibitor of VEGF and PDGF receptor tyrosine kinases in clinical development. *Proceedings of the National Academy of Sciences, USA, 21,* 375–767.

Messersmith, W. A., & Ahnen, D. J. (2008). Targeting EGFR in colorectal cancer. *The New England Journal of Medicine, 359,* 1834–1836.

Milella, M., Ciuffreda, L., & Bria, E. (2010). *Signal Transduction Pathways as Therapeutic Targets in Cancer Therapy*. New York: Springer Science and Business Media LLC Press.

Minic, S. L., Milcic, M., Stanic-Vucinic, D., Radibratovic, M., Sotiroudis, T. G., Nikolic, M. R., & Velickovic, T. C. (2015). Phycocyanobilin, a bioactive tetrapyrrolic compound of blue-green alga Spirulina, binds with high affinity and competes with bilirubin for binding on human serum albumin. *RSC Advances, 5,* 61787–61798.

Minkovsky, N., & Berezov, A. (2008). BIBW-2992, a dual receptor tyrosine kinase inhibitor for the treatment of solid tumors. *Current Opinion in Investigational Drugs, 9,* 1336–1346.

Molina-Bolívar, J. A., Galisteo-González, F., Ruiz, C. C., Donnell, M. M., & Parra, A. (2014). Spectroscopic investigation on the interaction of maslinic acid with bovine serum albumin. *Journal of Luminescence, 156,* 141–149.

Molina-Bolívar, J. A., Galisteo-González, F., Ruiz, C. C., Donnell, M. M., & Parra, A. (2015). Interaction between the anti-cancer drug diacetyl maslinic acid and bovine serum albumin: A biophysical study. *Journal of Molecular Liquids, 208,* 304–313.

Montero, M. T., Pouplana, R., Valls, O., & Garcfa, S. (1986). On the binding of cinmetacin and indomethacin to human serum albumin. *Journal of Pharmacy and Pharmacology, 38,* 925–927.

Moreno, F., & González-Jiménez, J. (1999). Binding of the Promen fluorescent probe to human serum albumin: A fluorescence spectroscopic study. *Chemico-Biological Interactions, 121,* 237–252.

Morris, G. M., Goodsell, D. S., Halliday, R. S., Huey, H., Hart, W. E., Belew, R. K., & Olson, A. J. (1998). Automated docking using a Lamarckian genetic algorithm and an empirical binding free energy function. *Journal of Computational Chemistry, 19,* 1639–1662.

Morris, G. M., Huey, R., Lindstrom, W., Sanner, M. F., Belew, R. K., Goodsell, D. S., & Olson, A. J. (2009). AutoDock4 and AutoDockTools4: Automated docking with selective receptor flexibility. *Journal of Computational Chemistry, 30,* 2785–2791.

Morrisett, J. D., David, J. S. K., Pownall, H. J., & Gotto, A. M. (1973). Interaction of an apolipoprotein (apoLP-alanine) with phosphatidylcholine. *Biochemistry, 12,* 1290–1299.

Moy, B., & Goss, P. E. (2006). Lapatinib: Current status and future directions in breast cancer. *The Oncologist, 11,* 1047–1057.

Mudge, G. H., Desbiens, N., & Stibitz, G. R. (1978). Binding of iophenoxate and iopanoate to human serum albumin. *Drug Metabolism and Disposition,* 6, 432–439.

Musolino, A., Campone, M., Neven, P., Denduluri, N., Barrios, C. H., Cortes, J., Blackwell, K., Soliman, H., Kahan, Z., Bonnefoi, H., Squires, M., Zhang, Y., Deudon, S., Shi, M. M., & André, F. (2017). Phase II, randomized, placebo-controlled study of dovitinib in combination with fulvestrant in postmenopausal patients with HR^+, $HER2^-$ breast cancer that had progressed during or after prior endocrine therapy. *Breast Cancer Research, 19,* 1–14.

Nabhan, C., Lestingi, T. M., Galvez, A., Tolzien, K., Kelby, S. K., Tsarwhas, D., Newman, S., & Bitran, J. D. (2009). Erlotinib has moderate single-agent activity in chemotherapy-naive castration-resistant prostate cancer: Final results of a phase II trial. *Urology, 74,* 665–671.

Neamtu, S., Tosa, N., & Bogdan, M. (2013). Spectroscopic investigation of tolmetin interaction with human serum albumin. *Journal of Pharmaceutical and Biomedical Analysis, 85,* 277–282.

Neidle, S., & Thurston, D. E. (2005). Chemical approaches to the discovery and development of cancer therapies. *Nature Reviews Cancer, 5,* 285–296.

Nicholson, J. P., Wolmarans, M. R., & Park, G. R. (2000). The role of albumin in critical illness. *British Journal of Anaesthesia, 85,* 599–610.

Nobili, S., Lippi, D., Witort, E., Donnini, M., Bausi, L., Mini, E., & Capaccioli, S. (2009). Natural compounds for cancer treatment and prevention. *Pharmacological Research, 59,* 365–378.

Olson, R. E., & Christ, D. D. (1996). Plasma protein binding to drugs. *Annual Reports in Medicinal Chemistry, 31,* 327–336.

Olsson, T. S. G., Williams, M. A., Pitt, W. R., & Ladbury, J. E. (2008). The thermodynamics of protein-ligand interaction and solvation: Insights for ligand design. *Journal of Molecular Biology, 384,* 1002–1017.

Oncley, J. L., Scatchard, G., & Brown, A. (1947). Physical-chemical characteristics of certain of the proteins of normal human plasma. *The Journal of Physical Chemistry, 51,* 184–198.

Ono, M., & Kuwano, M. (2006). Molecular mechanisms of epidermal growth factor receptor (EGFR) activation and response to gefitinib and other EGFR-targeting drugs. *Clinical Cancer Research, 12,* 7242–7251.

Painter, L., Harding, M. M., & Beeby, P. J. (1998). Synthesis and interaction with human serum albumin of the first 3,18-disubstituted derivative of bilirubin. *Journal of Chemical Society, Perkin Transactions (1), 18,* 3041–3044.

Pal, S., & Saha, C. (2014). A review on structure-affinity relationship of dietary flavonoids with serum albumins. *Journal of Biomolecular Structure and Dynamics, 32,* 1132–1147.

Papadopoulou, A., Green, R. J., & Franzier, R. A. (2005). Interaction of flavonoids with bovine serum albumin: A fluorescence quenching study. *Journal of Agricultural and Food Chemistry, 53,* 158−163.

Paul, M. K., & Mukhopadhyay, A. K. (2004). Tyrosine kinase – Role and significance in cancer. *International Journal of Medical Sciences, 1,* 101–115.

Peters, T. Jr. (1996). *All About Albumin: Biochemistry, Genetics, and Medical Applications.* San Diego: Academic Press.

Petitpas, I., Bhattacharya, A. A., Twine, S., East, M., & Curry, S. (2001). Crystal structure analysis of warfarin binding to human serum albumin: Anatomy of drug site I. *The Journal of Biological Chemistry, 276,* 22804–22809.

Pettersen, E. F., Goddard, T. D., Huang, C. C., Cough, G. S., Greenblatt, D. M., Meng, E. C., & Ferrin, T. E. (2004). UCSF Chimera – A visualization system for exploratory research and analysis. *Journal of Computational Chemistry, 25,* 1605–1612.

Pico, G. A. (1997). Thermodynamic features of the thermal unfolding of human serum albumin. *International Journal of Biological Macromolecules, 20,* 63–73.

Putnam, F. W. (1975). *The Plasma Proteins (2nd ed.)*. New York: Academic Press.

Quinlan, G. J., Martin, G. S., & Evans, T. W. (2005). Albumin: Biochemical properties and therapeutic potential. *Hepatology, 41,* 1211–1219.

Rahman, M. H., Yamasaki, K., Shin, Y. H., Lin, C. C., Otagiri, M. (1993a). Characterization of high affinity binding sites of non-steroidal anti-inflammatory drugs with respect to site-specific probes on human serum albumin. *Biological and Pharmaceutical Bulletin, 16,* 1169–1174.

Rahman, M. H., Maruyama, T., Okada, T., Yamasaki, K., & Otagiri, M. (1993b). Study of interaction of carprofen and its enantiomers with human serum albumin – I: Mechanism of binding studied by dialysis and spectroscopic methods. *Biochemical Pharmacology, 46,* 1721–1731.

Rastegari, B., Karbalaei-Heidari, H. R., Yousefi, R., Zeinali, S., & Nabavizadeh, M. (2016). Interaction of prodigiosin with HSA and β-Lg: Spectroscopic and molecular docking studies. *Bioorganic and Medicinal Chemistry, 24,* 1504–1512.

Raval, S.H., Singh, R. D., Joshi, D. V., Patel, H. B., & Mody, S. K. (2016) Recent developments in receptor tyrosine kinases targeted anticancer therapy. *Veterinary World, 9,* 80–90.

Raymond, E., Faivre, S., & Armand, J. P. (2000). Epidermal growth factor receptor tyrosine kinase as a target for anticancer therapy. *Drugs, 60,* 15–23.

Reed, R. G., Feldhoff, R. C., Clute, L., & Peters, T., Jr. (1975). Fragments of bovine serum albumin produced by limited proteolysis. Conformation and ligand binding. *Biochemistry, 14,* 4578–4583.

Rini, B. I., Tamaskar, I., Shaheen, P., Salas, R., Garcia, J., Wood, L., Reddy, S., Dreicer, R., & Bukowski, R. M. (2007). Hypothyroidism in patients with

metastatic renal cell carcinoma treated with sunitinib. *Journal of the National Cancer Institute, 99,* 81–83.

Rock, E. P., Goodman, V., Jiang, J. X., Mahjoob, K., Verbois, S. L., Morse, D., Dagher, R., Justice, R., & Pazdur, R. (2007). Food and drug administration drug approval summary: Sunitinib malate for the treatment of gastrointestinal stromal tumor and advanced renal cell carcinoma. *The Oncologist, 12,* 107–113.

Ross, P. D., & Subramanian, S. (1981). Thermodynamics of protein association reactions: Forces contributing to stability. *Biochemistry, 20,* 3096–3102.

Rowland, M., & Tozer, T. N. (2010). *Clinical Pharmacokinetics and Pharmacodynamics: Concepts and Applications (4th ed.).* Philadelphia: Lippincott Williams and Wilkins Press.

Rowinsky, E. K. (2003). Signal events: Cell signal transduction and its inhibition in cancer. *The Oncologist, 8,* 5–17.

Roy, A. S., Tripathy, D. R., Chatterjee, A., & Dasgupta, S. (2013). The influence of common metal ions on the interactions of the isoflavone genistein with bovine serum albumin. *Spectrochimica Acta Part A: Molecular and Biomolecular Spectroscopy, 102,* 393–402.

Russeva, V., Stavreva, N., Rakovska, R., & Michailova, D. (1994). Binding of sulindac to human serum albumin studied by circular dichroism. *Arzneimittel-Forschung, 44,* 159–162.

Saeidifar, M., Mansouri-Torshizi, H., & Saboury, A. A. (2015). Biophysical study on the interaction between two palladium (II) complexes and human serum albumin by multispectroscopic methods. *Journal of Luminescence, 167,* 391–398.

Sahai, E., & Marshall, C. J. (2002). Rho–GTPases and cancer. *Nature Reviews Cancer, 2,* 133–142.

Sahu, A., Prabhash, K., Noronha, V., Joshi, A., & Desai, S. (2013). Crizotinib: A comprehensive review. *South Asian Journal of Cancer, 2,* 91–97.

Saini, K. S., Taylor, C., Ramirez, A. J., Palmieri, C,. Gunnarsson, U., Schmoll, H. J., Dolci, S. M., Ghenne, C., Metzger-Filho, O., Skrzypski, M., Paesmans, M., Ameye, L., Piccart-Gebhart, M. J., & Azambuja, E. D. (2012). Role of the multidisciplinary team in breast cancer management: Results from a large international survey involving 39 countries. *Annals of Oncology, 23,* 853–859.

Salomon, D. S., Brandt, R., Ciardiello, C. & Normanno, N. (1995). Epidermal growth factor-related peptides and their receptors in human malignancies. *Critical Reviews in Oncology/Hematology, 19,* 183–232.

Samari, F., Shamsipur, M., Hemmateenejad, B., Khayamian, T., & Gharaghani, S. (2012). Investigation of the interaction between amodiaquine and human serum albumin by fluorescence spectroscopy and molecular modeling. *European Journal of Medicinal Chemistry, 54,* 255−263.

Sancataldo, G., Vetri, V., Fodera, V., Cara, G. D., Militello, V., & Leone, M. (2014). Oxidation enhances human serum albumin thermal stability and changes the routes of amyloid fibril formation. *PLoS ONE, 9,* e84552.

Sano, D., Fooshee, D. R., Zhao, M., Andrews, G. A., Frederick, M. J., Galer, C., Milas, Z. L., Morrow, P. K., & Myers, J. N. (2011). Targeted molecular therapy of head and neck squamous cell carcinoma with the tyrosine kinase inhibitor vandetanib in a mouse model. *Head & Neck, 33,* 349–358.

Sanner, M. F. (1999). Python: A programming language for software integration and development. *Journal of Molecular Graphics and Modelling, 17,* 57–61.

Schmid, T. A., & Gore, M. E. (2016). Sunitinib in the treatment of metastatic renal cell carcinoma. *Therapeutic Advances in Urology, 8,* 348–371.

Ségaliny, A. I., Tellez-Gabriel, M., Heymann, M. F., & Heymann, D. (2015). Receptor tyrosine kinases: Characterisation, mechanism of action and therapeutic interests for bone cancers. *Journal of Bone Oncology, 4,* 1–12.

Shahabadi, N., Hadidi, S., & Feizi, F. (2015). Study on the interaction of antiviral drug 'Tenofovir' with human serum albumin by spectral and molecular modeling methods. *Spectrochimica Acta Part A: Molecular and Biomolecular Spectroscopy, 138,* 169–175.

Shahabadi, N., Hadidi, S., & Kalar, Z. M. (2016). Biophysical studies on the interaction of platinum (II) complex containing antiviral drug ribavirin with human serum albumin. *Journal of Photochemistry & Photobiology, B: Biology, 160,* 376–382.

Shaw, A. T., Kim, D. W., Mehra, R. Tan, D. S., Felip, E., Solomon, B. J. Wolf, J., Thomas, M., Schuler, M., Liu, G., Santoro, A., Lau, Y. Y., Goldwasser, M., Boral, A. L., & Engelman, J. A. (2014). Ceritinib in *ALK*-rearranged non–small-cell lung cancer. *The New England Journal of Medicine, 370,* 1189–1197.

Shen, G. F., Liu, T. T., Wang, Q., Jiang, M., & Shi, J. H. (2015). Spectroscopic and molecular docking studies of binding interaction of gefitinib, lapatinib and sunitinib with bovine serum albumin (BSA). *Journal of Photochemistry and Photobiology B: Biology, 153,* 380–390.

Shih, I. M., & Wang, T. L. (2007). Notch signaling, γ-secretase inhibitors, and cancer therapy. *Cancer Research, 67,* 1879–1882.

Shrake, A., & Ross, P.D. (1988). Biphasic denaturation of human albumin due to ligand redistribution during unfolding. *The Journal of Biological Chemistry, 263,* 15392–15399.

Silva, D., Cortez, C. M., Silva, C. M., & Missailidis, S. (2013). A fluorescent spectroscopy and modeling analysis of anti-heparanase aptamers-serum protein interactions. *Journal of Photochemistry and Photobiology B: Biology, 127,* 68–77.

Sjöholm, I., Ekman, B., Kober, A., Ljungstedt-Paahlman, I., Seiving, B., & Sjödin, T. (1979). Binding of drugs to human serum albumin: XI. The specificity of three

binding sites as studied with albumin immobilized in microparticles. *Molecular Pharmacology, 16,* 767–777.

Smith, D. A., Di, L., & Kerns, E. H. (2010). The effect of plasma protein binding on in vivo efficacy: Misconceptions in drug discovery. *Nature Reviews Drug Discovery, 9,* 929–939.

Smith, M. R., Sweeney, C. J., Corn, P. G., Rathkopf, D. E., Smith, D. C., Hussain, M., George, D. J., Higano, C. S., Harzstark, A. L., Schimmoller, F., Basch, E. M., & Scher, H. I. (2014). Cabozantinib in chemotherapy-pretreated metastatic castration-resistant prostate cancer: Results of a phase II nonrandomized expansion study. *Journal of Clinical Oncology, 32,* 3391-3399.

Solomon, B., & Rischin, D. (2012). Progress in molecular targeted therapy for thyroid cancer: Vandetanib in medullary thyroid cancer. *Journal of Clinical Oncology, 30,* 119–121.

Stamler, J. S., Jaraki, O., Osborne, J., Simon, D. I., Keaney, J., Vita, J., Singeli, D., Valerit, C. R., & Loscalzo, J. (1992). Nitric oxide circulates in mammalian plasma primarily as an S-nitroso adduct of serum albumin. *Proceedings of the National Academy of Sciences, USA, 89,* 7674–7677.

Steward, W., Thomas, A., Morgan, B., Wiedenmann, B., Bartel, C., Vanhoefer, U., Trarbach, T., Riedel, U., Laurent, D., & Reitsma, D. (2003). Extended phase I/II study of the oral vascular endothelial growth factor (VEGF) receptor inhibitor PTK787/Zk222854 in combination with oxaliplatin/5-fluorouracil/leucovorin as first-line treatment for metastatic colorectal cancer. *American Society of Clinical Oncology, 22,* 1098–1113.

Stewart, B. W., & Wild, C.P. (2014). *World Cancer Report 2014*. World Health Organization.

Sudlow, G., Birkett, D. J., & Wade, D. N. (1975). The characterization of two specific drug binding sites on human serum albumin. *Molecular Pharmacology, 11,* 824–832.

Sugio, S., Kashima, A., Mochizuki, S., Noda, M., & Kobayashi, K. (1999). Crystal structure of human serum albumin at 2.5 Å resolution. *Protein Engineering, 12,* 439–446.

Sulkes, A. (2010). Novel multitargeted anticancer oral therapies: Sunitinib and sorafenib as a paradigm. *The Israel Medical Association Journal, 12,* 628–632.

Sulkowska, A. (2002). Interaction of drugs with bovine and human serum albumin. *Journal of Molecular Structure, 614,* 227–232.

Summers, K. C., Shen, F., Potchanant, E. A. S., Phipps, E. A., Hickey, R. J., & Malkas, L. H. (2011). Phosphorylation: The molecular switch of double-strand break repair. *International Journal of Proteomics, 2011,* 1–8.

Sun, Z., Xu, H., Cao, Y., Wang, F., & Mi, W. (2016). Elucidating the interaction of propofol and serum albumin by spectroscopic and docking methods. *Journal of Molecular Liquids, 219,* 405–410.

Taghavi, F., Moosavi-Movahedi, A. A., Bohlooli, M., Habibi-Rezaei, M., Hadi Alijanvand, H., Amanlou, M., Sheibani, N., Saboury, A. A., & Ahmad, F. (2014). Energetic domains and conformational analysis of human serum albumin upon co-incubation with sodium benzoate and glucose. *Journal of Biomolecular Structure and Dynamics, 32,* 438–447.

Tan, C. S., Gilligan, D., & Pacey, S. (2015). Treatment approaches for EGFR-inhibitor-resistant patients with non-small-cell lung cancer. *The Lancet Oncology, 16,* 447–459.

Tanford, C. (1950). Preparation and properties of serum and plasma proteins. XXIII. Hydrogen ion equilibria in native and modified human serum albumins. *Journal of the American Chemical Society, 72,* 441−451.

Tanaka, M., Asahi, Y., & Masuda, S. (1995). Interaction between drugs and water-soluble polymers. VII. Binding of berberine with bovine serum albumin. *Journal of Macromolecular Science, Part A: Pure and Applied Chemistry, 32,* 339–347.

Tesseromatis, C., & Alevizou, A. (2008). The role of the protein-binding on the mode of drug action as well the interactions with other drugs. *European Journal of Drug Metabolism and Pharmacokinetics, 33,* 225–230.

Tevaarwerk, A. J., & Kolesar, J. M. (2009). Lapatinib: A small-molecule inhibitor of epidermal growth factor receptor and human epidermal growth factor receptor-2 tyrosine kinases used in the treatment of breast cancer. *Clinical Therapeutics, 31,* 2332–2348.

Tiffany, N. M., Wersinger, E. M., Garzotto, M., & Beer, T. M. (2004). Imatinib mesylate and zoledronic acid in androgen-independent prostate cancer. *Urology, 63,* 934–939.

Toffalini, F. & Demoulin, J. B. (2010). New insights into the mechanisms of hematopoietic cell transformation by activated receptor tyrosine kinases. *Blood, 116,* 2429–2437.

Torre, L. A., Siegel, R. L., Ward, E. M., & Jemal, A. (2016). Global cancer incidence and mortality rates and trends – An update. *Cancer Epidemiology, Biomarkers and Prevention, 25,* 16–27.

Tourneau, C. L., Raymond, E., & Faivre, S. (2007). Sunitinib: A novel tyrosine kinase inhibitor. A brief review of its therapeutic potential in the treatment of renal carcinoma and gastrointestinal stromal tumors (GIST). *Therapeutics and Clinical Risk Management, 3,* 341–348.

Trnková, L., Boušová, I., Staňková, V., & Dršata, J. (2011). Study on the interaction of catechins with human serum albumin using spectroscopic and electrophoretic techniques. *Journal of Molecular Structure, 985,* 243–250.

Trzcinska-Daneluti, A. M., Nguyen, L., Jiang, C., Fladd, C., Uehling, D., Prakesch, M., Al-awar, R., & Rotin, D. (2012). Use of kinase inhibitors to correct F508-CFTR function. *Molecular and Cellular Proteomics, 11,* 745–757.

Tsang, R. Y., Sadeghi, S., & Finn, R. S. (2011). Lapatinib, a dual-targeted small molecule inhibitor of EGFR and HER2, in HER2-amplified breast cancer: From bench to bedside. *Clinical Medicine Insights: Therapeutics, 3,* 1–13.

Tu, B., Wang, Y., Mi, R., Ouyang, Y., & Hu, Y. J. (2015). Evaluation of the interaction between naringenin and human serum albumin: Insights from fluorescence spectroscopy, electrochemical measurement and molecular docking. *Spectrochimica Acta Part A: Molecular and Biomolecular Spectroscopy, 149,* 536–543.

Tunç, S., Çetinkaya, A., & Duman, O. (2013a). Spectroscopic investigations of the interactions of tramadol hydrochloride and 5-azacytidine drugs with human serum albumin and human hemoglobin proteins. *Journal of Photochemistry and Photobiology B: Biology, 120,* 59–65.

Tunc, S., Duman, O. & Bozoglan, B. K. (2013b). Studies on the interactions of chloroquine diphosphate and phenelzine sulfate drugs with human serum albumin and human hemoglobin proteins by spectroscopic techniques. *Journal of Luminescence, 140,* 87−94.

Tunc, S, Duman, O., Soylu, I., & Bozoglan, B. K. (2014). Spectroscopic investigation of the interactions of carbofuran and amitrol herbicides with human serum albumin, *Journal of Luminescence, 151,* 22–28.

Twine, S. M., Gore, M. G., Morton, P., Fish, B. C., Lee, A. G., & East, J. M. (2003). Mechanism of binding of warfarin enantiomers to recombinant domains of human albumin. *Archives of Biochemistry and Biophysics, 414,* 83−90.

Uversky, V. N., Narizhneva, N. V., Ivanova, T. V., & Tomashevski, A. Y. (1997). Rigidity of human α-fetoprotein tertiary structure is under ligand control. *Biochemistry, 36,* 13638–13645.

Vanneman, M., & Dranoff, G. (2012). Combining immunotherapy and targeted therapies in cancer treatment. *Nature Reviews Cancer, 12,* 237–251.

Wallace, A. C., Laskowski, R. A., & Thornton, J. M. (1995). LIGPLOT: A program to generate schematic diagrams of protein-ligand interactions. *Protein Engineering, 8,* 127–134.

Wan, X., Zheng, X., Pang, X., Zhang, Z., & Zhang, Q. (2015). Incorporation of lapatinib into human serum albumin nanoparticles with enhanced anti-tumor effects in HER2-positive breast cancer. *Colloids and Surfaces B: Biointerfaces, 136,* 817–827.

Wang, G., Wang, D., Li, X., & Lu, Y. (2011). Exploring the binding mechanism of dihydropyrimidinones to human serum albumin: Spectroscopic and molecular modeling techniques. *Colloids and Surfaces B: Biointerfaces, 84,* 272–279.

Wang, Q., Sun, Q., Tang, P., Tang, B., He, J., Ma, X., & Li, H. (2015). Determination of potential main sites of apixaban binding in human serum albumin by combined spectroscopic and docking investigations. *RSC Advances, 5,* 81696–81706.

Ware, W. R. (1962). Oxygen quenching of fluorescence in solution: An experimental study of the diffusion process. *The Journal of Physical Chemistry, 66,* 455–458.

Watanabe, H., Kragh-Hansen, U., Tanase, S., Nakajou, K., Mitarai, M., Iwao, Y., Maruyama, T., & Otagiri, M. (2001). Conformational stability and warfarin-binding properties of human serum albumin studied by recombinant mutants. *Biochemical Journal, 357,* 269–274.

Wedge, S. R., Ogilvie, D. J., Dukes, M., Kendrew, J., Chester, R., Jackson, J. A., Boffey, S. J., Valentine, P. J., Musgrove, H. l., Graham, G. A., Hughes, G. D., Thomas, A. P., Stockes, E. S., Curry, B., Richmond, G. H., Wadsworth, P. F., Bigley, A. L., & Hennequin L. F. (2002). ZD6474 inhibits vascular endothelial growth factor signaling, angiogenesis, and tumor growth following oral administration. *Cancer Research, 62,* 4645–4655.

Wetterskog, D., Shiu, K. K., Chong, I., Meijer, T., Mackay, A., Lambros, M., Cunningham, D., Reis-Filho, J. S., Lord, C. J., & Ashworth, A. (2014). Identification of novel determinants of resistance to lapatinib in ERBB2-amplified cancers. *Oncogene, 33,* 966–976.

Wicki, A., Mandala, M., Massi, D., Taverna, D., Tang, H., Hemmings, B. A., & Xue, G. (2016). Acquired resistance to clinical cancer therapy: A twist in physiological signaling. *Physiological Reviews, 96,* 805–829.

Xu, H., Yao, N., Xu, H., Wang, T., Li, G., & Li, Z. (2013). Characterization of the interaction between eupatorin and bovine serum albumin by spectroscopic and molecular modeling methods. *International Journal of Molecular Sciences, 14,* 14185–14203.

Yang, F., Yue, J., Ma, L., Ma, Z., Li, M., Wu, X., & Liang, H. (2012). Interactive associations of drug−drug and drug−drug−drug with IIA subdomain of human serum albumin. *Molecular Pharmaceutics, 9,* 3259−3265.

Yang, F., Zhang, Y., & Liang, H. (2014). Interactive association of drugs binding to human serum albumin. *International Journal of Molecular Sciences, 15,* 3580–3595.

Yamasaki, K., Maruyama, T., Kragh-Hansen, U., & Otagiri, M. (1996). Characterization of site I on human serum albumin: Concept about the structure of a drug binding site. *Biochimica et Biophysica Acta – Protein Structure and Molecular Enzymology, 1295,* 147–157.

Yamasaki, K., Chuang, V. T., Maruyama, T., & Otagiri, M. (2013). Albumin drug interaction and its clinical implication. *Biochimica et Biophysica Acta – General Subjects, 1830,* 5435–5443.

Yanase, K., Tsukahara, S., Asada, S., Ishikawa, E., Imai, Y., & Sugimoto, Y. (2004). Gefitinib reverses breast cancer resistance protein–mediated drug resistance. *Molecular Cancer Therapeutics, 3,* 1119–1125.

Yeggoni, D. P., Rachamallu, A., Kallubai, M., & Subramanyam, R. (2015). Cytotoxicity and comparative binding mechanism of piperine with human serum albumin and α-1-acid glycoprotein. *Journal of Biomolecular Structure and Dynamics, 33,* 1336–1351.

Yoh, K., Seto, T., Satouchi, M., Nishio, M., Yamamoto, N., Murakami, H., Nogami, N., Matsumoto, S., Kohno, T., Tsuta, K., Tsuchihara, K., Ishii, G., Nomura, S., Sato, A., Ohtsu, A., Ohe, Y., & Goto, K. (2016). Vandetanib in patients with previously treated RET-rearranged advanced non-small-cell lung cancer (LURET): An open-label, multicentre phase 2 trial. *The Lancet, 5,* 42–50.

Yoshikawa, D., Ojima, H., Kokubu, A., Ochiya, T., Kasai, S., Hirohashi, S., & Shibata, T. (2009). Vandetanib (ZD6474), an inhibitor of VEGFR and EGFR signalling, as a novel molecular-targeted therapy against cholangiocarcinoma. *British Journal of Cancer, 100,* 1257–1266.

Zhang, Y. Z., Dai, J., Zhang, X. P., Yang, X., & Liu, Y. (2008). Studies of the interaction between sudan I and bovine serum albumin by spectroscopic methods. *Journal of Molecular Structure, 888,* 152–159.

Zsila, F., Bikadi, Z., Malik, D., Hari, P., Pechan, I., Berces, A., & Hazai, E. (2011). Evaluation of drug–human serum albumin binding interactions with support vector machine aided online automated docking. *Bioinformatics, 27,* 1806–1813.

Zsila, F. (2013). Subdomain IB is the third major drug binding region of human serum albumin: Toward the three-sites model. *Molecular Pharmaceutics, 10,* 1668−1682.

Zunszain, P. A., Ghuman, J., Komatsu, T., Tsuchida, E., & Curry, S. (2003). Crystal structural analysis of human serum albumin complexed with hemin and fatty acid. *BMC Structural Biology, 3,* 1–9.

Zunszain, P. A., Ghuman, J., McDonagh, A. F., & Curry, S. (2008). Crystallographic analysis of human serum albumin complexed with 4Z,15E-bilirubin-IXα. *Journal of Molecular Biology, 381,* 394−406.

LIST OF PUBLICATIONS AND PAPERS PRESENTATED

Publications

1. **Kabir, M. Z.,** Feroz, S. R., Mukarram, A. K., Alias, Z., Mohamad, S. B., & Tayyab, S. (2016). Interaction of a tyrosine kinase inhibitor, vandetanib with human serum albumin as studied by fluorescence quenching and molecular docking. *Journal of Biomolecular Structure and Dynamics, 34*, 1693–1704.

2. **Kabir, M. Z.,** Mukarram, A. K., Mohamad, S. B., Alias, Z., & Tayyab, S. (2016). Characterization of the binding of an anticancer drug, lapatinib to human serum albumin. *Journal of Photochemistry and Photobiology B: Biology*, *160*, 229–239.

3. Tayyab, S., Izzudin, M. M., **Kabir, M. Z.,** Feroz, S. R., Tee, W-V., Mohamad, S. B., & Alias, Z. (2016). Binding of an anticancer drug, axitinib to human serum albumin: Fluorescence quenching and molecular docking study. *Journal of Photochemistry and Photobiology B: Biology*, *162*, 386–394.

4. **Kabir, M. Z.,** Tee, W-V., Mohamad, S. B., Alias, Z., & Tayyab, S. (2016). Interaction of an anticancer drug, gefitinib with human serum albumin: Insights from fluorescence spectroscopy and computational modeling analysis. *RSC Advances*, *6*, 91756–91767.

5. **Kabir, M. Z.,** Tee, W-V., Mohamad, S. B., Alias, Z., & Tayyab, S. (2017). Comprehensive insight into the binding of sunitinib, a multi-targeted anticancer drug to human serum albumin. *Spectrochimica Acta Part A: Molecular and Biomolecular Spectroscopy*, *181*, 254–263.

6. **Kabir, M. Z.,** Ghani, H., Mohamad, S. B., Alias, Z., & Tayyab, S. (2017). Interactive association between RhoA transcriptional signaling inhibitor,

CCG1423 and human serum albumin: Biophysical and *in silico* studies. *Journal of Biomolecular Structure and Dynamics* – In press (DOI: 10.1080/07391102.2017.1360207).

7. **Kabir, M. Z.,** Hamzah, N. A. B., Ghani, H., Mohamad, S. B., Alias, Z., & Tayyab, S. (2018). Biophysical and computational characterization of vandetanib–lysozyme interaction. *Spectrochimica Acta Part A: Molecular and Biomolecular Spectroscopy*, *189*, 485–494.

Presentations

1. **Kabir, M. Z.,** Feroz, S. R., Mukarram, A. K., Mohamad, S. B., Alias, Z., & Tayyab, S. (2015). Spectroscopic and molecular docking studies on the interaction of vandetanib, a tyrosine kinase inhibitor with human serum albumin. *Proceedings of the 40th Annual Conference of the Malaysian Society for Biochemistry and Molecular Biology, held at Putrajaya, Malaysia on June 10–11, 2015.* Abstract No. Poster 15, pp. 55. (selected for the Best Poster Award).

2. **Kabir, M. Z.,** Mukarram, A. K., Mohamad, S. B., Alias, Z., & Tayyab, S. (2015). Use of spectroscopic and computational methods to characterize the binding of an anticancer drug, lapatinib to human serum albumin. *Proceedings of the 20th Biological Sciences Graduate Congress, held at Chulalongkorn University, Bangkok, Thailand on December 09–11, 2015.* Abstract No. BC-PO 11, pp. 116.